Self-Assembly of Ordered Pyridinium Layers at Halide Precovered Copper(100)/Electrolyte Interfaces

Dissertation
zur
Erlangung des Doktorgrades (Dr. rer. nat.)
der
Mathematisch-Naturwissenschaftlichen Fakultät
der
Rheinischen Friedrich-Wilhelms-Universität Bonn

vorgelegt von
Martino Saracino
aus
Stuttgart

Bonn 2013

Angefertigt mit Genehmigung der Mathematisch-Naturwissenschaftlichen Fakultät der
Rheinischen Friedrich-Wilhelms-Universität Bonn

1. Gutachter Professor Dr. Klaus Wandelt
2. Gutachter Professor Dr. Rudolf Merkel
Tag der Promotion: 11. Juli 2013
Erscheinungsjahr: 2013

Abstract

The present work aims at elaborating a microscopic understanding of the monolayer formation of bi- and dipyridinium cations on an electrochemically controlled Cl anion covered or bare Cu(100) electrode surface as substrate, with particular focus on the role of the intra-molecular flexibility and spread of the molecular π-system. The application of organic cations and their monolayers are vast as they may serve as protective coatings, functional layers in the fields of organic electronics / optoelectronic or as key component in electrochemical state-of-the-art manufacturing processes.

Besides their practical application, the chosen organic cations are model systems to study the influence of molecular groups – in this work the pyridinium rings, benzyl substituents, pyridinium cations and saturated organic chains – on the formation of organic monolayers at electrode surface, as well as their effect on surface processes, such as the electrochemical Cu deposition/dissolution, in general. The insight gained from the performed experiments contribute to the fundamental understanding, which is necessary to develop, improve or specifically tailor organic building blocks for the construction of functional nano-architectures at surfaces.

Since the 3D structure of the electrolyte / Cu(100) interface is up to date under discussion in literature, at first combined Cyclic Voltametry (CV), *in situ* Surface X-Ray Diffraction (SXRD) and *in situ* Scanning Tunneling Microscopy (STM) are performed in order to study the 2D and 3D structure of an electrochemically controlled Cu(100) electrode in a 10 mM halide anion (Cl or Br anion) containing electrolyte solution. Both, Cl and Br anions, form at sufficiently high electrode potentials a full halide-c(2x2) monolayer on the Cu(100) electrode, occupying half of the available four-fold hollow sites of the Cu(100) substrate. The halide-c(2x2) monolayers affect the relaxations of the topmost Cu layers. In case of a Br-c(2x2) adlayer these layer relaxations depend on the electrode potential.

Several *in situ* SXRD studies proved that the 3D models of the halide-c(2x2) monolayer adsorbed on the Cu(100) electrode fail to explain the experimental SXRD data. Indeed, one also needs to consider the formation of a weakly bound but in-plane ordered Layer of Solvated CounterIons (LSCI) (K^+ and H_3O^+) adsorbed on top of the halide anion monolayer. These solvated counterions adsorb into the four-fold hollow sites of the halide-c(2x2)/Cu(100) electrode surface. The in-plane ordered LSCI is only occupied by 20% of a full monolayer (ML) and its symmetry is dictated by the underlying halide-c(2x2) structure, as the symmetry of the halide-c(2x2) is imposed by the Cu(100) electrode surface.

Subsequently two viologens (1,1'-disubstitued-4,4'-bipyridinium cations), namely DiBenzylViologen (DBV) and DiPhenylViologen (DPV), as well as a 1:1 mixture of both molecules is investigated by CV and *in situ* STM at the Cl-c(2x2)/Cu(100) electrode.

The study of the mixed viologen solution permits to analyze their relative adsorption energies and to study their competition for adsorption and reaction sites at the electrode surface. The dication DPV^{2+} is upon adsorption immediately reduced to the monocation radical $DPV^{+\bullet}$ and forms – in the pure DPV^{2+} and mixed viologen solution – its characteristic $DPV^{+\bullet}$ π-stacked stripe phase. The formed $DPV^{+\bullet}$ π-stacked stripes prevent the adsorption of DBV^{2+} and, consequently, the formation of the DBV^{2+} cavitand phase, as it occurs in pure DBV^{2+} solution on the Cl/Cu(100) substrate. Despite the densely packed $DPV^{+\bullet}$ π-stacked stripes adsorbed on the electrode surface, DBV^{2+} from solution can be electrochemically reduced at the Cu(100) electrode to its monocation radical state $DBV^{+\bullet}$ at electrode potentials lower than $E_{work} = -270\,mV$ [vs. RHE]. The formed monocation radicals $DBV^{+\bullet}$ substitute the stiffer $DPV^{+\bullet}$ on the Cl/Cu(100) electrode and subsequently arrange in *their* characteristic $DBV^{+\bullet}$ π-stacked stripe phase. The $DBV^{+\bullet}$ π-stacked stripe phase remains adsorbed on the Cl/Cu(100) electrode until either the Cl-c(2x2) monolayer desorbs at lower potentials or the adsorbed monocation radicals $DBV^{+\bullet}$ are re-oxidized to their dication state at higher potentials. The desorption of the Cl anion monolayer occurs at $E_{work} < -360\,mV$ [vs. RHE] and induces an order-disorder transition of the $DBV^{+\bullet}$ π-stacked stripe phase to an amorphous viologen layer. The oxidation of *adsorbed* monocation radical $DBV^{+\bullet}$ occurs at $E_{work} > -100\,mV$ [vs. RHE], which is $+130\,mV$ higher than the oxidation potential of $DBV^{+\bullet}$ *from solution*. Upon oxidation of the adsorbed $DBV^{+\bullet}$ to DBV^{2+}, the dication is displaced by the monocation radicals $DPV^{+\bullet}$, which again form their π-stacked stripe phase on the Cl/Cu(100) substrate. Therefore the DBV^{2+} cavitand phase can not be formed and remains unobserved in the study of the mixed viologen solution.

In earlier studies only the viologen substituents were varied, but the 4,4'-bipyridinium core (= viologen core) remained unchanged. In order to challenge this limitation, in this work the 4,4'-bipyridinium core of DBV was modified in three different ways, namely to a 3,3'-bipyridinium, as well as a 4,4'-(propane-1,3-diyl)-dipyridinium and a 4,4'-(heptane-1,7-diyl)-dipyridinium core. The resulting molecules are abbreviated as DB-3,3'-BP (1,1´-Dibenzyl-3,3´-bipyridinium), C3-DBDP (1,1'-Dibenzyl-4,4'-(propane-1,3-diyl)-dipyridinium) and C7-DBDP (1,1'-Dibenzyl-4,4'-(heptane-1,7-diyl)-dipyridinium). Due to the insertion of the C3 or C7 alkyl chain into the 4,4'-bipyridinium core (= viologen core), these new molecules are no longer part of the viologen family. Although the molecules are no longer part of the same molecular family, they all (DBV, DB-3,3'-BP, C3-DBDP and C7-DBDP) consist of two pyridinium-benzyl moieties, which are either directly connected (in DBV and DB-3,3'-BP) or separated by a saturated alkyl chain (in C3-DBDP and C7-DBDP). Therefore the pyridinium-benzyl moiety substitutes the 4,4'-bipyridinium core and becomes the new fundamental molecular unit common to all in this work studied organic cations.

All three new organic dications (DB-3,3'-BP^{2+} , C3-$DBDP^{2+}$ and C7-$DBDP^{2+}$) possess a lower redox activity than the reference organic dication (DBV^{2+}), as non of them is reduced to a lower redox state within the potential window of the Cu(100) electrode. The lower redox activity of C3-$DBDP^{2+}$ and C7-$DBDP^{2+}$ can be understood as a result of the fragmentation of the viologen bipyridinium π-system into two isolated pyridinium π-system. This fragmentation prevents the stabilization of the reduced molecular state,

i.e. radical state, through delocalization over the whole bipyridinium core, as the interaction between the two pyridinium π-systems is prevented by the saturated alkyl chain. In addition to the conservation of the dication state of C3-DBDP^{2+} and C7-DBDP^{2+} in solution, the conservation of the dication state throughout their adsorption and monolayer formation on the Cl/Cu(100) substrate was proven separately via *ex situ* X-ray Photoelectron Spectroscopy (XPS) experiments.

Furthermore the structure formation of all three – DBV related – organic dications was studied via *in situ* STM. DB-3,3'-BP^{2+}, which possess the same molecular flexibility as DBV^{2+}, does not form an ordered organic monolayer but an amorphous layer on the Cl/Cu(100) electrode surface. Neither the increase of the adsorption time to several days, nor the increase of the molecular concentration within the solution from 0.1 mM up to 25 mM did result in the formation of an ordered monolayer. In contrast to this, DBV^{2+} forms its cavitand phase almost instantaneously at a concentration of 0.1 mM on the same substrate. The missing ordered DB-3,3'-BP^{2+} monolayer was assumed to result from a sterical hindrance of the interaction between DB-3,3'-BP^{2+} dications and the Cl/Cu(100) electrode.

C3-DBDP^{2+}, which possess a higher molecular flexibility than DBV^{2+}, forms an ordered inter-linked stripe phase, in which the pyridinium-benzyl moieties arrange consecutively with a distance of 0.45 nm and form stripes. These stripes are linked alternating to the left and the right to neighboring pyridinium-benzyl stripes, which are at a distance of 1.2 nm. The inter-molecular electrostatic attraction between directly facing pyridinium cations and negative benzyl π-systems stabilizes the final C3-DBDP^{2+} inter-linked stripe phase, whereas adsorbate-substrate interactions are of minor importance for the final inter-linked stripe structure. Indeed, no epitaxial relation of the C3-DBDP^{2+} inter-linked stripe phase to the underlying Cl-c(2x2) anion layer was found. Furthermore the desorption of the Cl-c(2x2) monolayer results only in the appearance of a Moiré pattern on the C3-DBDP^{2+} monolayer, but no order-disorder phase transition occurs. However, adsorbate-substrate interactions act in the structure formation of this organic monolayer, as they compete with inter-molecular interactions and prolong the structure formation of the inter-linked stripe phase by several hours (compared to the instantaneous formation of both DBV monolayers).

C7-DBDP^{2+}, which possess an even higher molecular flexibility than C3-DBDP^{2+}, forms on the Cl/Cu(100) electrode two different ordered monolayers, namely the C7-DBDP^{2+} mesh phase and the C7-DBDP^{2+} stripe phase. Both C7-DBDP^{2+} phases are initially formed on the Cl/Cu(100) substrate, but the C7-DBDP^{2+} stripe domains are found to vanish over several hours in favor of the C7-DBDP^{2+} mesh structure. This proves that the C7-DBDP^{2+} mesh phase is the most favored arrangement of C7-DBDP^{2+} dications on the Cl-c(2x2)/Cu(100) electrode. In agreement to this, a clear epitaxial relation between the C7-DBDP^{2+} mesh phase and the underlying Cl-c(2x2) monolayer was identified, whereas the epitaxial relation of the C7-DBDP^{2+} stripe phase was neither verified nor fully excluded. The C7-DBDP^{2+} mesh phase is oriented along the close packed directions of the underlying Cl-c(2x2) monolayer, whereas the C7-DBDP^{2+} stripe phase is oriented 30° off this direction.

Besides the adsorbate-substrate interactions, the C7-DBDP^{2+} mesh phase formation

relies on the inter-molecular attraction between consecutive pyridinium-benzly moieties, as in the C3-$DBDP^{2+}$ inter-linked stripe formation. However, contrary to the C3-$DBDP^{2+}$ phase, consecutive C7-$DBDP^{2+}$ dications within the mesh phase are more distant from each other, namely 0.72 nm, in order to fit to the underlying Cl^- rows of the Cl-c(2x2) layer. The desorption of the Cl-c(2x2) monolayer at $E_{work} < -290\,mV$ [vs. RHE] induces an order-disorder transition only of the C7-$DBDP^{2+}$ mesh domains, but not of C7-$DBDP^{2+}$ stripe domains. In contrast to the order-disorder transition of the $DBV^{+\bullet}$ π-stacked stripe domains, the order-disorder transition of the C7-$DBDP^{2+}$ mesh domains does not lead to an immediate breakdown of the whole C7-$DBDP^{2+}$domains, but extends over several minutes and is, in addition, not accelerated by a further lowering of the electrode potential. Lowering the electrode potential below $E_{work} < -400\,mV$ [vs. RHE] induces the decay of the C7-$DBDP^{2+}$ stripe phase to an amorphous organic layer, which points to a second Cl anion species adsorbed above or within the C7-$DBDP^{2+}$ stripes.

Besides their structure formation, both, the C3-$DBDP^{2+}$ and C7-$DBDP^{2+}$ monolayers, are found to inhibit the Cu dissolution and, more importantly, to almost fully block the Cu re-deposition reaction. The latter appears as a damping of the Cu deposition current wave within CVs by 81% (C3-$DBDP^{2+}$) or 91% (C7-$DBDP^{2+}$). This blocking disappears after repetitive cycling deeper into the Cu dissolution regime, which points to the defect free organic monolayers to play a role. However, despite the extensive investigation of these C3-$DBDP^{2+}$ and C7-$DBDP^{2+}$ monolayers, it remains uncertain which of their properties provokes the remarkable blocking of the Cu deposition process.

Contents

1 Introduction

1.1 Nano-Structures at Solid/Liquid Interfaces

A promising route towards functional nano-architectures, which are stable even under environmental conditions and consist of functionalized, but e.g. thermally unstable, building blocks, is to study solid/liquid interfaces *in situ* by state-of-the-art surface probe techniques. These state-of-the-art surface probe techniques permit to study the properties of condensed matter in reduced dimensions with atomic resolution, which is of fundamental interest in science and technology in order to relate macroscopic phenomena to their origin on the atomic scale, such as the within this work proven almost complete blocking of the electrochemical copper deposition by a full self-assembled monolayer of C7-DBDP or C3-DBDP molecules[1].

The construction of nano-architectures is pursued in a number of different scientific and technological fields, in order to reduce the size of functional structures and therefore increase the efficiency per primary material. This is nowadays achieved by using sophisticated so-called top-down fabrication techniques, which are mostly combinations of state-of-the-art lithographic methods. These top-down techniques become more complex with decreasing architecture size, but nowadays they permit to produce architectures down to the 20 nm range. However, in order to overcome the lithographic limit and obtain functional structures on the low nanometer scale bottom-up techniques are investigated, in which the deposition and self-assembly of atomic or molecular building blocks is controlled and exploited. To fully control the self-assembly process a fundamental understanding of the driving forces and the relation between building block, substrate and self-assembly process is mandatory.

A profound understanding of solid/liquid interfaces at ambient conditions is further of general interest due to the common appearance of these interfacial regimes in the environment, as well as in technological (mostly chemical or electrochemical) key processes, such as in the fields of surface coating, metal plating, chemical synthesis, electrochemical energy storage and energy conversion. The relevant interfacial regime of the solid/liquid interfaces is not limited to the mere solid surface, but extends mostly several (atomic/molecular) layers into the homogeneous bulk of both, the solid and the liquid phase, as the structure and electronic state of those first layers are found to deviate from their bulk values. This structural and electronic deviations are a reaction of the interfacial regime to the discontinuity of the homogeneous bulk phases at the interface and gives rise to surface dipole moments, layer relaxations, layer reconstructions and the

[1] C3-DBDP = 1,1'-Dibenzyl-4,4'-(propane-1,3-diyl)dipyridinium; C7-DBDP = 1,1'-Dibenzyl-4,4'-(heptane-1,3-diyl)dipyridinium

ordering of ions within the liquid phase (e.g. Helmholtz Layer). These modified physical properties can be assumed to affect the chemical properties of solid surfaces, which is of particular interest in the various fields of surface science (e.g. catalysis), however, not investigated within the present work.

Electrochemical solid/liquid interfaces consist of a conductive solid, such as a metal, a semiconductor or graphite, in contact to an electrolyte solution, which contains a counter electrode. Applying a potential between this counter electrode in solution and the conductive solid, called working electrode, permits to control the electron density at the solid surface, which leads to tunable electrostatic fields at the interface and may result in electron transfer reactions between the solid and the liquid phase. Those electrochemical reactions are key processes giving e.g. batteries and fuel cells their functionality and are furthermore involved in a series of other functional or manufacturing processes, such as the electrochemical copper wiring of semiconductor structures [1, 2] known as "copper damascene process".

Studying the self-assembly of molecular building blocks at metal/electrolyte interfaces permits to introduce the molecular redox state and the electrostatic fields, originating from the working electrode, as variable experimental parameter. This is, however, in trade-off with the useable temperature range of the investigation or technological processes, as the temperature range is limited by the thermal stability of the liquid electrolyte solution. Within this work the thermal dependency of the self-assembly processes at metal/electrolyte interfaces is not investigated, and has to be addressed in future studies.

1.2 Molecular Building Blocks at Cl/Cu(100) Surfaces

The focus of the present work lies mainly on investigating molecular building blocks at solid/liquid interfaces for the following two reasons. First, using molecules, instead of atoms, as building blocks increases the experimental control, as adsorbate-substrate and intermolecular adsorbate-adsorbate interactions can be specifically tailored by consciously choosing molecules with suitable functional groups. These two interactions as well as possible solvent effects fully define the self-assembly process of the molecular building blocks at solid/liquid interfaces. Second, as mentioned above, organic cations at metal/electrolyte interfaces take a particular role in technological processes. Therefore investigating model organic cations at solid/liquid interfaces permits to elaborate a general understanding of the role of the molecular subunits and of specific functional groups in such surface processes. However, atomic ions, such as chloride and bromide, are not excluded from this study, as they have as well fundamental influence on the ordering of molecular building blocks at solid/liquid interfaces, as will be presented in the results section.

N-containing aromatic rings are studied for their relevance in nature and technology. They are produced in biological systems, such as in chlorophyll or the amino acids tryptophan and histidine, and in industry for technical and technologically applications, as for instance in the form of one of the most widely used herbicides, dimethylviologen

(paraquat). The molecules particularly chosen for the present study have to fulfill several requirements. For instance they shall have technological relevant properties and be soluble in water. It is further desirable that they have a "simple" molecular structure, which is modifiable, and that they are as harmless as possible. Molecular structures are defined to be "more simple", the smaller they are and the less different molecular subunits or functional groups they have. Both requirements make conclusions on the role of each molecular subunit in surface processes and on the molecular self-assembly more easy.

The substrate on which the self-assembly of the molecular building blocks is investigated are chloride precovered Cu(100) single crystal electrode surfaces. This choice is due to the general relevance of copper as conductor in technological applications, in particular in the "copper damascene process" [1, 2]. Chloride anions are known to be an essential additive for this process, therefore a detailed understanding of the role of chloride anions in surface processes at copper electrodes is mandatory.

It is known, that chloride and other halide anions, partially strip their solvation shell off in order to adsorb on and interact directly with metal electrode surfaces. This process, called "specific adsorption" [3], leads in case of halides to the formation of a full, negatively charged and well ordered monolayer. This halide monolayer has proven to significantly enhance the self-assembly process of organic cations, employed as molecular building blocks [4, 5, 6, 7]. This discovery proves halide precovered metal electrode surfaces to be suitable substrates for the investigation of the self-assembly of organic cations at solid/liquid interfaces.

1.2.1 Pyridinium Containing Molecular Building Blocks

One extensively studied group of molecules, which has all the previously requested properties, are viologens (1,1'-disubstituted-4,4'-bipyridines) [8]. Structurally simple representatives of the viologen family consist of only two different molecular groups, namely the bipyridinium core and the viologen substituents, e.g. methyl, phenyl [9], benzyl [5, 6, 7] or heptyl [10], the latter arranged symmetric to the molecular center. The complexity of viologens can be easily increased by attaching more complex (mostly bigger) substituents to the bipyridinium core. This permits a step wise increase of the complexity of the building blocks to be studied at the solid/liquid interfaces.

Viologens have three main oxidation states, namely dicationic V^{2+}, radical monocationic $V^{+\bullet}$ and uncharged V^0, as schematically imaged in figure 1.1. The radical monocation state is distinguished by its wide optical adsorption band and therefore chromaticity. The first electron transfer step, from the dication to the radical monocation state, is almost ideally reversible, and occurs at one of the lowest redox potentials among organic molecules [8]. This makes viologens promising candidates for a technological exploitation in various fields, e.g. as optically active and switchable building blocks. The low reduction potential of viologens can be furthermore exploited in order to reduce substances electrochemically, which are not electroactive per se [8]. This can be done by first reducing viologens electrochemically, which then in a second step chemically reduce the substances of interest.

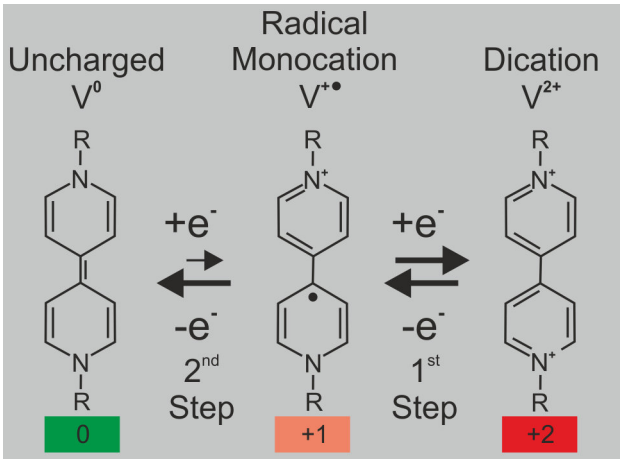

Figure 1.1: Schematic drawing of the viologen related redox steps. The first reduction from the dication to the radical monocation state is fully reversible, whereas the second reduction step to the uncharged viologen species is less reversible, as stated by Bird and Kuhn [8].

Previous EC-STM studies of Dibenzyl- (DBV) [5, 6, 7, 4], Diphenyl- (DPV) [9] and Diheptylviologen (DHV) [10] proved that viologens form full monolayers of self-assembled ordered structures on a chloride precovered Cu(100) surface, making viologens suitable candidates to study the molecular self-assambly at solid/liquid interfaces. These investigations focused mainly on the role of the external substituents in the structure formation. In order to establish a more fundamental understanding of the relation between molecular structure and the self-assembly process it is, however, as well necessary to modify the central 4,4'-bipyridinium core. Therefore within this work the effect of three modifications of the DBV bipyridinium core on the molecular self-assembly process are investigated as illustrated in figure 1.2. The modifications include the rotation of the pyridinium rings relative to each other, resulting in a 3,3'-bipyridinium core, and furthermore the separation of the bipyridinium core into two pyridinium rings by a propane-1,3-diyl or heptane-1,3-diyl chain, resulting in 4,4'-(propane-1,3-diyl)dipyridinium and 4,4'-(heptane-1,7-diyl)dipyridinium, respectively. The three new molecules, namely DB-3,3'-BP (1,1´-Dibenzyl-3,3´-bipyridinium), C3-DBDP (1,1'-Dibenzyl-4,4'-(propane-1,3-diyl)dipyridinium) and C7-DBDP (1,1'-Dibenzyl-4,4'-(heptane-1,7-diyl)dipyridinium), are no longer part of the viologen family.

Studying the self-assembly of those molecules and comparing their structure formation to that of DPV and DBV permits to elaborate a better understanding of the relation between "intramolecular steric flexibility" and the self-assembly of organic cations at solid/liquid interfaces. The steric flexibility of organic molecules is related to the number of possible intramolecular rotations around single bonds, i.e. between saturated (tetrahedral) C-atoms. Following this definition DPV has the lowest steric flexibility, as all molecular groups are forced to remain in the molecular plane defined by the bipyri-

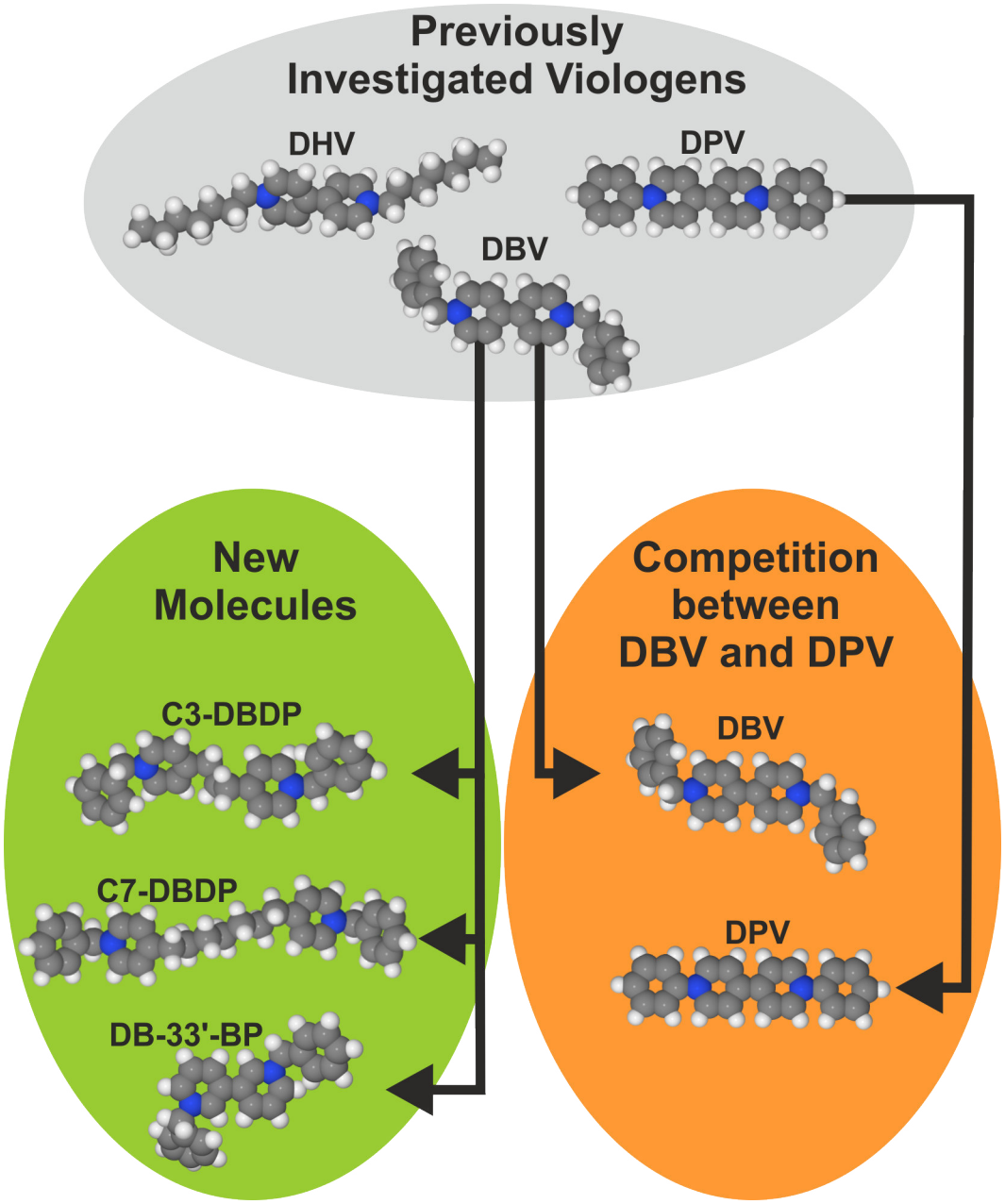

Figure 1.2: Relation between previously investigated viologen molecules and the investigations in the present work, in which the impact of three modifications of the DBV bipyridinium core and of the competition between DBV and DPV onto the self-assembly process of the molecular building blocks is investigated. DHV (Diheptylviologen), DPV (Diphenylviologen), DBV (Dibenzylviologen), C3-DBDP (1,1'-Dibenzyl-4,4'-(propane-1,3-diyl)dipyridinium), C7-DBDP (1,1'-Dibenzyl-4,4'-(heptane-1,3-diyl)dipyridinium), DB-3,3'-BP (1,1´-Dibenzyl-3,3´-bipyridinium).

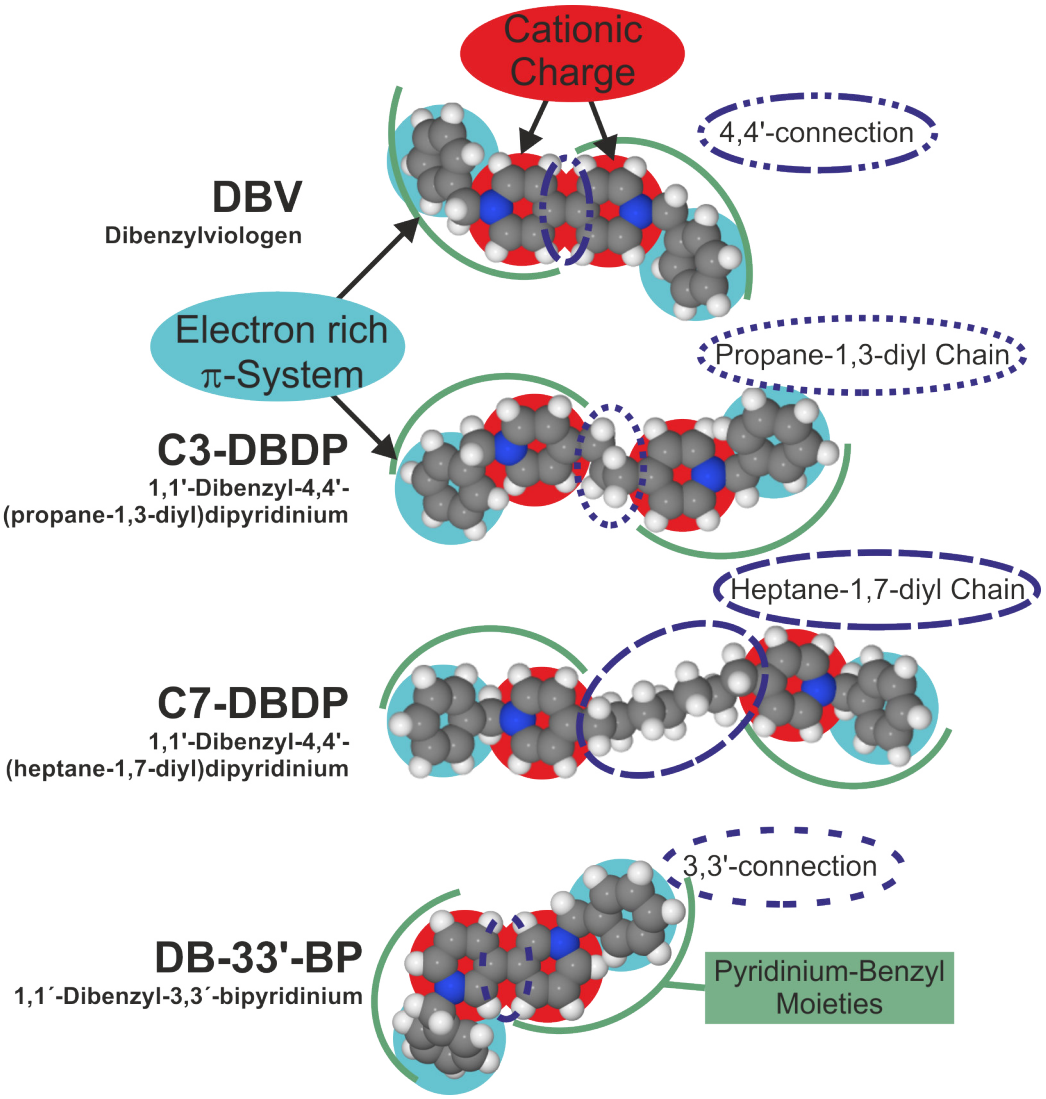

Figure 1.3: Structural motive of the DBV related molecules investigated within this work. All molecules consists of two pyridinium-benzyl moieties arranged symmetric to the molecular center and connected either directly (4,4'- or 3,3'-connection) or via a saturated propane-1,3-diyl or heptane-(1,7)-diyl chain.

dinium core. A higher steric flexibility is obtained by introducing between each phenyl ring and the bipyridinium core one CH_2 group, which results in the DBV molecule. The phenyl rings are then bound via single bonds in a tetrahedral angle to the molecular axis defined by the bipyridinium core, which permits to vary their position more freely. The DBV molecule consists of two directly connected pyridinium-benzyl moieties arranged symmetrically to the molecular center via a 4,4'-connection as imaged in figure 1.3. The pyridinium-benzyl moiety is the key structural motive as it appears in all DBV related molecules investigated within this work, namely DB-3,3'-BP, C3- and C7-DBDP. These molecules only differ by the way the two pyridinium-benzyl moiety are connected to each other as shown in figure 1.3.

Unambigously C3- and C7-DBDP are found to have a significantly higher steric flexibility than DBV. Introducing the saturated chain, here propane-1,3-diyl or heptane-1,7-diyl, between the pyridinium rings of DBV permits to vary the position and therefore mutual distance of the pyridinium-benzyl moieties, which is for C7- stronger expressed than for C3-DBDP.

A second approach to investigate the self-assembly process of molecular building blocks at solid/liquid interface is to study two or more molecular building blocks in competition for adsorption and reaction sites. This not only permits to compare and study their structure formation directly, but also to study possible synergies between them. Suitable molecular building blocks for this study are DPV and DBV, as they were extensively studied previously [4, 5, 6, 7, 9].

1.3 Outline of the Thesis

At first a general model of metal/electrolyte interfaces, including the common notations and relevant details, are presented in chapter 2. Subsequently the experimental methods, used to study the solid/liquid interface, are presented in chapter 3. The details of the experimental setup and the description of the experiments, including the sample preparations, are presented in the following chapter 4.

The core of the present study are the chapters 5 and 6, in which the solid/liquid interfaces are systematically investigated. This investigation begins with a study of the substrate itself, namely a halide covered Cu(100) electrode, as the structural details of this substrate are up to date still under discussion in literature (chap. 5). The used methods range from Cyclic Voltametry (CV) and *in situ* Surface X-Ray Diffraction (SXRD), to *in situ* Scanning Tunneling Microscopy (STM).

Subsequently to the study of the substrate, the up to now elaborated understanding of the structure formation of viologen cations at the Cl/Cu(100) electrode surface is expanded to a more general level (chap. 6). Previous investigations focused on the structure formation of different viologens, which differed from each other solely by their viologen substituents (the 4,4'-bipyridinium core remained unchanged) and were studied individually at the Cl/Cu(100) electrode surface. In this work both restrictions, namely to one molecule within the solid/liquid interface and to the viologen family, are lifted in two different studies.

First the interaction of two viologens (1,1'-disubstituted-4,4'-bipyridinium), namely Diphenylviologen (DPV) and Dibenzylviologen (DBV) as well as of a 1:1 mixture of both molecules at the Cl-c(2x2)/Cu(100) electrode is studied. Both organic cations may compete for adsorption and reaction sites or cooperate in the structure formation on the substrate surface.

Second the viologen core (= 4,4'-bipyridinium core) of Dibenzylviologen (DBV) is modified in three different ways, which results in DB-3,3'-BP, C3-DBDP and C7-DBDP. These new organic cations are no longer part of the viologen family. The organic cations are studied at the Cl/Cu(100) electrode surface via CV and *in situ* STM. Additional *ex situ* X-ray Photoelectron Spectroscopy (XPS) experiments are performed to verify the redox state of the adsorbed organic cations.

2 The Metal/Electrolyte Interface

In this chapter existent theories and knowledge of metal electrode surfaces in contact with halide containing electrolytes are presented in a condensed way. The focus lies on the theoretical background, common notations and important material specific parameters. Further the properties of the electrode material copper and its (100) surface are presented. The present summary has to be understood as a summary of a number of previously published works, in which the subject is addressed more exhaustively [11, 12, 3, 13, 14]. The detailed characterization of the halide/Cu(100) surface will be presented in chapter 5.2, including a characterization by means of SXRD.

2.1 Model of Metal/Electrolyte Interfaces

Introducing a metal into an electrolyte solution may lead to charge transfer reactions between the phases or charge rearrangements within one phase[1]. These charge transfer reactions are not limited to electron transfers but include as well the transfer of charges in form of ions, as it occurs in metal corrosion processes resulting at differing chemical potentials between the solid and liquid phase. The occurrence of the charge transfer or charge rearrangement processes depends on the effective fields at the interface and leads to the formation of the so-called electrical double layer at the metal surface in the equilibrium state. Such electrical double layers have been investigated since the 19th century [15] for their relevance in electrochemical processes, first by macroscopic, integral experiments [12] and more recently by *in situ* surface sensitive probe techniques.

The investigation of these electrical double layers by macroscopic, integral methods, e.g. by varying the electrode potential and measuring the current response, focuses on the charge distribution and the related electrical fields perpendicular to the surface within this electrical double layer [12]. This requires the absence of any charge transfer reactions, as its resulting currents would overlay the signal of the electrical double layer. In absence of charge transfer reactions electrodes are still polarizable, which is mostly valid in a system specific potential window. Furthermore, models of the interfacial regime are necessary in order to relate the results obtained by macroscopic, integral methods to the microscopic interfacial regime.

In the early stage of these interfacial studies models were improved in order to remove contradictions between experimental and predicted data. Nowadays the models are tested by surface sensitive probe techniques, which permit to investigate e.g. directly the structure of the electrode surface via scanning tunneling microscopy. Moreover within

[1] This processes are not restricted to metals in electrolyte solutions but may as well be observed at other types of interfaces.

this work it will be proved that even the highly mobile and in EC-STM experiments invisible part of the double layer can be imaged and investigated by sophisticated *in situ* SXRD experiments.

2.1.1 Model of Electrolytes at Electrode Surfaces

The nowadays accepted model of the interfacial regime consists of several subunits, which were found to be necessary in order to reproduce experimental parameters such as the electrical capacity of the solid/liquid interface. For instance, in the model of a Cu(100) electrode in a KCl electrolyte, shown in figure 2.1, three regions within the electrolyte solution can be distinguished, namely the inner Helmholtz Layer (HHL), the outer Layer of Solvated Counter Ions (LSCI) and the diffuse layer.

The existence of a layer of solvated ions, such as the outer LSCI, was originally suggested by Helmholtz [15], who assumed ions to be strongly attracted to the electrode surface with opposed charge state, which for convenience was expected to be totally flat and not to have any particular structure. The attracted ions would partially or fully neutralize the excess surface charge, which is the origin of the attractive forces. Therefore the coverage of this layer of solvated ions has to be related to the charge state of the electrode surface. This expectation will be of particular interest in the SXRD investigation of the solid/liquid interface and should be kept in mind. The neighboring of the two charged layers, electrode surface and ion layer in solution, gave rise to the term "electrical double layer" used to describe the solid/liquid interface. The assumptions made and the simple structure of this double layer permits to treat it as a plate capacitor. The potential drop between the layers has then to be linear $\varphi = c_1 x + c_0$, due to the absence of charges between the layers $\rho(x) = 0$ and the validity of the Poisson law $\frac{d^2\varphi}{dx^2} = -\frac{\rho}{\varepsilon_r \varepsilon_0}$. The linear potential drop is shown in a graph below the model of the solid/liquid interface (fig. 2.1).

As the Helmholtz model failed to describe measured electrode capacities Gouy [16] and Chapman [17] suggested the electrostatic fields to penetrate the electrolyte solution deeper and to affect a certain electrolyte layer, whose thickness depends on the ion concentration [11]. Ions accumulate at the electrode surface due to the electrostatic attraction to the electrode surface. In contrast to the previous model ions are not assumed to be immobilized at the electrode surface but to be "quasi-free", which permits diffusion processes to take place. As a consequence of the diffusion the ion density has to follow a Boltzmann type distribution, resulting in an exponential decay of the ion concentration – and therefore of the charge density – perpendicular to the electrode surface $\rho(x) = c_1 \cdot e^{\frac{-c_2 e\varphi(x)}{k_B T}}$. Consequently the potential also drops exponentially, as can be verified by solving the Poisson equation (fig. 2.1).

Both models of the electrolyte solution near the surface are insufficient to explain experimental results obtained for differing experimental parameters, such as the ion concentrations. Therefore Stern developed a more general model of the solid/liquid interface, in which both layers, a rigid layer of solvated ions and a diffuse layer, are present at the electrode surface. The Stern model permits ions to interact strongly

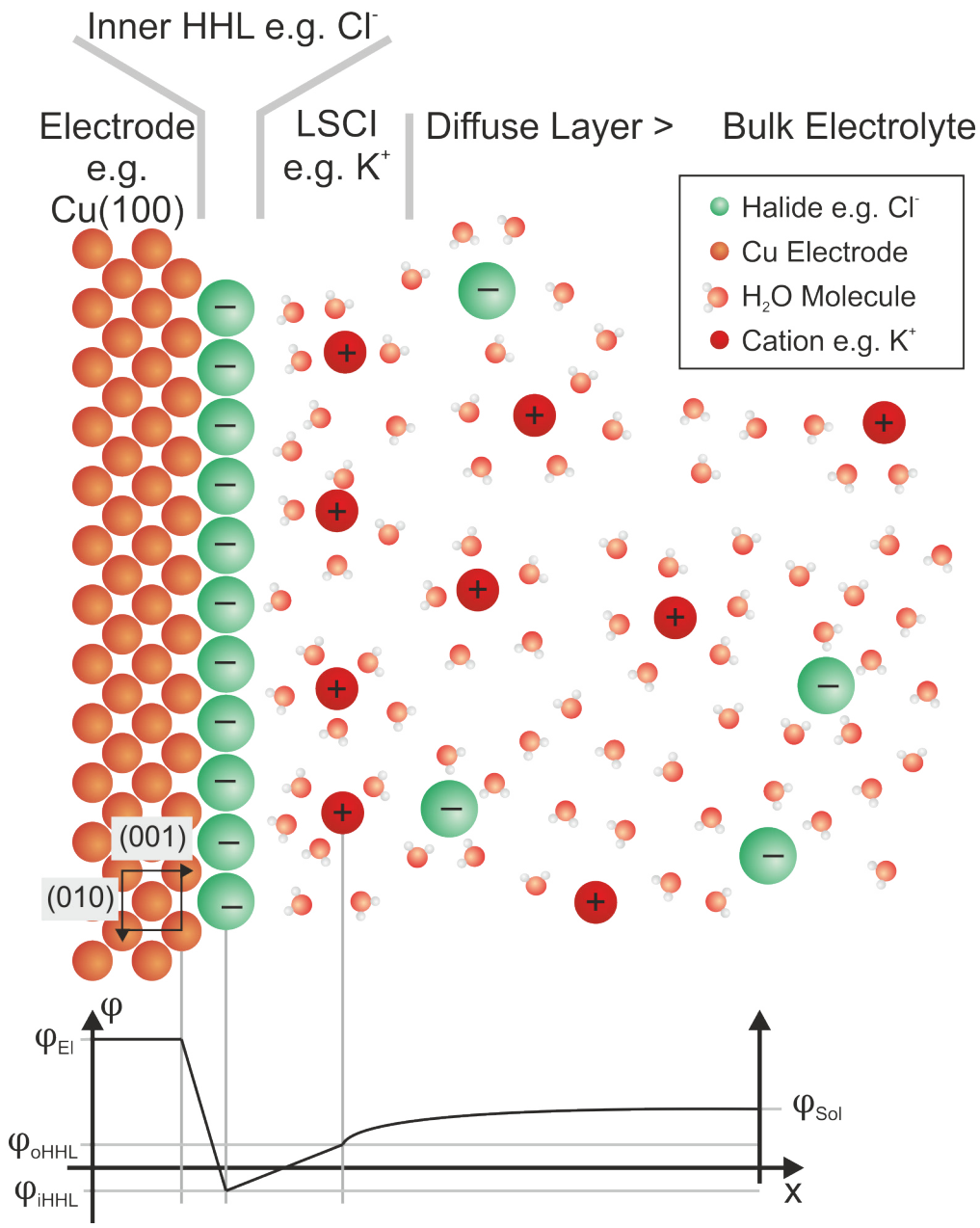

Figure 2.1: Model of the electrode/electrolyte interface including the inner Helmholtz Layer (HHL), outer Layer of Solvated Counter Ions (LSCI) and diffuse layer at the Cu(100) surface. Between the rigid electrode, inner HHL and outer LSCI the potential field drops linearly, such as in a plate capacitor. Within the diffuse layer the potential field drops exponentially, due to the Boltzmann distributed ion charge. This model is an example of the Cu(100) electrode in a KCl containing solution at a specific electrode charge state and is therefore not generally valid.

via electrostatic interactions with the electrode surface, but includes as well diffusion processes, which affect the ion density deeper in the electrolyte solution (typical values for the thickness of a diffuse layer are between 1 nm and 10 nm [11]). The resulting electrical properties, such as interfacial capacities, have to obey the rules of electrical wiring, such as the Kirchhoff laws. The interfacial capacity is then determined by two capacitors wired in series, which results in a total capacity of $\frac{1}{C_{total}} = \frac{1}{C_{rig-layer}} + \frac{1}{C_{diff-layer}}$, with the capacity of the rigid layer of solvated ions $C_{rig-layer}$ and the capacity of the diffuse layer $C_{diff-layer}$.

In the 1940s Grahame [18] adapted the Stern model of the solid/liquid interface, as he realized that two rigid layers, as shown in figure 2.1, are necessary to explain certain experimental data [12]. The outer LSCI consists of fully solvated ions, which are attracted to the electrode surface and are localized within one specific plane above the electrode surface. The inner HHL consists of ions interacting even stronger with the electrode surface and therefore stripping off their solvation shell in order to adsorb onto and directly interact with the electrode surface. These specifically adsorbed ions are found to strongly alter electrochemical reactions at the electrode surface [3, 19], making their investigation relevant in various sub-fields of electrochemistry.

Specific Adsorption of Halid Anions

An example for specifically adsorbing ions are halide anions, such as chloride, bromide or iodide, at metal electrode surfaces [3]. Specifically adsorbed halide anions are found to adsorb in well-ordered, close packed structures, which are defined by the available adsorption sites on the substrate and the radius of the ion. The maximum coverage of e.g. Cl or Br anions specifically adsorbed on a Cu(100) surface is found to be up to 0.5 monolayers (ML), which is significantly higher than within the outer LSCI, with an usual coverages lower than 0.2 ML [3]. The high coverage of the specifically adsorbed halide anion monolayer can be explained by the strong attractive ion-substrate interaction. This leads to the the partial removal of the halide anion solvation shell and balance the strong electrostatic repulsion between the close packed anions within the halide monolayer.

However, this high coverages halide adlayer is only formed at sufficiently high anion concentrations within the solution[2]. Low concentrations lead to sub-monolayer coverages, at which the specifically adsorbed anions do not form well-ordered, close packed structures, but may form a “two dimensional gas” on the electrode surface, in which the anions freely diffuse within the confinement of the electrode surface [20, 21, 3].

The energy balance between the two possible ion states, specifically adsorbed on the electrode surface or solvated within the electrolyte solution, leads to differing “tendencies to specifically adsorb” on a substrate surface for the various ions. For instance, ions with high solvation energies are hindered in the specifical adsorption process, as the solvation energy represents an energy barrier, which has to be overcome. In contrast to this, strong attractive forces between ion and substrate favor the specific adsorption process. The differing tendencies to specifically adsorb are relevant if different ions are present at

[2]The concentration varies for different halide anions and electrode surfaces, due to the adsorption energy.

the electrode surface, e.g. Cl or Br anions. The energetically most favored ion will, in such a competition, adsorb onto the electrode surface and remove previously adsorbed, but less favored anions from the electrode surface. This is as well exploited in the sample preparation procedure of the SXRD experiments within this work, where at first Cl anions are adsorbed on the Cu(100) surface in order to induce an "electrochemical annealing" process, which leads to a reduction of the surface roughness. In a second step the Cl/Cu(100) surface is exposed to bromide anions, which at sufficiently high bromide concentration leads to the complete substitution of Cl by Br anions on the electrode surface, due to the higher tendency of Br anions to specifically adsorb. In case of Br and Cl anion, the higher tendency to specifically adsorb of Br anions is assumed to be the result of the lower solvation energy of Br anions in aqueous solutions and its lower electronegativity. The lower electronegativity of Br anions favors the (partial) transfer the halide anion charge into the electrode surface – as will be discussed in the SXRD chapter 5.4 of this work –, which increases the ion-substrate attraction, and therefore the tendency to specifically adsorb of Br anions. In general, the following order for the specific adsorption for halide anions is valid: $F^- \ll Cl^- < Br^- < I^-$ [3]. Cl, Br and I anions are known to specifically adsorb, whereas F anions are assumed not to adsorb specifically[3].

The strong ion-substrate attraction of the specifically adsorbed ions even leads to an overcompensation of the metal electrode charge, as sketched in figure 2.1. This overcompensation is impossible to occur when only electrostatic fields and ion charges are the key elements in the adsorption process, such as initially suggested by Helmholtz in the formation of the rigid (outer) layer. Therefore besides electrostatic and van der Waals interaction also chemical interactions can be assumed to play a role in the specific adsorption processes of halide anions on metal electrode surfaces. This is supported by findings of Graham et al. [22] and Schmickler [23], who identified the electronegativity/polarisability of ions to influence the distance between metal electrode surface and inner HHL. These findings are in agreement with recent *in situ* SXRD studies of Cl [24, 25] and Br [26] anion covered Cu(100) electrode surface, where Cl anion compared to Br anion adlayers are situated at greater distance from the electrode surface, despite the bigger ionic radius of Br anions compared to Cl anions. This can be understood if a partial charge transfer from the halide adlayer to the metal electrode surface takes place. This would affect the ion radius of the more easily polarizable Br anions stronger than of the less polarizable Cl anions.

The overcompensation of the metal electrode charge by the negative halide anion layers can be exploited in order to obtain a negatively charged substrate for the study of organic cations, as proven by Safarowsky et al. [4] and Pham et al. [5, 6]. They proved the Cl anion covered Cu(100) surface to attract organic cations to the electrode surface even at the most positive electrode potentials within the Cu(100) potential window.

2.1.2 Model of Electrode Surfaces

The electrode surface was in early models of the solid/liquid interface assumed to be a structureless entity bearing a specific, but variable amount of charge. The charge

state of the electrode can be either defined in comparison to a reference reaction, which might occur in the same or in other electrolyte solutions, or by the potential difference between metal electrode and electrolyte solution. The first definition of the electrode charge state will be used in the present work, due to its simple experimental realization. The latter, more detailed definition of the electrode potential requires to renormalize the potential scale to its defined "potential of zero charge" ϕ_{pzc}, at which the electrode surface does not carry any excessive charge. This definition is more appropriate in the detailed study of the electrical double layer by electrochemical methods, as the double layer composition strongly depends on the excessive charge at the electrode surface. For instance electrode potentials above the ϕ_{pzc} attract anions and potentials below the ϕ_{pzc} attract cations to the electrode surface. This, however, may differ when an inner HHL is formed, which then attracts ions of opposite charge to the electrode surface within a wide range of the electrode potential window.

A remarkable fact is that the potential of zero charge ϕ_{pzc} is fully defined by the work function of the metal electrode ϕ_W, and the specific used reference electrode, which determines the offset κ [23]. This results in:

$$\phi_{pzc} = \phi_W + \kappa \tag{2.1}$$

ϕ_{pzc} is independent of the ion species within the solution or the composition of the electrical double layer, which makes ϕ_{pzc} an appropriate measure to characterize the charge state of the electrode surface. However, the ϕ_{pzc} potential will be less relevant for the present work, as a halide modified Cu(100) surface will be used as substrate. The overcompensation of the electrode surface charge by the halide anion layer will result in an almost potential independent attraction of cations to the electrode surface within the potential window[3], as verrified by IRRAS experiments of Röefzaad et al. [27, 13].

A more accurate model of the electrode surface, to which among others the ideas of Smoluchowski contributed [28], is the jellium model, in which the electrode is assumed to be a superposition of a constant, immobile, positive background charge with an inhomogenous, flexible, negative electron gas. The positive background charge, representing the crystal lattice, suddenly drops to zero in a discontinuous way at the electrode surface known as "jellium edge". The interaction of the flexible electron gas with the background charge leads at the jellium edge to a smearing out of the electron density, called the "electronic spillover", sketched in figure 2.2.a. The spillover of the electron density is found to decay above the solid surface typically on a length scale of $1-2$Å [23, 28]. The resulting surface dipole moment is oriented with its positive end in the direction of the crystal bulk and usually leads to a surface dipole potential of a few volts [23], which contributes to the work function.

This basic jellium model is sufficient to describe general trends and to investigate surfaces on a qualitative level. In order to simulate and describe, e.g. single crystal, surfaces more accurately it is necessary to use more complex pseudopotentials, which

[3]The potential window is defined by the electrochemical stability of the substrate, here Cu(100) surface, and the electrolyte solution. The dissolution of either the electrode or the electrolyte represents the positive, respectively negative limit of the potential window.

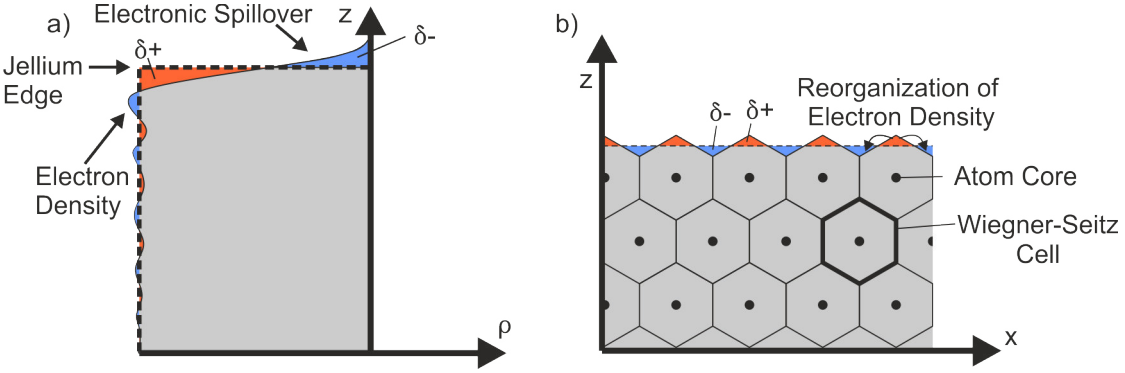

Figure 2.2: Dipole creation at solid surfaces. The superposition of negative and positive charge leads to neutral areas (gray). Excessive negative charges are marked in blue, excessive positive charge in red. a) Surface dipole described in the jellium model, induced by a mismatch of the positive background charge and negative electron density at surfaces (=jellium edge). The dominant contribution to the dipole moment originates from the charge distribution at the surface, marked as $\delta+$ and $\delta-$. The discontinuity of the charges within the bulk phase are neglected. [23]. b) Smoluchowski dipoles, induced by a reorganization of the electron density at solid surfaces. [28]

permit to describe the inhomogenous distribution of the previously as constant assumed background charge. This is, however, out of the scope of the present work but a detailed description of the proper theoretical treatment can be found in a review article of Schmickler [23].

Besides the surface dipoles, also so-called Smoluchowski dipoles appear at solid surfaces [28]. These Smoluchowski dipoles appear as a result of an electron density smoothing process at surfaces. Assuming the electron density to be confined within the bulk phase in atom related neutral polyhydral bodies, e.g. the Wiegner-Seitz cells as imaged in figure 2.2b, at surfaces this bulk "confinement" is unfavored, due to the missing atomic layers above the solid surface. The electron density then reorganizes, induced by the boundary condition and surface energy, and fills up the vacant "valleys" and reduce the electron "hills" as imaged in figure 2.2b. This reorganization leads to the appearance of the Smoluchowski dipole moments, which in contrast to the previously discussed surface dipoles are orientated with their negative charge in the direction to the crystal bulk, and therefore counteracts the surface dipole moment. However, it should be pointed out that the superposition affects the out-of-plane component, but leaves the in-plane component of the Smoluchowski dipoles unaffected.

Similar processes as discussed for the surface and Smoluchowski dipoles are valid at all discontinuities at surfaces, such as step edges, kink sites or point defects in/on terraces. It can be stated, the rougher the surface the more Smoluchowski dipole moments are created, which results in a global dipole moment specific and unique for each surface. This global dipole moment affects the integrally measured electron work function, which

represents the energy necessary to transport electrons from the crystal bulk state to the vacuum level. The work function is at solid/liquid interfaces of interest due to its relation to the potential of zero charge, as state in equation 2.1. This equation expresses the fact that the work function represents an offset for the electrochemical potential. However, in contrast to UHV studies, in which the work function is well appropriate to characterize surfaces, it is at solid/liquid interfaces affected by the applied electrode potential. The electrode potential is, indeed, a variable experimental control parameter of the solid/liquid interface, therefore the interfacial capacity is the appropriate parameter for the characterization of solid/liquid interfaces.

As stated in the previous section 2.1.1 the interfacial capacities depend on the inner HHL, outer LSCI and diffuse layer within the solution. However, capacities are defined by the potential difference between two charge bearing entities, for instance at solid/liquid interfaces the solid electrode and liquid solution $\phi_E - \phi_{Sol}$. The resulting interfacial capacity is then $\frac{1}{C} = \frac{\partial(\phi_E - \phi_{Sol})}{\partial\sigma}$, with the surface charge density σ, as stated in literature [23]. The interfacial capacity can be divided into two contributions, namely one for the electrode and one for the solution, to $\frac{1}{C} = \frac{1}{C_E} + \frac{1}{C_{Sol}}$ [23].

Atomic Structure of Halide/Cu(100) Electrodes

In the present work the (001)[4] low index surface of a copper single crystal is used as metal electrode (working electrode) in an electrolyte solution. Copper was chosen for various reasons in the present study. As stated in the introduction, the general technological interest of copper is based on its high electrical conductivity and ductility, which makes copper an ideal candidate for most electronic related technologies. In addition this study aims at expanding the knowledge of the structure formation of viologens to the more generalized scale of "pyridinium containing building blocks". This requires a well founded understanding of the structure formation of viologens, which is furnished by studies at Cl anion covered Cu(100) electrode surfaces [4, 5, 7, 6, 9, 10, 13].

Using a single crystal surface, such as Cu(100), in order to study surface processes and monolayers at solid/liquid interfaces has several advantages. For instance the well defined periodicity on the atomic scale of the Cu(100) electrode surface facilitates the interpretation of experimental results with atomic resolution. In addition experimental results of local methods apply to the whole substrate surface and experimental results of integral methods can be related to the atomic scale. In summary these advantages allow to gain an atomic understanding of surface processes, which is the essential aim of this study.

Copper crystallizes, as its neighbors in the 11th groups of the periodic table, gold and silver, in the close packed face centered cubic (fcc) Bravais lattice, sketched in figure 2.3. The Cu fcc lattice constant is $a_{Cu} = 0.362\,nm$ [29] and consequently the Cu-Cu interlayer distance is 0.18 nm along the fcc basis vectors, namely [100], [010] and [001].

[4]The (100), (010) and (001) Cu single crystal surface are identical. Therefore within this work the notation Cu(100) is used to describe the electrode surface, although the z-axis is chosen as surface normal. Naming the Cu(001) surface as "Cu(100)" is a common inaccuracy in literature and therefore also used in this work.

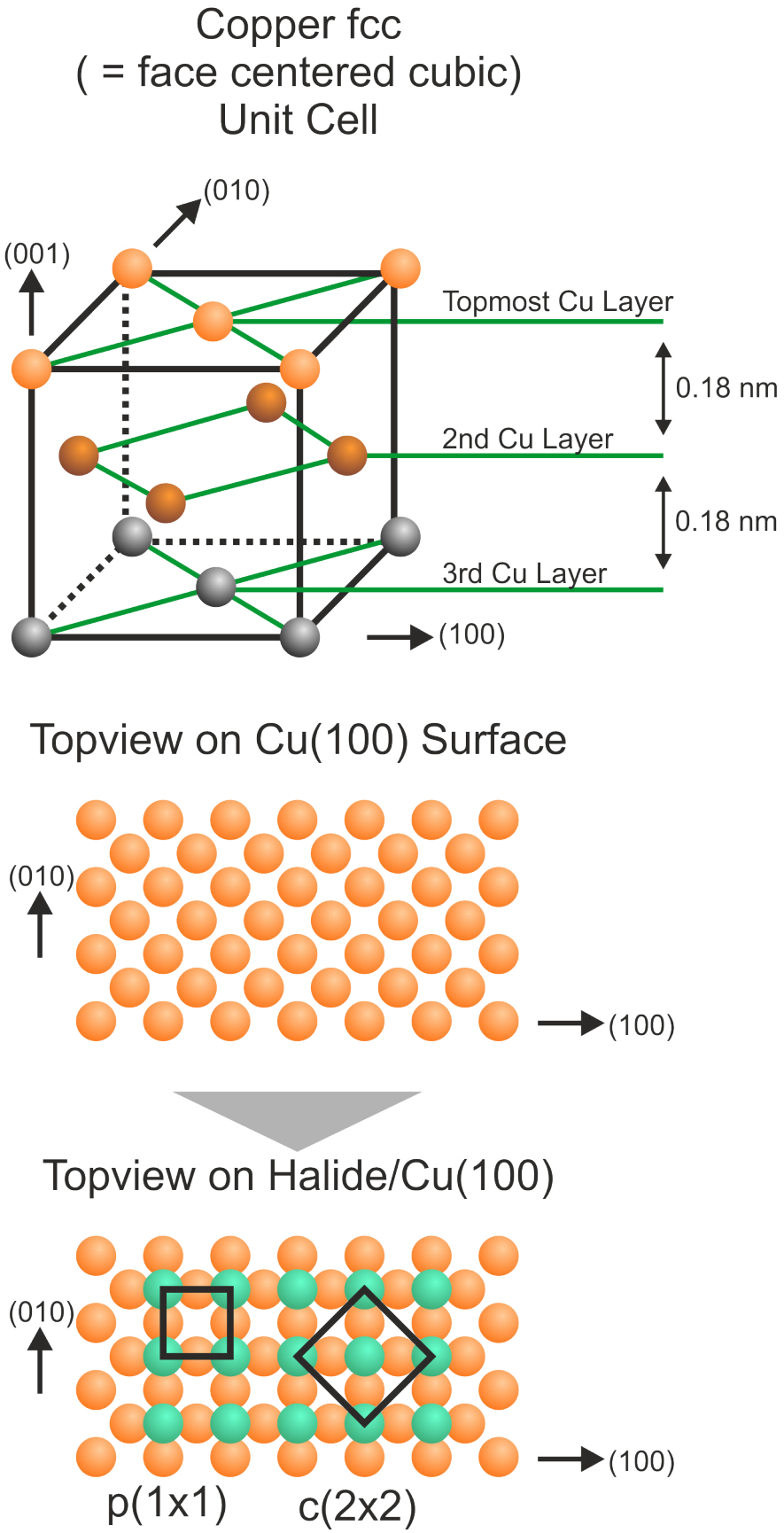

Figure 2.3: Copper fcc (face centered cubic) unit cell and unit cells of the halide (Cl or Br anion) adlayer.

The Cu layer stacking along the low crystal indexes (100), (010) and (001) is of AB-type, which provokes an offset between consecutive Cu terraces by half the Cu fcc unit cell.

As stated previously, Cl and Br anions may specifically adsorb on metal electrode surfaces. At the Cu(100) electrode both halide anions specifically adsorb into the four-fold hollow sites of the Cu surface, as imaged in figure 2.3 and proved in literature [3, 24, 25]. The Cl anions form an ordered full monolayer, which in literature is usually described as halide-c(2x2) monolayer. As sketched in figure 2.3 the halide-c(2x2) notation is related to the Cu next neighbor distance (NND) of the topmost Cu layer. This choice is fairly reasonable when the used experimental methods focus on the 2D structure, such as Scanning Tunneling Microscopy (STM), but the same choice is inconvenient in a 3D structure analysis of the solid liquid interface, as performed in this work. The 3D structure of the electrode surface is best described by the cubic Cu fcc Bravais lattice. In relation to the low index vectors of the Cu fcc unit cell, namely (100) and (010), the halide monolayer is described by a simple cubic p(1x1) unit cell. However, in order to be consistent with literature the halide adlayer will be addressed as c(2x2) monolayer, despite the fact that the 3D analysis of the XRD data is performed in the Cu fcc coordinate system.

The full 3D structure of the Cu(100)/electrolyte interface is up to this date under discussion in literature. Therefore in the present work also the 3D structure of the halide covered Cu(100) electrode surface was investigated. The experimental results are presented in chapter 5.

2.2 Electrochemistry of Organic Cations

Viologens and all other investigated organic cations are inserted as dichloride salts into a 10 mM HCl solution. The initial dication redox state of the organic cations can be *electrochemically* increased or reduced by applying sufficiently high or low working electrode potentials.

Viologens are known for their high redox activity in their dication V^{2+} and monocation radical state $V^{+\bullet}$. For instance applying sufficiently low electrode potentials at the Cu(100) surface permits to *electrochemically reduce* the initial viologen dications V^{2+} in a first electron transfer reaction to their monocation radical state $V^{+\bullet}$ (fig. 1.1). This first redox step $V^{2+} + e^- \rightleftharpoons V^{+\bullet}$ is fully reversible, which allows to electrochemically switch between both viologen redox states without significant side reactions.

The reduction of the dication to viologen monocation radical $V^{+\bullet}$ leads to the "viologen typical" change from a transparent to a colored state, for which viologens were initially studied as redox indicator [30]. The color change upon reduction is the consequence of the wide optical adsorption band of viologens in their monocation radical state.

Despite the sketch in figure 1.1, the monocation radical state of viologens can not be described as a neighboring of an uncharged radical pyridinium π-system and a cation pyridinium π-system, but the radical electron and cation charge are distributed over the whole 4,4'-bipyridinium core, as proven by XPS spectra [9]. This delocalization can

be assumed to significantly affect both, the adsorption band, as well as the high redox activity of the 4,4'-bipyridinium core.

The viologen monocation radicals $V^{+\bullet}$ can be further *electrochemically reduce* in a second electron transfer reaction to their uncharged state V^0 (fig. 1.1). In contrast to the first redox step, this second redox step $V^{+\bullet} + e^- \rightleftharpoons V^0$ is less reversible as uncharged viologens are known to form insoluble species [8]. This makes the second electron transfer reaction mostly unwanted in experiments.

The redox potentials of different viologens may differ by several hundred mV up to more than 1000 mV, as the redox potential depends on the viologen substituents [31]. It must be noted that the first and second redox potentials are not independent, as they are related linearly [31].

The viologen substituents have a second – for this work fundamental – effect, as they strongly contribute to the intermolecular interactions. As will be presented in the results chapter, the intermolecular interaction has a major impact on the adlayer structure of viologen monolayers, which therefore differs as a function of the viologen substituent [4, 5, 10, 9].

As stated in the introduction, the 4,4'-bipyridinium core of DBV^{2+} is modified in three different ways, which results in DB-3,3'-BP^{2+}, C3-$DBDP^{2+}$ and C7-$DBDP^{2+}$, in order to gain a deeper insight into the relation between self-assembly and molecular structure. Due to the modification of the 4,4'-bipyridinium core this new organic cations are no longer part of the viologen family. This points to a lower redox activity of these new organic cations compared to viologens, due to the modification of the, for its high redox activity distinguished, 4,4'-bipyridinium core.

Indeed, the study of various 4-substituted-benzyl-pyridinium cations [32] proves that the reduction of benzyl-pyridinium cations is possible, but occurs within the hydrogen evolution regime (HER). Processes within the HER are usually covered by the stronger HER currents and therefore not visible. The study of 4-substituted-benzyl-pyridinium cations [32] are assumed to be a suitable reference for both pyridinium π-systems within C3-$DBDP^{2+}$ or C7-$DBDP^{2+}$, as their π-systems are decoupled by a saturated chain consisting of sp^3-hybridized carbon atoms between them. The saturated chain prevents the direct interaction of the pyridinium π-systems and consequently the redox activity of both pyridinium cations are (almost) independent. The independence of the pyridinium π-systems would lead to a reduction of both pyridinium cations within C3-$DBDP^{2+}$ or C7-$DBDP^{2+}$ at (almost) the same electrode potential. This would prevent the formation of a stable C3-DBDP or C7-DBDP monocation radical, which requires the reduction of only one of both pyridinium cations within the C3-$DBDP^{2+}$ or C7-$DBDP^{2+}$. Indeed the C3-$DBDP^{2+}$ or C7-$DBDP^{2+}$ dication would be directly reduced to their uncharged diradical state.

In contrast to this, the DB-3,3'-BP^{2+} dications are assumed to possess a monocation radical state, which, however, has to be proven separately, as – to the knowledge of the author – no suitable reference studies were published yet.

The present study will not focus on elaborating a detailed understanding of the redox activity of DB-3,3'-BP^{2+}, C3-$DBDP^{2+}$ and C7-$DBDP^{2+}$. Therefore the investigation

of the redox activity of DB-3,3'-BP^{2+}, C3-$DBDP^{2+}$ and C7-$DBDP^{2+}$ is limited to the potential window of Cu(100) in an aqueous solution.

3 Theory of Experimental Methods

In this chapter all experimental methods used in the present study are introduced. The most important notations as well as the theories describing the performed experiments are elaborated and explained. The theoretical background is mandatory to properly analyze and interpret the obtained experimental results. However, all presented methods offer a much wider range of application than presented in this chapter. More extensive description of the experimental methods can be found in the references given later throughout the text.

3.1 Potentiodynamic Measurements: Cyclic Voltametry

Cyclic Voltametry (CV) is a potentiodynamic method, in which the current response of a solid/liquid interface to a potential change is analyzed, in order to conclude on the composition of the solid/liquid interface or dynamics of electrochemical processes. CV is an integral method as the current response of the whole electrode surface is registered and analyzed, therefore the registered CV signals have the dimension of a current density $\left[\frac{\mu A}{mm^2}\right]$.

In order to perform a CV scan the working electrode potential follows a saw tooth curve and is at first linearly increased and subsequently linearly decreased. Both potential sweeps together form one full cycle, which is the origin of its name: Cyclic Voltametry. The potential change of the working electrode may provoke a current response, which represents the flow of electrons to or from the electrode surface.

The origin of the current response to the potential changes can be electrochemical reactions, which involve electron transfer reactions between the solid electrode and liquid electrolyte solution. In addition a current response can occur without the exchange of electrons between the electrode and electrolyte. The most common examples are desorption and adsorption of adlayers, i.e. of halide anions or organic cations, and the reconstruction of the electrode surface. All three processes modify the border conditions of the electrode surface and therefore induces a corrective flow of electrons, however, a reconstruction of the electrode surface does not occur within the present study of the Cu(100) electrode surface.

Usually the range of the CV scans is chosen to be limited to the potential range, in which the electrolyte solution and the electrode are stable. For instance, at sufficiently low electrode potentials the aqueous electrolyte is decomposed by the hydrogen evolution reaction (HER) at the Cu(100) electrode surface. Processes which occur within the HER regime are usually inaccessible as they are covered by the currents provoked by the HER and in addition their dynamics is affected by the reaction dynamics of the HER. A

comparable situation occurs at sufficiently high electrode potentials at which the Cu(100) electrode is oxidized, and therefore the solid Cu electrode dissolved. Evidently dissolving the Cu electrode itself interferes with the investigation of processes at its surface.

If the study of processes beyond the limit of the potential window is unavoidable, then the limits of the potential window must be overcome by exchanging either the electrolyte solution or the electrode material by electrochemically more stable candidates. For instance, in order to study the electrochemistry of organic cations the Cu(100) electrode can be exchanged by a graphite working electrode (HOPG), which is stable beyond the Cu dissolution process and therefore widens the potential window by more than +1000 mV.

The processes at electrode surfaces may either involve adsorbed reactants or reactants situated in solution. The first class of processes are called surface processes, the latter are called solution processes. Surface processes are limited to reactants which are before and after the process on the electrode surface, therefore the amount of reactant is limited and the resulting current waves are symmetric to their peak maximum. Assuming the involved adsorption/desorption process follow the Langmuir isotherm, then their peak maximum depends linearly on the scan speed $I_p \sim \nu$ [12]. In order to verify this, scan speeds within the range of a few $\frac{mV}{s}$ to several hundred $\frac{mV}{s}$ can be chosen. Significantly higher scan speeds lead to experimental difficulties (e.g. related to the double layer charging), which have to be overcome [12].

In contrast to surface processes, solution process, i.e electrochemical reduction / oxidation, involve beside the limited amount of reactants at the electrode surface also reactants transported through diffusion from the bulk electrolyte to the electrode surface. If the concentration of the reactant in the electrolyte volume is weakly affected by the reaction at the electrode surface, then the bulk electrolyte acts as an infinite source of reactants with constant concentration.

The continuous transport of reactant through diffusion to the electrode surface and its reaction results in a continuous current signal. Therefore the current wave of solution processes have before and after its peak two different offsets and consequently current waves of solution processes are asymmetric to their peak maximum.

The electrochemical reduction / oxidation can be described by the Randles-Sevcik equation, as proven in literature [12]. The essential result is that the peak maximum of this solution process depends linearly on the reactant concentration, but on the square root of the scan speed $I_p \sim c\sqrt{\nu}$, which permits to distinguish it from surface processes.

Solution processes can be further classified into fully reversible, inhibited and fully irreversible processes. Fully irreversible processes are easily identified as they possess only one current wave and the back reaction is by definition excluded to occur. In contrast to this, fully reversible and inhibited electrochemical reduction / oxidation reactions possess two current waves, one appearing in the first and the other appearing in the second (inverse) potential sweep. However, they can be still distinguished, as the peak position E_p does not depend on the CV scan speed ν if the electrochemical reduction / oxidation is fully reversible. In contrast to this, inhibited electrochemical reduction / oxidation possess a current wave position E_p which shifts with increasing CV scan speed ν [12].

The presented methods to distinguish processes at electrode surfaces rely on isolated and well defined model processes and therefore represent a first approach to the field of Cyclic Voltametry. However, the interference of processes close to each other is common at solid/liquid interfaces and demands more sophisticated descriptions, as stated in literature [12, 19]. Within this work CV is not used on a more complex than the presented level, as quantitative and dynamic questions were addressed via STM, which as local probe method permits more easily to elaborate an atomic understanding of surface processes.

However, CV scans are necessary in order to investigate the redox activity of molecular building blocks. In addition series of CV scans, with increasingly wide scan range, permits to conclude on the current wave position E_p of processes and relate pairs of current waves, in the cathodic and anodic potential sweep, to each other. Furthermore, the CV experiments permit to confirm experimental results obtained via STM by relating electrochemical current waves to STM imaged processes. This strategy may even reveal processes at the solid/liquid interface, which are unresolved in only one of both experimental methods. The verification of STM results via CV scans increases the significance of conclusions, which are then based on several methods and a greater experimental basis.

3.2 Scanning Tunneling Microscopy

Scanning Tunneling Microscopy (STM) is the experimental exploitation of the quantum tunneling, aiming at imaging the local density of electron states of a sample directly with atomic resolution. The quantum tunneling is a process in which a particle, i.e. electron, passes with a non-zero probability through a barrier although its energy is lower then the barrier. This on the macroscopic scale impossible process is a direct consequence of the laws of quantum mechanics, which apply to particles on the atomic scale [33].

The quantum tunneling results from solving the time independent Schrödinger equation in one dimension $\psi''(x) + [E - U(x)]\,\psi(x) = 0$ at a simple potential barrier $U(x)$, e.g. a rectangular barrier of finite height and width. Particles on the atomic scale possess a wave-like character and are therefore described by plane waves, namely $\psi(x) = Ae^{ikx}$. The quantum tunneling is a standard problem in quantum mechanics, therefore the detailed description of the strategy to solve this equation can be found in literature [33].

The solution for the quantum tunneling proves, that particles initially in front of the barrier possess a non-zero probability $|\psi(x)|^2 \neq 0$ to be situated behind the barrier. Therefore the particles have a finite probability to pass (= tunnel) directly through the barrier without the need to be excited to a state above the given barrier. This conclusion remain valid for electrons within a bounded state of a metal sample in close proximity to a second metal, e.g. STM tip. The equivalent to the barrier is the void between the two metals, as electrons within the conductive band of both metals need to be excited in order to reach unbounded states within the void. However, the quantum tunneling permits bound electrons to directly tunnel from one conduction band into the other without the need of a direct contact between the metals. The only condition is that

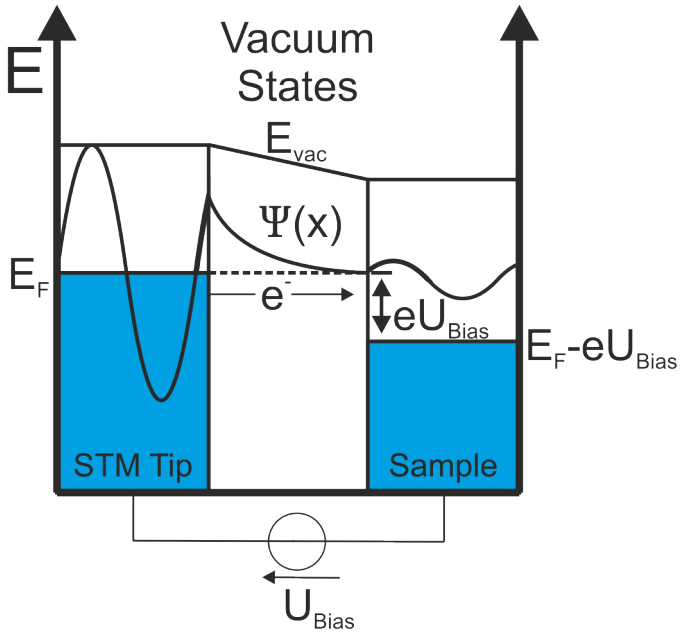

Figure 3.1: Sketch of the quantum tunneling in STM experiments, as described in literature [14, 33].

both metals, sample and STM tip, must be sufficiently close to each other, in order to have a sufficiently high probability for the electrons being situated behind the barrier.

The tunneling between sample and STM tip results in an equilibration of the Fermi level of both metals. In equilibrium the number of electrons, which tunnel from the sample into the STM tip is equal to the number of electrons in the reverse process, therefore no net charge is transferred between sample and STM tip. The idea behind the STM experiment is to create a constant potential difference between tip and sample, called the bias potential U_{Bias}. This creates a difference in the Fermi levels E_F of the two metals and consequently the number of tunneling events is not balanced anymore. The net charge transfer from one metal into the other results in the measurable tunneling current I_{Tunnel} or I_t. A sketch of this situation is shown in figure 3.1.

The tunneling current I_t depends linearly on the applied bias potential U_{Bias} and the density of electron states $\rho(E)$, but exponentially on the distance d between sample and STM tip, as proven via an approximation of the sample-tip couple [34].

$$I_t \sim U_{Bias} e^{-2kd} \rho(E) \tag{3.1}$$

The exponential dependence of the tunneling current on the distance between STM tip and sample is a result of the exponential decay of the electron wave function $\psi(x)$ within the barrier. It is this exponential decay which makes STM experiments highly sensitive to the topography of the sample surface.

Beside the topography, the density of states within the sample may cause changes of

the tunneling current[1]. A usually well working simplification is to assume that topography and density of states in the sample are related. This simplification holds as long as the sample is composed of one material, but fails mostly for samples composed of different chemical elements. In the latter case it must be proven separately, if variations of the tunneling current are related to the sample topography or chemical composition.

Sample surfaces are usually imaged by consecutive line scans of the STM tip, which provide a 2D image of the sample surface.[2] This STM scan can be performed in two different modes, namely the constant height or the constant current mode.

In the constant height mode the out-of-plane position of the STM tip is constant. When the STM tip is moved across the sample, the sample topography may change, i.e. by step edges, which modifies the distance between STM tip and sample. Consequently the tunneling current I_t responds exponentially to such topographic changes. Finally the STM image is obtained by plotting the measured tunneling current I_t vs. the in-plane coordinates (x,y) . The advantage of this mode is that no electrical controller is used and therefore higher scan speeds are possible. The disadvantage is that the risk of a collision between STM tip and sample is increased, therefore this mode should be used only in atomically flat areas of the surface.

In contrast to the constant height mode, in the constant current mode the out-of-plane position of the STM tip is adjusted by an electrical controller, in order to maintain a constant tunneling current I_t. This prevents collisions between tip and sample. The STM image is obtained by plotting the height correction signal, as it represents the sample topography and density of states. Although the risk of a collisions is lower in the constant current mode, the controller is not able to prevent all collision. A further disadvantage of the constant current mode is that the correction of the out-of-plane position of the STM tip requires time and therefore lowers the scan speed of the STM experiment.

In order to estimate the resolution of an STM experiment Δx, the tunneling process can be modeled to occur between a spherically ending STM tip of diameter R, which is at a distance d from a plane sample surface. The resolution is then approximated to $\Delta x = \sqrt{(R+d)\cdot 2\cdot 10^{-10}}$ [34]. Common distances between STM tips and sample surface are lower than 1 nm [35, 36], therefore the resolution with an atomically terminated tip can be expected to be better than 0.5 nm. Lowering an atomically terminated STM tip to 0.1 nm above the sample surface improves the lateral resolution to 0.2 nm, following the approximation of the lateral resolution. However, it can be assumed that the lateral resolution of the STM experiments depends strongly on the shape of the involved electron orbitals of both, the STM tip and sample. Therefore the lateral resolution is assumed to be better than predicted by the model [34].

[1] The electron density of states within the STM tip and bias potential between STM tip and sample are mostly constant in one STM scan, therefore they are not responsible for changes of the tunneling current I_t, which therefore must be related to the density of states in the sample and the sample topography.

[2] It should be mentioned that also 3D investigations of surfaces via STM are possible. However, this approach requires a significantly more complex analysis procedure of the tunneling current data and is therefore rarely used.

In the present work STM experiments are not performed in vacuum, but processes at electrochemically controlled solid/liquid interface are investigated *in situ* via STM. The difference between STM in vacuum and STM in solution is essentially the nature of the tunneling barrier, which therefore has to be corrected in the presented model. For instance molecules and ions from solution, i.e. H_2O, may be situated between the sample and the STM tip. This lowers the height of the barrier due to the electron states of the molecules and ions. More importantly, the electron states within the tunnel barrier are distributed inhomogeneously. This inhomogeneous tunneling barrier is superimposed to the sample topography and density of states and therefore alters the STM experiment in solution.

However, each STM data point is measured usually over $10^{-4}s$. In this time scale the inhomogeneous tunnel barrier evens out and appears therefore homogeneous, due to the motion of the molecules and ions in solution. The diffusion constant within solutions are usually of the order of $D \approx 10^{-9} \frac{m^2}{s}$ [37]. According to Einstein and Smoluchowski the average lateral displacement of diffusing particles is given as $\langle x \rangle \sim \sqrt{Dt}$ [38, 39, 37], and therefore the average lateral movement in solutions are of the order of 1 μm in $10^{-4}s$. This proves that the tunneling barrier can be assumed to be homogeneous on the time scale of the STM experiment.

Performing STM experiments at an electrochemically controlled solid/liquid interface leads to additional difficulties, as the electrochemistry disturbs the STM experiment. With respect to the electrochemical system, the STM tip is essentially an electrode at which reactions can occur. The currents arising from electrochemical processes are usually in the range of 0.1 $\frac{\mu A}{mm^2}$. In contrast to this, the signal of STM experiments (= tunneling current) is usually in the range of 0.1 - 10 nA. Therefore when electrochemical processes occur they fully obscure the STM signal and make STM experiment unfeasible. The most simple and effective counter-action is to isolate the surface of the STM tip – except the very STM tip ending – from the electrolyte solution, i.e. by a polymer shield as described in the experimental section (chap. 4) of this work. This reduces the surface of the STM tip in contact to the electrolyte solution to much less than 1 μm^2 and consequently lowers the noise originating from electrochemical reactions to approximately $10^{-5}nA$. The stated values are only rough estimations and are not experimental results.

3.3 X-Ray Diffraction at Solid/Liquid Interfaces

XRD (X-Ray Diffraction) is based on the elastic Thomson scattering of x-ray radiation at electrons to obtain structural information of the investigated sample. The incoming x-ray photons, described by the wave vector $\mathbf{k}$, are in the scattering event redirected without energy loss to the direction $\mathbf{k'}$. The conservation of energy leads to the condition $|\mathbf{k}| = |\mathbf{k'}| = \frac{2\pi}{\lambda} = const$ for all elastic scattering events. Besides the elastic Thomson scattering also non-elastic Compton scattering events of photons at electrons, in which energy is transmitted from the x-ray photon to the electron, may occur. The Compton

scattering[3] contributes a smoothly varying background signal to the XRD signals and can be therefore easily subtracted in the XRD signal treatment.

The cross-section for the elastic Thomson scattering of x-ray photons at one electron is found to be in a classical treatment

$$\sigma_T = (\frac{8\pi}{3})r_0^2 = 6,65 \times 10^{-29} m^2 \tag{3.2}$$

with $r_0 = (\frac{e^2}{4\pi\epsilon_0 mc^2})$ the classical electron radius or Thomson scattering length [40, 41]. Due to the low scattering cross-section (eq. 3.2) multiple scattering events can be neglected, which is also known as kinematic diffraction approximation.

In the following section the theoretical intensity profile of the x-ray scattering at a halide covered Cu(100) single crystal surface is deduced. The theoretical intensity profile depends mainly on the position of all atoms and ions in the crystal and the interfacial regime. The intensity profile is needed in the data analysis as the theoretical profile is adjusted in a fit procedure to reproduce the experimentally obtained XRD data. The result of the analysis is a structure model of the solid/liquid interface, which reproduces the experimental data.

3.3.1 Kinematic X-Ray Diffraction

In the kinematic diffraction limit the scattered x-ray intensity I_{sc}, which is the experimentally accessible quantity, is proportional to the square modulus of the structure factor $F(\mathbf{q})$ [40, 41]:

$$I_{sc}(\mathbf{q}) = \frac{I_o}{R^2}|F(\mathbf{q})|^2 r_0 P \tag{3.3}$$

with the incoming x-ray intensity I_0, the distance of the observer R, the classical electron radius r_0 and a polarization factor P.

The phase shift between all scattering centers, namely bound electrons, involved in the x-ray scattering is represented by the so-called structure factor $F(\mathbf{q})$. The structure factor is therefore the quantity, which actually contains all structural information of the sample. Structural changes lead to distinct variations of the structure factor and therefore variations in the measured intensity profile of the scattered x-ray radiation.

The position of the bound electrons is described by the electron density function $\rho_{el}(\mathbf{r})$, which is a continuous quantity. This leads to an integral definition of the atomic structure factor as $f_{at}(\mathbf{q}) = \int_V \rho_{el}(\mathbf{r}) e^{i\mathbf{q}\cdot\mathbf{r}} d^3\mathbf{r}$[4]. Atomic structure factors are approximated for computational reasons by $f_{at}(\frac{\mathbf{q}}{4\pi}) = \sum_{j=1}^{4} a_j e^{-b_j(q/4\pi)^2} + c$ [40, 41], with a_j, b_j and c as specific constants tabulated in the International Tables of Crystallography.

[3] The Compton signals are untreated, however, it should be pointed out that a sophisticated treatment of non-elastic scattering allows to obtain unique information about the electronic momentum distribution, which is beyond the technique used in the present work. [40]

[4] The atomic structure factor f_{at} is the Fourier transformation of the spacial electron charge distribution $\rho(\mathbf{r})$.

The structure factor for an arrangement of atoms, e.g. in a crystal unit cell, can be obtained by summing up the atomic structure factors and their relative phase shifts at the atom position $\mathbf{r_j}$ within the unit cell[5]:

$$F_{UC}(\mathbf{q}) = \sum_j f_{at,j} e^{i(\mathbf{k}-\mathbf{k}')\cdot\mathbf{r_j}} = \sum_{\mathbf{j}} f_{at,j} e^{i\mathbf{q}\cdot\mathbf{r_j}} \tag{3.4}$$

The structure factor of a crystal can be described – following the same ideas as stated before – by summing up all phase shifts between the unit cell structure factor, which are repeated at the positions defined by the vectors $\mathbf{R_n} = n_1\mathbf{a_1} + n_2\mathbf{a_2} + n_3\mathbf{a_3}$, with the crystal lattice vectors $\mathbf{a_i}$ and $n_i \,\epsilon\, \mathbb{Z}$:

$$F_{cryst}(\mathbf{q}) = \overbrace{\sum_j f_{at,j}(\mathbf{q}) e^{i\mathbf{q}\cdot\mathbf{r_j}}}^{F_{UC}(\mathbf{q})} \overbrace{\sum_n e^{i\mathbf{q}\cdot\mathbf{R_n}}}^{lattice\,sum} \tag{3.5}$$

Constructive interference of the x-rays scattered at each unit cell is obtained if the structure factor of the lattice sum fulfills $e^{i\mathbf{q}\cdot\mathbf{R_n}} = 1$. The exponent must then be of the form:

$$\mathbf{q}\cdot\mathbf{R_n} = 2\pi\cdot n \tag{3.6}$$

with $n \,\epsilon\, \mathbb{Z}$. The relation is true if the momentum transfer $\mathbf{q}$ has the following general form:

$$\mathbf{q} = h\mathbf{a_1^*} + k\mathbf{a_2^*} + l\mathbf{a_3^*} \tag{3.7}$$

with $\mathbf{a_1}\cdot\mathbf{a_1^*} = 2\pi\,\delta_{ij}$ [6] and $(h,k,l) \,\epsilon\, \mathbb{Z}^3$. The condition for constructive interference can be as well deduced from the Laue condition[7] $\mathbf{q} = \mathbf{G}$, with the reciprocal lattice vectors $\mathbf{G} = h\mathbf{a_1^*} + k\mathbf{a_2^*} + l\mathbf{a_3^*}$. The reciprocal lattice, and therefore the solution space of the momentum transfer $\mathbf{q}$, can be constructed from a given crystal lattice by using the equation $\mathbf{a_i^*} = \frac{\mathbf{2\pi}}{\mathbf{a_i}\cdot(\mathbf{a_j}\times\mathbf{a_k})}\mathbf{a_j}\times\mathbf{a_k}$ with $i \neq j \neq k$.

In the limit of an infinitely extended crystal $n \to \infty$ the contribution of the lattice sum in the scattered intensity profiles becomes a delta function $|S_N(\mathbf{q})|^2 = |\sum_n e^{i\mathbf{q}\cdot\mathbf{R_n}}|^2 \to Nv_c^*\delta(\mathbf{q}-\mathbf{G})$ [40, 41], leading to the sharp accumulation of the scattered x-ray intensity at the coordinates of the Bragg points.

Effect of Lattice Vibrations on the X-Ray Diffraction

The previous considerations assume that the position of each scattering center, e.g. atom/ion, can be identified by a set of three space coordinates. This is, however, not the case in reality, as atoms and ions within crystals are not immobile but vibrate around their crystal position, i.e. due to lattice vibrations and thermal motion.

[5] This is valid for scattering taking place at electrons in the kinematic diffraction limit.

[6] Kronecker delta δ_{ij} is zero and only one when $i = j$

[7] The Bragg condition can be deduced from the Laue condition. Both conditions are therefore identical. [40]

The vibrations around the average space coordinates are described by the displacement vector $\mathbf{u_n}$. The displacements $\mathbf{u_n}$ are supposed to be Gaussian distributed. The temporal average of the diffracted intensity at vibrating scattering centers is $I =< \sum_n f_{at}(\mathbf{q}) e^{i\mathbf{q}(\mathbf{r_n}+\mathbf{u_n})} \sum_m f^*_{at}(\mathbf{q}) e^{i\mathbf{q}(\mathbf{r_m}+\mathbf{u_m})} >$. Solving this equation proves that lattice vibrations can be described by a correction factor, which has to be applied on the previously defined atomic form factor $f_{at}(\mathbf{q})$. This correction factor has the form:

$$f^{DW}_{at}(\mathbf{q}) = f_{at}(\mathbf{q}) e^{-\frac{1}{2}q^2 < u_q^2 >_t} = f_{at}(\mathbf{q}) e^{-\frac{1}{16\pi^2} B_j q^2} \tag{3.8}$$

with the Debye-Waller factor $B_j = 8\pi^2 < u_q^2 >_t$ and the vibration amplitude parallel to the momentum transfer $u_q = \mathbf{u_n} \cdot \mathbf{q}$. This correction, known as Debye-Waller factor, acts as an attenuation with increasing strength for higher momentum transfers.

The Debye-Waller factor of the copper bulk is $B_{Cu} = 0.598 \text{Å}^2$, as published by Linkoaho [42]. At the electrode surface the vibrational amplitudes and therefore Debye-Waller factors are supposed to deviate from the copper bulk value, due to drastic changes in the boundary conditions at surfaces. Therefore the Debye-Waller factors of the topmost Cu layers are determined in the x-ray diffraction data analysis procedure.

3.3.2 X-Ray Diffraction at Surfaces

The above stated equations, which describe an crystal lattice of infinite dimensions, do reproduce experimental data obtained from crystal bulk samples. However, the equations fail to describe the in Surface X-Ray Diffraction (SXRD) experiments appearing CTR (Crystal Truncation Rod) [43], which are rod like intensity distributions interconnecting the Bragg points in the out-of-plane direction of a sample surface. In order to mathematically model SXRD experiments, the previous infinite crystal lattice has to be truncated in one of the three dimensions, e.g. the z-direction. This results in a crystal lattice which extends infinitely ($-\infty$ to $+\infty$) in the x- and y-direction but only half infinitely ($-\infty$ to 0) in the z-direction. This truncation results physically in a crystal surface and mathematically in a spreading and thus interconnecting of the scattered intensity at the Bragg points parallel to the surface normal. The half-infinite lattice sum can be rewritten to $\sum_{n_3=0}^{\infty} e^{-n_3(i\mathbf{q}\cdot\mathbf{a_3}+\varepsilon)} = \frac{1}{1-e^{-n_3(i\mathbf{q}\cdot\mathbf{a_3}+\varepsilon)}}$ with $\mathbf{a_3}$ parallel to the surface normal and the absorption of the x-ray beam $\varepsilon \in \mathbb{R}_{>0}$. The delta-function for an infinite crystal is for the half-infinite crystal in the out-of-plane direction substituted by the function $\frac{1}{1-e^{-n_3(i\mathbf{q}\cdot\mathbf{a_3}+\varepsilon)}}$. The x-ray radiation scattered at an infinitely extended flat crystal surface is therefore still localized in the in-plane directions, forming the well known Bragg points, but not localized in the out-of-plane direction, which results in the mentioned interconnection of the Bragg points along the surface normal. The x-ray scattering at a sample surface is then correctly described by the following equation:

$$F_{CTR}(\mathbf{q}) = \frac{F_{UC}(\mathbf{q})}{1 - e^{-n_3(i\mathbf{q}\cdot\mathbf{a_3}+\varepsilon)}} \sum_{\mathbf{G}_{||}} \delta(\mathbf{q}_{||} - \mathbf{G}_{||}) \tag{3.9}$$

with the in-plane momentum transfer $\mathbf{q}_{||}$ and the in-plane reciprocal lattice vector $\mathbf{G}_{||}$.

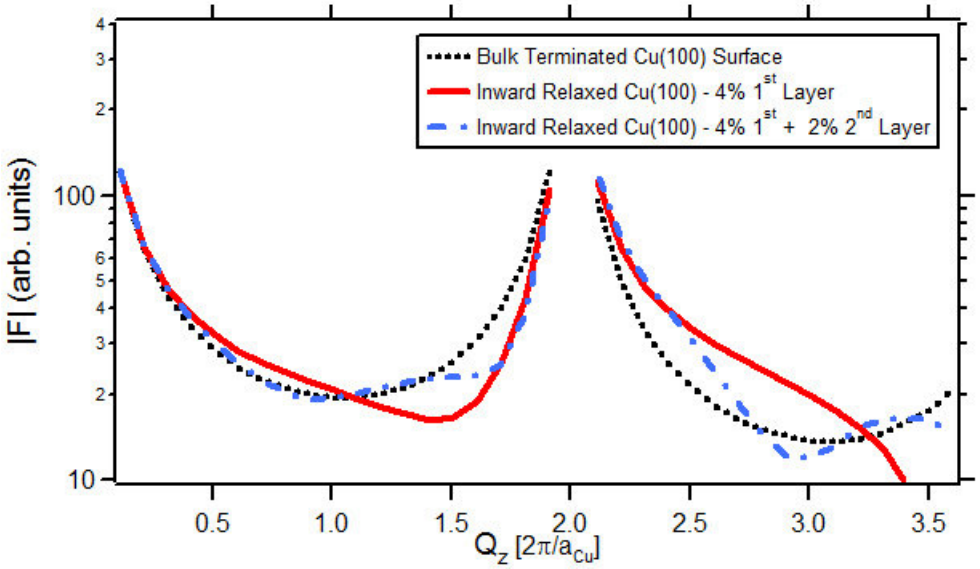

Figure 3.2: (2 0 L) CTR profiles of a bulk terminated Cu(100) surface compared to two exemplarily inward relaxed Cu(100) surfaces along the out-of-plane direction. The inward relaxation was chosen to be 8% (~ 0.14 Å) of the 1st Cu layer (red solid curve) or 8% of the 1st + 4% (~ 0.07 Å) of the 2nd Cu layer (blue dashed curve). The reciprocal coordinates refer to the copper fcc unit cell.

The intensity distribution within the CTR is highly sensitive on the near surface structure of the sample. Measuring the intensity profile along the CTR allows therefore to determine the full 3D-structure of the crystal surface regime.

The high sensitivity of the CTR intensity profile is exemplarily shown for a Cu(100) surface in figure 3.2. Layer relaxations of less than 0.1 Å already strongly affect the shape of the CTR intensity profile as can be seen by comparing the three calculated CTR profiles imaged in figure 3.2.

3.3.3 X-Ray Diffraction at Halide Covered Cu(100) Surfaces

Applying the equation 3.9 and the Debye-Waller correction (eq. 3.8) to the Cu(100) surface with the commonly used copper fcc unit cell leads to the copper bulk structure factor

$$F_{CTR-Cu(100)}(\mathbf{q}) = \frac{f_{Cu}(\mathbf{q})e^{-\frac{1}{16\pi^2}B_j q^2}(1+e^{i\pi(h+k)}+e^{i\pi(k+l)}+e^{i\pi(h+l)})}{1-e^{-n_3(i2\pi l+\varepsilon)}}\sum_{\mathbf{G}_{||}}\delta(\mathbf{q}_{||}-\mathbf{G}_{||}) \tag{3.10}$$

The x-ray radiation scattered at the fcc unit cell of the copper bulk can only interfere constructively when H, K and L are all even or all odd. Arbitrary H, K and L coordinates do not interfere constructively, whereas mixed even and odd H, K and L coordinates lead

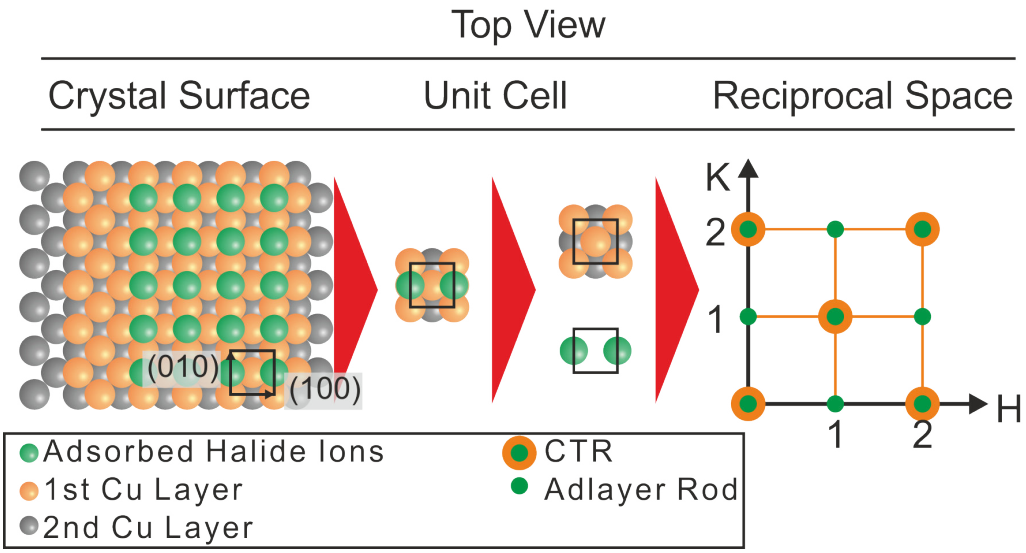

Figure 3.3: Relation between structure and diffraction patters of the halide covered Cu(100) surface. Left: Halide p(1x1) adsorbed on a Cu(100) surface. Center: Decomposition of the surface unit cell into the c(1x1) motive of copper and p(1x1) motive of the adsorbed halide. Right: Cut-out of reciprocal space showing the coordinates where the x-ray radiation is scattered. Orange circles represent x-ray radiation scattered at the copper fcc lattice. Green circles represent x-ray radiation scattered at the p(1x1) halide monolayer.

to a destructive interference, which is known as extinction rule of the fcc lattice. The extinction rule of the fcc lattice arises naturally from equation 3.10 where the phase factor $P_{fcc}(1 + e^{i\pi(h+k)} + e^{i\pi(k+l)} + e^{i\pi(h+l)})$ becomes zero whenever the extinction rule is fulfilled.

Due to the fcc extinction rule Bragg points can only be found along the CTR at the (H K) position (2 0), (0 2), (1 1) and (2 2) as imaged in figure 3.3 and 3.4. Contrary to the fcc lattice, the simple cubic p(1x1) halide adlayer scatters x-ray radiation to all (H K) $\epsilon\, \mathbb{Z}^2$. This results in so-called adlayer rods [26] at mixed even and odd (H K) coordinates, where no fcc copper contribution but purely scattering events from the surface regime appear. The absence of the bulk contribution makes the adlayer rods highly surface sensitive to the surface structure of the metal electrode. The intensity profile of the adlayer rod is solely influenced by the first halide adlayers and all copper layers underneath, which do not conserve their cubic centered motive. This latter condition results from the fact that the fcc extinction rules act layerwise as can be seen in the phase factor of a single atomic layer of the fcc lattice $P_{layer} = (e^{i2\pi(0\cdot h+0\cdot k)} + e^{i2\pi(\frac{1}{2}\cdot h+\frac{1}{2}\cdot k)}) = (1 + e^{i\pi(h+k)})$. The phase factor P_{layer} is non zero if and only if the coordinates H and K are both even or odd. Therefore only copper layers loosing their centered motive contribute to the intensity profile of the adlayer rod. This is forbidden for the first, third, fifth, ... copper layer, due to symmetry reason with respect to the adsorption of halide anions. Indeed the analysis of the x-ray diffraction experiment proved that the second copper layer looses its central motive, as proposed previously [26, 25].

The SXRD data analysis revealed, the halide/Cu(100) surface regime to extend three copper layers into the copper crystal. Lower copper layers are found to stay in their fcc bulk coordinates and are therefore included within the structure factor of the half-infinit copper crystal. The structure model of the surface unit cell is shown in figure 3.4. The x-ray diffraction pattern of the halide/Cu(100) surface is fully described by a global structure factor $F_{sum}(\mathbf{q}) = F_{surf}(\mathbf{q}) + F_{CTR-Cu(100)}(\mathbf{q})$, which is the coherent sum of the structure factor of the surface regime $F_{surf}(\mathbf{q})$ with the structure factor of the half-infinit Cu(100) crystal $F_{CTR-Cu(100)}(\mathbf{q})$ (eq. 3.10). The recently found lateral ordering of the electrolyte at chloride/Cu(100) surfaces [44] explains systematic deviations between SXRD data and model data of the adlayer rods as observed in previous publications [26, 25]. Therefore the new model of the surface regime shown in figure 3.5 is extended from the halide-c(2x2)/Cu(100) surface into the liquid electrolyte phase. In this model solvated potassium cations adsorb into the four-fold hollow sites of the negatively charged halide adlayer.

3.4 X-Ray Photoelectron Spectroscopy

X-ray Photoelectron Spectroscopy (XPS) is a chemical and surface sensitive probe technique, which permits to directly probe the chemical state of adsorbats on the Cl/Cu(100) electrode surface and therefore ideally complements CV and STM experiments. XPS is surface sensitive as the electrons, which are upon irradiation emitted from the sample bulk, are inelastically scattered and therefore do not contribute to the specific XPS sig-

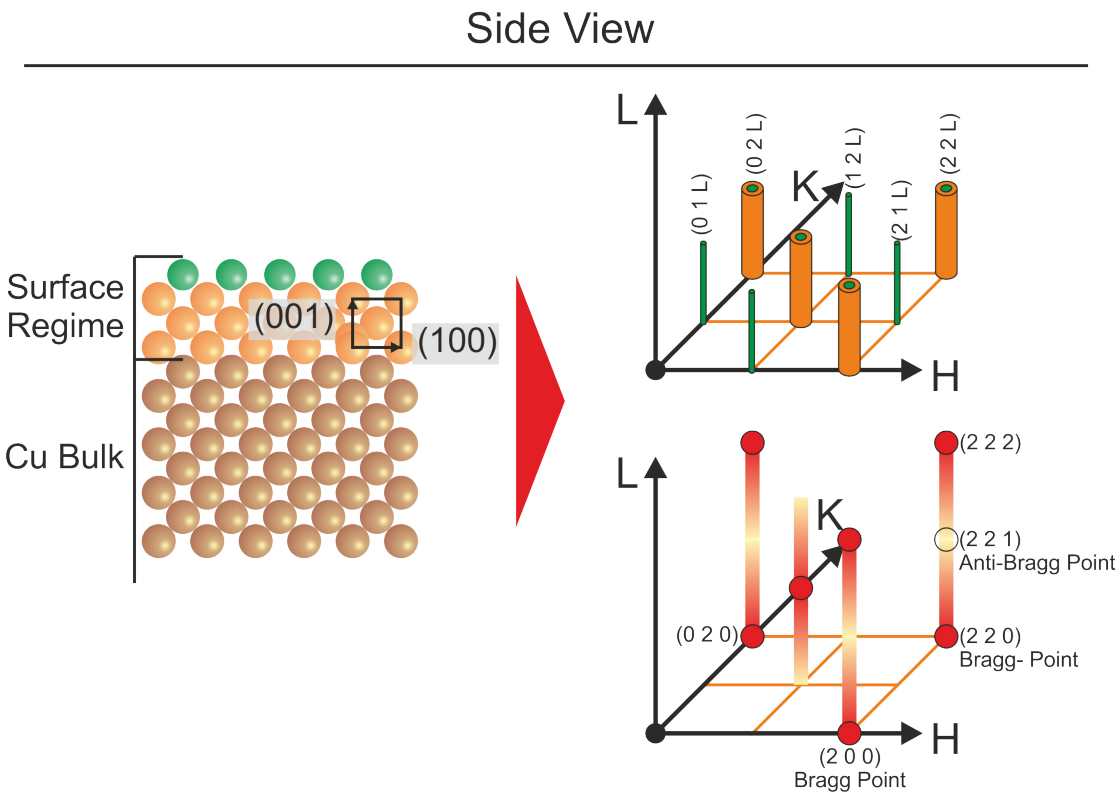

Figure 3.4: Relation between structure and diffraction pattern of the halide covered Cu(100) surface. Left: Side view of the halide covered Cu(100) surface regime and copper bulk. Right: Side view of a cut-out of the reciprocal space map. Upper Coordinate System: Illustration at which coordinates the copper fcc lattice scatters x-ray radiation (orange) and at which coordinates the halide monolayer scatters x-ray radiation (green). Lower Coordinate System: Bragg points of the fcc copper crystal and CTRs (crystal truncation rods) connecting the Bragg points along the L-coordinate.

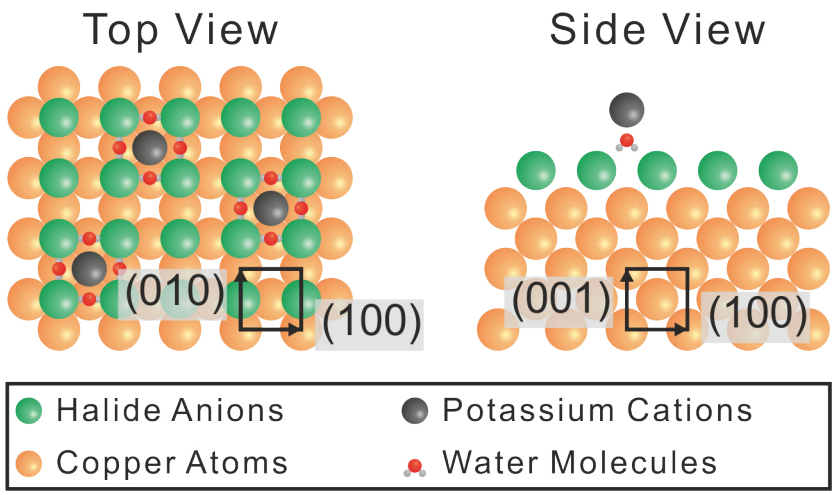

Figure 3.5: Model of the surface regime of the electrolyte/Cu(100) interfacial regime. Chloride and bromide anions form a monolayer of a p(1x1) pattern on the Cu(100) surface.

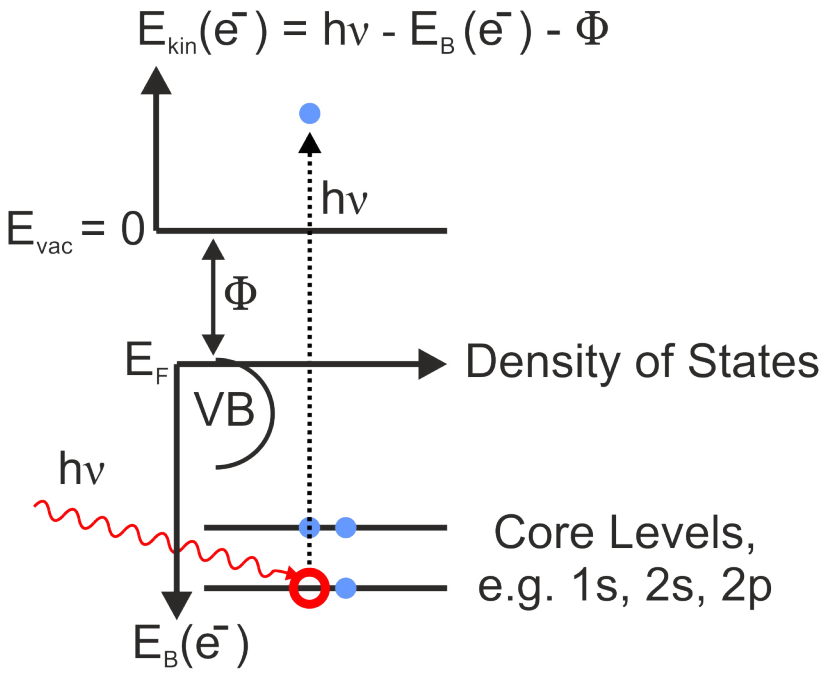

Figure 3.6: Model of the photoelectric effect exploited in the XPS experiment.

nals. In contrast to this, electrons emitted from the topmost atomic layers leave the sample unaffected.

XPS is based on the photoelectric effect, in which a photon of the energy $h\nu$ is absorbed by a bound electron in the sample, as sketched in figure 3.6. The photon energy is imposed by the x-ray radiation source, e.g. Mg-K_α or Al-K_α radiation. X-ray photons possess sufficient energy to excite core level electrons, e.g. from the 1s orbital, to an unbound vacuum state, as sketched in figure 3.6. The kinetic energy E_{kin} of the emitted electrons is then the photon energy $h\nu$ diminished by the electron binding energy (with respect to the Fermi level E_F) and the work function Φ:

$$E_{kin}(e^-) = h\nu - E_B(e^-) - \Phi \tag{3.11}$$

In order to relate the detected kinetic energy to one specific binding energy the energy of the incoming x-ray radiation $h\nu$ should be as monochromatic as possible. Equation 3.11 describes the kinetic energy of the electron upon emission from the sample, which is not the kinetic energy detected by the XPS spectrometer, as on the initial kinetic energy an instrument specific offset is added. This offset originates from the grounding of the sample, i.e. of the copper crystal, and of the XPS spectrometer, which is required to prevent a distortion of the experimental data through the charging of the sample or XPS spectrometer. The grounding leads to an alignment of the Fermi levels of the sample and XPS spectrometer, consequently their vacuum levels differ and therefore a setup specific offset is added to the detected kinetic energy of the photoelectrons [14, 45].

For solids the electron binding energies are related to the Fermi level as origin of the energy scale (sketched in figure 3.6). Electrons at the Fermi level are the weakest bound and therefore they are upon emission the most energetic ones. Consequently the Fermi level is determined by the upper cut-off of the detected kinetic energy spectra of photoelectrons. The determination of the Fermi level in the registered spectra permits to conclude on the electron binding energy of the photoelectrons.

The investigation of various samples proved that the binding energy of electrons from the same chemical element may differ up to several eV. This differences originate from the specific redox state and environment of the emitting atom. For instance the redox state of the atom affects the bond strength of its electrons. The higher (= more positive) the redox state, the stronger the electrons are bound to the atom, and consequently the higher the binding energy. The electron binding energy is as well affected by the next neighbor of the emitting atom. This results from a partial charge transfer as a result of different electronegativities. This charge transfer also affects the charge state of the emitting atom and therefore the binding energy of its electrons. This makes the same chemical element within one molecule distinguishable, if their next neighbors differ. Both chemical effects, redox state and next neighbor interaction, are known as the “chemical shift”.

In addition to the chemical shift, the interaction to the second next neighbor can as well affect the electron binding energy, however weaker than the chemical shift. This contribution is known as Madelung term and most expressed in ionic crystals.

The photoelectron may upon or after its emission interact with the emitting atom.

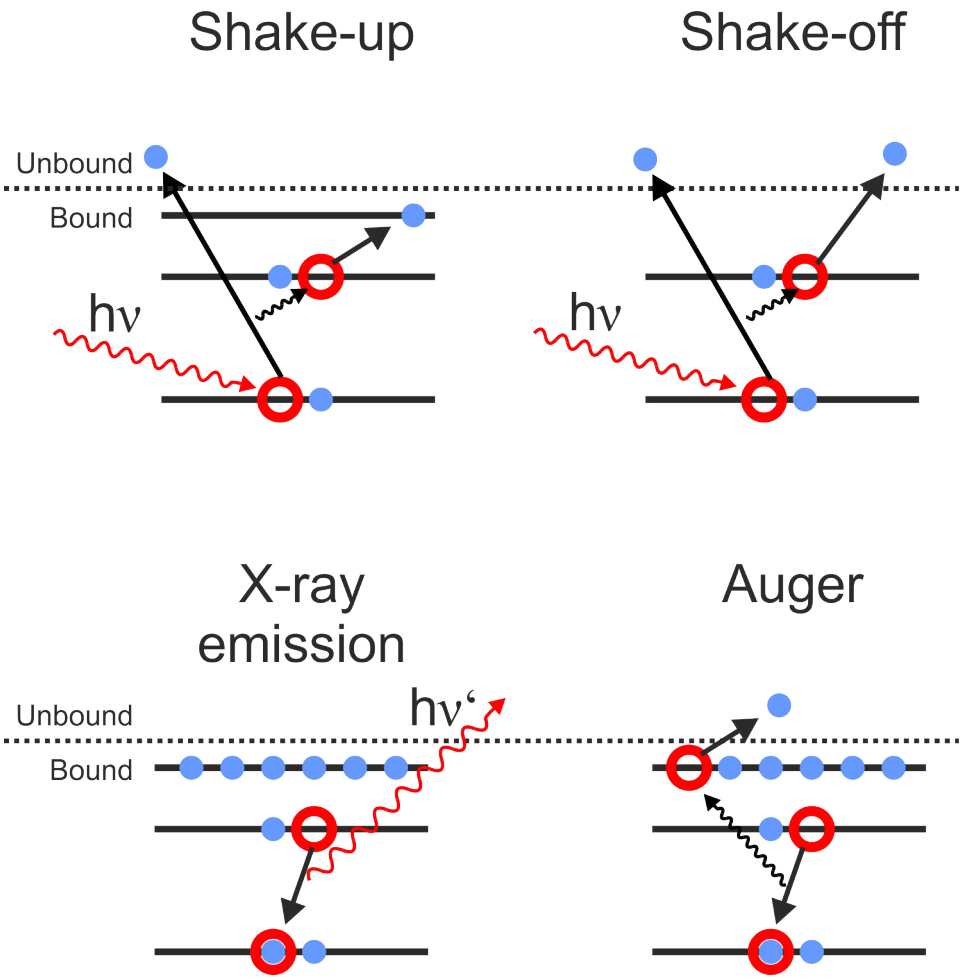

Figure 3.7: Secondary processes related to the XPS experiment.

This affects the kinetic energy of the photoelectron and consequently leads to a peak shift (or additional peaks) in the registered XPS spectra. Upon emission three such interactions may occur, namely the shake-up, shake-off and plasmon excitations. In the shake-up / shake-off processes the photoelectron transfers upon emission energy to one electron in a weaker bound states, e.g. valence electron, which may then be excite to a higher bound state (shake-up) or excited to an unbound state (shake-off), as sketched in figure 3.7. In contrast to this, the plasmon excitation is not based on the excitation of one single electron, but based on the vibration of the metal electron plasma as a whole. These latter excitations of the electron density are quantized, as photons and phonons, and therefore known as plasmons.

After its emission the photoelectron can interact with the excited atom. This interaction can be assumed to depend on the lifetime of the excited atom state. The lifetime of excited atom states are limited by secondary processes, such as the x-ray emission or Auger electron emission upon relaxation, as sketched in figure 3.7. The relaxation of a weaker bound electron into the strongly bound and vacant core level state results in an energy gain. In the x-ray emission process this energy is emitted via an x-ray photon. However, the energy gain through relaxation of the excited atom can be also transferred intra-atomically to a weaker bound electron. This can result in the excitation of this secondary electron into an unbound vacuum state and therefore to the emission of the secondary electron from the atom. These secondary electrons are known as Auger electrons and deliver element specific information, as exploited in the Auger electron spectroscopy.

The Auger process leads to additional peaks within the registered XPS spectra. In order to distinguish between Auger and Photoelectrons the primary x-ray energy can be changed. Changing the energy of the incoming x-ray photons does affect the kinetic energy of the photoelectrons, but not of the Auger electrons, which are emitted due to the intra-atomic relaxation and not by the primary x-ray photons. Consequently comparing the XPS spectra registered at two different x-ray photon energies permits to distinguish between photoelectrons and Auger electrons, due to their shift along the binding energy axis.

In order to verify the sample state survey XPS spectra are most suitable, as they reveal a possible contamination through their chemical sensitivity. Figure 3.8a shows a typical survey XPS spectrum of C3-DBDP^{2+} electrochemically adsorbed on a Cl/Cu(100) substrate. The photoelectron peaks are designated with the element symbol of the emitting atom and the orbital from which the photoelectron originates, e.g. 1s, 2s or 2p orbital. Besides the sharp XPS signals an electron background of about 10^4 counts appears. This background is mostly attributed to inelastic scattering events of the photoelectrons. In agreement with this, at electron binding energies higher than the Cu3p XPS signal the electron background increases. This background results from inelastically scattered Cu3p photoelectrons, which possess a lower kinetic energy and therefore appear at lower binding energies in the XPS spectrum than the unscattered Cu2p photoelectrons.

In the XPS spectrum, additional to the expected signals of Cu, Cl, C and N, also small contaminations of oxygen (O) and silver (Ag) appear. The oxygen signal may be provoked by a slight oxygen contamination of the Cu(100) surface, or – more likely

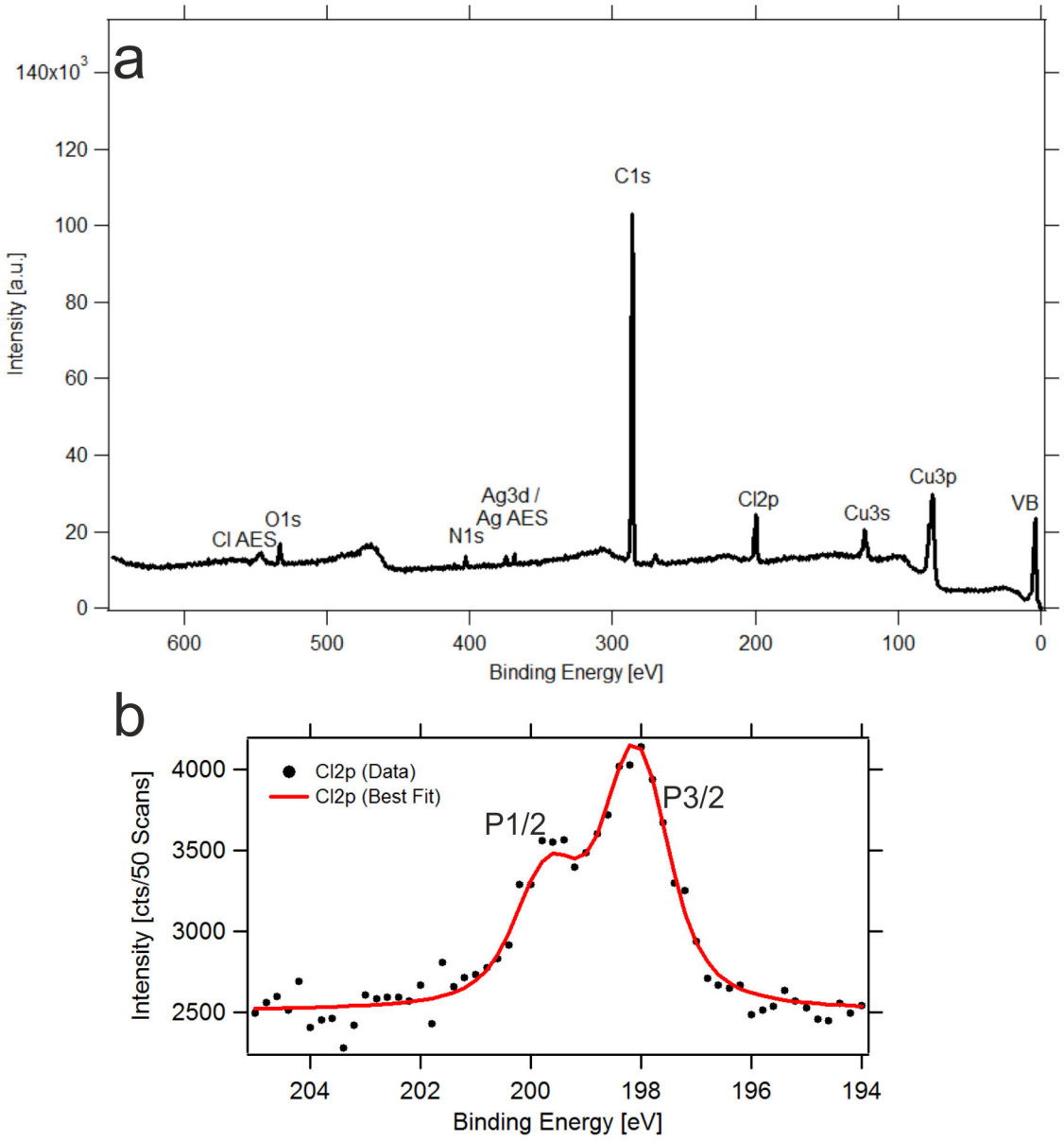

Figure 3.8: Example XPS spectra. (a) Survey XPS spectra of a full monolayer of C3-DBDP^{2+} electrochemically adsorbed on a Cl/Cu(100) substrate. (b) Highly resolved XPS spectrum of Cl2p.

– by traces of residual water within or above the organic monolayer. The Ag signals originates from the electrochemical sample preparation, as the reference electrode was chosen to be a silver wire.

After the verification of the sample state through a survey XPS spectrum, usually highly resolved scans of single XPS signals are registered. Such highly resolved XPS spectra permit to determine the binding energy of the photoelectrons with high precision. In order to determine the binding energy the XPS spectra are reproduced by an appropriate underground and fit function. Within this work – and usually – Voigt functions are used to reproduce XPS data. The Voigt function is the convolution of a Gaussian and Lorentzian peak. Voigt functions can be substituted by either the summation or multiplication of a Gaussian and Lorentzian peak, which may still deliver satisfying results in certain cases [46]. However, as the XPS investigations in this work did not aim on a quantitative determination of elements, only the peak position and not the peak area is of interest. This makes the XPS data analysis overall less susceptible to errors. Indeed, when XPS experiments are used for quantitative investigations a number of possible sources of errors have to be taken into account [14].

As an example of a highly resolved XPS spectrum the Cl2p XPS signal is shown in figure 3.8b. The Cl2p signal consists of two peaks, namely the $p_{1/2}$ and $p_{3/2}$ contribution, which are both reproduced by Voigt functions. The notation $p_{1/2}$ and $p_{3/2}$ is a result of the spin-orbital interaction with the total angular momentum $j = l + s$ (l the orbital angular momentum and s the electron spin). For the p-orbital ($l = 1$) it follows $j = 1 \pm \frac{1}{2}$. The multiplicity (= degeneration of energy level) is $j(j+1)$ and therefore 4 when $j = \frac{3}{2}$ and 2 when $j = \frac{1}{2}$. The different multiplicities lead to different peak intensities, namely $2:1$, which agrees with the in figure 3.8b observed peak heights.

4 Experimental Details

General Remarks

The copper and HOPG (Highly Ordered Pyrolytic Graphite) single crystals tailored and produced to fit inside the experimental setup were produced by MaTeck GmbH Germany [47]. All copper crystals were cut and mechanically polished to the crystallographic (100) plane with a maximum mis-cut of 0.1°. The HOPG crystal was chosen to have a maximum mosaic spread of 0.4°.

In order to control the experimental environment at the solid/liquid interface high purity conditions are mandatory. In this work chloride anion adsorption on the Cu(100) surface is exploited to obtain a negatively charged template on which the adsorption and ordering of positively charged organic cations is studied. Contamination by bromide or iodide anions is a major issue as those two halide anions displace the adsorbed chloride from the Cu(100) surface, due to their higher tendency to specifically adsorb as presented in the previous section. This may lead to distinct differences in the electronic and/or morphological structure of the Cu(100) surface. In order to obtain high purity conditions reagent grade chemicals were furnished by Merck GmbH Germany [48] (Merck "suprapur" quality) and then used to prepare the electrolyte solutions, e.g. HCl or H_2SO_4 electrolytes.

All organic molecules investigated in this work were di-chloride salts with the highest available purity in order to avoid bromide or iodide anion contamination. Further, the absence of these halide anions was assured by an adequate production procedure and/or chemical certificates. DPV (Diphenylviologen) and DBV (Dibenzylviologen) were produced by Fluka and acquired via established vendors. The specifically tailored DB-3,3'-BP (1,1'-Dibenzyl-3,3'-Bipyridinium), C3-DBDP (1,1'-Dibenzyl-4,4'-(Propane-1,3-diyl)-Dipyridinium) and C7-DBD P(1,1'-Dibenzyl-4,4'-(Heptane-1,7-diyl)-Dipyridinium) compounds were synthesized by the Group of Professor Dr. Sigurd Höger (Department of Organic Chemistry, University of Bonn). In all home synthesis procedures of these molecular building blocks it was consciously taken care to avoid a contamination, i.e. by the above mentioned critical Br and I anions. Details of the synthesis are published elsewhere [49].

Furthermore all reservoirs and units of the electrolyte supply set-up were routinely cleaned previous to experiments by flushing with electrolyte solution and/or several cycles of cleaning in an ultrasonic bath of always fresh milli-Q grade water. All experimental parts, which are sufficiently chemically inert (e.g. glass units or teflon parts) were regularly cleaned in a bath of oxidant acid (peroxymonosulfric acid), namely a 1:1 volume ratio of sulfuric acid (conc. 95%) and hydrogen peroxide (conc. 30%) (H_2SO_4 : H_2O_2, purity: "for analysis") leading to the oxidation of present – especially organic –

contaminants. After the oxidizing bath the units were flushed several times with milli-Q grade water and cleaned several times in the ultrasonic bath, which led to the removal of all contamination.

High purity water, the basic reagent of all solutions and the standard flushing liquid, was obtained daily from an in-house milli-Q purification system, with a resistivity of 18.2 $M\Omega \cdot cm$.

All electrolyte solutions were degassed prior to all experiments for at least one hour by a continuous flow of argon gas through the electrolyte solution leading to the removal of present oxygen. The argon gas used to degas the electrolytes as well as to obtain an oxygen free experimental containment (STM cube, SXRD cell) was furnished by Air Liquid [50] with a purity of 99.999 Vol.%.

4.1 Preparation of the Cu(100) Surface

Copper is easily oxidized in the presence of even traces of oxygen. Thus, an adequate preparation procedure to obtain a clean and oxygen free Cu(100) surface has in a first step to remove the native copper-oxide layer and other superficial contamination, as well as in a second step to protect the bare copper surface from re-oxidation while the sample is transferred into the oxygen free experimental containment. A widely accepted method to obtain defined copper single crystal surfaces under ambient condition is a combination of electrochemical etching/polishing and, if applicable, oxidation protection by anion adsorption [51, 52]. The published procedures differ in the composition of the etching solution as well as in the applied voltage or polishing time from author to author, which represents the fact that a detailed understanding of the etching process is still missing.

A crucial factor for the success of SXRD (Surface X-Ray Diffraction) experiments is the roughness of the investigated sample surfaces. Rough surfaces lead to low signal/noise ratios in SXRD experiments [40], which leads to high experimental errors, i.e. at the anti-Bragg points in reciprocal space situated between two Bragg points. Often the line shape close to anti-Bragg points contains most information for the surface sensitive structure analysis, making a possibly high signal/noise ration mandatory for high quality results. As a consequence an adequate surface preparation procedure for the present work has to focus on minimizing the sample surface roughness.

For all experiments a sample preparation procedure inspired by those published by Huemann et al. [24] was used, as this procedure has proven to produce a sufficiently smooth Cu(100) surface to perform high quality SXRD measurements. In order to polish the Cu(100) surface electrochemically the (100) surface is immersed into a 50% phosphoric acid solution (50% H_3PO_4, purity: "for analysis") and a voltage $U_{polishing}$ of +2V to +2.2V is applied for 20 - 40 sec between the copper anode and a platinum foil (about $1cm^2$) as cathode as shown in figure 4.1. This leads to the removal of superficial copper-oxide and contamination from the surface. The copper crystal is in this procedure held by a crocodile clamp via a tantalum wire. The tantalum wire is situated within a groove around the copper crystal, as imaged in figure 4.1. When solely the Cu(100) surface is wetted by the phosphoric acid solution, then a meniscus between crystal surface

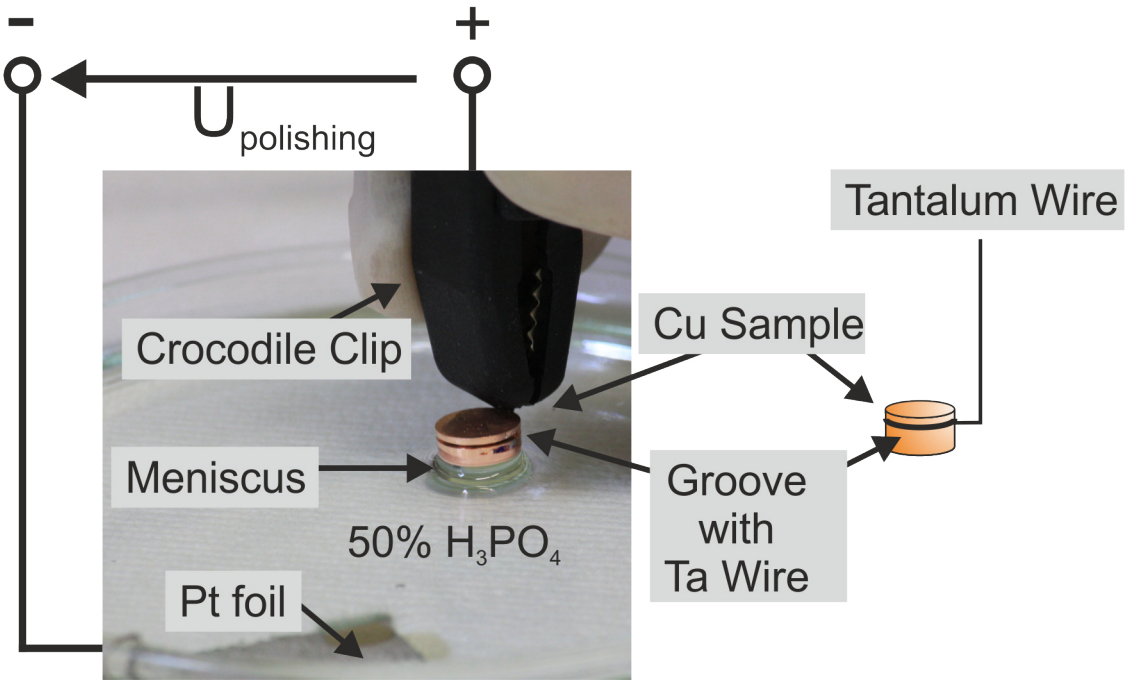

Figure 4.1: Electrochemical polishing of a single crystal copper surface in a 50% H_3PO_4 solution. The Cu crystal is held by a tantalum wire situated within a groove around the crystal. The tantalum wire electrically connects the Cu crystal via a crocodile clip to a potential source.

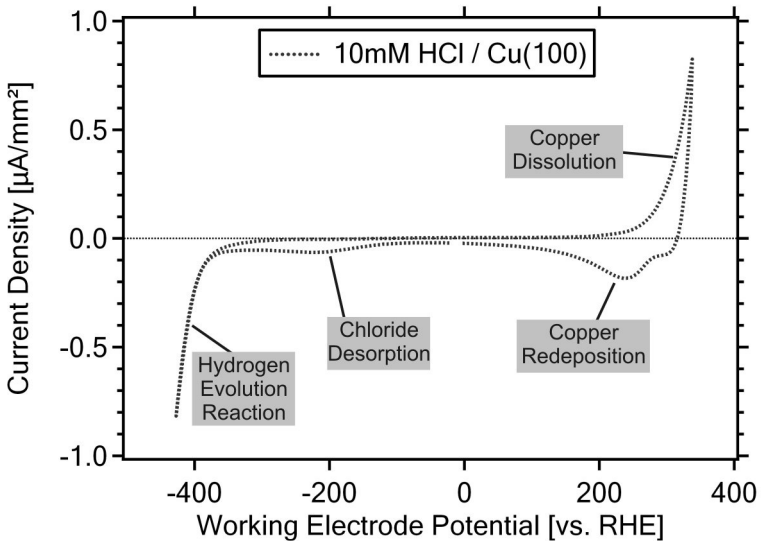

Figure 4.2: Steady state CV (Cyclic Voltamogram) of an oxygen free Cu(100) surface in a degassed 10 mM HCl solution. Scan speed 10 mV/sec.

and liquid (fig. 4.1) appears. The meniscus assures the selective wetting of only the Cu(100) surface, which minimizes the etching and loss of copper at the crystal flanks and therefore protects the cylindrical crystal shape (relevant for a possibly long usability of the Cu crystal as sample).

After the electrochemical polishing the Cu(100) surface is rinsed first with a 5 mM sulfric acid solution to remove the orthophosphoric acid solution (including copper cations and contamination) from the Cu(100) surface. Subsequently the Cu(100) surface is rinsed with a chloride containing solution (10 mM HCl or 5 mM H_2SO_4 + 10 mM KCl) leading even under open circuit conditions to the adsorption of a full monolayer of chloride anions on the Cu(100) surface [24]. The adsorbed chloride monolayer acts as a physical and chemical barrier and, thus, inhibits the copper re-oxidation and protects the unoxidized Cu(100) surface while the sample is transferred through air into the argon filled, and therefore oxygen free and clean, experimental containment.

However, the Cu(100) surface can occasionally still be contaminated by oxygen even when the surface is protected by a full monolayer of adsorbed chloride anions. The sample transfer into the oxygen free atmosphere or the subsequent filling of the electrochemical cell with the degassed solution are possible sources for these oxygen contamination. The presence of oxygen results in the appearance of a broad peak at a electrode potential of about -250 mV [vs. RHE], which was proven by intentionally exposing the copper/electrolyte interface under potential control to an oxygen containing atmosphere. The peak appearing in the CV at about -250 mV [vs. RHE] is most likely the overlay of several redox processes related to the presence of oxygen. One of the possible processes

is the reduction of copper-(I)-oxide to copper with an equilibrium potential of -350 mV [vs. SHE][1] [11]:

$$Cu_2O_{(s)} + H_2O + 2e^- \rightleftharpoons 2Cu_{(s)} + 2OH^- \tag{4.1}$$

This occasionally appearing small contamination by oxygen can be removed, while the sample rests within the EC-STM setup, by applying a working electrode potential lower than the copper-oxide reduction potential or by voltametric cycles between 0 mV and the onset of the HER (hydrogen evolution reaction) for approximately 30 min. Lowering the electrochemical potential below the reduction potential associated with the redox-process in eqn. 4.1 leads to a removal of the present oxygen and, thus, to a vanishing of the copper-oxide peak in the CV (cyclic voltamogram). In this post-preparation procedure it was avoided to reach the hydrogen evolution regime as the hydrogen evolution reaction usually roughens the sample surface, which had to be prevented for the reason given above, as well as for a maximum comparability of the experimental results.

Exposing the Cu(100) surface to a chloride anion containing solution leads further to the so-called "electrochemical annealing" [53], which is induced by an enhanced mobility of superficial copper via – probably – the formation of soluble chlorocopper complexes [20, 21, 24, 3]. This self-annealing of the chloride/copper system is a highly advantageous effect as at solid/liquid interfaces the under UHV conditions used temperature induced annealing and sputtering are not applicable. In order to obtain flat surfaces the UHV-"annealing and sputtering procedure" is replaced under ambient conditions by the chloride induced self-annealing of the solid/liquid interface, which as well heals surface defects and therefore flattens the etch-roughened Cu(100) surface.

Prior to all experiments the freshly prepared Cu(100) surface in a 10 mM HCl was characterized by cyclic voltametry. The typical response of a Cu(100) / 10 mM HCl interface is imaged in figure 4.2. This registered CV curve was obtained with a scan speed of 10 $\frac{mV}{sec}$ from a starting value of 0 mV [vs. RHE] scanning in cathodic direction to a lower limit of -420 mV [vs. RHE]. Subsequently the potential is increased in anodic direction to an upper value of +330 mV [vs. RHE] to be finally lowered back to the initial starting potential. At -150 mV a negative current appears, which originates from a capacitive change at the interface due to the desorption of chloride anions from the Cu(100) surface as proven by means of SXRD [25]. Lowering the copper electrode potential below -390 mV [vs. RHE] leads to the production of hydrogen by a reductive decomposition of water. The increase to potentials higher than +200 mV [vs. RHE] induces the corrosive decomposition of the sample surface by the Cu oxidation. Consequently at copper electrode potentials above +200 mV [vs. RHE] copper cations accumulate within the interfacial regime. These produced copper cations can be reduced at and readsorbed onto the electrode surface by lowering of the copper potential sufficiently below +200 mV.

After the verification of the successful surface preparation via cyclic voltametry the ions of interest (e.g. bromide or organic cations) were introduced into the solid/liquid interface by exchanging the initial electrolyte under potential control, usually at an electrode potential of $E_{work} = 0$ mV [vs. RHE] if not stated otherwise, by the adequate reagent containing electrolyte. The potential of $E_{work} = 0$ mV [vs. RHE] lies within

[1] SHE = Standard Hydrogen Electrode

the so-called non-reactive regime for all in this work investigated substances, meaning no redox-reactions or phase transitions occur under these electrochemical conditions[2].

4.2 Electrochemistry Controlled via the Three Electrode Set-Up

The so-called "Three Electrode Set-Up" allows to control and monitor the electrically induced chemistry at a solid/liquid interface and is therefore the basic arrangement used in all experiments performed in this work. The set-up is presented in this sub-chapter in a over-simplified way[3] making the working principle of the Three Electrode Set-Up most transparent. The more complex scheme, which was actually used for all experiments presented in this work, can be found elsewhere [54].

The Cu(100) electrode, which is in the center of interest for all investigations in this work, is called in electrochemistry the WE (Working Electrode). In order to control the electrochemical conditions at the WE a so-called CE (Counter Electrode) is needed as between WE and CE an electric potential must be applied. This electrical potential may induce surface processes at the WE surface, which leads to the flow of the electrochemical current. In a set-up consisting of solely a WE and CE either the applied potential difference between WE and CE can be measured (and therefore controlled) or the current flowing from/to the WE can be monitored, but never both at the same time. This is a consequence from the fact that measuring the potential between WE and CE requires an infinite resistance between them (= no current shall flow). Therefore to simultaneously control and observe both parameters (electrochemical potential and electrochemical current) a third, so-called RE (Reference Electrode) is needed. The third electrode permits to measure the working electrode potential, with respect to a constant potential reference, namely the RE, while the electrochemical current between WE and CE is flowing. The realization is known as Three Electrode Set-Up, whose working principle is explained in more detail in the following paragraph.

Figure 4.3 shows a simplified scheme of the Three Electrode Set-Up and the potential stabilizing circuit known as "potentiostat". In the circuit (fig. 4.3) the WE is electrically grounded. To create an electrochemical potential at the WE surface a potential E_p is applied at the non inverting input "+" of an OA (Operation Amplifier). The not inverting input "+" essentially transmits the potential E_p to the output of the OA. At the inverting input "-" of the OA the reference potential E_{ref} is applied, which is transmitted with inverted sign to the output of the OA . Thus at the OA output the potential $E_p - E_{ref}$ is applied. When the OA output potential $E_p - E_{ref}$ is not zero then the CE is charged or discharged by the OA output. The change of the CE potential leads to a feedback at the RE, which is within microseconds transmitted to the OA output. The feedback regulation is ongoing till the CE is sufficiently charged and the condition

[2]The reactive adsorption of organic cations was recently investigated by D.T. Pham [7].

[3]Over-simplified means here that crucial feedback connections in the circuit or electric filter circuits were left out in order to focus on the most fundamental parts and functions of the circuit. The more complex schemes are not presented here. More detailed explanations can be found elsewhere [54].

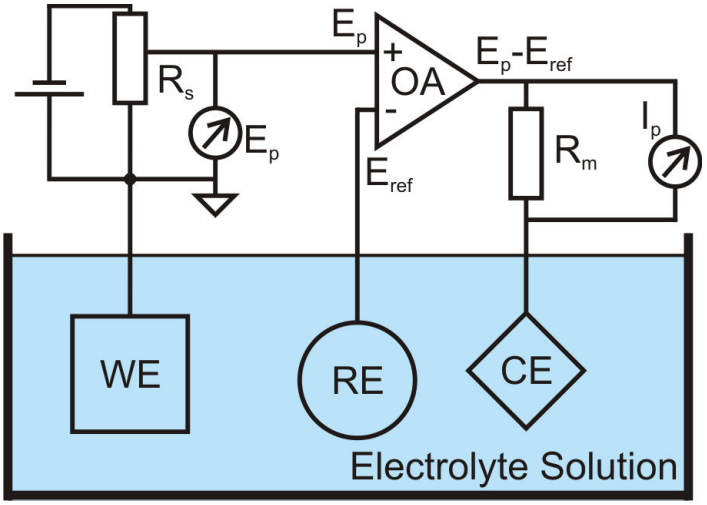

Figure 4.3: Simplified scheme of the Three Electrode Set-Up consisting of WE (Working Electrode), RE (Reference Electrode) and CE (Counter Electrode). The electrical circuit outside of the liquid phase is the simplified version of a potentiostat. A potentiostat controls and stabilizes the electrochemical conditions at the WE.

$E_p - E_{ref} = 0$ is fulfilled. The circuit (potentiostat) stabilizes the potential sensed at the RE and, thus, neutralizes fluctuations of the potential field between WE and CE.

In equilibrium the potential of the RE is known to be $E_{ref} = E_p$. The used RE has, however, a specific offset mainly caused by the nature of the RE but as well caused by the geometry of the set-up. The potential applied at the WE is therefore depended on the unknown RE offset, which is expressed by the following equation: $E_{work} = E_{ref} + E_{offset}$. The applied potential E_p has therefore no physical meaning at the WE surface but must be understood as a regulation parameter which permits to control the potential state of the WE. However, physically meaningful are all potential differences, e.g. the separation of two surface processes along the potential axis, as potential differences are unaffected by the offset of the used RE.

For the experiments presented in this work two different reference electrodes were used and are thus outlined here:

Reference Hydrogen Electrode (RHE)

In all EC-STM experiments a RHE (Reference Hydrogen Electrode) was used as reference electrode. A sketch of the RHE is shown in figure 4.4. The RHE consists usually of a platinated platinum electrode immersed in 0.5 M H_2SO_4 solution and exposed to H_2 gas thereby forming a three-phase interface (metal/gas/liquid). At the interface the equilibrium $H_2 \rightleftharpoons 2H^+ + 2e^-$ defines the reference potential E_{ref} of the RHE leading to a stable definition of a reference potential and thus to a well defined working electrode potential. The RHE is situated in all experiments outside of the STM cube

(see section 4.3) and is separated by a frit made of glass from the solid/liquid interface. Therefore the conditions defining the RHE potential are independent from the conditions, i.e. electrolyte solution, at the solid/liquid interface.

Pseudo Silver-Halide Reference Electrode

In contrast to the EC-STM experiments where a RHE was used in all x-ray experiments (SXRD and XPS) a pseudo silver-halide reference electrode was chosen to furnish the reference potential for its easy applicability. The RHE, as a real reference electrode, is independent of the conditions at the solid/liquid interface and furnishes a stable reference potential for the electrochemical control of the sample. In contrast to the RHE, the pseudo silver-halide reference electrode depends on the concentration and nature of the halide anions in the electrolyte solution, as the Ag-halide concentration of the equilibrium $Ag + halide^- \rightleftharpoons (Ag - halide) + e^-$ is *not* saturated. Therefore the Ag-halide concentration ($\hat{=}$ silver electrode charge) depends on the halide anion concentration in solution. However, the benefits of the compact and stable pseudo silver-halide RE outweigh its disadvantage.

The pseudo silver-halide electrode is realized by simply exposing a high purity silver wire to the experimental electrolyte solution. In a chloride containing solution the equilibrium reaction $Ag + Cl^- \rightleftharpoons AgCl + e^-$ defines the reference potential. However, changing the experimental conditions, e.g. by increasing the chloride concentration in the electrolyte, leads to the accumulation of the AgCl species at the silver wire surface. The accumulation of AgCl leads as well to an increase of the electron density within the silver wire resulting in an higher potential state of the silver reference electrode.

Substituting the electrolyte from a chloride containing to a bromide containing one leads as well to a shift of the reference potential, as the AgBr and AgCl formation reactions differ obviously in their equilibrium constants leading to different reference potentials.

Therefore the pseudo silver reference electrode potential is valid only in constant experimental environments, whereas the RHE potential remains valid even when the experimental environment changes. However, the RHE is more difficult to implement into the given diffractometer set-up for the SXRD measurements and more susceptible to vibrations. The pseudo silver-halide reference electrode, being only a high purity silver wire situated within the electrolyte solution, allows very compact set-ups and delivers a stable reference potential even when the set-up is moved as it happens in SXRD experiments.

4.3 Electrochemical Scanning Tunneling Microscope (EC-STM)

4.3.1 Four-Electrode-Set-Up

The EC-STM set-up allows to perform the STM experiments parallel to all electrochemical experiments, namely to investigate the solid/liquid interface and electrochemical

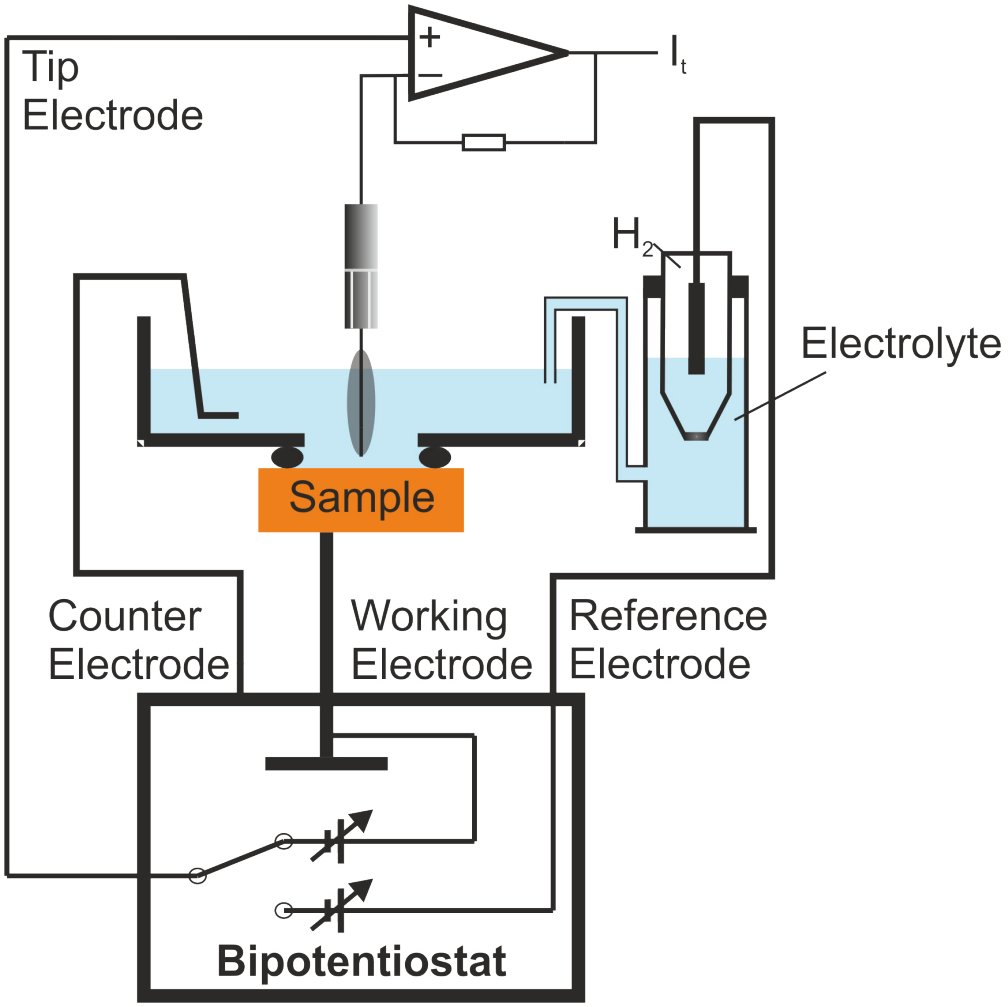

Figure 4.4: Working principle of the four electrode set-up as described and published by Wilms et al. [55, 54]. TE = Tip Electrode; WE = Working Electrode; CE = Counter Electrode; RE = Reference Electrode.

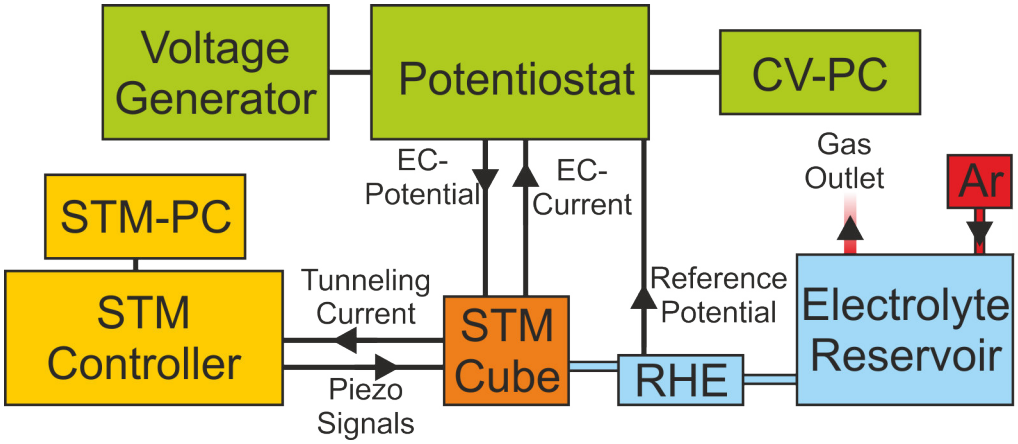

Figure 4.5: Scheme of the EC-STM set-up showing the inter-connection of all subunits.

surface processes *in situ*. Besides the three electrodes of the Three-Eletrode-Set-Up (Sec. 4.2), which control the surface chemistry, the STM tip constitutes a fourth electrode. A scheme of the circuit used to combine electrochemical and STM experiments is shown in figure 4.4. As in the Three-Electrode-Set-Up (sec. 4.2), the WE (Working Electrode) is also in the Four-Electrode-Set-Up defined to be ground (fig. 4.4). This allows to apply between WE and CE (Counter Electrode) the electrochemical potential and simultaneously to apply a bias potential E_{bias} at the TE (Tip Electrode) with reference to the WE ground potential (switch S pos. 1 in fig. 4.4). As shown in figure 4.4 the TE potential can be as well defined vs. the RE potential (switch S pos. 2), which allows to couple the bias potential to changes of the working electrode potential leading to a constant bias with respect to the electrochemical potential at the sample surface.

In order to prevent electrochemical reactions at the STM tip the tip surface has to be screened from the electrolyte, which is realized by a polymer film. The tip shielding has to cover most of the STM tip, only the very ending of the tip is allowed to be in direct contact to the electrolyte. This minimizes the amount of chemical reactions taking place, leading to a low amount of electrochemical currents flowing through the STM tip, thereby also significantly reducing the perturbation of the given electrochemical surface state.

The single crystal surface (= sample surface) is exposed to the electrolyte inside the electrochemical cell by a hole in the basement of the cell (fig. 4.4). This prevents the crystallographicly undefined sample borders to be exposed to the electrolyte and, thus, to be active in electrochemical experiments thereby increasing the significance and correlation of electrochemical and surface probe findings. The CE is a high purity (99.999%) platinum wire situated inside the electrochemical cell. A photo of the CE as well as the WE built inside the electrochemical cell can be seen in figure 4.6a.

4.3.2 EC-STM Set-Up

In situ STM (Scanning Tunneling Microscopy) experiments were performed in a home built set-up developed and described in detail by Wilms et al. [54, 55]. A basic understanding of the specifically used set-up is, however, necessary to properly interpret the experimental results presented within this work. The EC-STM set-up is therefore presented in a condensed form focusing on the specific set-up used.

The so-called EC-STM (ElectroChemical Scanning Tunneling Microscope) combines the electrochemical Three Electrode Set-Up presented above (Sec. 4.2) with an STM, allowing to perform experiments with the local surface probe technique originally developed by Binnig and Rohrer et al. [56]. The adaptation of the STM set-up working under UHV (Ultra High Vacuum) conditions to work as well at the solid/liquid interface was first realized by Sonnenfeld and Hansma [57].

The EC-STM set-up is schematically shown in figure 4.5. The main part of the set-up is the STM cube containing the electrochemical cell as well as the STM scanner and preamplifier. The STM cube made of aluminum serves as electromagnetic, thermal and vibrational shield for the STM experiment. Further, the cube is the containment for the argon atmosphere which prevents the solid/liquid interface to be contaminated by oxygen. The STM cube is connected with the electrolyte reservoir, which allows to directly introduce the degassed base electrolytes, i.e. 10 mM HCl, into the argon filled STM cube avoiding again the contamination of the sample surface by oxygen. The RHE, between the electrolyte reservoir and the STM cube, is used as reference electrode (RE, Sec. 4.2) in all EC-STM experiments. The connection of the RHE to the electrochemical cell inside the STM cube is realized via an electrolyte bridge.

The electrochemical condition at the solid/liquid interface is controlled by a home built potentiostat, which is described in detail elsewhere [54]. The potentiostat relies on the reference potential, here furnished by the RHE, to control and stabilize the electrochemical potential at the solid/liquid interface. Further the potentiostat registers the EC-current flowing between working and counter electrode. A function generator sends a saw-tooth voltage to linearly drive the EC-potential from a starting potential to a predefined potential limit and back. Both the saw-tooth EC-potential and the simultaneously measured current response of the solid/liquid interface are registered by the CV-PC to finally plot CVs (cyclic voltamograms).

Within the STM cube contains the piezos for the displacement of the STM tip and a preamplifier to amplify the tunneling current. The STM controller transmits all piezo signals for the approach and displacement of the STM tip to the STM cube. The measured and amplified tunneling current is transmitted from the STM cube to the STM controller. The measured tunneling current is not only used to obtain the experimental result but also to adjust automatically the tip height. All experiments were performed in the "constant current" mode in which the distance between sample surface and STM tip is constant. The "constant height" mode, in which no regulation of the STM tip distance to the sample is made, was not used as this mode leads more often to a crash of the STM tip with the sample, which usually results in the destruction of the STM tip. To control the STM experiment the STM-PC with specific software is attached to the

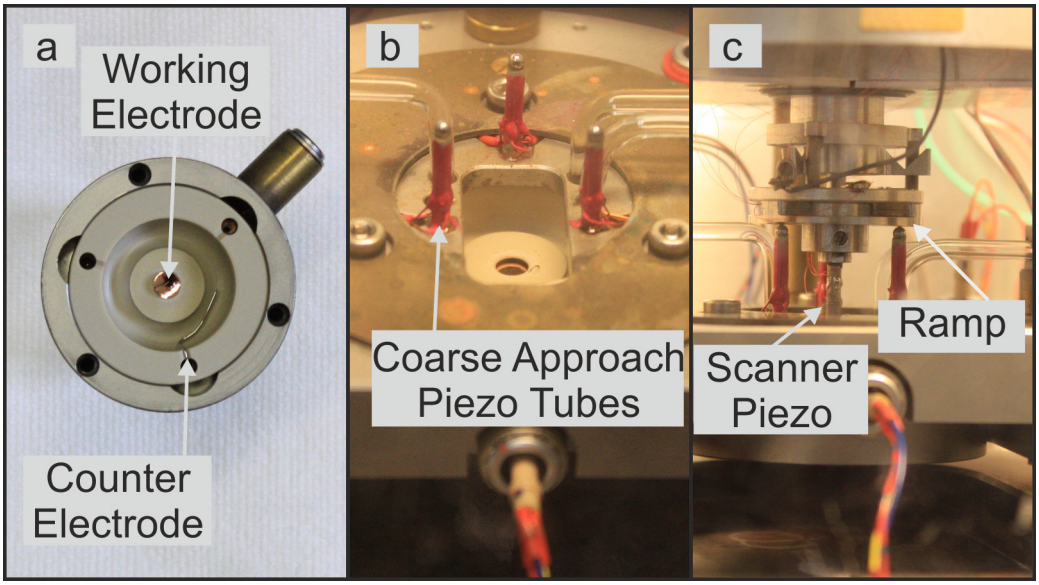

Figure 4.6: (a) Electrochemical cell containing a Cu(100) surface as working electrode and a high purity (99.99%) platinum wire as counter electrode. (b) The electrochemical cell installed underneath the STM-Base. (c) STM-Head and STM scanner unit above the STM-Base and electrochemical cell.

STM controller. The way the STM experiment is controlled by the STM-PC is described in detail elsewhere [54].

Figure 4.6 shows photographs and figure 4.7 a sketch of the main elements inside the STM cube, namely STM-Head, STM-Base and electrochemical cell. The STM-Head, which contains the tunneling current preamplifier and holds the scanner unit including a ramp for the tip approach, is installed on the STM-Base and stabilized by grub screws. As shown in figure 4.6c the ramp for the coarse approach rests on three piezo tubes attached at the STM-Base, which is typical for Besocke type beetle STM set-ups [58], however, with inverted tip and sample positions, dictated by the presents of the electrolyte. The ramp in this type of set-up is responsible for the coarse approach of the tip electrode to the sample surface via a "stick and slip mechanism" [55, 59, 60]. Figure 4.6a shows the electrochemical cell containing the sample and a platinum counter electrode. The cell volume, which can be filled with the electrolyte, is 2.3 ml, which is for the performed experiments sufficient to assume stable electrochemical conditions and to treat the electrolyte as an infinite reservoir for the reactive species. The STM-Base (fig. 4.7 and 4.8) is the central unit inside the STM-cube and unifies in a predefined geometry the electrolyte in-/outlets, the electrochemical cell and the STM-scanner.

Several damping stages decouple the STM experiment from ambient vibration sources situated within and outside of the building. The STM-cube rests (decoupled by a rubber mat, thickness 5 mm) on a massive granite plate (thickness 4 cm). The massive granite plate stands on four conically shaped rubber feet, in order to damp high frequency

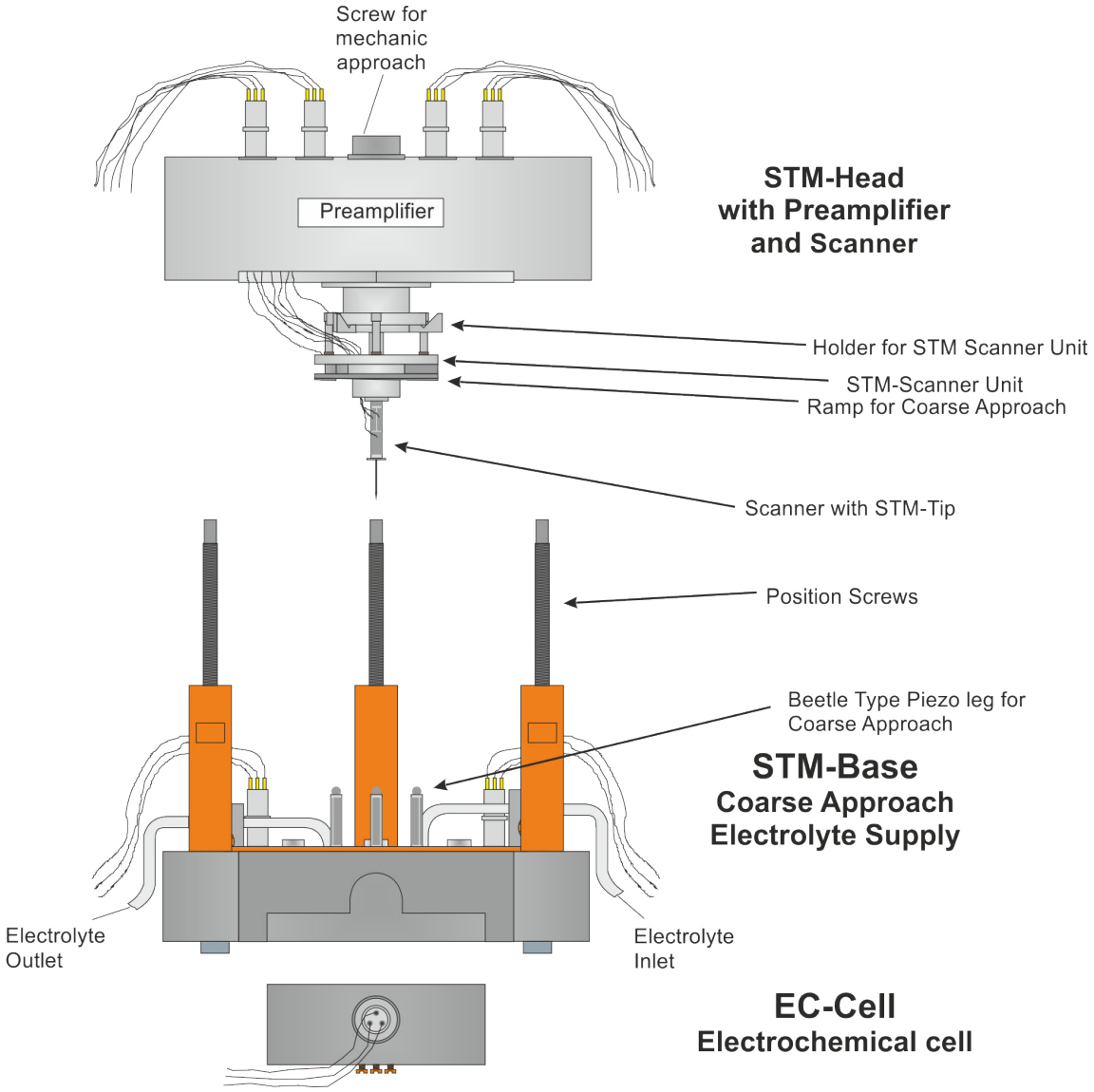

Figure 4.7: Main elements inside the STM cube (STM-Head, STM-Base and Electrochemical cell) as described and published by Wilms et al. [55].

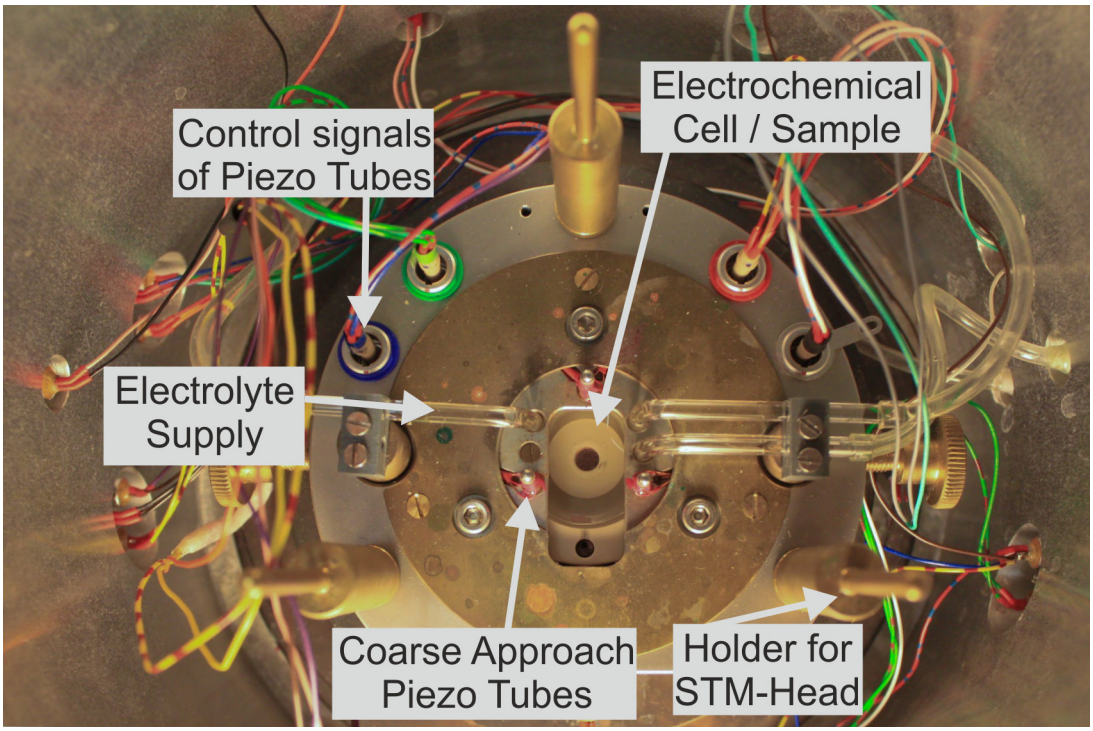

Figure 4.8: Top view inside the STM cube showing the STM-Base and installed electrochemical cell. The three base piezo tubes are responsible for the coarse approach.

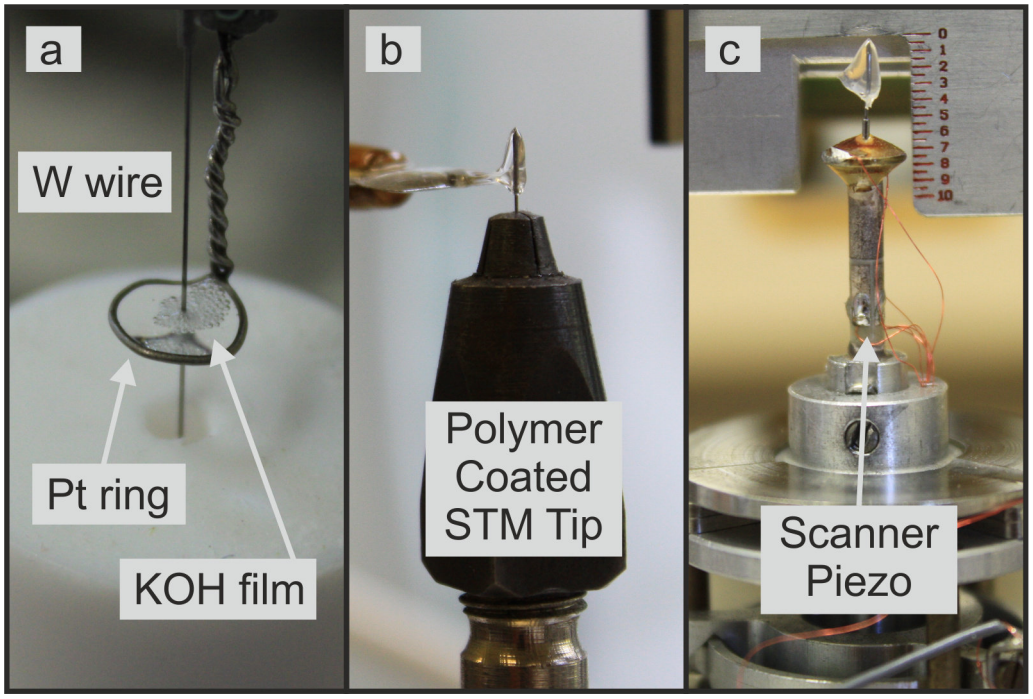

Figure 4.9: STM tip production procedure. (a) Electrochemical etching of a 99.95% pure W wire [61]. (b) Coating of the STM tip by a polymer. (c) STM tip on the scanner piezo. A metal disk shields the STM tip from the signals applied at the scanner piezo.

vibrations transmitted by the building. The table, which holds the STM-cube and massive granite plate, is attached via four springs to the room ceiling, which damps low frequency vibrations transmitted by the building. In addition to this external damping, a series of damping stages within the STM-cube reduces vibration amplitudes on their way from the STM-cube to the solid/liquid interface. For instance three subsequent brass plates serve as basement for the STM-base. These plates are decoupled from each other by three rubber feet, minimizing the transmission of vibrations to the STM-base. Further, during the STM experiments the whole "STM scanner unit", which consists of the scanner piezo and the ramp (fig. 4.6), rests on the coarse approach piezo tubes. For the electrical connection of the piezo tube thin and light electrical wires were chosen. Finally, the vibrational damping is complemented by the inherent advantages of the beetle-type STM set-up itself, which were presented elsewhere [58, 55, 59, 54].

4.3.3 Tunneling Tip

All tunneling tips (STM tips) used in this work were made of pure tungsten wire (99.95%, WHS Sondermetalle, Germany). The reasonable price of tungsten wire permits a high

throughput of tunneling tips, which is desirable as this permits to select tips with high lateral resolution (sec. 3.2) , while tips of lower quality can be discarted.

The production procedure for the STM tips is a two step process as imaged in figure 4.9. First a tungsten wire (diameter 0.25 mm) is etched in a thin lamella of 2 M KOH, which was suspended by a ring cathode made of platinum as shown in figure 4.9a. A rectangular AC voltage was applied to the ring electrode, which led to the dissolution of the tungsten in contact to the 2 M KOH etching solution. The cylindrical geometry of the etching set-up allows to dissolve the tungsten equally from all sides, which results in a reduction of the wire diameter.

The rate of the etching process depends on the applied AC voltage at the ring electrode. In this work the etching is subdivided into three separate steps. First a voltage between 11 V to 12 V (peak to peak) is applied for about 90 to 120 seconds in order to diminish the diameter of the tungsten wire quickly. In the second step a voltage of 5 V to 6 V (peak to peak) is applied for 15 to 30 seconds, which allows to reduce the diameter in a more controlled manner. The final step at 4 V (peak to peak) etches the wire at a low rate, which minimizes the vibrations related to the chemical reaction. This is important as strong vibrations lead to an earlier rupture of the wire, at a stage of the tip production process, in which the tungsten diameter is still rather large. Therefore minimizing vibrations permits to maximize the etching time in the last step of the tip etching, and therefore to minimize the tip diameter at its ending. However, choosing AC voltages significantly lower than 4 V are assumed to influence the tip quality negatively, as long and thin tunneling tips are produced, which are susceptible to vibrations during the latter performed STM experiment at the solid/liquid interface.

After the etching step, the STM-tips were cleaned in Milli-Q grade water to remove residual etching solution and possible contamination. Subsequently the tips were air dried for approximately 30 min under ambient conditions. The drying removed residual water, which may otherwise disturb the second production step, namely the tunneling tip coating by a polymer film. The coating of tunneling tips is necessary, as described in section 4.3.1, to minimize chemical reactions at the tunneling tip surface during the STM experiments and, thus, electronic noise. In order to deposit the coating, the tunneling tip is pushed through a heated hot glue polymere (Pattex, Germany), which leads to a covered shaft but an uncovered tip end (fig. 4.9b). Finally, after a cool down and hardening time of usually 12 h, the tunneling tip was installed on top of the scanner piezo, the tip height adjusted to the required set-up geometry (fig. 4.9c) and the STM experiment performed.

4.3.4 Analysis of STM Images

The STM images were analyzed in WSxM, a software published and maintained by Nanotec [62]. The software permits to plot line profiles, Fourier transform the images, adjust their contrast and apply filters, i.e. Gaussian. In order to avoid to introduce false information into the picture most of these techniques were not applied. Usually the contrast was slightly adapted and linear backgrounds subtracted. Rarely the image size was reduced in order to increase the size of details and highlight them. Fourier

filtering or very slight Gaussian filtering were used to decrease the level of noise in the final image. However, in the analysis of the STM images unfiltered data were used. This avoids the risk of analysis induced distortions.

4.4 X-Ray Methods

4.4.1 Surface X-Ray Diffraction (SXRD) Set-Up

A home built SXRD-cell as shown in figure 4.10 was used in all SXRD experiments as sample containment. The SXRD-cell allows to perform surface sensitive x-ray diffraction experiments under electrochemical control, allowing to investigate *in situ* surface processes at an electrode / electrolyte interface within a protective and clean argon gas atmosphere. In order to garantee the electrochemical control a Three-Electrode-Set-Up including a potentiostat as presented in section 4.2 is used. Crucial for SXRD experiments is the possibility to maximize the access to the sample surface in angular space. Therefore the SXRD-cell consists of one base plate, which holds the sample, connected by a single thin metal bar to one head plate, which holds the electrochemical set-up including electrolyte, reference and counter electrode. This set-up grants an in-plane accessibility of the sample surface of 345° (see fig. 4.11). A wide in-plane accessibility is important to maximize the angular space for scattering events. The scattering geometry is visualized in figure 4.10 by the incoming x-ray beam k_{in} (blue) and the diffracted x-ray beam k_{out} (red). The SXRD-cell geometry allows to detect x-ray radiation diffracted at the sample surface up to 45° to 50° in the out-of-plane direction as indicated by the red lines in figure 4.10.

The oxygen free containment is realized by surrounding the head and base plate by a $8\mu m$ thin kapton foil and continuously flushing the inner cell volume with high purity argon or nitrogen gas (5.0 quality). The electrolyte reservoir is split up in a small reservoir of about 2 ml within the oxygen free containment and an external 100ml reservoir, which is continuously degassed. The inner electrolyte reservoir contains a platinum wire as counter electrode and a silver wire as pseudo reference electrode (Sec. 4.2) both situated in a distance of 5 - 15 mm to the sample surface. Both electrodes within the containment are connected to the external of the SXRD-cell via sealed electronic feed-throughs (fig. 4.10, 3).

The sample is etched as described in section 4.1 and installed in the SXRD-cell for the final preparations steps. Through a teflon valve the inner "small" electrolyte reservoir can be accessed from outside of the SXRD-cell. This allows to substitute the chloride containing electrolyte by continuously flushing the inner electrolyte reservoir with the new electrolyte solution, while the electrochemical control is preserved.

A hanging meniscus, as proposed and used by Dickertmann et al. [63], which is stabilized on the sample surface by a glass capillary defines the electrochemically active sample surface and avoids the crystallographicly undefined sample borders to participate in the electrochemical experiments (fig. 4.10 right, 9). Preventing the undefined sample borders to participate in the electrochemical processes increases the significance and comparability of the electrochemical and SXRD findings.

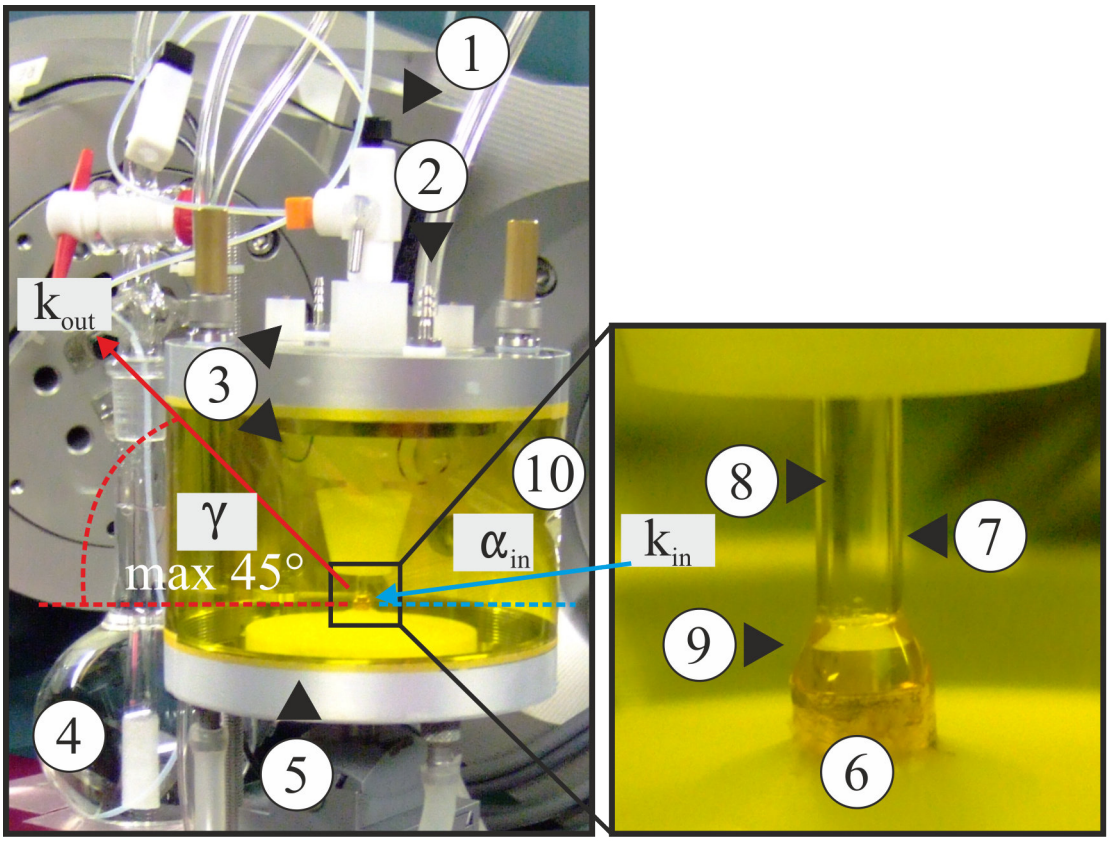

1	Electrolyte Inlet	6	Working Electrode / Cu(100)
2	Argon Gas Inlet	7	Glass Capillary
3	Electrical feed-through	8	Reference Electrode
4	Electrolyte Reservoir	9	Hanging Meniscus
5	Kapton Foil	10	Angle of Incidence

Figure 4.10: SXRD-Cell build-up. Left: SXRD-Cell installed onto the diffractometer of the beamline ID32 at the ESRF, Grenoble. In red the angular space of 45° in the out-of-plane direction for k_{out}, x-ray radiation leaving the Cu(100) surface. In blue k_{in}, the incoming x-ray beam. Right: Zoom of the electrolyte / Cu (100) interface showing the glass capillary and hanging meniscus.

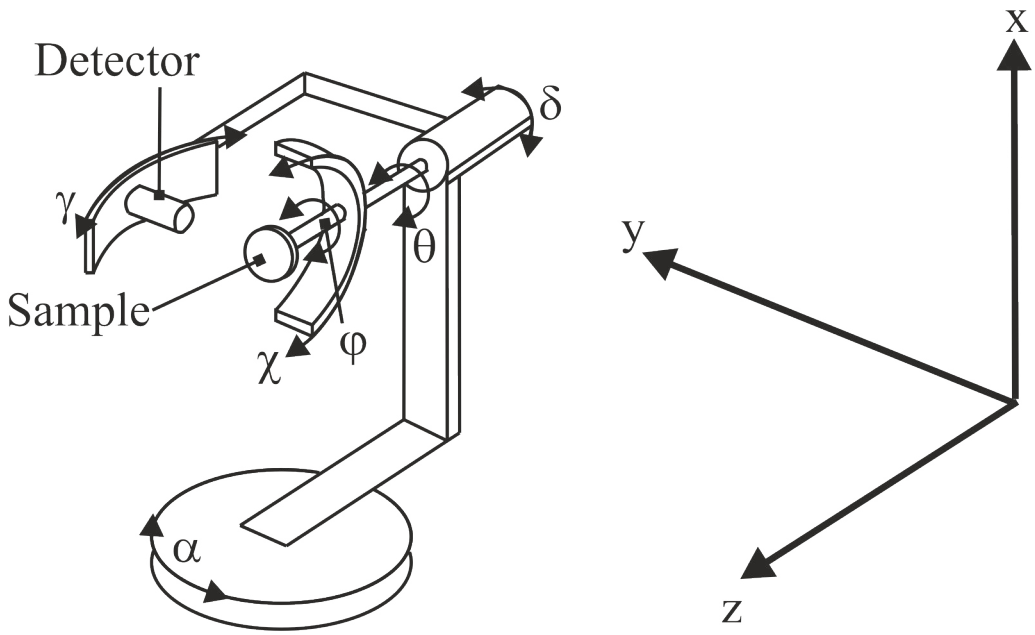

Figure 4.11: Sketch of a Six-Circle diffractometer inspired by the publication of E. Vlieg [64], but with the within this work used angular notation.

The sample orientation and the detector position, both versus the incoming beam, have to be controlled with high accuracy in order to perform XRD experiments. Instruments giving the necessary control and accuracy are known as diffractometers[4]. A diffractometer allows to perform scans by rotating the detector on so-called "circles" around the sample as their center (fig. 4.11) and/or rotate the sample, depending on the actual need of the experiment. In addition diffractometers usually permit to translate the sample in all three space directions in order to maximize the footprint of the x-ray beam on the sample surface.

All SXRD experiments were performed in the z-axis geometry as described by E. Vlieg [64]. In z-axis geometry the angle of incidence of the incoming x-ray beam is kept constant $\alpha_{in} = const.$ (fig. 4.11) throughout the whole experiment. In this geometry the sample surface normal, here the Cu(001) crystal lattice vector, is adjusted to be parallel to the z-axis of the diffractometer. The detector position is defined by the $\delta-$ and $\gamma-$angles.

The major issue common to all SXRD experiments is the low number of diffraction centers at a sample surface, and therefore the intensity of the scattered x-ray beam. In order to increase the surface sensitivity of the XRD experiment the angle of incidence of the incoming beam is chosen to be small and close to the critical angle of the total

[4]Typical accuracies of diffractometers are $\triangle = 0.002°$.

external reflection. At small angles of incidence two effects, first a geometric and second a physical effect, lead to a significant increase of the surface sensitivity of the XRD:

1. Due to the extremely low angle of incidence the x-ray beam propagates almost parallel to the Cu(100) surface. This leads to long propagation paths through the experimentally relevant first atomic layers close to the sample surface, thus maximizing diffraction in the superficial crystal regime. The total penetration length into the crystal is up to several micrometers.

2. At incident angles equal or smaller than the critical angle of the total external reflection $\alpha \leq \alpha_{crit}$ the incident radiation is almost totally reflected. However, a so-called evanescent wave within the copper crystal appears under this condition. The evanescent wave propagates parallel to the surface, but decays exponentially within increasing penetration ($-\hat{\mathbf{e}}_\mathbf{z}$ direction) and vanishes after only few nanometers. The exponential decay is a property of the wave itself and not related to scattering events [40].

The finite diameter and divergence of the beam leads to a part of the beam being incident with angles lower and a part with angles higher than the critical angle of the total external reflection. Thus at values close to the critical angle both presented effects increasing the surface sensitivity are supposed to play a role.

At a copper-water interface the critical angle for the total external reflection of 18 keV x-ray radiation (used in this work) is $\alpha_{crit} \approx 0.174°$ with respect to the Cu(100) surface plane. The value of 0.174° results from the relation $\alpha_{crit} = \sqrt{2\delta}$, deduced with $n = 1 - \delta + i\beta$ from the Snell's law $cos\alpha = ncos\alpha'$, with $n = \frac{n_{Cu}}{n_{H_2O}}$ the tabulated copper and water refraction indices [65]. The angle of incidence of the incoming x-ray beam was chosen to be slightly above the critical value, namely $\alpha_{in} = 0.25°$.

4.4.2 X-Ray Photoelectron Spectroscopy (XPS)

XPS – the only *ex situ* method used in this work – was used to probe the electronic state of organic molecules and anions adsorbed on the Cu(100) surface. XPS is performed under UHV (Ultra High Vacuum) conditions to prevent electron-gas interactions and, thus, maximize the signal intensity. Due to the UHV requirement the XPS experiments can not be performed *in situ* at the solid/liquid interface[5].

XPS experiments presented in this study were performed either at the in-house XPS chamber [66] or at the SoLiAS (Solid-Liquid-Analysis-Systems) station [67] at the synchrotron radiation facility BESSY II (Helmholtz-Centre, Berlin). Both set-ups allow a direct transfer of the sample without exposure to air from the electrochemical preparation cell (under Ar atmosphere) to the XPS analysis chamber (UHV) leading to a highly defined and contamination free sample state. A general scheme of both set-ups is shown in figure 4.12. At BESSY the U-49/2-PGM-2 beamline providing photons from 86 eV to 1890 eV with an energy resolution of 10000 (minimum flux $3\,x\,10^{12}\,\frac{photons}{sec}$) or in

[5]There are ideas and plans for XPS with very high photon energies. The resultant very high energy photoelectrons may then pass a liquid layer of limited thickness elastically.

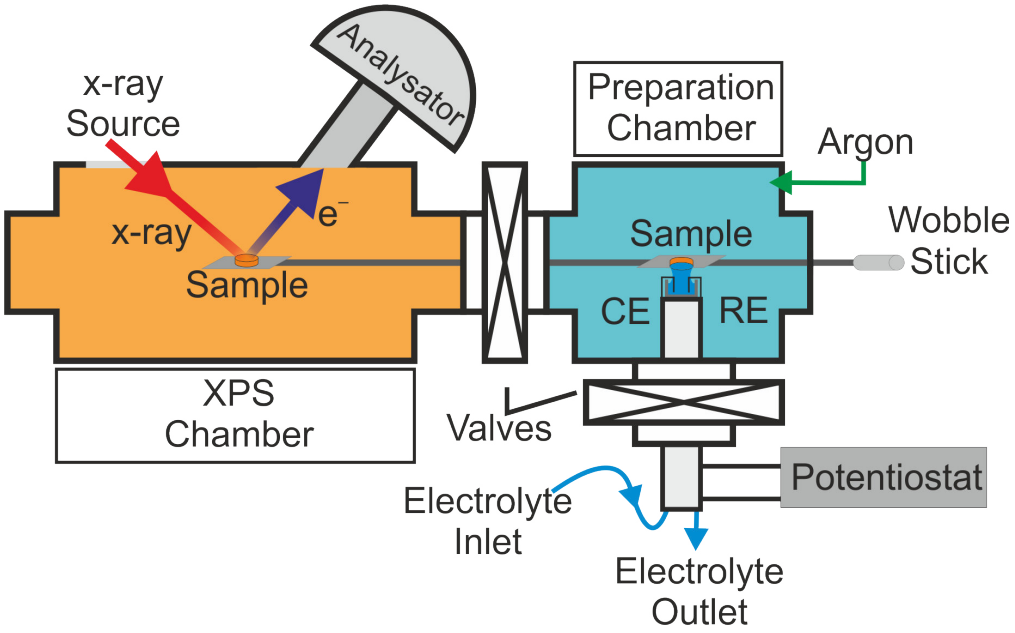

Figure 4.12: Scheme of the working principle of the XPS set-up used for the in-house as well as the synchrotron XPS experiments.

Bonn a non-monochromatized Mg/Al-twin-anode were used as X-ray sources [49]. The photoelectrons were collected by a SPECS Phoibos 150 MCD-9 analyzer (SoLiAS) or a SPECS EA 10 analyzer (XPS-system, Bonn). In both cases the binding energies are referred to the Fermi level. All XPS experiments were performed under UHV conditions, namely less than $10^{-8}\,mbar$ at the laboratory chamber and less than $10^{-9}\,mbar$ at the SoLiAs station at BESSY II.

Prior to the XPS experiment the Cu(100) surface was etched following the steps mentioned in section 4.1. The copper crystal is subsequently transferred into a preparation chamber, as sketched in figure 4.12, where the final steps of the sample preparation are carried out (sec. 4.1), such as the removal of residual oxygen and the characterization of the sample via cylic voltametry. The sample is protected by a continuous flow of high purity argon gas (Ar 5.0) through the preparation chamber during the whole sample preparation procedure, which prevents contamination and especially oxygen from reaching the sample. The electrochemistry was controlled via a home-built potentiostat described in details elsewhere [54]. A platinum wire served as counter electrode and a silver wire was used as pseudeo silver-halide reference electrode (sec. 4.2).

After the sample preparation, which is identical to that for the in situ EC-STM or SXRD experiments, is completed the electrochemical control is released by emersing the Cu(100) surface from the electrolyte solution. The sample, still situated within the argon filled preparation chamber, is no longer controlled by the potentiostat and therefore the electrochemical conditions are undefined. In this “open circuit” condition previously

adsorbed monolayers of ions, investigated in this work, remain adsorbed on the Cu(100) surface, as was verified prior to the XPS experiments via STM pre-studies.

The removal of the electrochemical preparation unit from the preparation chamber allows to isolate the preparation chamber fully from the ambient environment, as no connection of the sample to the external is necessary anymore. The sealed preparation chamber is than evacuated with a rotary vane pump leading to the removal of the protective argon gas, as well as traces of residual water on the sample surface originating from the sample preparation.

Both XPS set-ups permit to vary the incoming x-ray photon energy. This is beneficial in two ways for XPS experiments.

1. Increasing the energy of the incoming x-ray beam increases the kinetic energy of the emitted photoelectrons $E_{kin}(e^-) = h\nu_{photon} - E_B(e^-) - \phi$ (eq. 3.11). In contrast to this, Auger electrons, which are emitted via the Auger process, do not change their kinetic energy when the incoming radiation increases in energy, as Auger electron emission depends solely on the intra-atomic relaxation process. This difference between photoelectron and Auger electrons makes them distinguishable simply by comparing two spectra registered at two different x-ray photon energies.

2. Increasing the energy of the incoming x-ray beam increases the kinetik energy of the photoelectrons, which permits electrons being emitted from atoms deeper within the sample to leave the sample environment unaffected. Therefore comparing the peak intensities of various XPS spectra registered at different radiation energies allows to register indepth concentration profiles. However, this was not done in this work.

4.4.3 X-Ray Sources

Synchrotron Radiation Facilities

Within this work only the working principle of a synchrotron radiation facility will be described. A detailed description of the set-up of state-of-the-art synchrotron facilities, including the actual electron containing ring and x-ray producing and monochromatizing set-up, can be found elsewhere [40].

Using the total external reflection to obtain surface sensitivity in XRD experiments (as in this work) leads to a part of the x-ray photons to be simply reflected by the Cu(100) surface and thus to be lost for the diffraction experiment. In addition, the small number of diffraction centers at the copper surface leads to a further decrease of the XRD signal intensity. Therefore an x-ray beam of high brilliance[6] is mandatory in order to successfully perform SXRD experiments with a satisfactory signal/noise ratio. The best sources for high brilliance x-ray radiation are nowadays 3rd generation synchrotron radiation facilities, e.g. the ESRF[7], SLS[8] or BESSY[9]. 3rd generation synchrotron radiation

[6] $Brilliance = \frac{Delivered\, X-Ray\, Photons/second}{angular\, divergences[mrad^2]\, source\, area[mm^2]\, relative\, bandwidth[0.1\%]}$

[7] European Synchrotron Radiation Facility

[8] Swiss Light Source

[9] Berliner Elektronenspeicherring-Gesellschaft für Synchrotronstrahlung

facilities achieve a brilliance of up to 10^{20} $[\frac{Photons}{sec\,mrad^2\,mm^2\,0.1\%bw}]$ by using insertion devices, i.e. wigglers and undulators, to produce x-ray beams. However, the adaptation to specific experimental needs may significantly reduce this high photon flux.

As SXRD experiments require very high photon fluxes they can not be performed at low brilliance lab sources[10], which deliver usually 10^8 $[\frac{Photons}{sec\,mrad^2\,mm^2\,0.1\%bw}]$. However, this photon flux is sufficiently high for common *ex situ* XPS experiments performed under UHV conditions. Therefore some XPS experiments of this work were performed at an in-house x-ray lab source.

Synchrotron radiation is produced by radially accelerating ($\mathbf{a} \perp \mathbf{v}$) relativistic electrons. The radial acceleration originates from the magnetic field, i.e. within bending magnets or within insertion devices. Bending magnets force the relativistic electrons to follow the circular path of the electron storage ring. In order to produce intense x-ray beams, nowadays insertion devices are used. The insertion devices (wiggler or undulator) are arrays of dipoles with alternating orientation leading to magnetic fields alternating between upward and downward orientation. A wiggler is a compact series of bending magnets, which produces significantly more intense, but still polychromatic, x-ray radiation than a single bending magnet. The x-ray beam emitted by relativistic electrons passing through an undulator possess an even higher beam intensity. This results from the coherent emission of the x-rays at all emission points[11], which leads to the destructive interference of most wave lengths. Only one defined x-ray wavelength and all its higher harmonics are emitted. Therefore the undulator produces quasi-monochromatic x-ray radiation and consequently more x-ray photons of the desired energy are obtained than in a wiggler [40]. Both wiggler and undulator do allow to adjust the x-ray photon energy of the high brilliance beam within a certain window, which permits to perform a wide range of different experiments at the same x-ray source.

The by the insertion device emitted x-ray radiation is monochromized by Bragg scattering at crystals and total external reflection at coated Si-mirrors to increase the energetic resolution of the x-ray beam to typical values of $\frac{\triangle E}{E} \leq 10^{-4}$.

The x-ray beam energies chosen for the SXRD experiments in this work had to fulfill three conditions. First the energy must be sufficiently high to include a maximum of reflexes in the reciprocal space, second the beam energy must be far from any x-ray adsorption edges of all chemical elements participating in the SXRD experiments, and third the chosen x-ray energy had to be produced with high brilliance by the insertion device thus maximizing the photon flux. The *in situ* x-ray scattering experiments at the Br/Cu(100) surfaces reported here were performed at the beamline ID32 of the European Synchrotron Radiation Facility in Grenoble, which provided a synchrotron radiation

[10] Typical classical laboratory sources for x-ray radiation are metal (Mg, Al, Cu) anodes furnishing the metal K_α radiation.

[11] In an undulator each electron emits x-ray radiation in coherence with its own previous emission but not coherent with the other electrons passing through the undulator. A further increase of the x-ray beam brilliance would be possible if all electrons emit x-rays coherently. This, however, demands a spacial ordering of the electrons with a resolution better than the emitted x-ray wavelength. The device making such a coherent x-ray emission possible is called a free electron laser and is under development [40].

beam with an energy of 18keV. The investigation of the Cl/Cu(100) surface was mainly carried out at the beamline X04SA of the Swiss Light Source SLS in Villigen, which provided a synchrotron radiation beam with an energy of 20 keV. The XPS experiment was performed at the SoLiAS UHV chamber of the beamline U49-2/PGM at BESSY II in Berlin.

Metal-Anode as X-Ray Laboratory Source

X-ray laboratory sources usually have a significantly lower brilliance than synchrotron radiation sources, namely about 10^8 $[\frac{Photons}{sec\,mrad^2\,mm^2\,0.1\%bw}]$. However, those x-ray lab sources are an easy to set-up, cheap and robust technique, which delivers a sufficiently high x-ray photon flux for a number of investigation, such as the in this work presented *ex situ* XPS experiments.

In the present work aluminium and magnesium were used as metal anodes to obtain the corresponding K_α x-ray radiation. Electrons emitted by a heated filament are accelerated in the direction of a metal plate (Al or Mg) by a high electric field. The impact of fast electrons on metal plates lead to an x-ray emission spectrum consisting of the polychromatic "bremsstrahlung" and spike like high intensity x-ray lines. Bremsstrahlung is a typical x-ray radiation, which is emitted by all electrons being negatively accelerated (slowed down) by colliding with the metal atoms within the plate. The polychromatic bremsstrahlung spectrum does, however, not deliver very high x-ray intensities at one photon energy. The spike like high intensity x-ray lines do contain significantly more photons at an defined energy. Those x-ray emission lines result from the removal of electrons from the inner shell and subsequent relaxation of an electron of a higher shell into the energetically favored hole of the inner shell level. The well defined and high intensity K_α lines of Al and Mg are therefore used as laboratory source for some of the performed XPS experiments in this work.

5 Results: Specific Halide Anion Adsorption on Cu(100)

5.1 Chloride or Bromide Adsorption on Cu(100)

Chloride (Cl) as well as bromide (Br) anions are known to specifically adsorb on metal electrode surfaces [3] by partially stripping their solvation shell off and interact directly with the metal surface. The stripping of the solvation shell between ion and surface leads to a strong adsorbate-substrate interaction, which results in the formation of a long-range ordered halide adlayer, i.e. a c(2x2) superstructure of Cl or Br on the Cu(100) surface. The formation of a long-range ordered halide adlayer is a desirable effect, as this adlayer can be used as *anionic* substrate on which the potential dependent structure formation of organic *cations*, such as viologens, can be studied [4].

The solvation energy, the adsorbate-substrate and the adsorbate-adsorbate interaction differ between Cl and Br anions. This leads to different tendencies of Cl and Br anions to specifically adsorb on the Cu(100) electrode surface. The tendency of halide anions to specifically adsorb on metal surfaces is found to increase in the following order $F^- \ll Cl^- < Br^- < I^-$ [3], as already mentioned in section 2.1.1. Therefore it can be concluded that in a competing situation of Cl and Br anions the, in the adsorption on the Cu(100) electrode surface energetically favored Br anions, would preferably adsorb specifically resulting in a displacement of a previously adsorbed Cl-c(2x2) adlayer.

5.2 Electrochemical and Structural Characterization of the Halide Covered Cu(100) Surface

Figure 5.1a shows the CV curve of a Cu(100) electrode surface in a 10 mM HCl solution, as registered in the sample preparation procedure. The CV visualizes the potential window of the specific chemical environment (Cu(100) electrode in 10 mM HCl). Within this potential window investigations can take place without the decomposition of the Cu substrate by oxidation or the decomposition of the aqueous solution by the HER (Hydrogen Evolution Reaction). At the anodic (positive) end of the registered CV curve (fig. 5.1a) the strong anodic current corresponds to the oxidation of the Cu electrode. In the reverse potential sweep the reduction and redeposition of previously generated Cu cations results in the appearance of a reductive current wave. Following the CV to potentials below -380 mV [vs. RHE] leads to the appearance of the strong reductive currents representing the hydrogen evolution.

At sufficiently high Cu potentials, above -100 mV [vs. RHE], both anions, Cl and

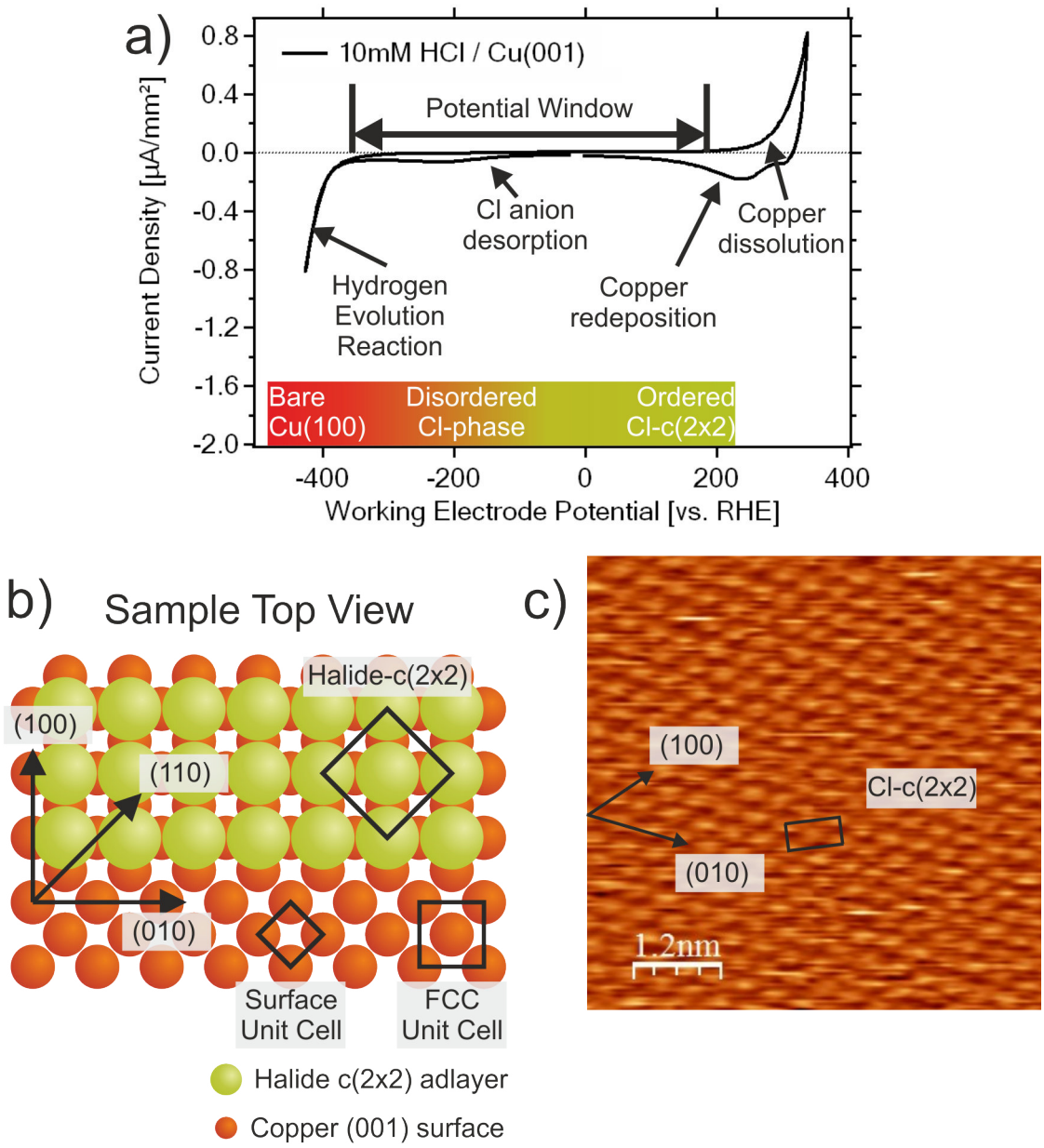

Figure 5.1: (a) Steady-state CV of Cu(100) in a 10 mM HCl solution, registered at a speed of 10 mV/sec. The potential window is limited at high potentials by the oxidative dissolution of the copper electrode and at low potentials by the decomposition of the electrolyte solution and the hydrogen evolution reaction (HER). (b) Hard sphere model of the halide c(2x2) adlayer adsorbed within the four-fold hollow sites of the Cu(100) surface. (c) Untreated, and therefore heavily drift distorted, STM image of the Cl covered Cu(100) surface. Cl-c(2x2) unit cell deformation due to drift. Close packed Cl anion rows along the (100) and (010) directions of the Cu-fcc crystal. $E_{Work} = 0\,mV$, $E_{Bias} = 30\,mV$, $I_{Tunnel} = 1.2\,nA$

Br, specifically adsorb in the fourfold hollow sites of the Cu(100) surface forming a full monolayer of a halide-c(2x2) structure, as shown in figure 5.1b. The formation of the p4mm symmetric halide-c(2x2) adlayer originates from the underlying quadratic Cu(100) fcc surface, which acts as template in the adlayer formation. Halide anions specifically adsorbed in half of all fourfold hollow sites of the Cu(100) surface. This results in a total halide coverage of the Cu(100) surface of half a monolayer ($\theta_{Cl/Br} = 0.5$ ML) [24, 26].

The maximum of the adlayer coverage of 0.5 ML is not only related to the anionic charge of the halide anions, as neutral chlorine [68, 69] and bromine [70] atoms are found to form as well a c(2x2) superstructure on the Cu(100) surface under UHV conditions. A higher coverage than 0.5 ML must be therefore prevented by the anion and atom size, which is described by the ionic and Van-der-Waals radius. The effective atom or anion radii depend on the specific system, but average values are tabulated in literature [71]. For instance Cl and Br anions are found to have an ionic radius of 181 pm / 196 pm (Cl/Br) as six-fold coordinated ions [71]. The resulting next neighbor distance of 362 pm / 392 pm represents an approximation of the maximum value, which may be about 20% smaller due to lower coordination of the anions on the Cu(100) surface [71] and the differing chemical environment. The corrected ionic radius of the bigger Br anion with 314 pm allows the formation of the c(2x2) structure with a next neighbor distance (NND) of 361.5 pm but prevents the occupation of the remaining four-fold hollow sites, as this would result in a Br anion NND of 255 pm. Besides this commensurable adlayer, as well incommensurable halide adlayers might be possible, which then possess a wider NND than the halide radius (e.g. 314 pm of Br) but smaller NND than within the c(2x2) adlayer (361.5 pm). Indeed, such an incommensurable adlayer is found for I anions on Cu(100) [72], in which a potential dependent uni-axial compression occurs leading to an uni-axial incommensurable adlayer and consequently higher anion density. However, such an incommensurable adlayer consisting of Cl or Br anions was never observed on Cu(100) electrode surfaces, neither in this work nor in literature.

Continuously decreasing the electrode potentials from 0 mV [vs. RHE] to the onset of the HER (fig 5.1a) leads to an order-disorder transition of the Cl-c(2x2) superstructure, as proved by *in situ* STM and *in situ* SXRD studies [25, 21]. This order-disorder transition is a relevant process affecting the construction of nano-architectures at the 10 mM HCl/Cu(100) electrode surface, as the Cl-c(2x2) represents the effective substrate mainly influencing the adsorption and ordering process of organic cations. The order-disorder transition of the Cl-c(2x2) layer is essentially a gradual desorption process, in which the strongly bounded (so-called chemisorbed) Cl anions in the c(2x2) adsorption sites desorb to a less strongly bounded state (so-called physisorbed). The physisorbed state is no longer related to specific adsorption sites on the electrode surface, making the Cl anions highly mobile. This transition is most likely accompanied by a complete desorption of, at first, a fraction of Cl anions from the Cu(100) surface, as free space is needed for the phase transition from the densely packed Cl-c(2x2) into a less densely packed and highly mobile "Cl lattice gas"-phase on the Cu(100) electrode surface. The continues reduction of the electrode potential is finally assumed to lead to a complete desorption of Cl anions from the electrode surface. Both desorption processes affect the interfacial capacity at the solid/liquid interface and are therefore as well visible in the CV in form of

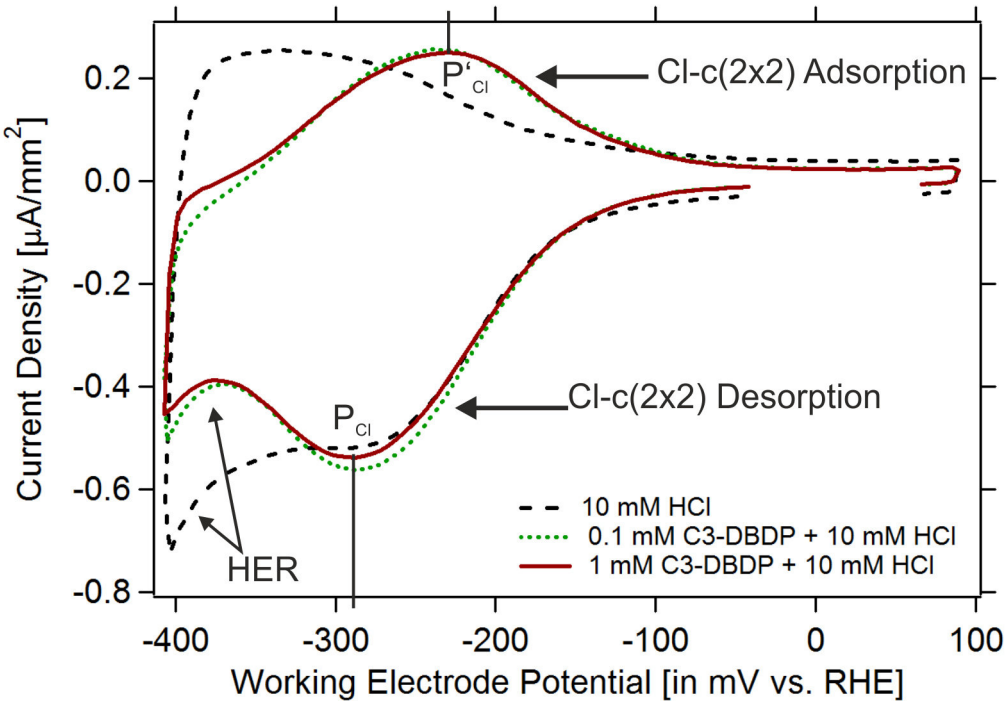

Figure 5.2: CV of the Cu(100) electrode surface in pure 10 mM HCl, 0.1 mM C3-DBDP + 10 mM HCl or 1 mM C3-DBDP + 10 mM HCl solution. Scan speed 200 mV/sec.

a cathodic current between -100 mV [vs. RHE] and the onset of the hydrogen evolution (figure 5.1a).

Additional CV experiments at higher scan rates, i.e. 200 mV/sec (fig. 5.2) instead of 10 mV/sec (fig. 5.1a), were made in order to obtain additional information about the currents close to the onset of the hydrogen evolution reaction. All CV imaged in figure 5.2 were obtained from one initial sample preparation procedure, as the investigated pure 10 mM HCl electrolyte was *in situ* substituted to first a 0.1 mM and later a 1 mM C3-DBDP containing electrolyte solution.

Higher CV scan speeds amplify even small charge fluxes flowing to/from the electrode surface resulting in a significant electrochemical current signal (current = charge flux per time). This amplification is obvious when the CV registered with 10 mV/sec (fig. 5.1a) is compared to the one registered with 200 mV/sec (fig. 5.2). The CV curve registered at a scan speed of 200 mV/sec reveals currents in the anodic (positive) potential sweep of the CV, which are invisible in the with 10 mV/sec registered CV. Neither the line shape nor the peak maximum of this new signal is symmetric to the Cl anion desorption signal. Indeed, the Cl adsorption peak overlaps with the HER regime and appears to consist of two single processes. This indicates that the currents related to the Cl adsorption can not be modeled by a simple Cl de-/adsorption process.

Subtracting the exponential HER (exponential, as the Buttler-Volmer equation applies [12]) reveals that the Cl de- and adsorption peaks areas differ between the CV registered in pure 10 mM HCl and in presence of C3-DBDP in solution. However, the Cl anion de-/adsorption can in both CVs still be the origin of the observed signals as was proven by Stuhlmann et al. [19]. The authors investigated the complex CV shape close to the HER of a Cl anion covered Cu(111) electrode and proved the dependency of the HER rate of the Cl anion coverage θ on the copper electrode surface. This correlation between the two processes leads to complex and at first sight unusual CV shapes. The authors proved two differing HER reaction rate constants, one valid at the bare Cu(111) and one valid at the Cl anion covered Cu(111) surface. In addition a strong dependency of the CV shape from the scan speed was revealed, which can be understood to result from the HER reaction dynamics. However, the study of Stuhlmann et al. [19] explains the here observed differing peak areas between Cl ad- and desorption signal, as well as the non trivial peak shape of the Cl adsorption process occurring within the HER regime.

Additional experiments were done in order to support the above statements and provide further clarification for the origin of the observed signals. For instance a full monolayer of organic cations was adsorbed onto the Cl-c(2x2)/Cu(100) electrode surface. Such an organic film acts as an physical barrier for the Cl anion de-/adsorption processes, and may as well hinder the HER by the blocking of reaction sites and/or electrostatic repulsion as already observed by Pham et al. [5, 6]. Introducing 0.1 mM or 1 mM C3-DBDP^{2+} cations into the solution leads to the formation of a full cation monolayer on the Cl/Cu(100) electrode surface, as will be presented in section 6.2.2 by STM results. The adsorption of the C3-DBDP^{2+} monolayer, leads to a shift of the observed "Cl adsorption" signal to more positive potentials and reshapes both, the Cl ad- and desorption, processes into a more "peak like" form (peak pair P_{Cl} / P'_{Cl}; fig. 5.2). Further CV measurements (not shown here) indicate the HER to be shifted by -30 mV to more negative electrode potentials, but due to the significant reshaping of the CV and proximity of the Cl anion signal (P_{Cl} / P'_{Cl}) to the HER regime this can not be concluded with absolute certainty.

Further, as can be seen in figure 5.2, the CV is almost independent of a change of the C3-DBDP^{2+} cation concentration in solution (0.1 mM to 1 mM C3-DBDP^{2+}), which indicates that the CV peak, which is formed due to the adsorption of C3-DBDP^{2+} on the surface, must be related to *surface* processes. This assumption is supported by CV measurements at different scan speeds (not shown here), namely 25 mV/sec, 50 mV/sec, 100 mV/sec and 200 mV/sec, as the peak height is found to be linearly depended on the scan speed ν, whereas following the Randles-Sevcik equation processes involving *solution* species are expected to be depended on the square root of the scan speed $\sqrt{\nu}$ [12].

Despite the overall good agreement between both C3-DBDP^{2+} related CV curves they show distinct deviations from each other, namely an earlier and stronger rise of the HER currents, as well as a higher Cl desorption peak in the CV of 0.1 mM C3-DBDP^{2+} compared to the CV with 1 mM cations. These deviations are assumed to be the result of rearrangement / ripening processes of the Cu(100) surface occurring in each of the numerous registered voltametric cycles. However, to prove this and exclude other factors, such as the specific interfacial capacities, more experiments have to be

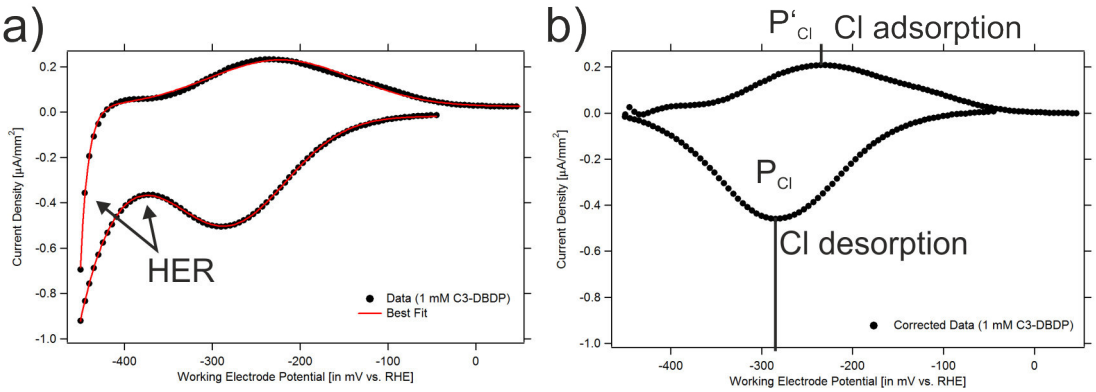

Figure 5.3: (a) CV registered at a scan speed of 200 mV/sec; Cl ad- and desorption approximated by a Gaussian shaped peak overlayed with an exponential background component originating from the HER. (b) Cl ad- and desorption peak obtained by subtracting the exponential HER from the original CV data.

performed in future studies. Those studies are out of scope of the present work, which is mainly devoted to the understanding of the structure formation of organic cations.

The registered CVs can be analyzed by assuming an exponential background signal from the HER, as expected from the Buttler-Volmer equation. This exponential background can be subtracted from the CV resulting in figure 5.3b, in order to obtain the current density solely related to the Cl anion process. However, this analysis does not lead to satisfactory results, as the total current density of the Cl adsorption and desorption processes differ by a factor close to two. This deviation was already expected and agrees well with the result obtained for Cl/Cu(111), where the correlation between Cl anion coverage and HER reaction rate was found to be the physical reason behind this observation [19]. The up to here presented data prove that this correlation is still valid for the Cl/Cu(100) surface and, furthermore, even when covered by a full monolayer of a organic cation, namely C3-DBDP^{2+}.

The agreement of the presented CV data and related observations with literature results [19, 5, 6] strongly indicates the peak pair P_{Cl}/P'$_{Cl}$ to be fully related to the Cl anion de-/adsorption. However, the significance of this conclusion can be improved by *ex situ* XPS experiments. In such experiments it is exploited that adsorbates and their redox state on metal electrode surfaces are conserved upon emersion from solution and subsequent transfer to an *ex situ* experiment, as proven with XPS for e.g. viologens on Cu(100) by Breuer et al. [9].

Therefore transferring the C3-DBDP/Cl/Cu(100) sample at 0 mV [vs. RHE] into the XPS chamber is expected to conserve the Cl anion layer as well as organic cation layer adsorbed on the Cu(100) surface. Indeed, the registered XPS spectra prove the presence of Cl anions by the Cl2p signal (fig. 5.4a/b). The Cl2p signal consists of two peaks, namely the Cl2p$_{1/2}$ at 199.6 eV and Cl2p$_{3/2}$ at 198.2 eV. Both Cl2p-electron binding

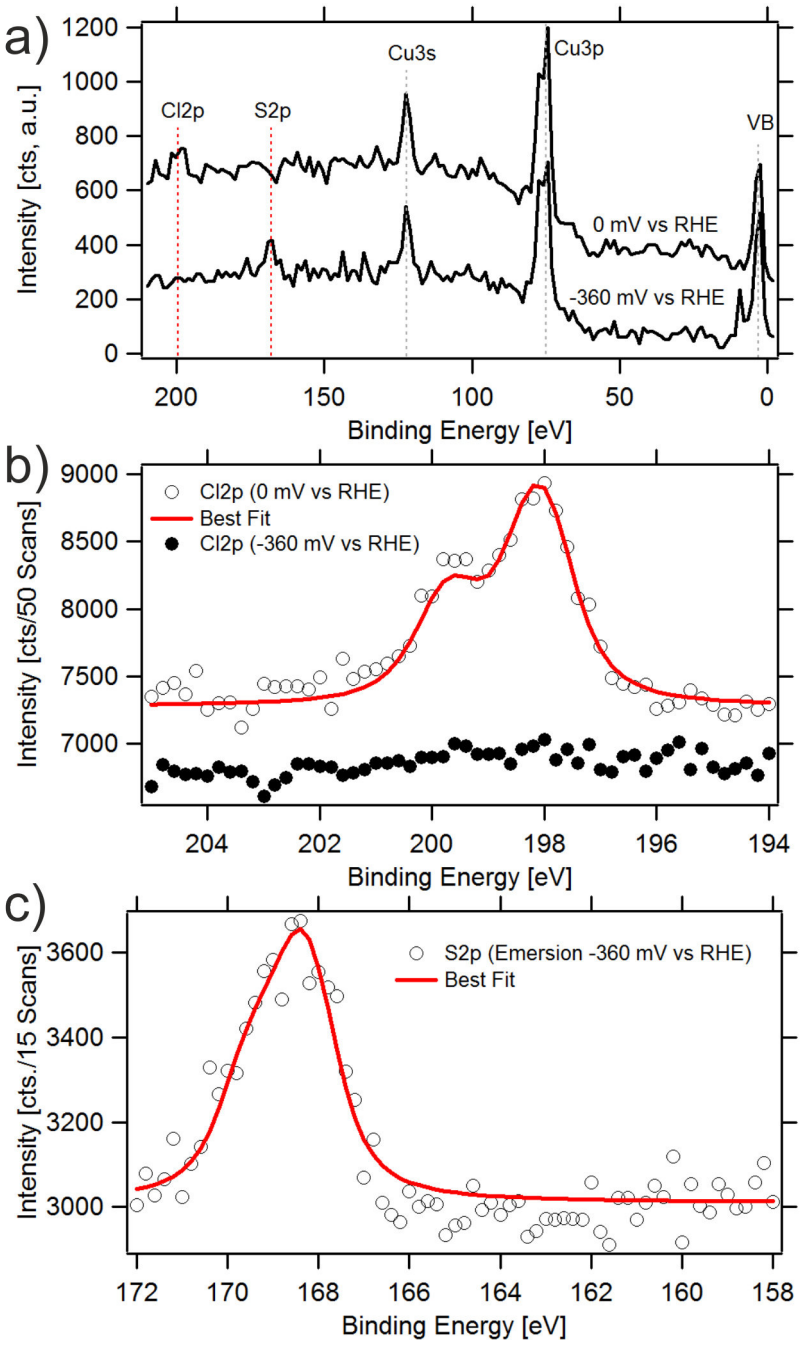

Figure 5.4: XPS spectra registered after two different sample preparations. (a) Survey spectra of both experiments showing the presence of the Cl2p signal when the sample is emersed from solution at 0 mV [vs. RHE]. This signal vanishes when the sample is emersed at -360 mV [vs. RHE], in exchange a S2p signal can be observed, due to experimental reasons as described in detail in the text. (b) High resolution spectra of the Cl2p signal for both preparations and best fit. (c) High resolution spectra of the new S2p signal.

energies of the electrochemically prepared sample agree well with literature values of chloride compounds, e.g. $Cl2p_{1/2}$ 200.1 eV ($HgCl_2$) [73] and $Cl2p_{3/2}$ 198.2 eV (CuCl) [74]. In addition to the Cl signal the presence of the C3-DBDP layer on the Cu(100) surface was proven by highly resolved scans of the N as well as C signals in the XPS spectra. However, the relevant C3-DBDP related spectra will be shown and discussed in the C3-DBDP related part of this work, namely in subsection 6.2.2.

Lowering the electrode potential in the sample preparation procedure below P_{Cl} , e.g. to -360 mV [vs. RHE], leads to the desorption of the Cl anion layer from the Cu(100) surface. Prior to the sample transfer the electrolyte was substituted from a 0.1 mM C3-DBDP + 10 mM HCl to a Cl anion free 5 mM H_2SO_4 solution in order to prevent the re-adsorption of Cl anions from solution on the Cu(100) surface upon emersion of the sample. After the electrolyte substitution took place the sample was emersed from solution and transferred to the *ex situ* XPS experiment. The subsequently obtained spectra are imaged in figure 5.4a and b and prove the absence of the Cl anion signal, which verifies the desorption of the Cl anion layer in the *in situ* preparation process. In exchange, a new S2p signal appears in the XPS spectra 5.4a and c, which may originate from a sulfate layer adsorbed onto the Cu(100) electrode, as well as from sulfate anions co-adsorbed with the C3-$DBDP^{2+}$ cation layer. The *in situ* formation of an ordered sulfate anion layer at such negative electrode potentials (-360 mV vs RHE) can be, however, excluded, as the even more strongly adsorbing Cl anions are proved to desorb from the Cu(100) electrode surface at that potential. More likely is sulfate being co-adsorbed within the organic cation layer or an sulfate adsorption on the Cu(100) surface solely related to residual electrolyte on the Cu(100) surface and induced at open circuit conditions in the emersion step.

5.3 Morphology of the Halide Covered Cu(100) Surface

Both halide-c(2x2) adlayers affect the morphology of the underlying Cu(100) surface by changing the copper step and kink energies [20, 21, 24]. This induces a reorganization of the Cu(100) surface known as step faceting [20]. In the step faceting process the randomly orientated and fringed steps of the bare Cu(100) surface reorganize upon formation of the Cl- or Br-c(2x2) adlayer to follow the close-packed directions of the halide adlayers, namely [100] and [010] (fig. 5.1c and 5.5). This leads to the appearance of almost exclusively 90° angles between two steps of the Cl covered Cu(100) surface as exemplarily shown in figure 5.5.

The reorganization of the Cu steps is a Ostwald ripening type process [75] leading to a minimization of the free energy of the surface by dissolving the topmost small Cu terraces in favor of the lower big terraces. This reduction of the surface roughness is known as halide induced “electrochemical annealing” of the Cu(100) surface and is assumed to be enhanced by the weakening of the topmost Cu-Cu bond as a result of the halide adsorption, which enhances the copper mobility via e.g. the formation of the soluble halide-copper complex, e.g. $[CuCl_2]^-$ [24].

The step faceting highly depends on the presence of the Cl-c(2x2) monolayer, as the

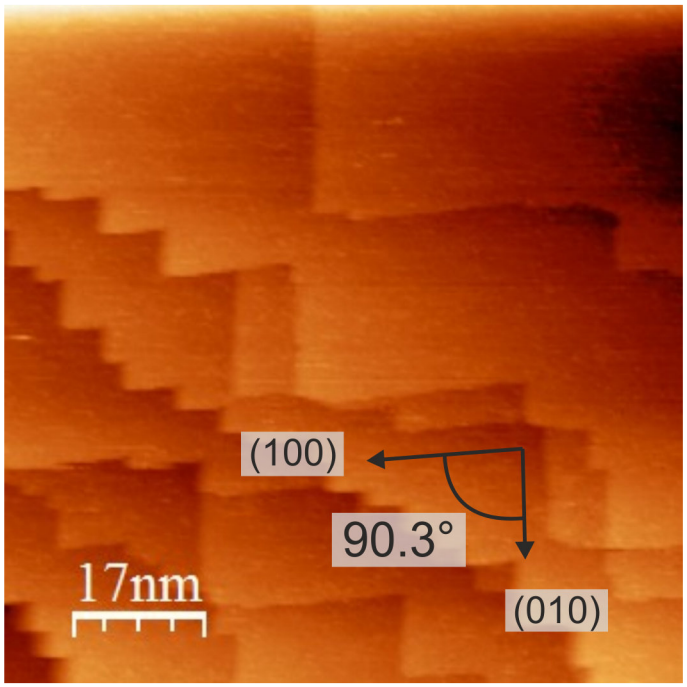

Figure 5.5: Chloride induced step faceting of the Cu(100) surface. 85 nm x 85 nm, $E_{Work} = 0\,mV$, $E_{Bias} = 250\,mV$, $I_{Tunnel} = 0.1\,nA$

desorption of Cl anions leads to a quasi-reversible transition to an again more fringed morphology [20, 21]. Therefore the Cu(100) step geometry is a suitable indicator for the presence of Cl anions on the Cu(100) surface, which will be proved to be valid even when a full monolayer of organic cations is co-adsorbed on the electrode surface in the chapter of C3-DBDP^{2+} (sec. 6.2.2).

5.4 3D Structure Studies of Halide-c(2x2)/Cu(100) Surfaces

While STM images provide mainly information about the 2D (two dimensional) surface structure Surface X-Ray Diffraction (SXRD) allows to study the full 3D (three dimensional) structure of the halide covered Cu(100) electrode surface. The experiment is best performed by working in the coordinate system of the Cu fcc lattice, as the Cu fcc unit cell (fig. 5.1b) is the most simple cell describing the whole symmetry of the 3D copper crystal. Changing the Cu unit cell affects as well the notation of the halide adlayer, as the superstructure c(2x2) is related to the underlying Cu unit cell. In relation to the Cu fcc unit cell the Cl-c(2x2) has to be renamed to a Cl-p(1x1) structure, which is a uncommon notation in surface science literature. In order to be consistent with literature and throughout the present work only the notation Cl-c(2x2) will be used. However, it should be kept in mind that other notations of the SXRD experiments, e.g. in definition of the reciprocal space, do still relate to the Cu fcc lattice and the Cl-p(1x1) adlayer.

Previous *in situ* SXRD studies investigated the full 3D structure of the Cl covered [24, 25] or Br [26] covered Cu(100) electrode surface. This is usually done by analyzing the intensity distribution along the CTRs (crystal truncation rods) [43], whose intensity profile represents scattering events in the crystal bulk as well as surface regime (chap. 3.3). In order to significantly increase the surface sensitivity of the SXRD studies so-called adlayer rods [26] can be measured in addition to the classical CTRs. The intensity distribution along the adlayer rods consists solely of scattering events in the surface regime, due to the canceling out of the fcc Cu bulk contribution making these rods highly sensitive to the structural details at the solid/liquid interface. Adlayer rods of the halide-c(2x2)/Cu(100) surface are found at, e.g. the in-plane coordinates (1 0)[1].

However, the intensity profiles of these adlayer rods, published for the Cl/Cu(100) surface by Gründer et al. [25] and for the Br/Cu(100) surface by Saracino et al. [26], are found to significantly deviate from the best fit at values of $L < 0.5$, where L is the momentum transfer in the out-of-plane direction. This deviation between model and data for the Br/Cu(100) surface was initially assumed to be related to the resolution of the experiment and therefore inherent to the experimental method. In contradiction to this interpretation the later registered adlayer rods of the Cl/Cu(100) surface reveal an even stronger intensity loss for values of $L < 0.5$. This indicates that the proposed model of the halide/Cu(100) surfaces are incomplete. This is also indicated by results of adsorbed neutral chlorine-c(2x2) on a Cu(100) surface, investigated under UHV conditions by Tolentino et al. [69]. The adlayer rod in this study is fully reproduced by the best fit of the surface regime, with a model comparable to those published in other studies of the solid/liquid interface.

The deviations between data and fit observed at the halide/Cu(100) surfaces are therefore most likely related to the presence of the electrolyte solution, indicating a surface induced ordering of the near electrolyte regime, namely the outer LSCI (chap. 2.1), as proven recently by SXRD experiments at the SLS (SwissLightSource, Paul-Scherrer Institut, Switzerland) [44]. This study was initiated by the Department of Chemistry & Biochemistry at the University of Berne. The findings of that study demands to re-investigate as well previously published data [26] in order to conclude on the validity of the new model of the halide/Cu(100) surface, as well as to conclude on the validity of the previously published results, such as the sub-surface buckling of the 2nd Cu layer and the potential dependence of the interfacial structure [26].

5.4.1 Model of the Cu(100) Surface in 5 mM H_2SO_4 + 10 mM KBr

A model for the 5 mM H_2SO_4 + 10 mM KBr/Cu(100) interface is sketched in figure 5.6. The model consists of a Br-c(2x2) adlayer specifically adsorbed on the Cu(100) electrode surface, as well as an in-plane ordered outer LSCI consisting of solvated K

[1] The notation (1 0) for the adlayer rod results from the Cu fcc unit cell, which is commonly used in x-ray diffraction experiments. In contrast to the 2D surface coordinate system, in which the Cl-c(2x2) adlayer is usually described, the Cu fcc unit cell consists of three orthogonal basis vectors of the same length. Therefore working in the fcc coordinates significantly simplifies experiments as well as data treatment, in which all three space dimensions are involved.

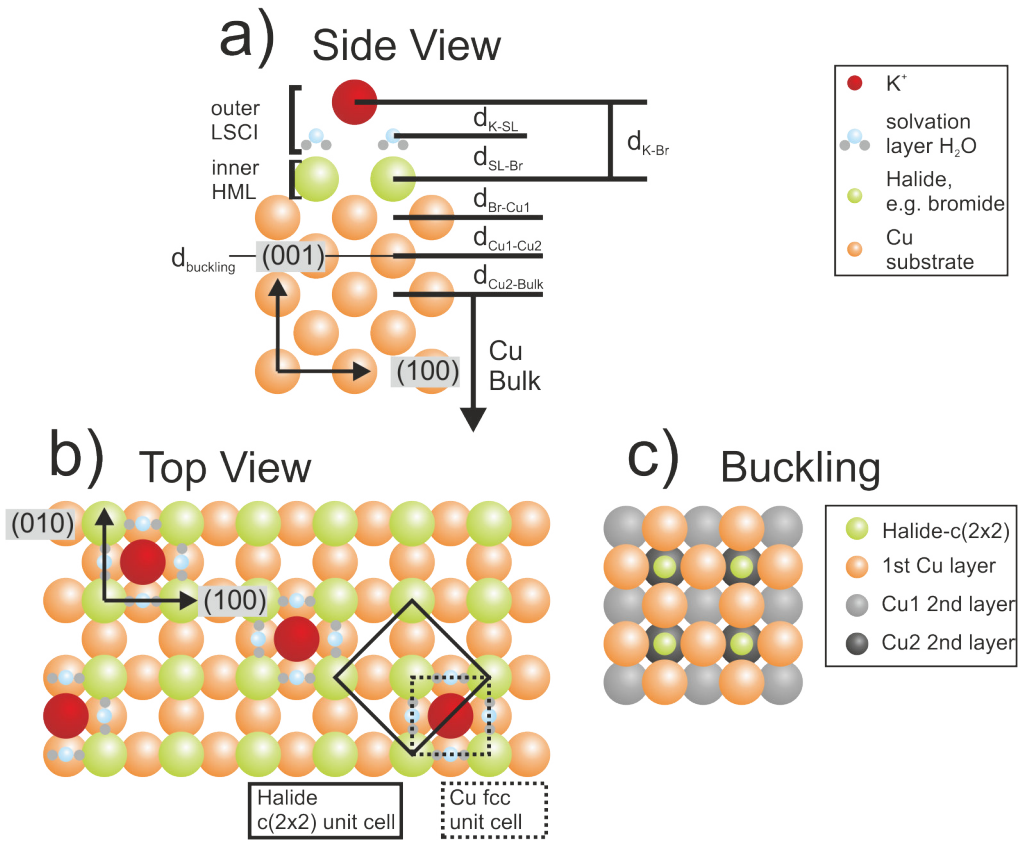

Figure 5.6: SXRD model of the whole solid/liquid interface, including the solid metal electrode surface as well as the inner HHL (Helmholtz Layer) and outer LSCI (Layer of Solvated Counter Ions). (a) Side view of the interfacial regime. (b) Top view of the SXRD model. (c) Halide induced symmetry break in the 2nd Cu layer, making two atoms, Cu1 and Cu2, within the second Cu layer distinguishable.

(potassium) cations. The lateral order of the outer LSCI can be assumed to be the result of a symmetry transfer from the adsorbed negatively charged halide template, namely Br-c(2x2), into the outer LSCI leading to solvated K cations located in the fourfold hollow sites of the Br-c(2x2) adlayer. The structure fit parameters are only the atomic z-coordinates, as all in-plane coordinates of the atoms must stay fixed throughout the fit procedure due to the given p4mm symmetry. The z-coordinate of the K cation layer, solvation layer, Br-c(2x2) adlayer and of the first Cu layer describe for symmetry reasons all atoms within the same layer. However, to describe the 2nd Cu layer two z-coordinates are necessary, as the Br adlayer leads to a symmetry break in the 2nd Cu layer. The symmetry break makes two Cu atoms distinguishable, namely Cu1 and Cu2, as sketched in figure 5.6c. Therefore Cu1 and Cu2 atoms, both situated in the 2nd Cu layer, can relax independently from each other (fig. 5.6c). This may give rise to the previously observed buckling of the 2nd Cu layer [26]. The buckling is a corrugation of the 2nd Cu layer with, however, an inverted amplitude to the buckling found under UHV conditions [69] as stated by Gründer et al. [25].

In addition to the structure fit parameters, three atom related Debye-Waller (DW) factors are included in the model, representing the vibrations of the atoms in the Cu bulk, the first and the second Cu layer. Only the two latter DW factors are free fit parameters, as the DW factor of the Cu bulk is expected to be constant throughout the experiment. The DW factors are assumed to be isotropic with a minimum value of 0.598 $\AA^2$, as found for the Cu bulk at 300K [42]. The isotropy of the DW factors is a simplification, as the discontinuity at the Cu(100) surface should result in non-isotropic vibrations and therefore demands to distinguish between in-plane and out-of-plane DW factors. However, this simplification on the other hand increases the significance of the fit results (smaller fit errors), which outweighs the benefit of a more detailed model.

Besides the atom related fit parameters, a number of global structure parameters are involved in the fit procedure. The surface regime is represented by a 3D surface unit cell, situated above a constant Cu bulk unit cell. The fit parameter θ_{surf} represents the fraction of the Cu bulk surface covered by the surface unit cell. Further a global scale factor S and an occupancy factor for the outer LSCI θ_{LSCI} is included in the model. A single pseudo DW factor is introduced in the model in order to account for the vibrations in the outer LSCI and inner HHL. A single DW factor of the outer LSCI was not used, as it correlated with the occupancy parameter θ_{LSCI} and therefore prevented a stable minimum in the fit procedure. The correlation between these fit parameters results from the *mathematical* fact, that both parameters, DW factor of the LSCI and θ_{LSCI}, damp the contribution of the outer LSCI in the total structure factor. The *physical* background for the correlation between both fit parameters is the coupling between cation vibrations and exchange processes between the weakly bounded outer LSCI and the bulk electrolyte. Using the pseudo DW factor permits to estimate the average vibration amplitude of the inner HHL and outer LSCI. This average vibration amplitude is the minimum amplitude of the vibrations in the outer LSCI. A surface roughness, which would have modeled the statistical occurrence of up and down steps, was investigated in the SXRD analysis, but found to be insignificant and therefore not included in the model. The whole model contains a total of only 12 fit parameters.

SXRD Study of the K-c(2x2)/Br-c(2x2)/Cu(100) Interface

Applying and optimizing the presented model of the halide-c(2x2)/Cu(100) surface to fit the measured SXRD data of the Br/Cu(100) surface leads to a qualitative good reproduction of the (1 0) adlayer rod profile as can be seen in figure 5.7. The anti-phase relation between inner HHL and outer LSCI decreases the structure factor of the adlayer rod (fig. 5.7a) for values of $L = Q_z < 0.5$ and removes the systematic deviation, which appeared in the previously published model of the solid/liquid interface [26]. Further the wavy line profile of the adlayer rod is significantly better reproduced [26]. The qualitatively better reproduction of the adlayer rod profiles does, however, not result in a decrease of the χ^2 values. χ^2 is used to measure the goodness of the fit by

$$\chi^2 = \frac{1}{N-p} \sum_{hkl} \frac{||F_{hkl}^{calc}|^2 - |F_{hkl}^{exp}|^2|}{\sigma_{hkl}} \tag{5.1}$$

with the quantity of measured structure factors N, the quantity of fit parameters p and the experimental error σ_{hkl} of the measured structure factor F_{hkl}^{exp}. Contrary to the better qualitative reproduction of the adlayer rod profile, the χ^2 values of the new surface model are found to be slightly increased by 0.11/0.47 (= worse) for SXRD data measured at electrode potentials of $E_{work} = -50\,mV / -150\,mV\,[vs.\,RHE]$ (tab. 5.1.a). This increase can be partially explained by the increased quantity of fit parameters p necessary to describe the ordered outer LSCI in the new surface model, which affects directly the χ^2 value (eq. 5.1). However, in general using only the χ^2 value to evaluate the goodness of the fit is insufficient, as χ^2 does not contain sufficient information about the qualitative reproduction of the rod profiles. The χ^2 value must therefore always be combined with a qualitative evaluation of the fit profile.

All fit parameters and calculated layer relaxations, resulting from the structure refinement procedure of the SXRD data, are summarized in table 5.1. The structural response of the Cu electrode to a change of the electrode potential is shown in figure 5.8. The distance between the 2nd Cu layer to the Cu bulk expands with increasing electrode potentials from an inward relaxation of -0.3% at -150 mV [vs. RHE] to an outward relaxation of +0.23% at -50 mV [vs. RHE] and +1.03% at +50 mV [vs. RHE]. This layer expansion indicates a reduction of the attractive forces (bond strength) between the 2nd Cu layer and the Cu bulk, which is interpreted as a reduction of the electron density within the surface regime of the Cu electrode, leading to a less efficient screening of the positive Cu cores from each other.

Contrary to this the distance between 1st and 2nd Cu layer follows an inverted trend. This layer distance is at -150 mV [vs. RHE] maximal expanded by +2.6%, which is reduced with increasing Cu potential, first slightly to +2.17% at -50 mV [vs. RHE] and more significantly to +0.75% at +50 mV [vs. RHE]. The decrease of the topmost Cu-Cu layer distance in the first potential increase (-150 mV to -50 mV [vs. RHE]) can be related to the inward movement of the negatively charged Br anion adlayer situated above the Cu surface. The Br anion layer is, in the same potential step, found to be attracted to the Cu electrode from a layer distance of 107% at -150 mV [vs. RHE] to a distance of 104.8% at -50 mV [vs. RHE]. This may exert pressure on the first layer of the

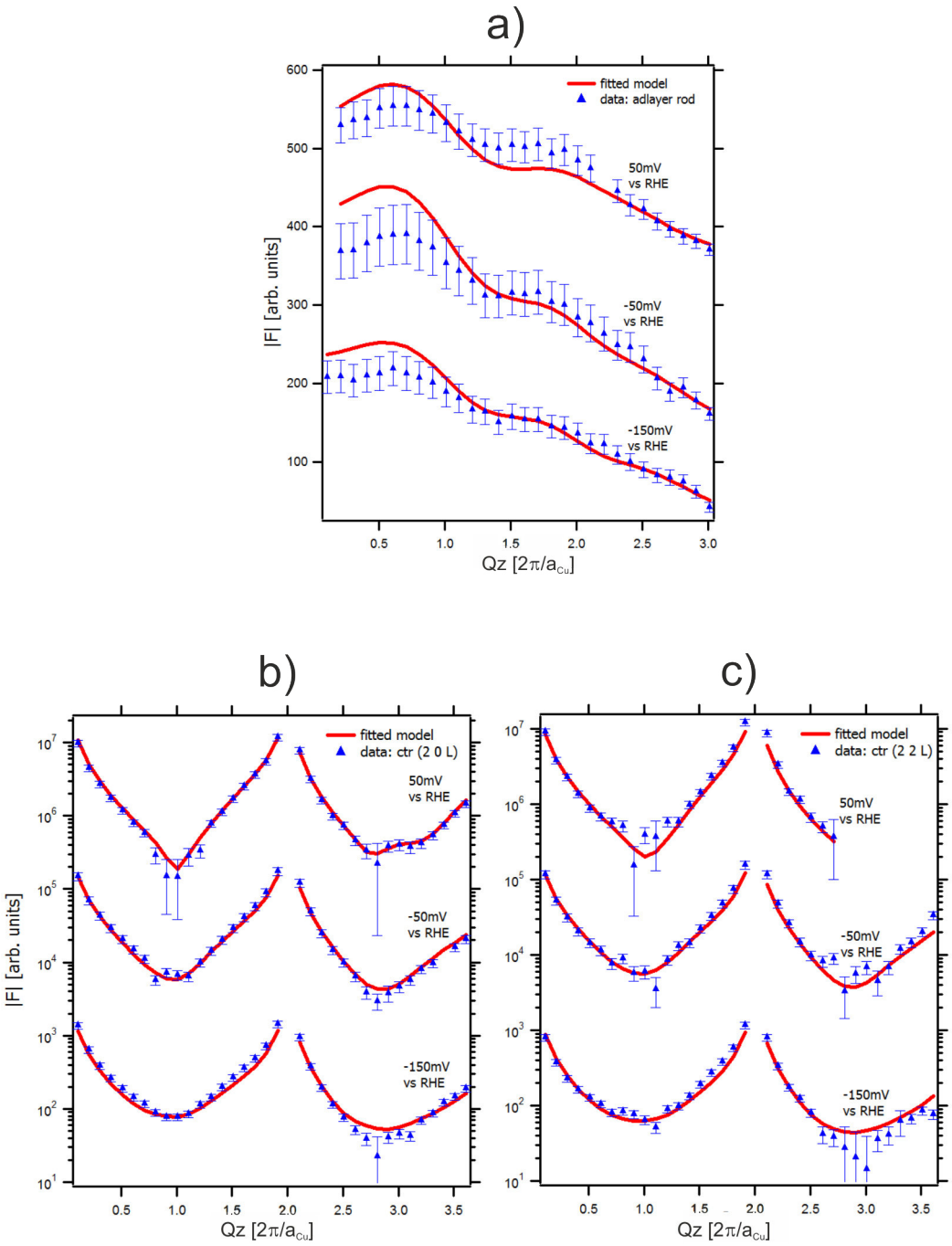

Figure 5.7: *In situ* SXRD data of the Br/Cu(100) surface (triangles) and best fit (solid line). From up to down: (a) (1 0 L) adlayer rod, (b) (2 0 L) CTR, (c) (2 2 L) CTR.

a

E_{work} [vs. RHE]	Goodness of fit χ^2: New Surface Model	Old Surface Model	Difference $\Delta\chi^2$	Quantity of Measured Structure Factors
+50 mV	1.17	1.44	-0.27	90
-50 mV	1.2	1.09	+0.11	98
-150 mV	2.19	1.72	+0.47	99

b

Atom Ion Molecule	x [a_{Cu}]	y [a_{Cu}]	Potential Dependend Layer Relaxations: z [a_{Cu}] E_{work} = -150mV [vs. RHE]	z [a_{Cu}] E_{work} = -50mV [vs. RHE]	z [a_{Cu}] E_{work} = +50mV [vs. RHE]
K^+	0.500	0.500	1.77 (1)	1.743 (8)	1.737 (5)
H_2O	0.500	0.000	1.30 (2)	1.36 (1)	1.537 (8)
H_2O	0.000	0.500	1.30 (2)	1.36 (1)	1.537 (8)
Br^-	0.000	0.000	1.046 (4)	1.036 (2)	1.0335 (5)
Cu	0.500	0.000	0.511 (1)	0.5120 (4)	0.5089 (3)
Cu	0.000	0.500	0.511 (1)	0.5120 (4)	0.5089 (3)
Cu	0.500	0.500	0	0.0023 (3)	0.0060 (3)
Cu	0.000	0.000	-0.003 (1)	0	0.0043 (3)

c

E_{work} [vs. RHE]	Debye-Waller Factors [Å]: Inner HHL / outer LSCI	1st Cu Layer	2nd Cu Layer	Cu Bulk	Occupancies: Coverage θ_{Surf}	Occupancy θ_{LSCI}
+50 mV	4.18 (4)	1.37 (1)	0.65 (1)	0.598	1.0 (1)	0.215 (9)
-50 mV	6.33 (5)	1.58 (1)	0.598	0.598	0.971 (2)	0.18 (2)
-150 mV	6.0 (2)	2.07 (9)	0.81 (6)	0.598	0.84 (1)	0.14 (5)

d

E_{work} [vs. RHE]	Electrolyte: $d_{K\text{-}SL}$ [a_{Cu}/2]	$d_{SL\text{-}Br}$ [a_{Cu}/2]	$d_{K\text{-}Br}$ [a_{Cu}/2]	$d_{Br\text{-}Cu1}$ [a_{Cu}/2]	Copper Electrode: $d_{Cu1\text{-}Cu2}$ [a_{Cu}/2]	$d_{Buckling}$ [Å]	$d_{Cu2\text{-}Bulk}$ [a_{Cu}/2]	$d_{Bulk\text{-}Bulk}$ [a_{Cu}/2]
+50 mV	0.40 (1)	1.007 (9)	1.406 (6)	1.0492 (8)	1.0075 (9)	0.0063 (6)	1.0103 (6)	1
-50 mV	0.77 (2)	0.65 (1)	1.413 (9)	1.048 (2)	1.0217 (7)	0.0083 (3)	1.0023 (3)	1
-150 mV	0.94 (8)	0.51 (5)	1.45 (3)	1.070 (5)	1.026 (2)	0.029 (1)	0.997 (1)	1

Table 5.1: Results of the structure refinement procedure of the Br/Cu(100) surface. (a) Comparison of the goodness of fit between the new surface model (present work) and the old surface model [26]. Quantity of measured data points (=structure factors) in the SXRD experiment. (b) Coordinates of all atoms/ions/molecules within the surface unit cell in units of the Cu fcc lattice constant $a_{Cu} = 0.3615\,nm$. (c) Debye-Waller factors and occupancy/coverage parameters. (d) Calculated potential dependent layer relaxations in units of the Cu bulk (100) layer distancies $\frac{a_{Cu}}{2} = 0.18075\,nm$.

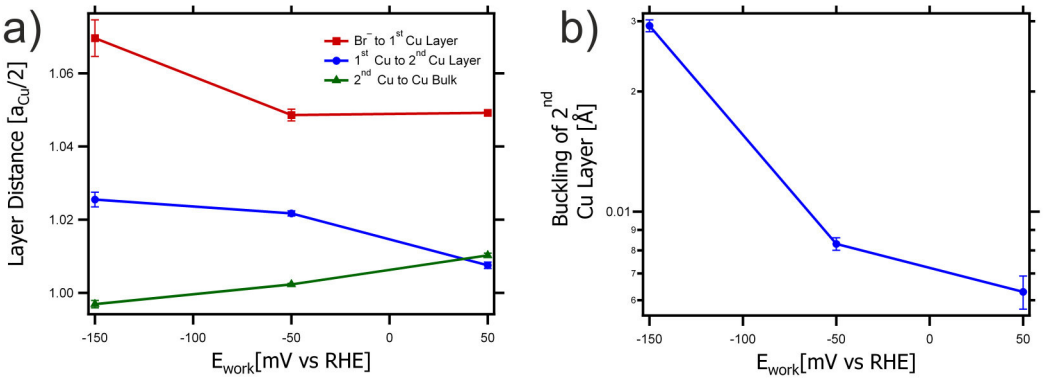

Figure 5.8: Structural variation of the Cu electrode as a function of the electrode potential. (a) Relaxations of the topmost Br-c(2x2), 1st and 2nd Cu layers of the (100) surface as a function of the potential state of the Cu electrode. Layer relaxations are in units of the bulk Cu-Cu layer distance in (001) direction $\frac{a_{Cu}}{2} = 0.18075\,nm$. (b) Potential dependent amplitude of the 2nd Cu layer buckling.

Cu(100) surface and therefore lead to the observed decrease of the topmost Cu-Cu layer distance. However, this process is apparently also accompanied by an electron density transfer from the anionic Br adlayer into the first Cu layer. This can be assumed because the second potential increase (-50 mV to +50 mV [vs. RHE]) does not affect the Br-Cu layer distance which stays within the experimental error constant. In contrast to this the first Cu-Cu layer distance is, yet again, reduced to an outward relaxation of only +0.75% at +50 mV [vs. RHE]. This strong decrease of the first Cu-Cu layer distance in the second potential step indicates a significant increase of the attractive forces between first and second Cu layer. The most likely cause of the increased attraction between the two topmost Cu layers is a transfer of electron density from the topmost Br-Cu regime deeper into the Cu electrode, which leads to a strengthening of the bond between the first two Cu layers by the screening of the positive Cu cores from each other [26].

As this latter observation indicates the (partial) transfer of the Br anion charge into the Cu electrode surface, it can be assumed – but not fully proven – that this transfer occurs in the first potential step (-150 mV to -50 mV [vs. RHE]). This assumption is supported by the potential dependent amplitude of the buckling of the second Cu layer [76, 26, 69, 25], which as well indicates a significant electron density transfer from the Br adlayer into the Cu electrode in the first potential step.

The buckling of the second Cu layer originates from a symmetry transfer of the Br anion c(2x2) monolayer into the Cu electrode, which alters the electron density distribution within the second Cu layer, and consequently makes two kinds of Cu atom within the second Cu layer distinguishable, namely Cu1 and Cu2 (fig. 5.6c). The effect of the Br anion adsorption on the second Cu layer must depend on the interaction between them. For instance, a fully charged Br anion is expected to lead to a reduction of the electron density close to the anion. Consequently a (partial) transfer of the anion charge

to all Cu atoms of the first Cu layer reduces this "symmetry transfer" from the Br c(2x2) into the second Cu layer.

Indeed, the analysis of the SXRD data related to the Br/Cu(100) electrode reveals the existence of the buckling of the second Cu layer, whose amplitude is found to be reduced with increasing electrode potential from 2.9 pm at -150 mV [vs. RHE] to 0.83 pm / 0.63 pm at -50 mV / +50 mV [vs. RHE], respectively (fig. 5.8b). The decrease of the buckling amplitude with increasing Cu potential is in agreement with the idea of an electron density transfer from the Br anion adlayer into the first Cu layer, as the reduced anion charge density within the Br c(2x2) monolayer lowers, as stated above, also its altering effect on the electron density within the second Cu layer.

In agreement to this interpretation, the most significant reduction of the buckling amplitude occurs in the first potential step (-150 mV to -50 mV [vs. RHE]), which then proves a significant discharge of the Br anions and, therefore, a change from a mainly ionic to a more covalent Cu-Br bond. A subsequent increase to +50 mV [vs. RHE] affects the buckling amplitude weakly and therefore indicates a weaker effect of this potential step on the Br-Cu bond, which is in full agreement with the observed constant Br-Cu layer distance during the potential increase from -50 mV to +50 mV [vs. RHE].

To summarize these observations the first potential step (-150 mV to -50 mV [vs. RHE]) affects mainly the Cu-Br bond. The Br anion charge density is (at least partially) transferred to all Cu atoms within the 1st Cu layer leading to a stronger and therefore shorter Cu-Br bond. As a consequence of the (partial) anion charge transfer the buckling amplitude of the second Cu layer is found to decrease strongly.

In the second potential step (-50 mV to +50 mV [vs. RHE]) the buckling amplitude is found to remain almost unaffected. The Br anion charge, assumed to be equally distributed on all four Cu-Br bonds, seems to be transferred deeper into the Cu crystal, as the topmost Cu-Cu bond is found to contract more strongly than in the first potential step. At the same time the Cu-Br bond stays unaffected, which indicates that a minimum bond length is achieved.

Beside the structure analysis of the inner HHL and the solid electrode surface, the new model of the interfacial regime permits to conclude also on the potential dependence of the outer LSCI (fig. 5.9a). Surprisingly the K-Br layer distance (distance between inner HHL and outer LSCI) is hardly affected by the charge state of the electrode surface (Cu potential). For potentials of +50 mV and -50 mV [vs. RHE] the K-Br layer distance is with 0.189 nm. Reducing the electrode potential to -150 mV leads to an 2% outward relaxation to a value of 0.193 nm, which indicates a reduction of the K cation attraction in the direction of the electrode surface, although the solid electrode surface is charged more negatively and is therefore expected to attract positive charges more strongly.

This result is, however, in agreement with the decrease of the occupancy of the ordered outer K cation layer θ_{LSCI} (fig. 5.9b). The occupancy θ_{LSCI} is found to decrease from 21.5% ±0.9% at +50 mV [vs. RHE] to 14% ±5% at -150 mV [vs. RHE]. The high inaccuracy of this parameter at low electrode potentials does not allow to decided if θ_{LSCI} either decreases significantly or stays close to an occupancy of 20%. But even the observed slight decrease of the occupancy θ_{LSCI} at -150 mV [vs. RHE] is in agreement with the weakening of the K-Br bond expressed by the increased layer distance at the

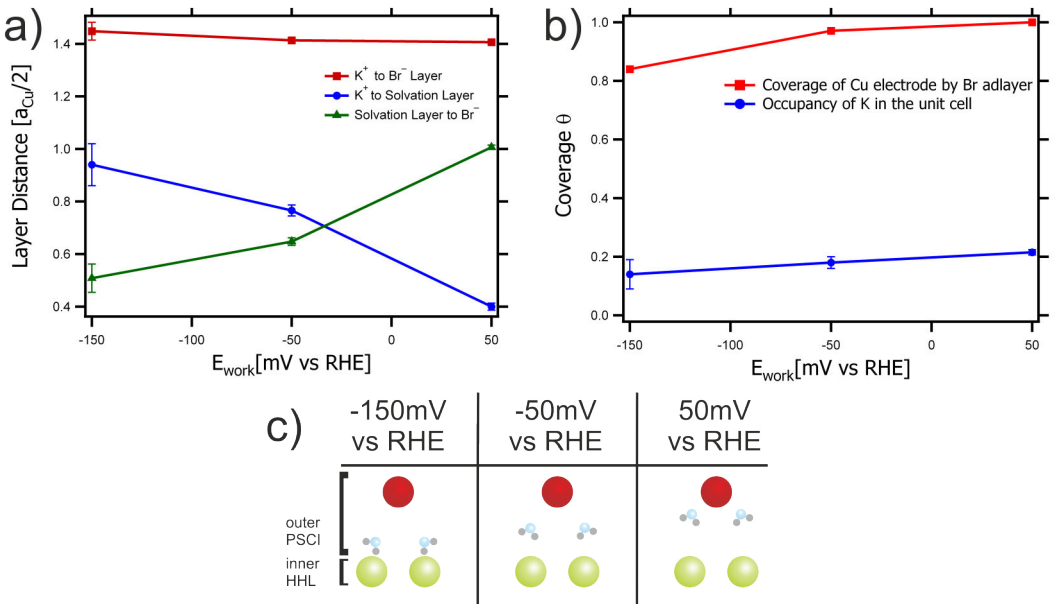

Figure 5.9: (a) Potential dependent layer distances of the outer LSCI. (b) Potential dependent coverage of the Cu(100) surface by the Br adlayer and occupancy of the K cations in the outer LSCI. (c) Simplified sketch of the potential dependent layer distances of the outer LSCI and inner HHL.

low electrode potential. This is contrary to what is expected from simple electrostatic models, in which the attractive forces between more negatively charged surface and K cation should increase.

It must be noted that the occupancy parameter θ_{LSCI} only describes the ordered part of the outer LSCI, consisting of K cations interacting directly with the Br-c(2x2) adlayer and adsorbing in their fourfold hollow sites. The existence of a disordered part of the outer LSCI can not be excluded as it only contributes as diffuse background in the SXRD data. However, the observed occupancy of 20% in the θ_{LSCI} is usually the maximum coverage of non-specifically adsorbed ions, as revealed by classical electrochemical investigations [3]. Therefore it is assumed that no significant disordered outer LSCI, exists at the same distance.

It could be concluded that the Br adlayer acts as dominant binding partner to solvated cations of the outer LSCI. This is in agreement with IRRAS (Infrared Reflection Absorption Spectroscopy) studies of Röefzaad et al. [13, 77], in which the dominant role of the Br adlayer as binding partner to organic cations was proven as well. The binding energy between adsorbed Br anions and organic cations was found to stay constant throughout the investigated potential window. A similar behavior was found when the inner HHL was the less polarizable Cl-c(2x2). An influence of the electrode potential on the cation binding energy was only observed if the Cu(100) electrode was precovered by the more polarizable I (iodine) adlayer [13, 77].

An explanation of this potential independence of the bond strength between inner HHL (e.g. Br anions) and outer LSCI (e.g. K cations) can be found in the high anion density within the inner HHL, which creates a negative substrate throughout the whole potential window. Indeed, this is exploited within this work to study the ordering of cations on halide precovered Cu(100) surfaces, as even for the most positive Cu potentials the charge state of the electrode surface remains negative. Indeed, at the most positive electrode potentials, at which electrostatic repulsion would force the desorption of adsorbed organic cations, the organic cations remain adsorbed on the halide c(2x2) covered electrode, as proven by STM experiments within this work.

In contrast to the K-Br layer distance, the position of the SL (solvation layer, fig. 5.6a) between the K and Br ions is found to be strongly affected by the Cu electrode potential. The SL, consisting of water dipoles, has at +50 mV [vs. RHE] a distance of 0.4 [$\frac{a_{Cu}}{2}$] (= 0.72 Å) to the K layer and a distance of 1.007 [$\frac{a_{Cu}}{2}$] (= 1.82 Å) to the Br adlayer, from which it can be concluded that at this potential state the partially uncharged Br adlayer interacts weakly with the SL. Therefore the water dipoles – mainly interacting with the fully charged K cations of the ordered outer LSCI – are attributed to the K cation solvation shell. Reducing the Cu electrode potential to -50 mV [vs. RHE] leads to a detachment of the SL from the K cations, which is assumed to be the result of an increasing attraction of the water dipoles by the more negatively charged Br adlayer. At -50 mV [vs. RHE] the distances between the SL to both, the K and Br layer, are comparable, namely 0.77 [$\frac{a_{Cu}}{2}$] (= 1.39 Å) to the K and 0.65 [$\frac{a_{Cu}}{2}$] (= 1.17 Å) to the Br layer. A further reduction of the Cu potential to -150 mV [vs. RHE] leads to a strong attraction of the SL by the now fully charged Br anion layer, resulting in a SL-Br layer distance of only 0.51 [$\frac{a_{Cu}}{2}$] (= 0.92 Å) and a K-SL distance of 0.94 [$\frac{a_{Cu}}{2}$] (= 1.70 Å). Those layer distances indicate that at -150 mV [vs. RHE] the former K cation solvation shell must be fully attributed to the charged Br anions.

The stripping of the K cation solvation shell by the Br anions and subsequent formation of the Br solvation shell at -150 mV [vs. RHE] most likely forces a rearrangement of the water dipoles [78, 79], sketched in figure 5.9c. The loss of the lower (electrode sided) K cation solvation shell may reduce the attractive forces in the direction of the electrode surface, and therefore explain the outward movement observed for the K cation layer at -150 mV [vs. RHE].

The attraction of water dipoles by Br anions at -150 mV [vs. RHE] is expected to occur also on the LSCI free Br-c(2x2) areas. In the analysis this can be described by a separate occupancy parameter of the SL. However, the low scattering of the synchrotron radiation at the SL and consequently the weak effect of the SL in the SXRD data does not permit to conclusion on this with certainty. Indeed, the occupancy of the SL was found to be negligible in the SXRD analysis. However, assuming the SL is formed at -150 mV [vs. RHE] over the whole Br c(2x2) monolayer, then it hinders the adsorption of solvated K cations. The equilibrium of the K cation ad- and desorption would then be disturbed, namely more K cations would desorb then adsorb at that potential state. This is in full agreement with the observed reduction of θ_{LSCI} (fig.5.9b) upon reduction of the electrode potential to -150 mV [vs. RHE].

Figure 5.9b shows further the potential dependence of the Br adlayer coverage on the

Cu(100) surface θ_{Surf}. At +50 mV [vs. RHE] the Cu(100) surface attracts Br anions strongly, which are found to adsorb and form a full monolayer of the Br-c(2x2) adlayer ($\theta_{Surf} = 0.5\,ML$). Reducing the Cu potential to -50 mV [vs. RHE] leads to an increase of the negative charge at the Cu(100) surface and therefore to a slight decrease of the Br adlayer coverage θ_{Surf} to 97%. A further decrease of the Cu potential to -150 mV [vs. RHE] leads finally to the beginning of the Br anion desorption process, resulting in a reduction of the Br coverage θ_{Surf} to 84%, which is in agreement with the previously discussed formation of the Br anion solvation shell at -150 mV [vs. RHE] facilitating the Br anion desorption.

Summary

The SXRD data of the in this work studied electrolyte/Br/Cu(100) interface is best explained by an in-plane ordered outer LSCI above the Br/Cu(100) electrode surface. The LSCI was modeled by solvated K cations, which, however, can be substituted by H_3O^+ cations without significant changes of the results. Therefore it is assumed that both cations adsorb in the fourfold hollow sites of the Br anion adlayer, which is in agreement with the assumptions made in the study of the Cl/Cu(100) surface [44].

The potential dependent data of the Br/Cu(100) surface revealed the full interfacial structure (tab. 5.1) including the solid Cu electrode, inner HHL and outer LSCI. A charge transfer of the Br anion adlayer into the electrode surface explains the observed layer relaxations and their potential dependence. This charge transfer leads in a first potential step (-150 mV to -50 mV [vs. RHE]) to a strengthening of the Br-Cu bond by the partial transfer of the anion charged equally to all Cu atoms of the 1st Cu layer. This lowers the symmetry breaking effect of the Br anion charge and leads to a strong decrease of the sub-surface buckling of the 2nd Cu layer. Furthermore a slight reduction of the 1st Cu-Cu layer distance is observed in this potential step. In a second potential step (-50 mV to +50 mV [vs. RHE]) a fraction of the Br anion charge is transferred more deeply into the Cu electrode surface. This leads to a stronger contraction of the 1st Cu-Cu layer distance, whereas the buckling amplitude is only weakly and the Br-Cu distance almost not affected.

Throughout both investigated potential steps the first two Cu layers are detached from the Cu bulk almost linearly, which can be explained by the general reduction of the electron density at the Cu electrode surface. Indeed, the observed layer contractions are attributed to electron density transfer from the anionic Br adlayer into the Cu electrode.

In contrast to this the outer LSCI is hardly affected by potential changes of the Cu electrode. This is due to the high anion charge density at the electrode surface, which represents the dominant binding partner of the K cations with the outer LSCI. Changes of the electrode potentials do not significantly weaken the overall negative charge state of the electrode surface. This result is in agreement with EC-STM studies within this work and IRRAS experiments by Röefzaad et al. [13, 77], which prove that the Br-c(2x2) adlayer acts as negatively charged substrate throughout the whole potential window of the Cu electrode.

The K cation solvation shell on the other hand is strongly affected by the electrode

				Huemann et al.	Gründer et al.	Keller et al.
Distances in [$a_{Cu}/2$]	Br/Cu(100)			Cl/Cu(100)	Cl/Cu(100)	Cl/Cu(100)
	-150 mV [vs. RHE]	-50 mV [vs. RHE]	+50 mV [vs. RHE]	+95/+260 mV [vs. RHE]	-200mV [vs. Ag/AgCl, 3M KCl]	+150 mV [vs. RHE]
Inner HHL to outer PSCI	1.45 (3)	1.413 (9)	1.406 (6)			1.9 (1)
SL to outer PSCI	0.94 (8)	0.77 (2)	0.40 (1)			0.72 (4)
Inner HHL to SL	0.51 (5)	0.65 (1)	1.007 (9)			1.18 (6)
1st Cu Layer to inner HHL	1.070 (5)	1.048 (2)	1.0492 (8)	1.08 (2)	1.026 (8)	1.10 (3)
2nd to 1st Cu Layer	1.026 (2)	1.0217 (7)	1.0075 (9)	1.022 (4)	0.992 (8)	1.008 (4)
Buckling of 2nd Cu Layer	0.029 (1)	0.0083 (3)	0.0063 (6)	-	0.014 (4)	-

Table 5.2: Comparsion of the results of various SXRD studies [24, 25, 44]. The values of the layer distances are in units of $[\frac{a_{Cu}}{2}]$ and their accuracy of the last digit is stated in parenthesis behind the value.

potential state. At high potentials (+50 mV [vs. RHE]) the solvation layer (SL) between Br anions and K cations is fully attributed to the K cations. Reducing the electrode potential leads to a stronger localization of the Br anion charge within the inner HHL and therefore to a stronger attraction of the water dipoles. This results in the partial stripping of the K cation solvation shell and the subsequent formation of a Br anion solvation shell at -150 mV [vs. RHE].

The coverage of the Cu(100) surface by the Br anions is found to be reduced for decreasing electrode potentials. This is in agreement with the coverage drop of the Cl-c(2x2) adlayer, which is found to be stronger than for Br anions in the same potential range [25]. The occupancy in the outer LSCI θ_{LSCI} is, in contrast to this, found to be hardly affected by the Cu electrode potential, which on the other hand agrees well with the previously discussed potential independent distance between inner HHL and outer LSCI.

5.4.2 Comparison Between Br-c(2x2)/Cu(100) and Cl-c(2x2)/Cu(100)

Comparing the potential dependent experimental results of the Br-c(2x2)/Cu(100) surface with those of the Cl-c(2x2)/Cu(100) surface [24, 25, 44] permits to conclude on the charge state of the Cl-c(2x2) anion substrate, which is used as negatively charged substrate in the subsequent sections. Table 5.2 summarizes the results of previous works of the Cl/Cu(100) electrode surface. The earlier works of Huemann et al. [24] and Gründer et al. [25] do not include an ordered outer LSCI in their structure model, therefore the work by Keller et al. [44] is the most suitable for a comparison with the results found in this work.

The comparison reveals that the interfacial structure of the Cl/Cu(100) surface is most similar to the interfacial structure of Br/Cu(100) at high electrode potentials (green columns table 5.2). Indeed, the effect of both halide-c(2x2) adlayers on the topmost Cu-Cu layer distance is comparable. The Cl-c(2x2) leads to a layer distance of 1.008 $[\frac{a_{Cu}}{2}]$ (= 1.822 Å) at +150 mV [vs. RHE], whereas the more polarizable Br-c(2x2) adlayer

leads to a layer distance of 1.0075 [$\frac{a_{Cu}}{2}$] (= 1.8210 Å) at +50 mV [vs. RHE]. These almost identical values, both obtained in the upper quarter of the potential window, indicates that the Cl anion charge is as well partially transferred into the electrode surface, as it was previously stated to occur for the Br anion charge. This assumption is consistent with the absence of a buckling of the 2nd Cu layer in the structure model of the Cl/Cu(100) electrode, as a fully charged Cl anion adlayer is expected to lead to a strong buckling amplitude comparable to those observed at the Br/Cu(100) electrode at electrode potentials of -50 mV [vs. RHE] and lower. The charge transfer of both halide-c(2x2) layers into the Cu(100) electrode surface apparently does not significantly affect the negative potential state of the Cu(100) surface, as it leaves the binding energies between organic cations and the halide adlayer unaffected, as proven by IRRAS studies of Röefzaad et al. [77, 13]. This at first sight astonishing result indicates, that the overall charge state at the halide/Cu(100) surface remains negative throughout the whole potential window (up to +150 mV [vs. RHE]). This results from the high anion charge density created by the specific adsorption of halide anions in the close-packed c(2x2) structure. Although the charge state of the electrode surface is not significantly affected, the increase of the electrode potentials leads to a – at least partial – transfer of the anion charge into the Cu(100) surface. This transfer leads to an equally transfer of the anion charge to all Cu atoms in the first atomic layer of the Cu electrode and therefore weakens the symmetry transfer from the Br anion c(2x2) into the second Cu layer.

Comparing the structure parameters of the inner HHL and outer LSCI (tab. 5.2) reveals differences between the here proposed model of the Br/Cu(100) and Cl/Cu(100) [44] interface. For instance the distance between the Cu(100) surface and the inner HHL is for the smaller Cl anions 1.10 [$\frac{a_{Cu}}{2}$] (= 1.99 Å) but only 1.0492 [$\frac{a_{Cu}}{2}$] (= 1.896 Å) for the bigger Br anions at +50 mV [vs. RHE]. This indicates differing types of bonds between the halides and the Cu surface, where the CuBr bonds can be assumed to be more covalent and therefore shorter compared to the CuCl bonds. Indeed the bond length of CuBr is increased with decreasing electrode potential up to 1.070 [$\frac{a_{Cu}}{2}$] (= 1.934 Å) at -150 mV [cs. RHE]. At this more negative electrode potentials the Br anion charge is stronger localized within the Br adlayer and the then more ionic Br anion is situated at greater distance from the Cu electrode surface. This agrees with the assumption that the wider CuCl bond indicates a more ionic Cl anion state. The qualitative statement of more or less ionic bonds must be, however, addressed in more detail in separate studies.

The results of both models disagree on the distance between inner HHL and outer LSCI, which is found to be 1.406 [$\frac{a_{Cu}}{2}$] (= 2.541 Å) for Br anions at +50 mV [vs. RHE] but 30% larger, namely 1.9 [$\frac{a_{Cu}}{2}$] (= 3.4 Å), for the smaller Cl anions. In both cases K cations are assumed to be solvated, which is modeled by the solvation layer (SL) between K and halide ions. The fully solvated K cations can be assumed to interact mainly electrostatically with the adsorbed halide anions, therefore the significantly differing halide-K ion distances seem to be conflicting. However, comparing the distances between the outer LSCI and the SL shows, yet again, the good agreement between the published Cl/Cu(100) structure model [44] and the Br/Cu(100) structure at +50 mV [vs. RHE], as the SL is in both models found to be more close to the K cations than to the halide

adlayer. The less charged halide anions attract at positive electrode potentials the water dipoles of the SL less strongly, therefore the SL is fully attributed to the K cations.

The previously stated difference in the distances between inner HHL and outer LSCI may be related to differing occupancies in the outer LSCI θ_{LSCI} between the models. The outer LSCI in the model of the Br/Cu(100) electrode surfaces consists only of solvated K cations, which results in a coverage of 0.2 ML. This value is in good agreement with typical coverages of non-specifically adsorbed ion layers [3]. In contradiction to that, in the proposed model of the Cl/Cu(100) electrode surface the "voids" of the K cation layer are filled by hydronium ions. Although the coverage of K cations is found to be 0.15 ML, the positive charge density is significantly higher due to a coverage of 0.3 ML of hydronium cations [44]. The coverage of the outer LSCI, consisting of hydronium and K cations, is then 0.45 ML.

6 Results: Pyridinium Based Self-Assembled Monolayers (SAMs)

Specifically adsorbed halide adlayers on Cu(100) surfaces, e.g. Cl- or Br-c(2x2), have proven to be suitable substrates for the investigation of the ordering and structure formation of organic cations at solid/liquid interfaces [4, 5, 6, 7, 9, 10, 14]. The high anion density of these halide adlayers leads to a negative surface charge throughout most of the potential window of the Cu electrode, which manifests itself in the attraction and stabilization of cations even for the most positive potentials close to the copper corrosion reaction at +250 mV [vs. RHE]. For instance, solvated K cations are attracted by the electrode surface and form an in-plane ordered outer LSCI above the halide adlayer as discussed in the previous chapter. Furthermore organic cations, such as viologens, in the electrolyte solution may adsorb on e.g. a Cl precovered Cu(100) electrode surface and form condensed monolayers. These organic monolayers are found to be stable even at high Cu electrode potentials as proven by various authors [4, 6, 10].

Dense organic monolayers are interesting for a number of reasons. They invert the charge state of the electrode surface in contact to the solution from a negative (halide anion covered) to a positive (organic cation covered) one. In the out-of-plane direction the electrode surface consists then of three subsequent 2D layers with opposite charge, namely the metal electrode surface with variable charge followed by the negative halide and finally positive organic monolayer. In the present context, the final dipole/multipole moment of the electrode surface depends amongst others on the charge distribution within the organic monolayer, making an understanding of the structure of the latter and the conditions for their formation desirable. Moreover, adsorbed organic cations affect surface processes, such as the Cu corrosion and deposition, which makes them relevant additives in electrochemical reactions. Third and finally, organic monolayers are interesting even in non-reactive potential regimes, as they represent functional nano-architectures by their own. These nano-architectures may be exploited either directly for their intrinsic properties or as cationic templates/matrices for the assembly of more complex architectures on the lower nanometer scale.

In order to consciously tailor organic monolayers and adjust their properties for specific (scientific or technological) applications a detailed understanding of the structure formation is desirable. Generally the structure formation of organic building blocks at a solid/liquid interface is a complex interplay of adsorbate-substrate and inter-adsorbate interactions, as well as possible solvent effects. Solvent effects are assumed to be less dominant and therefore not within the focus of the present work. However, the possibility of solvent effects must be kept in mind in the data analysis, as they can not be ruled out. The inter-adsorbate interactions depend fully on the structure and redox state of

the molecular building block and are generally a combination of strong hydrogen bridge bonds, weak van der Waals like and strong electrostatic interactions. Consciously adjusting the balance between these inter-adsorbate interactions permits (up to a certain degree) to control the structure formation of the organic adlayer. For instance various studies have proven the transfer of the molecular symmetry into the by them formed organic monolayer, such as the work by Su et al. [80] at a solid/liquid interface for trimesic acid. This symmetry transfer is a simple consequence of the attractive inter-adsorbate interactions, which forces the molecules to arrange in a specific symmetry to each other in order to maximize attractive and minimize repulsive interactions.

Besides the interactions within an organic film, the substrate also influences the film formation, as it imposes – mostly periodic – boundary conditions for the structure formation of the adsorbates. For example in the present study an electrostatic field, created by the negative Cl-c(2x2) adlayer, is used to attract organic cations from solution. The corrugation of the potential field created by the specifically adsorbed Cl anions leads to distinguishable adsorption sites, such as "on-top sites" on Cl anions and "bridge" or "fourfold hollow sites" between Cl anions. Differing adsorption energies at these sites induce a substrate related ordering of molecular adsorbates, which may result in commensurable organic monolayers [4, 5, 10]. This symmetry transfer from the substrate into the organic monolayer is known as "template effect" [4, 5] and is not restricted to solid/liquid interfaces, but is also observed in UHV studies.

In contrast to solid/liquid interfaces, under UHV conditions a wide temperature range can be addressed in order to influence the dynamic of the adsorbates on the surface. At solid/liquid interfaces the liquid phase above a solid limits this temperature range to the usually smaller thermal stability range of the liquid phase, compared to most solid surfaces. However, at solid/liquid interfaces the surface charge state of the solid surface, known as the electrochemical potential, can be used as additional control parameter. The variability of the electrochemical potential requires the solid to be conductive. This adjustable surface charge state may then – in addition to the previously discussed interactions – strengthen or weaken the adsorbate-substrate interaction [21, 6]. The control of the surface charge permits a direct modification of the adsorbate-substrate interaction and is therefore more convenient than the control of the interfacial temperature. Furthermore, varying the electrochemical potential may provoke reactions. Those electrochemical reactions increase or decrease the redox state of substances at the electrode surface. For instance, changes of the molecular redox state affect not only the molecular properties, but may affect the molecular structure of the organic adlayer as well. Both may lead to phase transitions of the organic adlayer, as proven for viologens [4, 5, 10].

Both, inter-adsorbate and adsorbate-substrate, interactions depend on the molecular structure. In order to better understand the relation between the molecular and adlayer structure, as well as the role of each molecular group in the adlayer formation, a step wise modifications of a given molecular building block seems to be the most adequate way. Therefore the well studied structure formation of two viologens, namely Dibenzyl- (DBV) and Diphenylviologen (DPV), at a Cl-c(2x2)/Cu(100) electrode surface is chosen to be the starting point of this study [4, 5, 6, 7, 13, 77, 9]. In a second step the effect of three modifications of the DBV molecule – resulting in the molecules DB-

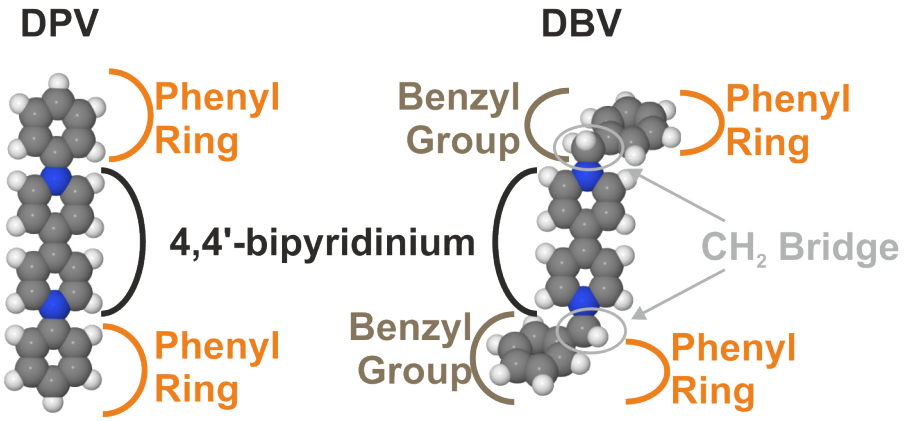

Figure 6.1: Model of DPV (Diphenylviologen) and DBV (Dibenzylviologen), with the common 4,4'-bipyridinium core and their viologen substituents, namely phenyl or benzyl.

3,3'-BP (1,1´-Dibenzyl-3,3´-bipyridinium), C3-DBDP (1,1'-Dibenzyl-4,4'-(propane-1,3-diyl)dipyridinium) and C7-DBDP (1,1'-Dibenzyl-4,4'-(heptane-1,7-diyl)dipyridinium), on the adlayer formation are studied as stated in the introduction chapter of this work.

6.1 Viologens as Building Blocks

6.1.1 DPV and DBV Monolayers on Cl/Cu(100)

All molecules of the viologen family possess the same structural core, namely the 4,4'-bipyridinium core, at which the viologen substituents, e.g. phenyl- (DPV) or benzyl-groups (DBV) (fig. 6.1), are attached via the N-centers. Further, all molecular groups within viologen molecules are arranged symmetrically to the geometric center of the molecule. Beyond these structural details common for all viologens, DPV and DBV, chosen for this study, possess an even more similar molecular structure, as they both consist of two pyridinium and two phenyl rings, as shown in figure 6.1. DPV and DBV differ solely by two additional CH_2 bridges introduced between the bipyridinium core and the DPV phenyl rings. This grants DBV a higher molecular flexibility compared to DPV. These additional rotations, granted by the additional CH_2 bridges, permit to arrange the phenyl rings of DBV in a wider conformational space compared to the phenyl rings of the DPV molecule.

Electrochemical Characterization

Although both viologens, DPV and DBV, are structurally similar they differ significantly in their redox-activity at the Cu(100) electrode surface, as proved by their CVs in figure 6.2.

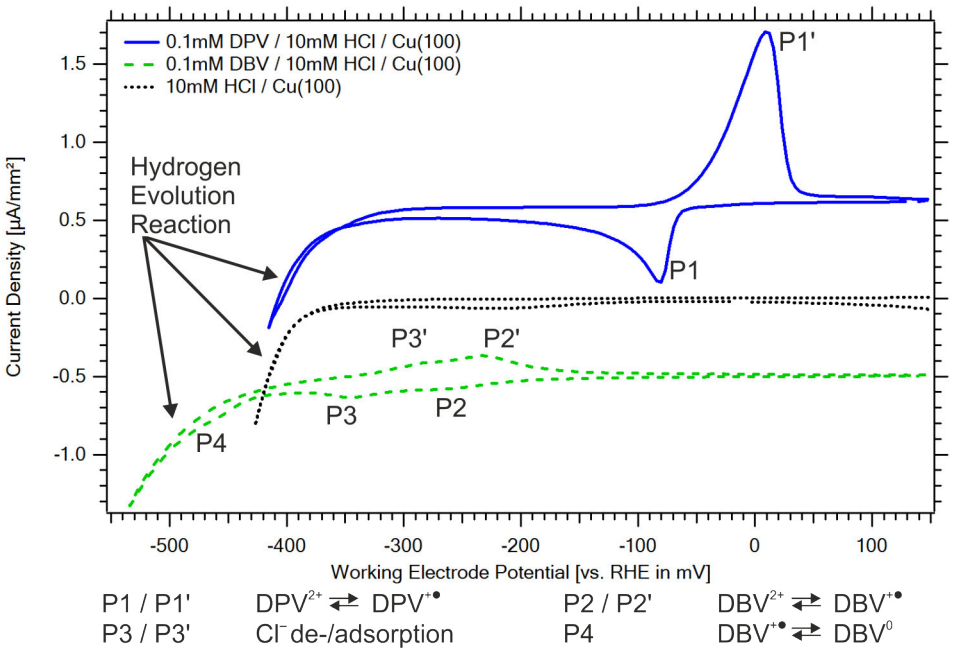

Figure 6.2: Cyclic Voltamogram (CV) registered with a Cu(100) electrode surface in three different electrolyte solutions, namely a pure 10 mM HCl solution as reference, and 0.1 mM DPV or 0.1 mM DBV containing HCl solution of the same concentration.

The DPV CV contains one dominant pair of peaks (P1/P1'), which was attributed to the first reversible electron transfer reaction from the dication DPV^{2+} to the monocation radical $DPV^{+\bullet}$ [9]. Additionally, experiments, in which several CVs with increasing negative cathodic (lower) limit were registered, revealed the existence of an *irreversible* surface process within the hydrogen evolution regime. This is concluded from an *irreversible* change of the peak shapes of P1 and P1', which occurs once the electrode potential is lowered into the hydrogen evolution regime, as proven by the three subsequently registered CV imaged in figure 6.3. Such an irreversible process was never observed for the Cu(100) electrode surface in pure 10 mM HCl solution, neither in this study nor in literature [20, 21], therefore it must be assumed that the irreversible surface process is related to the DPV molecule present at the electrode surface.

The irreversible process within the HER modifies the shape of the initially symmetric peaks P1 and P1' (fig. 6.3, 1st CV). P1 and P1' become asymmetric to their peak maximum as soon as the first CV scan reaches the HER regime (fig. 6.3, 2nd and 3rd CV). In addition, the onset of the peak P1 is shifted to more negative potentials and simultaneously the electrochemical currents rise stronger and more abruptly. Both observations, the negative shift of the onset and the abrupt rise of the reductive current of P1, indicate a passivating organic film on the electrode surface, which inhibits the reaction taking place at the potential of P1, namely the reduction of DPV^{2+} to its monocation radical $DPV^{+\bullet}$. In contrast to the reduction, the inverse reaction, namely the oxidation of $DPV^{+\bullet}$, which occurs at the peak P1', is assumed to be facilitated, as the onset of the peak P1' is shifted to more negative potentials.

The up to here stated observations point to a passivating barrier formed within the HER regime on the electrode surface, which most likely consists of the uncharged species DPV^0. Such a passivating barrier could block the redox reaction at P1, which results in a shift of the onset of P1 to more negative electrode potentials. However, when a sufficiently negative over-potential is applied the reaction may break through the passivating barrier, which results in a strong rise of the electrochemical current. In the inverse reaction, which occurs at P1', a fraction of DPV^0 could comproportionate with DPV^{2+} dications from solution, therefore facilitating the $DPV^{+\bullet}$ oxidation and increasing the $DPV^{+\bullet}$ concentration at the electrode surface. The comproportionation would not only explain the negative shift of P1', but also the sudden increase of the peak maximum of P1' upon reaching the HER regime within one CV scan (fig. 6.3, 2nd CV).

The presented interpretation of the experimental results is consistent with literature results. Bird and Kuhn [8] state that uncharged viologen species, such as DPV^0, are usually less reactive than ionic viologens. This explains the irreversibility of the CV change, which was proven to persist over the experimental time of usually several hours, although the electrode potential is increased to the most anodic (positive) potentials within the potential window of the Cu(100) surface. Further, the assumption that the second viologen reduction step lies within the HER regime is consistent to published results of various other viologen derivates [31, 5, 10].

Like the second reduction step of DPV, namely of $DPV^{+\bullet}$ to DPV^0, also the Cl anion ad-/desorption processes are, in presence of DPV in solution, assumed to occur within the HER regime. Indeed, in pure 10 mM HCl the Cl anion desorption extends from -

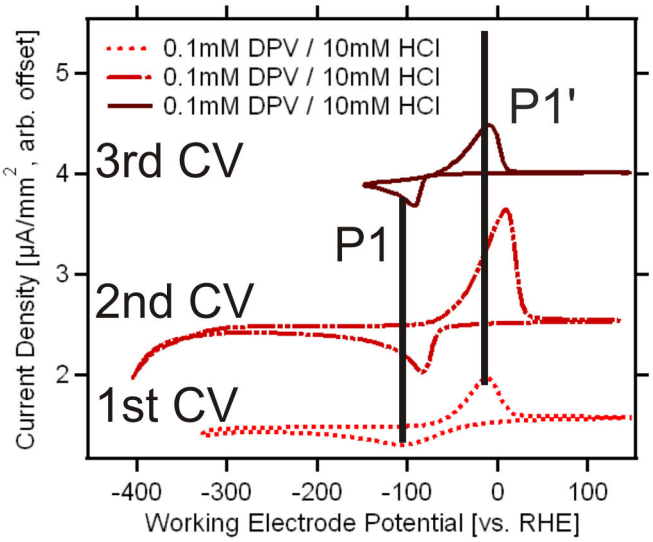

Figure 6.3: Series of three subsequently registered Cyclic Voltamogram (CV) of a Cu(100) electrode surface in 0.1 mM DPV containing 10 mM HCl solution.

150 mV [vs. RHE] till the onset of the HER, as proven via SXRD [25], and therefore leads to reductive currents in this extended potential range in the CV (fig. 6.2, central CV). In contrast to this, within the DBV CV (fig. 6.2, lower CV) the Cl anion desorption occurs close to an electrode potential of -350 mV [vs. RHE] (peak P3) [5]. However, the HER regime begins in presence of DPV at -300 mV, therefore – assuming a comparable effect of DPV and DBV on the Cl anion ad-/desorption – the weak Cl anion related current waves must be covered by the HER. Indeed, the Cl anion ad-/desorption (P3/P3') in the DBV CV is only visible due to the inhibition of the HER in presence of DBV at the electrode surface. The onset of the HER is shifted in presence of DBV by -110 mV (at a current of -0.8 $\frac{\mu A}{mm^2}$) to more negative electrode potentials compared to pure 10 mM HCl solution. In agreement with this inhibition, the exponential increase of the HER related currents is flattened, which indicates a blocking of a fraction of the active HER reaction sites on the electrode surface.

A further difference between DPV and DBV is their redox activity. DBV^{2+} dications have a lower redox reactivity, as DPV^{2+} is reduced to $DPV^{+\bullet}$ at -80 mV [vs. RHE] (peak P1), whereas the DBV^{2+} is reduced to $DBV^{+\bullet}$ at -260 mV [vs. RHE] (peak P2, fig. 6.2 [9, 5]). The additional peak P4 is attributed to the second reduction step of DBV, namely of $DBV^{+\bullet}$ to DBV^{0} [5]. This attribution of P4 is consistant with the observation, that reaching P4 leads to a rise of the peak maximum of P2' situated at -230 mV [vs. RHE] in the reverse potential sweep. Such an increase was assumed to be a result of the two different oxidation reactions, namely at first from DBV^{0} to $DBV^{+\bullet}$ and subsequently to DBV^{2+}, occurring at the same electrode potential [5]. This is only one possible explanation. Another explanation for the increase of P2' is the comproportionation between the at P2' produced DBV^{2+} dications and on the surface precipitated DBV^{0},

which might lead to an increase of the interfacial $DBV^{+\bullet}$ cation concentration and therefore increased current density at that potential. Both explanations do fit to the observations and both attribute the current wave at P4 to the reduction of $DBV^{+\bullet}$ to DBV^{0}, which is therefore the essential conclusion.

Structure of DPV and DBV Monolayers on Cl-c(2x2)/Cu(100)

The higher reactivity of DPV compared to DBV observed in the electrochemical characterization is confirmed by *in situ* STM experiments of both organic cations. The dications DPV^{2+} are upon adsorption reduced, even for the most anodic (positive) potentials within the potential window of the Cu(100) electrode, to their monocation radical $DPV^{+\bullet}$ state [9]. The reduction peak P1 at -80 mV [vs. RHE] in the DPV-CV (fig. 6.2) does therefore represent solely the reduction of the DPV^{2+} *solution* species, as proven by Breuer et al. [9]. The monocation radical $DPV^{+\bullet}$ monolayer formation is assumed to be driven by an attractive intermolecular charge transfer interaction between the molecular π-systems and results in a π-stacked stripe phase on the Cl-c(2x2)/Cu(100) electrode surface [9]. Figure 6.4c shows an STM image of the $DPV^{+\bullet}$ stripe phase and reveals a stripe distance of 1.8 (2) nm. The $DPV^{+\bullet}$ stripes are orientated parallel to the (100) and (010) Cu fcc directions, which represent the close packed rows of the underlying Cl-c(2x2) monolayer. The stripes in the STM image are composed of bright rods, where each rod is assumed to represent one bipyridinium core, which is then found to be aligned along one of the close packed directions of the Cl anion lattice. The distance between these bipyridinium cores in one stripe is, within the experimental accuracy, equal to the next neighbor distance of the Cl anion lattice of 0.36 nm [9]. The diameter of the bipyridinium core (N-N distance) is estimated to be 0.71 nm, which is almost the double Cl anion next neighbor distance of approximately 0.72 nm. These almost identical structure parameters are assumed to be the origin of strong substrate induced orientation of the $DPV^{+\bullet}$ molecules, which are aligned with their molecular axis (defined by the line connecting the pyridinium N atoms) co-linear with the close packed directions of the underlying Cl anion lattice.

The presented experimental results and available literature data [9, 13, 77] permit to derive a model of the monocation radicals $DPV^{+\bullet}$ adsorbed on the Cl-c(2x2) lattice, shown in figure 6.5. The model assumes an adsorption geometry in which the pyridinium rings are rather flat with respect to the surface. This is concluded from IRRAS results, which indicate the pyridinium ring plane and the Cl anion monolayer to enclose an angle of 28° [13, 77]. Further, the pyridinium ring planes are assumed to be parallel to each other, which is the result of DFT simulation which revealed an dihedral-angle close to zero degrees for the monocation radical $DBV^{+\bullet}$ [5].

In contrast to DPV, DBV can be stabilized on the electrode surface at high electrode potentials as dication DBV^{2+}. Four DBV^{2+} dications form on the Cl-c(2x2) lattice quadratic subunits called “cavitands”. These cavitands are repeated on the surface every 2.6 nm along directions, which are 16° off the main crystallographic directions of the Cu fcc lattice. The resulting pattern is a two dimensional repetition of cavitands, as immediately clear from the obtained STM image 6.4b. One possible model of the

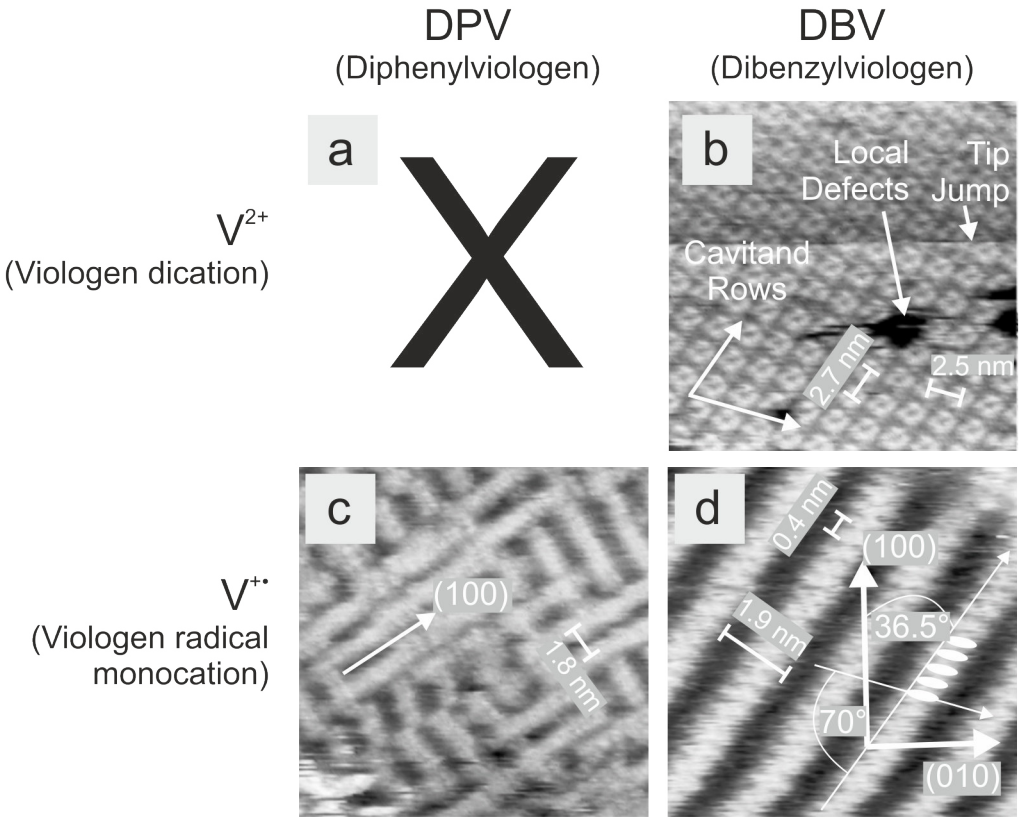

Figure 6.4: Phases of DPV and DBV on c(2x2)-Cl/Cu(100) at different electrode potentials. (a) No Dicationic DPV^{2+} phase is found within the potential window of the Cu(100) electrode surface. (b) Dicationic DBV^{2+} cavitand phase (28.4 nm x 28.4 nm, $E_{Work} = 0\ mV$, $U_{Bias} = +303\ mV$, $I_{Tunnel} = 0.45\ nA$), (c) π-stacked monocationic radical $DPV^{+\bullet}$ stripe phase (18.6 nm x 18.6 nm, $E_{Work} = +100mV$, $U_{Bias} = +100mV$, $I_{Tunnel} = 0.2nA$), (d) π-stacked monocationic radical $DBV^{+\bullet}$ stripe phase (8.8 nm x 8.8 nm, $E_{Work} = -250\ mV$, $U_{Bias} = +200\ mV$, $I_{Tunnel} = 0.4\ nA$).

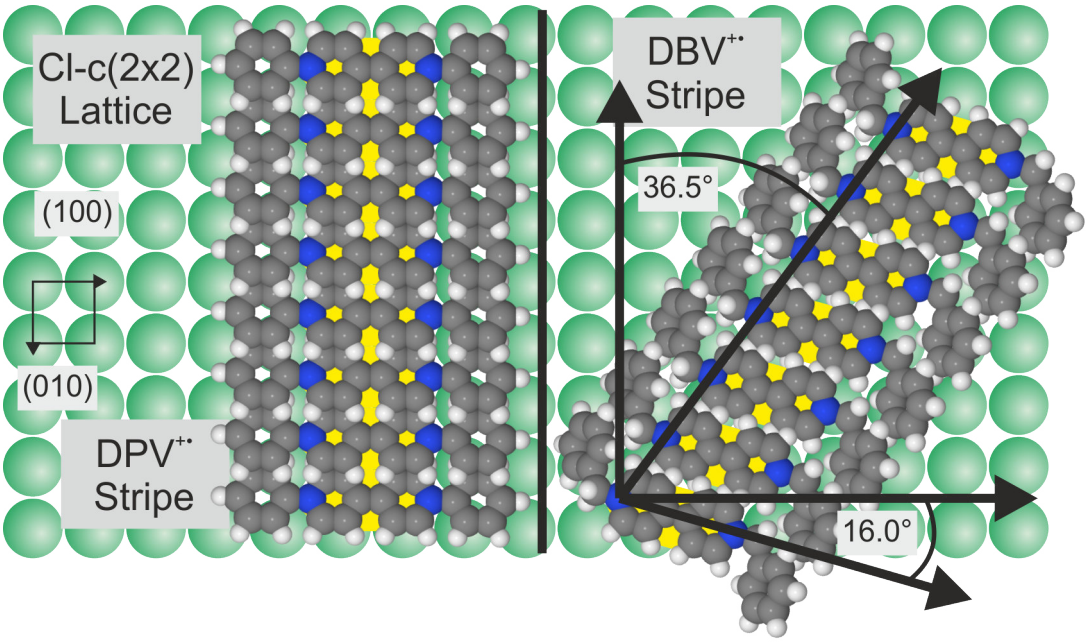

Figure 6.5: Model of the $DPV^{+\bullet}$ and $DBV^{+\bullet}$ π-stacked stripe phases adsorbed on the Cl-c(2x2) lattice. The rather flat adsorption geometry was proven in IRRAS studies of the appropriate viologen π-stacked stripe phase [13, 77], where the plane of the parallel pyridinium rings to the surface normal was proven to be 62° ($DPV^{+\bullet}$) or 75° ($DBV^{+\bullet}$).

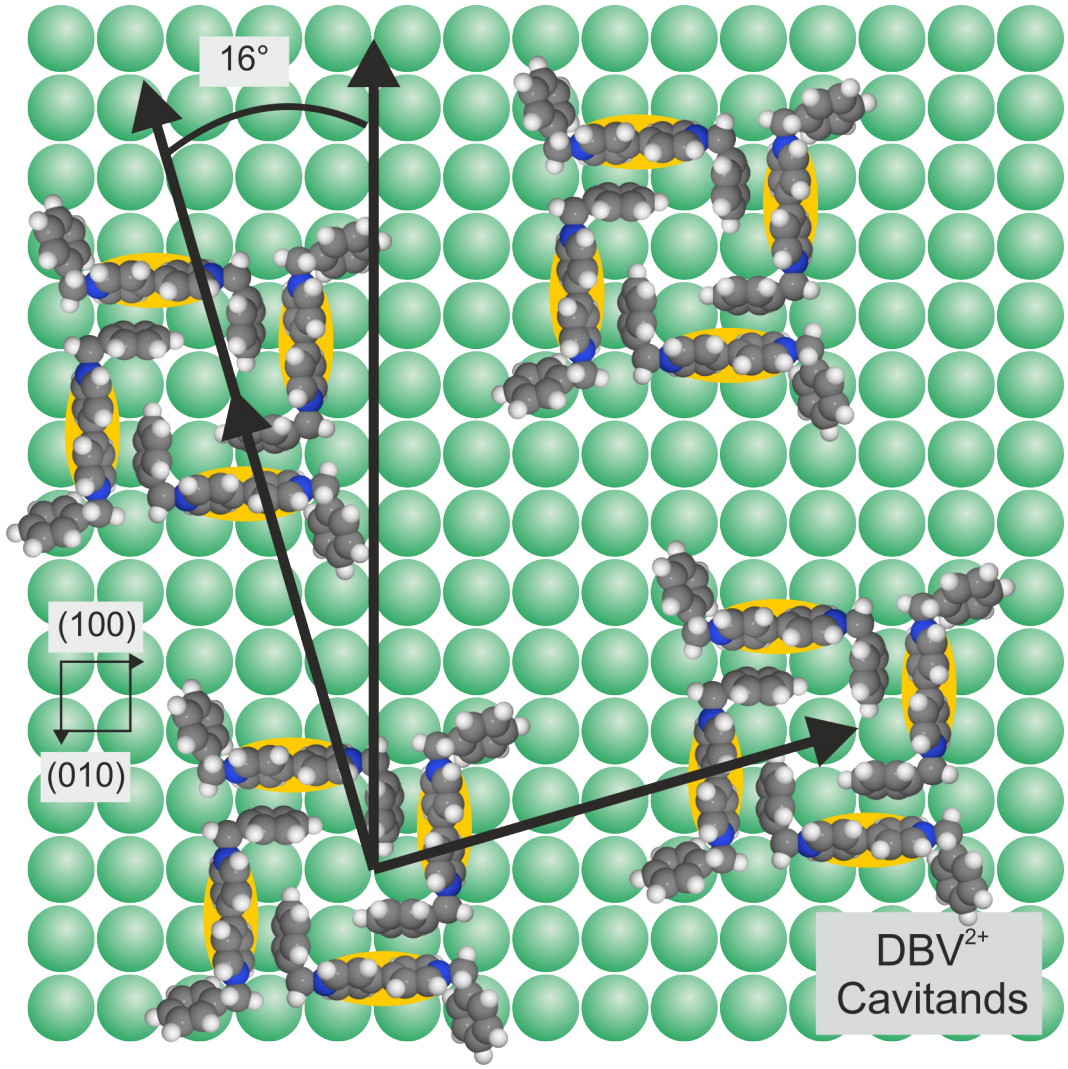

Figure 6.6: Model of the DBV^{2+} cavitand phase adsorbed on the Cl-c(2x2) lattice. This model is one possible interpretation of STM and IRRAS results [4, 77, 13, 14]. Dihedral angle of the bipyridinium core: 40° [5].

DBV^{2+} cavitand phase derived from experimental and literature results [4, 14] is imaged in figure 6.6. The model is a result of the given STM data, which provide only *intra*-layer information about the *inter*-cavitand distance of 2.6 nm, the cavitand row direction and the cavitand diameter of about 1.1 nm. The exact position of the molecules and their groups, here the bipyridinium core and benzyl groups, with respect to the Cl-c(2x2) anion lattice, is not unequivocally known.

Contrary to the rather flat arrangement of the pyridinium ring plane in the $DPV^{+\bullet}$ π-stacked stripe phase, the pyridinium rings of the DBV^{2+} dications are, in the here presented model of the cavitand phase (fig. 6.6), assumed to stand almost perpendicular to the Cl anion monolayer. Indeed, literature data suggest the pyridinium rings to enclose a dihedral-angle between their planes of 40.1° [5]. Further IRRAS results indicate the pyridinium rings to enclose an 20° angle to both sides of the Cu(100) surface normal [13, 77]. The conclusion must be an arrangement of the bipyridinium core on the Cl anion substrate, in which one pyridinium ring plane is tilted +20° and the other -20° to the surface normal as sketched in figure 6.6.

The arrangement in the cavitand structure is a result of a complex interplay of attractive adsorbate-substrate interactions and inter-adsorbate interactions. The latter are assumed to be the key factor for the quadratic arrangement of the DBV^{2+} dications in cavitand units. Assuming that exclusively the electrostatic attraction between Cl anion substrate and organic cations would govern the structure formation, then a homogenous distribution of the cation charge would be the logical consequence, as this minimizes the electrostatic repulsion between the dication bipyridinium cores. Indeed, such an homogenous distribution of the cation charge was observed for the DHV^{2+} dication (DiHeptylViologen) monolayer by Jiang et al. [10]. However, even the homogeneously distributed dications DHV^{2+} require the attractive van der Waals interaction between the DHV heptyl chains in order to form an ordered monolayer. Indeed, shorter organic chains, i.e. methyl groups, prevent the formation of an ordered DMV monolayer on the Cl/Cu(100) electrode surface [4]. This proves the relevance of the intermolecular interaction, in the structure formation process of viologen monolayers.

A detailed understanding of the intermolecular interaction between DBV^{2+} dications in the cavitand structure can not be obtained from the experimental results. Clearly electrostatic repulsion between the cationic bipyridinium cores is one contribution. This repulsive forces must be compensated by inter-molecular attraction, which initially was assumed to be the result of van der Waals like interaction between the benzyl groups. However, the investigation of the structure formation of C3-$DBDP^{2+}$ revealed another type of strong intermolecular attraction, in which the negative phenyl π-system is assumed to electrostatically interact with the pyridinium cation charge of neighboring molecules. This interaction was found to be particularly stable in the study of C3- and C7-$DBDP^{2+}$ monolayers within this work. and is therefore assumed to be relevant also in the cavitand phase formation. The resulting model of the DBV^{2+} cavitand phase is imaged in figure 6.6. In this model the pyridinium rings face directly the phenyl rings of neighboring DBV^{2+} molecules. The sketched quadratic geometry is not the only possible molecular arrangement of DBV^{2+} dications, in which pyridinium and phenly ring face each other. However, since other, e.g. linear, arrangements of DBV^{2+} dications on

the Cl/Cu(100) electrode surface were never observed in any STM experiment [5, 6, 4] other intermolecular and/or adsorbate-substrate interactions must favor the quadratic cavitand structure [1]. In order to clarify which contribution forces the quadratic arrangement of DBV^{2+}, and therefore cavitand formation, a more detailed understanding of the relation between adlayer structure and substrate is necessary.

Lowering the electrode potential from the DBV^{2+} cavitand phase regime, e.g. 0 mV [vs. RHE], to the reduction potential of DBV^{2+} at -260 mV [vs. RHE] (peak P2, fig. 6.2) reduces both DBV^{2+} species, in solution and adsorbed on the electrode surface. The reduction of adsorbed DBV^{2+} dications, which form the cavitand phase, induces the complete substitution of the cavitand phase by a full monolayer of a π-stacked stripe phase consisting of the produced monocation radicals $DBV^{+\bullet}$ (fig. 6.4d). This phase transition takes place in a "cavitand domain decay" type scenario. In this scenario the phase transition begins at defect sites of the cavitand phase, e.g. point defects or domain borders [5], where first short $DBV^{+\bullet}$ π-stacked stripes are formed. These stripes grow into the cavitand domains by favoring the reduction of neighboring DBV^{2+} molecules and subsequent rearrangement of the $DBV^{+\bullet}$ molecule.

The above discussed phase transition starts at defect sites of the cavitand phase. However, also new defects are created by the reduction of adsorbed DBV^{2+} molecules within one intact cavitand phase (intact as far STM images can prove this). At this newly created defect sites again π-stacked stripes are formed, which subsequently grow into the cavitand phase [5]. The creation of new defect sites within an intact cavitand domain is energetically less favored than the $DBV^{+\bullet}$ π-stacked stripe phase formation at existing defect sites. The first requires to reduce adsorbed DBV^{2+}, which is stabilized by undisturbed interaction to neighboring molecules of the cavitand phase. In contrast to this, the interaction of DBV^{2+} molecules to neighboring molecules is disturbed at defect sites, which results in a low activation barrier for the reduction of these adsorbed DBV^{2+} dications. Therefore the creation of new defects demands to lower the electrode potential several tens of mV below the onset of the DBV^{2+} reduction reaction, as then the overpotential permits to overcome the activation barrier more easily [5]. During the following phase transition from the DBV cavitand to the π-stacked stripe phase more monocation radicals $DBV^{+\bullet}$ must adsorb on the Cl/Cu(100) surface, due to the significant higher molecular density within the DBV stripe phase.

The $DBV^{+\bullet}$ π-stacked stripe phase formation is, as the $DPV^{+\bullet}$ π-stacked stripe phase formation, governed by the strong intermolecular interactions between the bipyridinium cores of the viologen monocation radicals [5]. In contrast to DPV-stripes, DBV-stripes do not grow along the main crystallographic directions of the Cu fcc lattice, namely (100) and (010), but are found to deviate from this directions by 37° [5]. This stripe orientation is a result of a horizontal shift between subsequent molecules, which may originating from the maximization of attractive forces between benzyl groups. The STM results further indicate the bipyridinium axis to be 16° off the close packed rows of the Cl anion lattice, which is consistent with observations in literature [5]. Summarizing

[1] First indications for a more complex cavitand structure, in which essentially more DBV^{2+} adsorb on the electrode surface were found recently by D.T. Pham [7].

all these experimental observations a model (fig. 6.5) can be obtained. The rather flat arrangement of the pyridinium rings in the model of the $DBV^{+\bullet}$ π-stacked stripe phase is a conclusion made from an IRRAS study, which proved the $DBV^{+\bullet}$ pyridinium ring plane and Cl anion monolayer to enclose an angle of only 15° [13, 77].

Summary of the Viologen Structure Formation

The comparison of the structure formation of DPV, DBV and DHV permits to identify trends, as well as distinct differences in the viologen structure formation. All three viologen monolayers are commensurable to the underlying Cl-c(2x2) anion lattice, which indicates adsorbate-substrate attraction to specific adsorption sites to be relevant in the structure formation of viologen cation monolayers. The source of the adsorbate-substrate attraction is the cationic bipyridinium core, which acts as *cationic anchor* of the viologen molecule on the Cl anion monolayer. The viologen cation anchoring is supported by the almost identical structural parameter of the substrate and the viologen molecules, namely the diameter of the bipyridinium core (N-N distance, estimated to 0.71 nm) and twice the Cl anion next neighbor distance (approximately 0.72 nm). This agreement of structural parameters of the adsorbate and substrate permits both viologen nitrogen atoms (within the pyridinium rings) to interact with equivalent adsorption sites of the Cl anion lattice, e.g. on-top, bridge or four-fold hollow sites.

In the structure formation of the viologen dication V^{2+} monolayers the *electrostatic anchoring* leads to a molecular orientation parallel to the close packed directions of the Cl lattice ([100] or [010]). Not all available adsorption sites on the Cl anion substrate are occupied, which is due to inter-adsorbate interactions. The inter-adsorbate interactions are a combination of attractive forces, such as van der Waals attraction, e.g. between heptyl chains (DHV [10]), and strong electrostatic repulsion between the dicationic bipyridinium cores and determine the inter-molecular distance between V^{2+} dications adsorbed on the electrode surface. The repulsive forces demand the bipyridinium cores to be at a maximum distance from each other, whereas the attractive forces demand the molecular "ends", namely phenyl rings or heptly chains, to be close enough to establish sufficiently strong attractive forces between them.

The relevance of the inter-adsorbate attraction in the structure formation becomes apparent, when the differing monolayer structures of DBV^{2+} and DHV^{2+} are compared. The molecular arrangement of viologens in these monolayers is a result of the inter-adsorbate attraction, as DHV^{2+} molecules adsorb within one domain of the "DHV-dot phase" only along one of the two possible closed packed directions of the Cl anion lattice [10]. This is imposed by the heptyl chains, which align co-linearly with the molecular axis (defined by the bipyridinium core) and maximize in this configuration the van der Waals attraction to neighboring DHV^{2+} molecules concomitant to a minimization of the electrostatic repulsion between the bipyridinium cores. In contrast to this, DBV^{2+} adsorbes within one domain in both possible close packed directions of the Cl anion lattice and forming therefore cavitand subunits. The experimental results indicate that the cavitand formation is a direct consequence of the presence of the benzyl groups, whose ring plane can not align co-linear to the molecular axis (defined by the bipyridinium core)

but is forced into a non-linear configuration. The type of inter-molecular interaction between adsorbed DBV^{2+} was unresolved so far, but results of the structure formation of C3-$DBDP^{2+}$ indicate that strong interactions between the negative phenyl π-systems and the positive pyridinium cation charge may also govern the structure formation of the DBV^{2+} cavitand phase. Such an interaction would require a parallel alignment of the pyridinium and phenyl ring planes of neighboring molecules, which enforces an angle of 90° between these neighboring DBV^{2+} dications and therefore finally explains the formation of DBV^{2+} cavitands. It must be pointed out that the cavitand formation is well explained by the reasoning above, but the presented arguments do not explain the absence of other DBV^{2+} phases. The latter is most likely a result of total energy minimization, in which the cavitand structure represents the energetically favored arrangement.

The role of the inter-adsorbate attraction in the viologen V^{2+} monolayer formation can be also proved by weakening them, i.e. by reducing the heptyl to a methyl group. The resulting molecule, Dimethylviologen (DMV), is forced to reduce the inter-molecular distance in order to establish significant van der Waals attraction between the methyl groups. The reduction of the inter-molecular distance increases the electrostatic repulsion between the dicationc bipyridinium cores, as the electrostatic force follows the $1/r^2$-Coulomb law. This repulsion is not compensated by the now weaker van der Waals attraction between the methyl groups, which can be concluded from the absence of any ordered DMV^{2+} monolayer on the Cl-c(2x2) substrate [4].

The previously presented electrostatic anchoring of the bipyridinium core even persists when viologen dications V^{2+} are reduced to their radical monocation state $V^{+\bullet}$. The reduction to the monocation radical $V^{+\bullet}$ is induced by lowering the electrochemical potential at the working electrode below the viologen reduction potential, e.g. $E_{work} = -270\,mV$ for DBV^{2+} and $E_{work} = -150\,mV$ for DBV^{2+} [vs. RHE] [5, 10][2]. The dicationic viologen monolayers of DBV^{2+} and DHV^{2+} undergo upon reduction to $V^{+\bullet}$ a phase transition to a π-stacked stripe phase, whereas DPV^{2+} is upon adsorption already reduced to $DPV^{+\bullet}$, even for the most positive electrode potentials in the Cu potential window, and forms therefore immediately a π-stacked stripe phase on the Cl/Cu(100) surface. The consequence is, that no DPV^{2+} phase is formed on the Cl/Cu(100) substrate and the observed reduction peak in the DPV-CV represents only the reduction of DPV^{2+} from *solution*. The persisting cationic anchoring results in viologen π-stacked stripe phases, which are all commensurable to the underlying Cl anion substrate [5, 9, 10].

Contrary to the electrostatic anchoring, which is preserved upon reduction of the viologen dications V^{2+}, the inter-adsorbate interactions are strongly modified by the viologen reduction. The previously strong electrostatic repulsion between the dicationic bipyridinium core of V^{2+} is upon reduction replaced by an attractive interaction between the monocation radicals $V^{+\bullet}$, which is assumed to be the result of charge transfers aiming at stabilizing the unpaired (radical) electron by a π-system overlap of neighboring $V^{+\bullet}$ in a face-to-face conformation of the radical bipyridinium cores [5, 6, 7]. This is

[2]The reduction potentials of viologen dications were proven to depend on the viologen ligand groups and therefore differ between DPV^{2+}, DBV^{2+} and DHV^{2+} [31].

derived from the small next neighbor distance and direct neighboring of monocationic radical bipyridinium cores within one π-stacked stripes, which is exactly (for $DPV^{+\bullet}$ and $DBV^{+\bullet}$ stripes) or slightly below (for $DHV^{+\bullet}$ stripes) the Cl anion next neighbor distance of 0.36 nm. Although all viologen monocation radicals form π-stacked stripes, their monolayers are easily distinguishable due to their stripe orientation to the underlying Cl anion substrate and therefore to the Cu steps. Furthermore, the $DPV^{+\bullet}$ stripes growing along the main crystallographic directions of the Cu fcc crystal (= Cl close packed directions) stabilize the Cu steps, whereas $DBV^{+\bullet}$ stripes growing with 36.5° off the main crystallographic directions induce a reconstruction of the Cu steps, as will be discussed in the next section of this work, in which the competition for adsorption sites of DPV and DBV is studied.

6.1.2 Competition of DBV and DPV at the Solid/Liquid Interface

The study of individual viologen derivates, as model building blocks, revealed the formation of ordered monolayers on the Cl/Cu(100) electrode surface [4, 5, 6, 10, 9]. These viologen derivates possess a high electrochemical activity [8], which permits to reduce viologen dications to their monocation radical state (and vice versa) by applying the appropriate electrochemical potential to the Cu(100) electrode. Both, viologens in solution or adsorbed on the electrode surface, can be oxidized/reduced if the proper electrochemical potential is applied. Changing the molecular redox state strongly alters the interadsorbate and adsorbate-substrate interactions and therefore induces phase transitions of the ordered viologen monolayer on the Cl/Cu(100) surface. This remarkable result proves that the *microscopic* molecular redox state of viologens and the *microscopic* structure of the ordered viologen monolayer can be controlled, within the limits of the molecular self-organization, by a *macroscopic* experimental parameter, namely the electrochemical potential applied to copper electrode.

The cited studies [4, 5, 6, 10, 9] limited their investigations to one viologen building block at a time at the Cl/Cu(100) electrode surface. In order to expand the microscopic understanding of the structure formation of these model building blocks to more complex multi-component systems additional studies are necessary. The logic step to approach multi-component systems is to study the co-adsoprtion of two viologen building blocks at the Cl/Cu(100) electrode surface. Therefore the Cl/Cu(100) electrode surface was exposed to a 10 mM HCl solution containing both – individually well characterized –, DPV^{2+} and DBV^{2+}, building blocks [4, 5, 6, 9].

Electrochemical Characterization

Redox-active viologen molecules are introduced into the solid/liquid interface by exchanging the pure 10 mM HCl electrolyte solution under potential control by a solution containing additionally the viologen dications DPV^{2+} and DBV^{2+} in a 1:1 ratio. Introducing this redox-active viologens into the electrolyte lead to a number of additional peaks, P1 to P5, and related counter-peaks, P1' to P4', appearing in the CV (fig. 6.7). The CV of the mixed DPV-DBV systems (fig. 6.7, central CV) is for electrode potentials

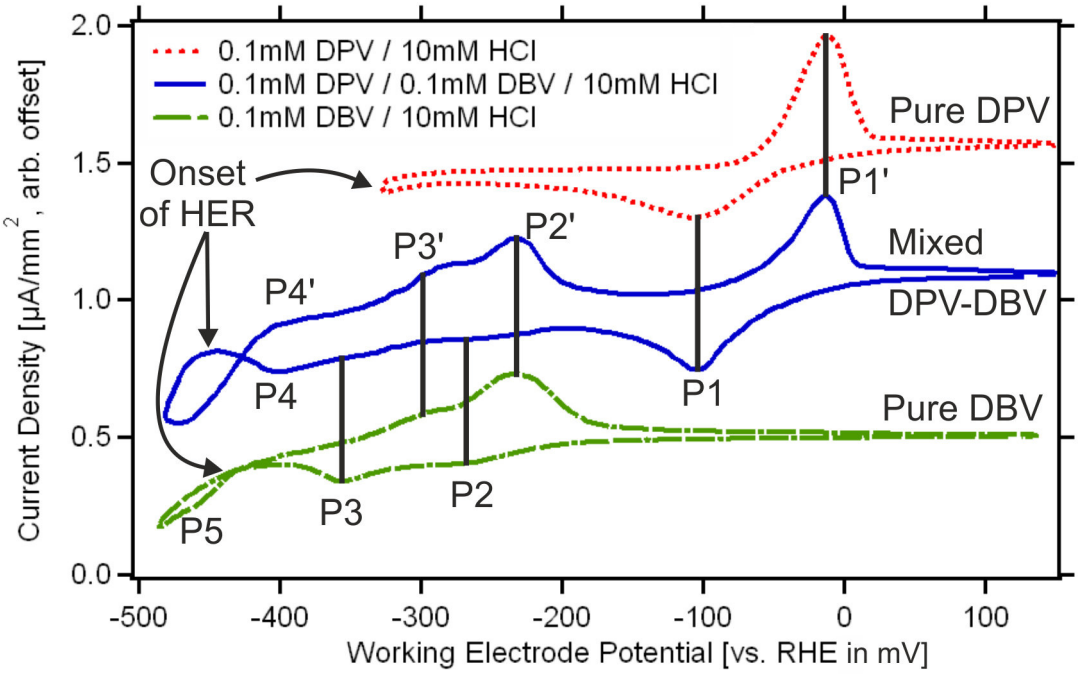

Figure 6.7: Comparison of the voltammetric behavior of a 0.1 mM DPV^{2+}, 0.1 mM DBV^{2+} and 0.1 mM DPV^{2+} + 0.1 mM DBV^{2+} in 10 mM HCl solution, at Cl/Cu(100) electrode.

E_{work} above -400 mV [vs. RHE] essentially the superposition of the current waves (= peaks) appearing in the individual study of DPV (fig. 6.7, upper CV) or DBV (fig. 6.7, lower CV) [5, 9]. The attribution of surface processes to current waves is based on the later presented experimental results and the published works studying DPV or DBV solutions [5, 4, 9]. Based on the available experimental results it can be concluded with high certainty that the peak pair P1/P1' at -100 mV / -12 mV [vs. RHE] represents the first redox step of DPV, namely $DPV^{2+} + e^- \rightleftharpoons DPV^{+\bullet}$ [9]. In agreement to literature [4, 5, 6], the peak pair P2/P2' at -267 mV / -231 mV [vs. RHE] represents the first redox step of DBV, namely $DBV^{2+} + e^- \rightleftharpoons DBV^{+\bullet}$. The reduction of DBV^{2+} results, as proven before, in the formation of a $DBV^{+\bullet}$ π-stacked stripe phase on the Cl/Cu(100) electrode surface, which remains valid in the mixed viologen system (see next sub-section). Lowering the electrode potential to P3 at -355 mV [vs. RHE] induces an order-disorder transition of the adsorbed $DBV^{+\bullet}$ π-stacked stripe phase, which is a result of the desorption of Cl anions situated underneath the $DBV^{+\bullet}$ π-stacked stripes [6]. A subsequent increase of the electrode potential to P3' at -285 mV [vs. RHE] permits the readsorption of Cl anions and therefore the amorphous viologen phase reorders and forms the initial $DBV^{+\bullet}$ π-stacked stripe phase.

In contrast to this clear attribution between surface processes observed via STM and current waves in the CV, the identification of surface processes at potentials of -400 mV [vs. RHE] and lower are less certain. For instance, the shape of the CV related to the mixed DPV-DBV solution differs for potentials lower than $E_{work} <$ -420 mV [vs. RHE] from the shape of the CV related to the pure DBV solution. In the pure DBV solution the HER is inhibited, which results in a shift of the HER by about -100 mV to lower electrode potentials and a damping of its exponentially rising currents compared to pure 10 mM HCl solution (in agreement to Pham et al. [5]). The damped exponential shape of the HER appears in both, the cathodic and subsequent anodic, potential sweeps, which indicates a blocking of the hydrogen evolution reaction, by a stable interaction between adsorbed $DBV^{+\bullet}$ and the HER reaction sites.

The onset of the HER in the CV of Cu(100) in the mixed DPV-DBV solution is also shifted to more negative electrode potentials. However, no damping of the exponentially rising HER currents occurs. In addition, in the anodic potential sweep of the mixed DPV-DBV CV the HER currents are upon reveral of the scan direction at first independent of the applied electrode potentials. If, in the anodic potential sweep, the electrode potential is sufficiently increased, the HER currents follow again the expected exponential curve. This reaction of the electrochemical current to a change of the applied electrode potential points to a layer formation, which passivates the electrode surface by inhibiting the HER. Applying a sufficiently strong over-potential at the electrode permits the onset of the HER despite the passivating layer on the Cu(100) surface. Sufficiently strong HER currents are then assumed to lead to a removal of the passivating layer from the electrode surface. The HER currents are in the reverse anodic potential sweep at first weakly affected by an increase of the electrode potentials, which is a result of the applied over-potential. A further increase of the electrode potential cancels the over-potential and subsequently the HER currents follow again an exponential curve as a function of the applied electrode potential.

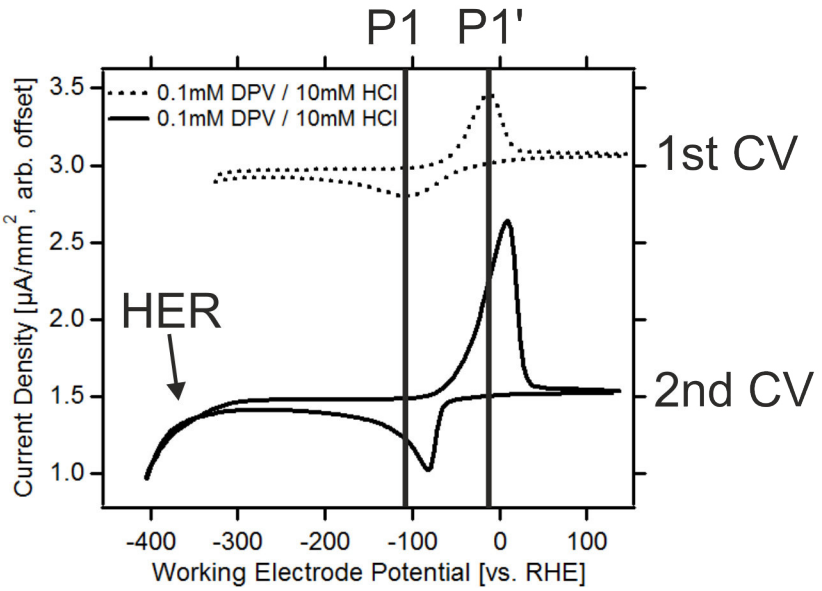

Figure 6.8: Irreversible change of the current wave pair P1/P1' at the Cu(100) electrode in DPV containing solution [0.1mM DPVCl2 + 10mM HCl], when lowering the working potential into the hydrogen evolution regime.

Comparing the CV of the pure DBV and the mixed DPV-DBV system it can be concluded that the passivating layer is caused by DPV (most likely by the uncharged DPV^0). Indeed, in the study of Cu(100) in a pure DPV solution a similar passivating layer had to be assumed to form on the electrode surface, as the study revealed an irreversible change of the CV shape upon reaching the HER regime. This irreversible change is visible through its effect on the peak pair P1/P1', as imaged in figure 6.8 and discussed in section 6.1.1. Lowering the electrode potential into the hydrogen evolution regime results in a drastic increase of P1' and an asymmetrically shaped peak P1. Although a passivating layer of DPV^0 is assumed to be responsible for the observations made in the study of DPV, this can not be proven directly due to the overlay of the second viologen reduction step and the HER regime. However, in the study of the mixed DPV-DBV solution the onset of the HER is shifted to lower electrode potentials, which reveals an additional pair of peaks P4/P4' at -400 mV [vs. RHE] in the CV (fig. 6.7, central CV). This pair of peaks does not appear in the CV related to the pure DBV system and therefore this peak pair is attributed to the reduction of $DPV^{+\bullet}$ to the uncharged DPV^0.

Although the presented interpretation of the experimental results explains the observations made, some uncertainty remains. For instance, P4 is assumed to represent the hidden process appearing in the study of the pure DPV solution, but in contrast to the pure DPV solution in the mixed DPV-DBV system no effect of P4 on the shape of P1/P1' is observed. This could be, however, explained by the presence of DBV, which is via STM proven to remove adsorbed DPV from the electrode surface upon forma-

tion of the $DBV^{+\bullet}$ π-stacked stripe phase. As the $DBV^{+\bullet}$ π-stacked stripe formation lies on the potential scale between P4/P4' and P1/P1' it might remove the remaining parts of the passivating layer. However, a definitive determination lacks a more detailed understanding of the related DPV surface processes.

A second difference between the single viologen and the mixed viologen system is the vanishing of the peak P5, which was attributed to the reduction of $DBV^{+\bullet}$ to the uncharged DBV^0 [5]. It might be that this process is in the mixed study covered by the stronger increase of the exponential HER currents. However, in the study of the pure DBV solution a rise of the peak P2' was observed upon reaching P5 [5]. This was attributed to a superposition of both oxidation steps, from the uncharged to the monocation radical and from the monocation radical to the dication DBV. However, it can not be excluded that the rise of P2' results from the comproportionation $DBV^0 + DBV^{2+} \rightleftharpoons 2DBV^{+\bullet}$, which increases the concentration of the monocation radical $DBV^{+\bullet}$ and therefore of the peak P2'.

This second possible reaction is relevant, as in the study of the mixed DPV-DBV solution a rise of the peak P2' is observed upon reaching the peak P4. Therefore either the previous interpretation was wrong, and P4 is, indeed, peak P5 shifted to higher electrode potentials, or another process/reaction leads to the same increase of P2'. Assuming the comproportionation to be the right interpretation in the study of the pure DBV solution, then the increase of P2' might result from the following reaction $DPV^0 + DBV^{2+} \rightleftharpoons DBV^{+\bullet} + DPV^{+\bullet}$, in which DPV^0 takes the place of DBV^0. P4 would then represent the reduction of $DPV^{+\bullet}$. However, in order to verify the assumptions additional studies are necessary.

Adlayer Formation on the Cl-c(2x2)/Cu(100)

Exposing the Cu(100) electrode at $E_{work} = 0\,mV$ [vs. RHE] to the mixed DPV-DBV solution, namely [0.1 mM DPVCl2 + 0.1 mM DBVCl2 + 10 mM HCl], leads to the adsorption and instant reduction of the dication DPV^{2+} to the monocation radical $DPV^{+\bullet}$ even for potentials more anodic (higher) than the reduction potential of DPV^{2+} solution species. The adsorbed monocation radical $DPV^{+\bullet}$ forms on the Cl/Cu(100) substrate a full monolayer of a π-stacked stripe phase, as imaged in figure 6.9a. The bipyridinium core of DPV appears in the highly resolved STM image as two bright spots (see red arrows), which are alignd in rows and therefore form the $DPV^{+\bullet}$ π-stacked stripes.

The structure parameter of this $DPV^{+\bullet}$ π-stacked stripes are equal, within the experimental accuracy, to those of the $DPV^{+\bullet}$ π-stacked stripes formed on Cu(100) in the pure DPV solution [9]. This includes the stripe distance of 1.9 nm, the distance of 0.36 nm between consecutive $DPV^{+\bullet}$ molecules within one π-stacked stripe and finally the stripe orientation, which is parallel to the close packed directions of the Cl anion monolayer. Therefore it is concluded that DBV^{2+}, although present at the solid/liquid interface, does not interfere with the structure formation of the monocation radicals $DPV^{+\bullet}$. More importantly, the absence of the DBV^{2+} cavitand phase (fig. 6.9c) on the Cl/Cu(100) electrode surface, which usually is formed by DBV^{2+} at $E_{work} = 0\,mV$

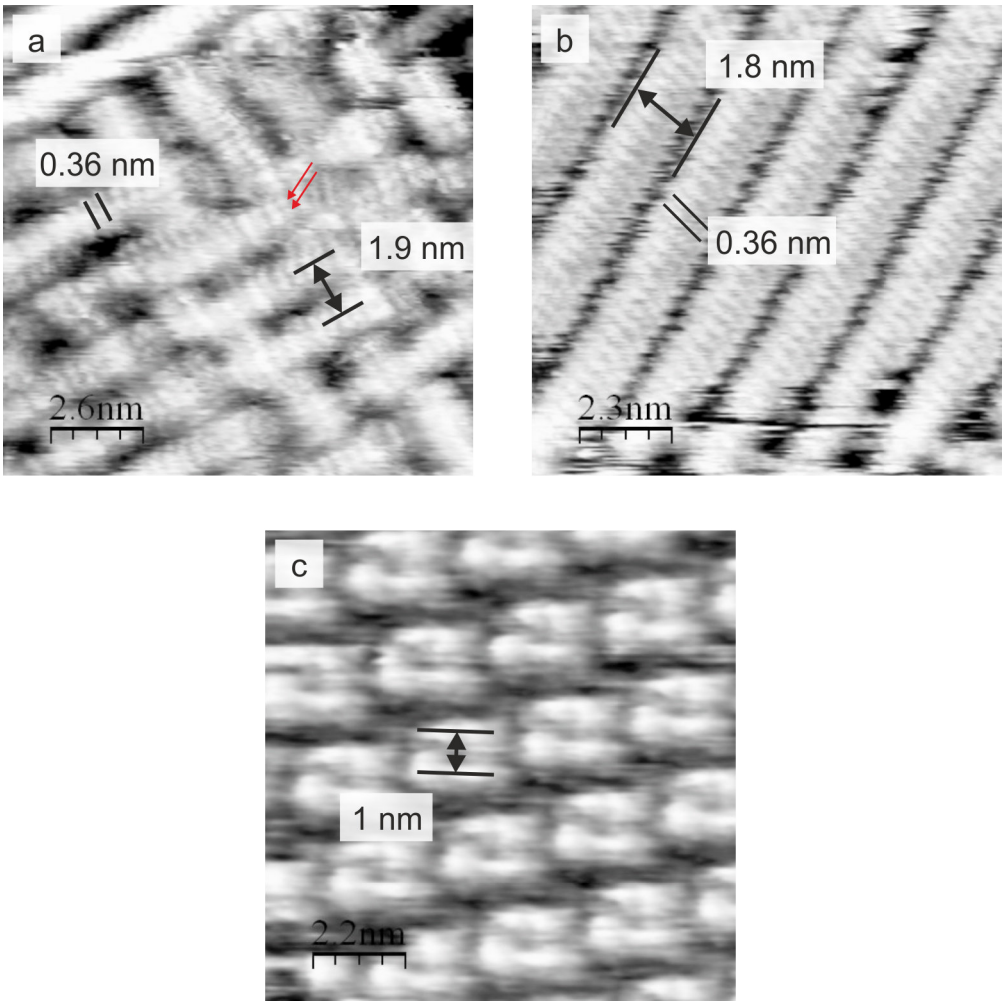

Figure 6.9: Highly resolved monocationic (a,b) and dicationic (c) viologen phases. Measured dimensions agree within their experimental accuracy of ±0.2 nm with previous works [9, 5]. (a) $DPV^{+\bullet}$ π-stacked stripe phase on Cl/Cu(100), 12.8 nm x 12.8 nm, $U_{Bias} = +150\,mV$, $I_{Tunnel} = 0.1\,nA$, $E_{Work} = +100\,mV$ [vs. RHE]. (b) $DBV^{+\bullet}$ π-stacked stripe phase on Cl/Cu(100), 11.3 nm x 11.3 nm, $U_{Bias} = +164\,mV$, $I_{Tunnel} = 0.1\,nA$, $E_{Work} = -300\,mV$ [vs. RHE] (c) DBV^{2+} cavitand phase on Cl/Cu(100), 10.9 nm x 10.9 nm, $U_{Bias} = -113\,mV$, $I_{Tunnel} = 0.1\,nA$, $E_{Work} = 0\,mV$ [vs. RHE].

[vs. RHE] [4, 5] proves the $DPV^{+\bullet}$ π-stacked stripes to be the energetically favored arrangement.

Lowering the electrode potential of the with $DPV^{+\bullet}$ π-stacked stripes covered Cl-c(2x2)/Cu(100) electrode from $E_{work} = +100\,mV$ [vs. RHE] to the DBV^{2+} reduction potential at $E_{work} = -250\,mV$ [vs. RHE] (peak P2 in fig. 6.7) leads to the replacement of the existing $DPV^{+\bullet}$ π-stacked stripe phase by a $DBV^{+\bullet}$ π-stacked stripe phase (fig. 6.10). This proves, that the adsorbed $DPV^{+\bullet}$ π-stacked stripe phase does not prevent the reduction of the DBV^{2+} dications at the electrode surface to take place. The nucleation centers for the phase transition process are domain boundaries, as well as defect sites within the $DPV^{+\bullet}$ π-stacked stripe phase, which are marked by black circles in figure 6.10b.

The correlation of STM and CV results prove that the $DBV^{+\bullet}$ π-stacked stripe phase is significantly more stable than the $DPV^{+\bullet}$ π-stacked stripe, as the phase substitution takes place instantaneously upon formation of the monocation radical $DBV^{+\bullet}$. The rate of the phase transition from a $DPV^{+\bullet}$ π-stacked stripe to a $DBV^{+\bullet}$ π-stacked stripe phase depends on the redox reaction rate, as was proven by applying a more negative over-potential, which accelerated the phase transition process.

The replaced $DPV^{+\bullet}$ π-stacked stripe is distinguished from the stronger adsorbing $DBV^{+\bullet}$ π-stacked stripes by the angle in which the stripes grow relative to the substrate lattice (fig. 6.10a and f). Further the monocation radical $DPV^{+\bullet}$ arranges along the Cu (100) and (010) steps mostly in long stripes (longer than 30 nm) but within the Cu terraces $DPV^{+\bullet}$ arranges only in short stripes (shorter than 20 nm) (fig. 6.10a). In contrast to this behaviour of $DPV^{+\bullet}$, $DBV^{+\bullet}$ species form after a post-adsorption ripening process long stripes, which are only limited by the Cu terrace boarders as they extend over the whole Cu terraces.

As for the $DPV^{+\bullet}$ phase, the structure parameters of the $DBV^{+\bullet}$ π-stacked stripe phase formed in the mixed DPV-DBV solution on the elecctrode (fig. 6.9b) are comparable with those formed in the pure DBV solution on the electrode [5]. The monocation radical $DBV^{+\bullet}$ arranges in both phases in stripe structures, as shown in the highly resolved STM picture (fig. 6.9b). The monocation radical $DBV^{+\bullet}$ is imaged as bright rod-like element with an intermolecular distance of 0.36 nm within one π-stacked stripe and a stripe distance of 1.8 nm. The stripes are oriented 33° off the close packed directions of the Cl anion lattice (fig. 6.10f and [4, 5]). Therefore it can be concluded that the $DBV^{+\bullet}$ π-stacked stripe phase formed on the Cl/Cu(100) electrode in the mixed DPV-DBV solution is equal to that formed in pure DBV solution. Although the monocation radical $DPV^{+\bullet}$ is present at the solid/liquid interface it does not interfere in a way which modifies the observed $DBV^{+\bullet}$ adlayer on the Cl/Cu(100) electrode surface.

The substitution of the $DPV^{+\bullet}$ π-stacked stripe phase by the $DBV^{+\bullet}$ π-stacked stripe phase proves the latter to be an energetically more favored arrangement on the Cl/Cu(100) electrode surface below -250 mV. This is assumed to be independent of the applied electrode potential, as IRRAS experiments proved the binding strength of the DPV and DBV to the chloride adlayer to be unaffected by a potential change [13, 77]. This is in agreement with the potential dependent study of the $DBV^{+\bullet}$ π-stacked stripe phase, which is stable on the Cl/Cu(100) electrode surface up to electrode potentials of -100 mV [vs.

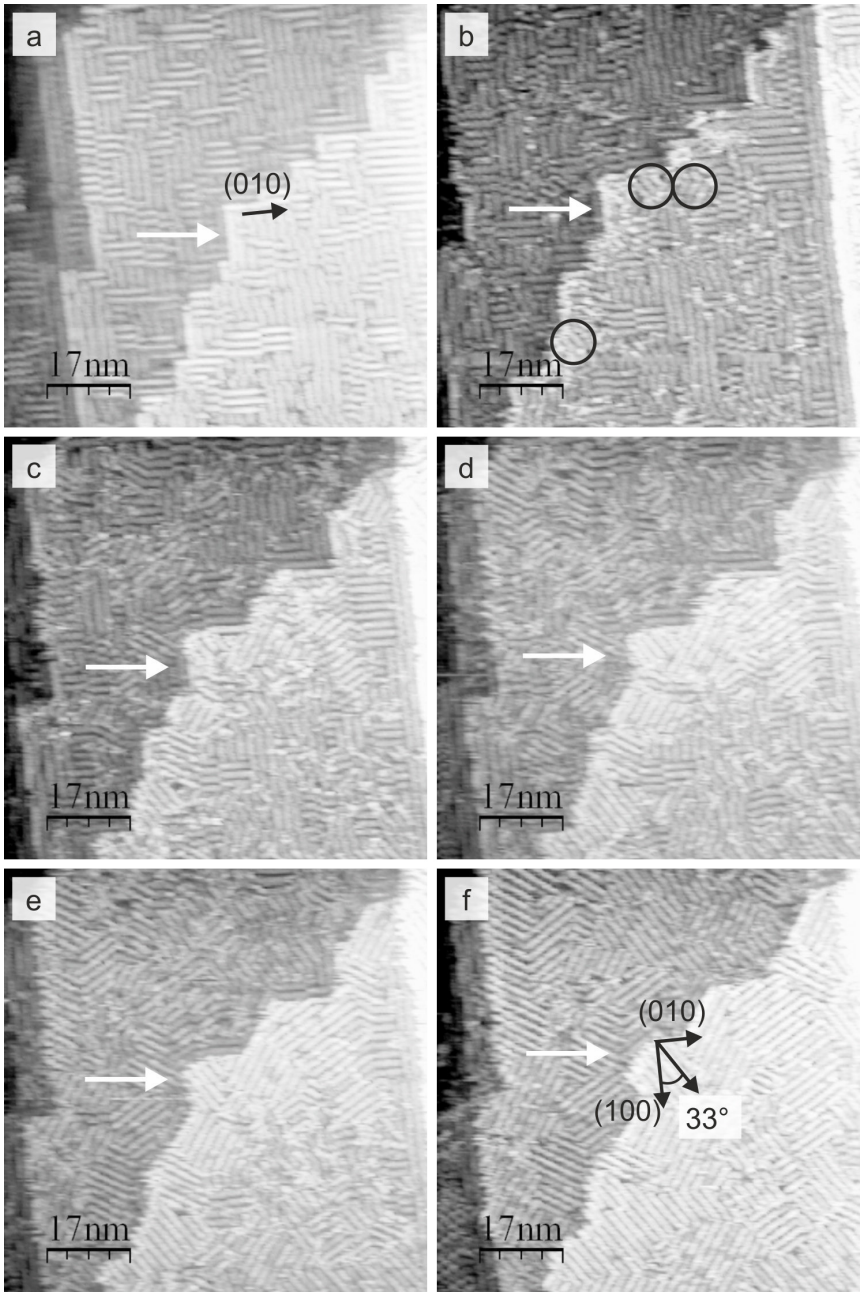

Figure 6.10: Phase transition from a full monolayer of a $DPV^{+\bullet}$ π-stacked stripe phase (a) to a full monolayer of a $DBV^{+\bullet}$ π-stacked stripe phase (f). White arrow marks a constant position in all images throughout the phase transition. (a - f) 86.4 nm x 86.4 nm, $I_{Tunnel} = 0.5\,nA$. (a) $DPV^{+\bullet}$ π-stacked stripe phase, $U_{Bias} = +250\,mV$, $E_{Work} = +100\,mV$ [vs. RHE]. (b) Onset of phase transition marked by black circles, $U_{Bias} = +235\,mV$, $E_{Work} = -250\,mV$ [vs. RHE]. (c) $U_{Bias} = +235\,mV$, $E_{Work} = -270\,mV$ [vs. RHE]. (d) $U_{Bias} = +166\,mV$, $E_{Work} = -270\,mV$ [vs. RHE]. (e) $U_{Bias} = +166\,mV$, $E_{Work} = -270\,mV$ [vs. RHE]. (f) $DBV^{+\bullet}$ π-stacked stripe phase, $U_{Bias} = +235\,mV$, $E_{Work} = -300\,mV$ [vs. RHE].

RHE]. For potentials higher than -100 mV [vs. RHE] the adsorbed monocation radicals $DBV^{+\bullet}$ are oxidized. Subsequently to the oxidation of $DBV^{+\bullet}$ to DBV^{2+} the dications are substituted on the Cl/Cu(100) electrode surface by the adsorption of the monocation radical $DPV^{+\bullet}$, which forms again its π-stacked stripe phase. This leads to a vanishing of $DBV^{+\bullet}$ π-stacked stripe domains in favor of $DPV^{+\bullet}$ π-stacked stripe domains.

As stated, the oxidation of the solution species of $DBV^{+\bullet}$ occurs at -230 mV [vs. RHE], whereas adsorbed $DBV^{+\bullet}$ is oxidized at -100 mV [vs. RHE]. This more positive oxidation potential of adsorbed $DBV^{+\bullet}$ must result from the stabilizing effect due to the interaction to neighboring monocation radical $DBV^{+\bullet}$ of the π-stacked stripe structure on the Cl/Cu(100) substrate. Indeed, the oxidation of adsorbed $DBV^{+\bullet}$ requires to break the intermolecular bond between the radical π-systems and the bond to the substrate surface, which requires additional energy and therefore occurs at more positive electrode potentials. The lower redox activity of adsorbed $DBV^{+\bullet}$, compared to its solution species, is consistent with the redox activity of adsorbed $DPV^{+\bullet}$, which forms also a stable $DPV^{+\bullet}$ π-stacked stripe phase even for potentials more positive than the oxidation potential of $DPV^{+\bullet}$ in solution.

Comparing the Cu steps imaged in various STM images of figures 6.10 reveal the reconstruction of the Cu steps upon formation of the $DBV^{+\bullet}$ π-stacked stripe phase. The Cu steps rearrange parallel to the $DBV^{+\bullet}$ stripe orientation, consistent with the observations in literature [5].

Lowering the electrode potential to $E_{work} = -370\,mV$ [vs. RHE] induces the desorption of the Cl anion monolayer through the close packed $DBV^{+\bullet}$ π-stacked stripe phase (not shown here), as reported to occur in pure DBV solution as well [6]. The Cl anion desorption induces an order-disorder transition from the $DBV^{+\bullet}$ π-stacked stripe phase to an amorphous viologen layer. The composition of this amorphous viologen layer is unproved yet, as besides $DBV^{+\bullet}$ also $DPV^{+\bullet}$ may adsorb on the bare Cu(100) electrode surface. The order-disorder transition of the $DBV^{+\bullet}$ π-stacked stripe phase is reversible, as increasing the potential to $E_{work} = -250\,mV$ [vs. RHE] leads to a re-adsorption and formation of the Cl-c(2x2) anion layer and subsequent formation of the $DBV^{+\bullet}$ π-stacked stripe phase on the Cl/Cu(100) electrode surface.

Figure 6.11 visualizes the experimental results of the STM study of the Cu(100) electrode in a mixed DPV-DBV and pure DPV / pure DBV containing 10 mM HCl solution.

6.2 Role of the Bipyridinium Core on the Structure Formation

The results of the viologen monolayer formation raises the question: "How do modifications of the molecular building blocks – in general – affect the monolayer structure formation?" Previous works investigated mainly the role of the viologen substituents by exchanging them with other functional groups [5, 7, 10, 9]. Instead of modifying or adding functional groups, in this work the focus lies on preserving the given functional groups but arranging them differently to each other or separating them, to allow a freer arrangement on the Cl/Cu(100) substrate. The studied molecules are no longer part

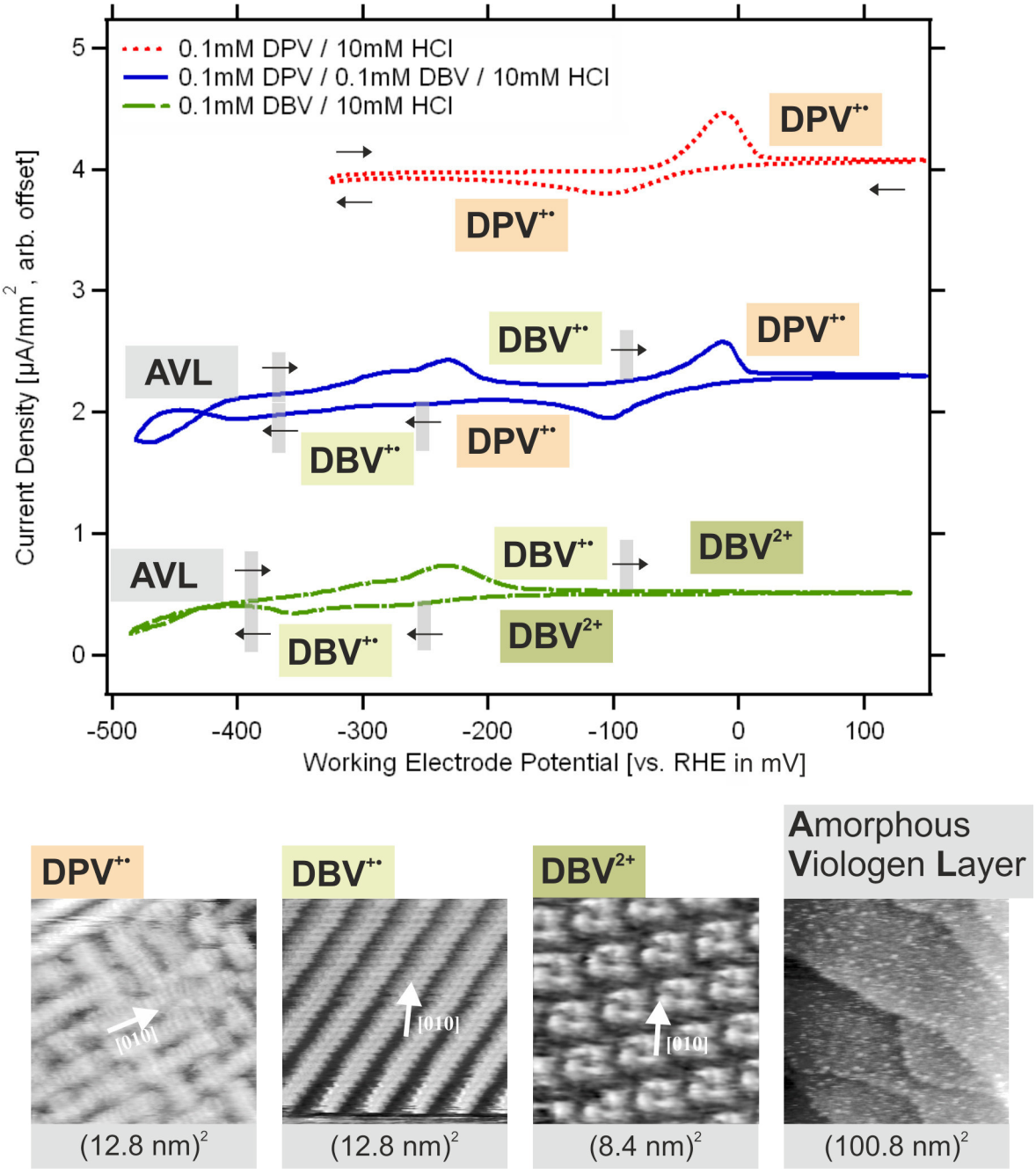

Figure 6.11: Overview of the potential depended formation of DPV or DBV adlayers on the Cl/Cu(100) electrode surface. Scan speed 10 mV/sec.

of the viologen family, which permits to elaborate a more general understanding of the structure formation of pyridinium containing molecular building blocks.

The starting point of this study is the DBV molecule, which consists of two pyridinium benzyl moieties arranged symmetrically to the 4,4-connection of the bipyridinium core as presented in the introduction and imaged in the reprinted figure 6.12 (for convenience of the reader the image 1.3 is reprinted here as figure 6.12). The first modification, which will be presented, is the substitution of the 4,4'-connection of the DBV bipyridinium core to a 3,3'-connection. This results in the molecule DB-3,3'-BP (1,1´-Dibenzyl-3,3´-bipyridinium), which consists of exactly the same number of (carbon, nitrogen, hydrogen) atoms and number of functional groups as DBV, but sterically differs significantly due to the position of the benzyl groups with respect to the bipyridinium core and the molecular axis.

The second and third investigated modification is the separation of the two pyridinium-benzyl moieties (see fig. 6.12) by the introduction of a three carbon long propane-1,3-diyl or seven carbon long heptane-1,7-diyl chain between the two pyridinium rings, which results in C3-DBDP (1,1'-Dibenzyl-4,4'-(propane-1,3-diyl)dipyridinium) or C7-DBDP (1,1'-Dibenzyl-4,4'-(heptane-1,7-diyl)dipyridinium), respectively. This second and third modification permits to investigate the role of the molecular flexibility in the structure formation process of organic monolayers. The longer the organic chain between the pyridinium rings, the higher the molecular flexibility, which permits the pyridinium benzyl moieties to more freely respond to the various forces in the adsorption process on the Cl/Cu(100) surface.

6.2.1 DB-3,3'-BP as Building Block

Electrochemical Characterization

Figure 6.13 shows the CV curves of 10 mM HCl with and without 1 mM DB-3,3'-BP^{2+} dications in the solution. The concentration of 1 mM DB-3,3'-BP^{2+} dications was chosen exemplarily but in non of the registered CV, at concentrations of DB-3,3'-BP^{2+} between 0.01 mM to 10 mM, a redox peak was observed. The absence of a redox peak as well as the absence of a continuous electrochemical current (constant offset signal) indicates that the reduction of the DB-3,3'-BP^{2+} dications is shifted out of the Cu(100) potential window, to potentials beyond the onset of the HER. In comparison to viologen dications, DB-3,3'-BP^{2+} is less reactive and therefore more stable in its dication state.

Comparing both CVs in figure 6.13 further reveals that neither the HER nor the Cl desorption are significantly affected by the presence of DB-3,3'-BP^{2+}, at least as far as can be concluded within the resolution of the CV experiments. Indeed, a small shift of -9 mV between the HER in presence or absence of DB-3,3'-BP^{2+} can be observed, but no significant change in the exponential increase of the HER current. The small shift by -9 mV is insufficient to decided whether the offset is related to the presence of DB-3,3'-BP^{2+}, as it might also result from changes in the topology of the Cu(100) electrode surface induced by repetitive cycling.

The Cl c(2x2) monolayer desorption signal is superimposed by a reductive (negative)

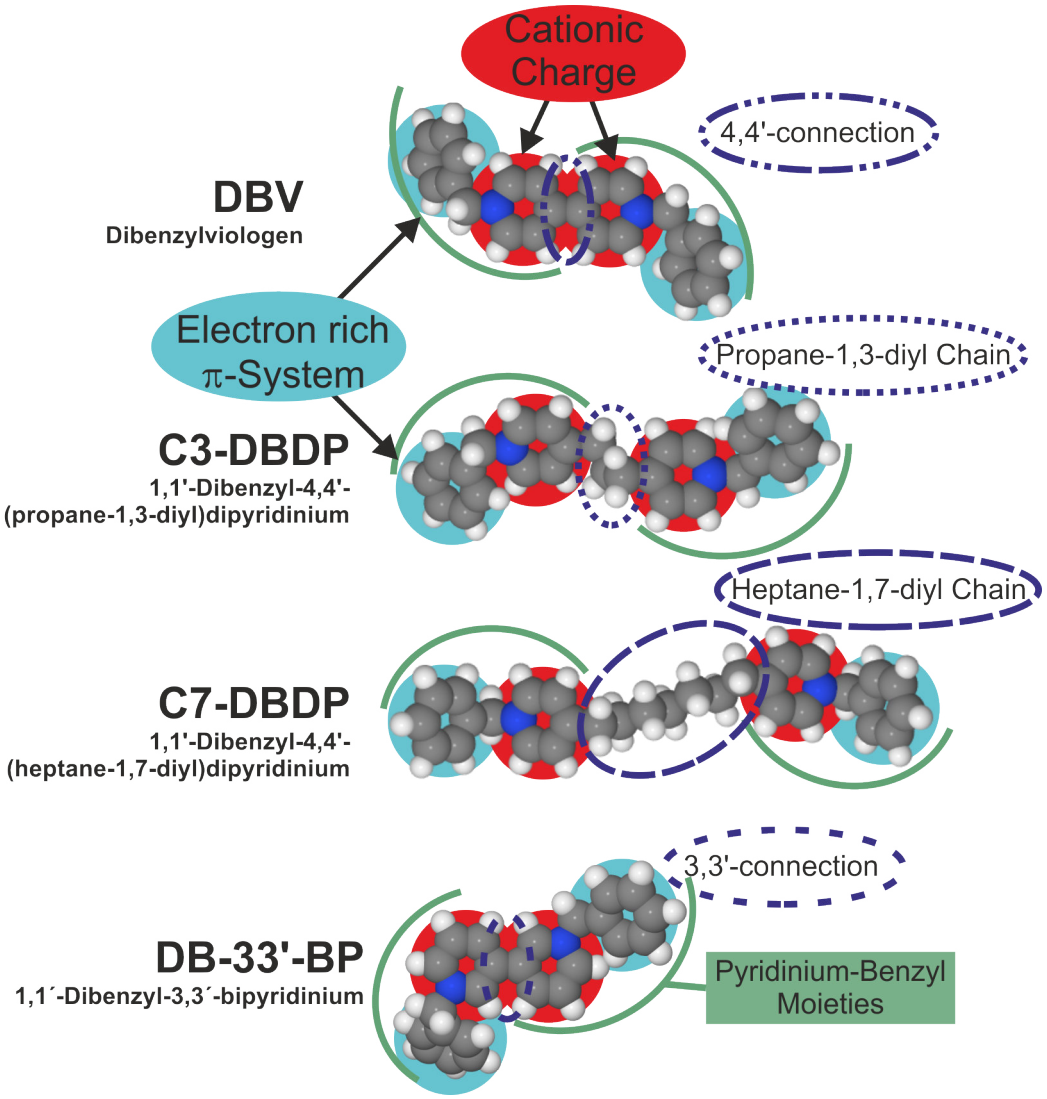

Figure 6.12: Reprint of figure 1.3. Structural motive of the DBV related molecules investigated within this work. All molecules consist of two pyridinium-benzyl moieties arranged symmetrically to the molecular center and connected either directly (4,4'- or 3,3'-connection) or via a saturated propane-1,3-diyl or heptane-(1,7)-diyl chain.

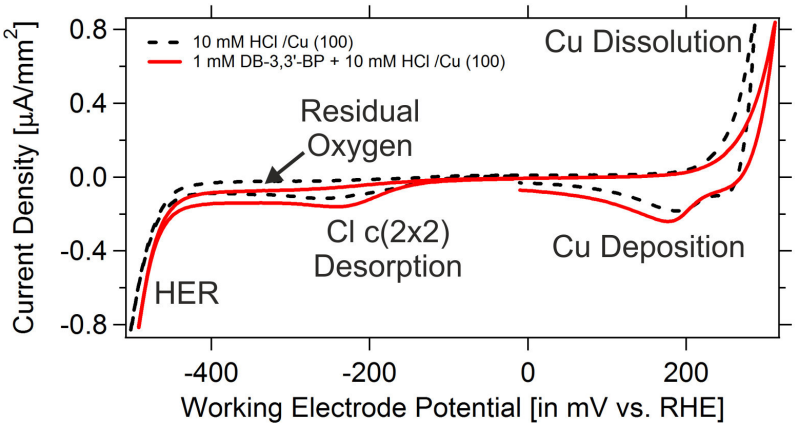

Figure 6.13: Comparison between the CV of 10 mM HCl with and without 1 mM DB-3,3'-BP on Cu(100). Scan speed 10 mV/sec.

current appearing in the CV at electrode potentials below -150 mV [vs. RHE]. This current can be attributed to residual oxygen, which is usually introduced in the solid/liquid interface by the electrolyte exchange procedure necessary to transport the organic cations to the solid surface. This interpretation is supported by the fact, that choosing electrode potential within the reactive regime of the oxygen residue (lower -150 mV [vs. RHE]) leads first to a lowering and finally to a vanishing of this electrochemical signal. Finally this interpretation is consistent with all experimental results obtained in the study of pure 10 mM HCl solution or the study of viologen building blocks.

In contrast to the HER, the Cu dissolution and subsequent redeposition signals in the CV are both affected by the presence of DB-3,3'-BP^{2+} dications in the interfacial regime. The Cu dissolution is inhibited, which results in a change of the exponentially increasing current. Therefore higher electrode potentials are necessary to obtain the same electrochemical current density as in the pure 10 mM HCl solution, namely +22 mV at 0.84 $\frac{\mu A}{mm^2}$. This is most likely a result of a physical barrier consisting of DB-3,3'-BP^{2+} adsorbed on the Cu(100) electrode surface. Consistent to the inhibition of the Cu dissolution, also the Cu deposition is inhibited as the maximum of the Cu deposition peak is shifted by -18 mV to more negative potentials.

Amorphous Organic DB-3,3'-BP Layer on Cl-c(2x2)/Cu(100)

In situ STM images of the electrode surface reveal a diffuse layer consisting of DB-3,3'-BP adsorbed on the substrate surface. This diffuse layer is best resolved in high resolution images such as shown in figure 6.14. In that high resolution STM image the DB-3,3'-BP diffuse layer appears to consist of two DB-3,3'-BP species, namely a mobile and (at least temporarily) immobile DB-3,3'-BP species. The immobile DB-3,3'-BP molecules are marked by white circles in the STM image (real space) shown in figure 6.14. The redox state of this mobile or immobile molecules can not be probed via STM,

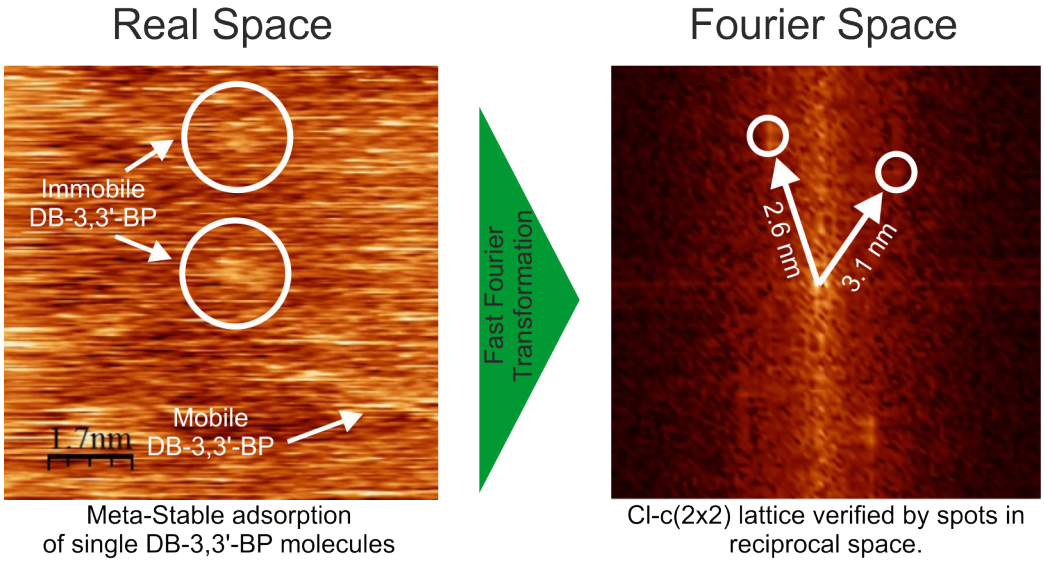

Figure 6.14: Uncorrected STM image proving the adsorption of single DB-3,3'-BP molecules on the Cl/Cu(100) substrate. The Cl-c(2x2) structure is obscured by the noise due to the amorphous layer of DB-3,3'-BP molecules. Pictures are untreated and not drift corrected. (8.73 nm x 8.73 nm, $E_{Work} = +0mV$, $U_{Bias} = +30\,mV$, $I_{Tunnel} = 5\,nA$)

but due to the lower redox activity of DB-3,3'-BP^{2+} in solution it can be assumed that the initial dicationic state is preserved in the adsorption on the Cl/Cu(100) surface and, consequently, that the diffuse layer consists of DB-3,3'-BP^{2+} dications.

The mobile DB-3,3'-BP^{2+} dications are in a physisorbed state, in which the DB-3,3'-BP^{2+} dications may freely diffuse on the Cl/Cu(100) substrate. Characteristic for the presence of mobile organic cations are short bright lines as found in the right part of the STM picture (fig. 6.14, marked by white arrow in the real space image). This STM signal results from the presence of the molecule between STM tip and substrate while one line in the STM image is scanned. The scan of the subsequent line in the STM image occurs one tenth of a second later, a time period at which mobile organic cations move via diffusion elsewhere.

In contrast to this, the (at least temporarily) immobile DB-3,3'-BP^{2+} dications are chemisorbed, which involves the interaction of the molecule to specific adsorption sites of the substrate surface. The apparently weakly chemisorbed DB-3,3'-BP^{2+} dications are only temporally bound to adsorption sites of the Cl/Cu(100) substrate, but may jump to a neighboring adsorption site or desorb into a physisorbed / unbound state. This was proven by the vanishing of the immobile DB-3,3'-BP^{2+} dications in subsequently registered STM images.

The interaction between adsorption sites on the substrate and the organic building blocks is assumed to play a key role in the monolayer formation of organic molecules, as

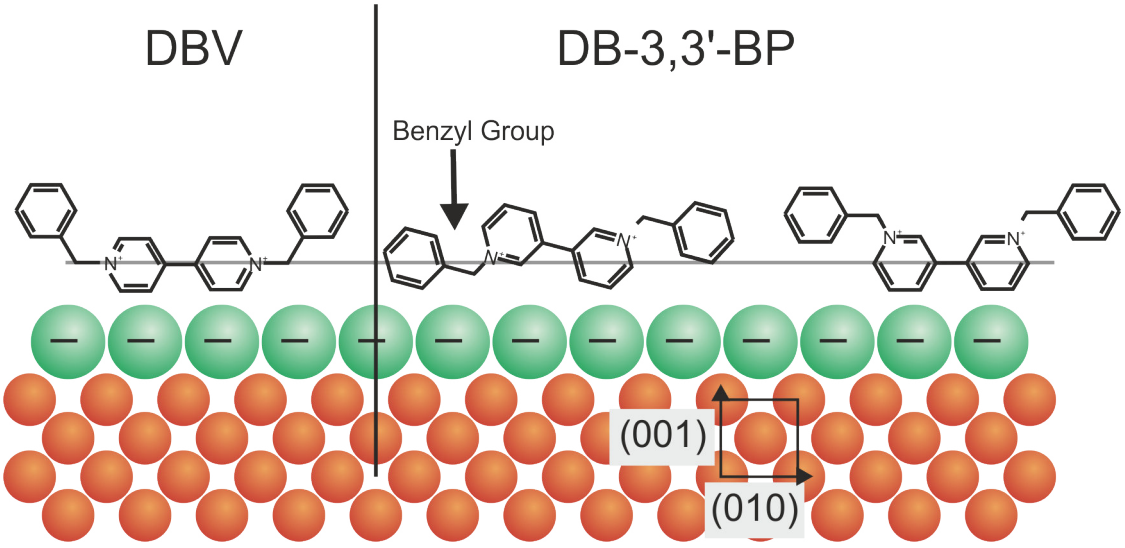

Figure 6.15: Sketch of the building block arrangement, namely the comparison between DBV^{2+} and DB-3,3'-BP^{2+} , on the Cl/Cu(100) substrate.

discussed in the previous sub-chapter for viologen cations. Therefore the observation of immobile DB-3,3'-BP^{2+} molecules suggests the existence of a DB-3,3'-BP^{2+} monolayer, which might be formed at sufficiently high molecular densities of DB-3,3'-BP^{2+} on the Cl/Cu(100) substrate. At high molecular densities directly neighboring chemisorbed (immobile) DB-3,3'-BP^{2+} may interact with each other, which stabilize them in their chemisorbed state and finally lead to the formation of an ordered DB-3,3'-BP^{2+} monolayer on the electrode surface. However, investigating DB-3,3'-BP^{2+} concentrations of 0.01 mM, 0.1 mM, 0.5 mM, 1 mM, 5 mM, 10 mM and finally 25 mM did *not* lead to the formation of an ordered DB-3,3'-BP^{2+} monolayer on the Cl/Cu(100) substrate.

In figure 6.15a DBV^{2+} and DB-3,3'-BP^{2+} at the Cl/Cu(100) substrate are sketched. As discussed in the previous chapter the adsorbate-substrate as well as inter-adsorbate attraction are essential for the formation of an ordered viologen monolayer. In the case of DBV this is realized by aligning the molecular axis of DBV parallel to the Cl anion monolayer, with both N atoms at the same distance from the negative Cl anion monolayer.

In contrast to DBV^{2+}, the interaction of the bipyridinium core of DB-3,3'-BP^{2+} is disturbed by its benzyl groups. As imaged in figure 6.15 (center) the benzyl group forces half of the bipyridinium core to be situated at greater distance from the Cl anion layer compared to DBV^{2+}. This weakens the interaction between the cationic bipyridinium core and the Cl anion monolayer. Apparently the inter-adsorbate interactions does not compensate this weaker adsorbate-substrate interaction of the DB-3,3'-BP^{2+} dications, as no ordered DB-3,3'-BP^{2+} monolayer was observed in the STM experiments.

Rotating half of the DB-3,3'-BP^{2+} molecule around the central 3,3'-bond, which is situated between the pyridinium rings, locates both benzyl groups of the DB-3,3'-BP^{2+}

on the same side of the molecule. In this conformation DB-3,3'-BP^{2+} may interact with either both benzyl groups or with the bipyridinium core directly with the Cl anion monolayer. The latter is assumed to maximize the adsorbate-substrate interaction and is therefore sketched in figure 6.15 (right). In this adsorption geometry the benzyl groups are forced to be situated above the DB-3,3'-BP^{2+} bipyridinium core. As no ordered DB-3,3'-BP^{2+} monolayer is observed it must be concluded that either the inter-adsorbate interaction based on the interaction between their benzyl groups is not sufficient to result in the formation of the DB-3,3'-BP^{2+} monolayer, or the previously introduced electrostatic anchoring of the 4,4'-bipyridinium core (viologen) is weakened / lifted for the 3,3'-bipyridinium cores, as a result of the larger distance of the N^+ centers from the Cl anion monolayer.

The in this section discussed adsorption geometries assume that the DB-3,3'-BP^{2+} dications adsorb with their bipyridinium plane perpendicular to the Cl anion monolayer, as imaged in figure 6.15 and observed by IRRAS for viologen dications V^{2+} [13, 77]. The adsorption of the bipyridinium plane parallel to the Cl anion substrate is not excluded per se, but if it occurs it apparently is neither an energetically favored adsorption geometry which permits the formation of an ordered DB-3,3'-BP^{2+} monolayer.

6.2.2 C3-DBDP as Building Block

Electrochemical Characterization

Figure 6.16 shows the CV of Cu(100), registered at 10 mV/sec, in a 0.1 mM C3-$DBDP^{2+}$ containing 10 mM HCl solution in comparison to a CV in a 0.1 mM DBV containing 10 mM HCl solution registered at the same scan speed and comparable ambient conditions. The modification of the molecular structure of DBV to C3-DBDP leads to a vanishing of all current waves, i.e. of P2 and P4. Furthermore no constant reductive current throughout the whole potential window can be observed. Summarizing both observations, it can be concluded that C3-$DBDP^{2+}$ possesses a lower redox-activity than DBV^{2+} dications and therefore neither a reduction nor an oxidation can be observed in the potential window of the Cu(100) electrode.

The absence of any electrochemical signals related to the reduction or oxidation of the organic cation C3-$DBDP^{2+}$ is assumed to result from the fragmentation of the DBV bipyridinium π-system into two isolated C3-DBDP pyridinium π-systems. This *decoupling* of the pyridinium π-systems is a consequence of the increase of intra-molecular flexibility, which was achieved by the introduction of the propane-1,3-diyl chain (consisting of sp^3-hybridized carbon atoms) between the sp^2-hybridized pyridinium rings. The propane-1,3-diyl chain prevents any electron exchange between the pyridinium π-systems and therefore leads to a localisation of each pyridinium redox state to one ring. The *coupling* of the pyridinium π-systems is assumed to be of central relevance for the electrochemical reduction of the dications to a lower redox state, as within viologens the cation charges and radical electrons of the monocation radicals $V^{+\bullet}$ are delocalized (and therefore stabilized) over the whole bipyridinium π-system, as proven via XPS experiments [9]. This distribution of the radical state and the cation charge over the whole

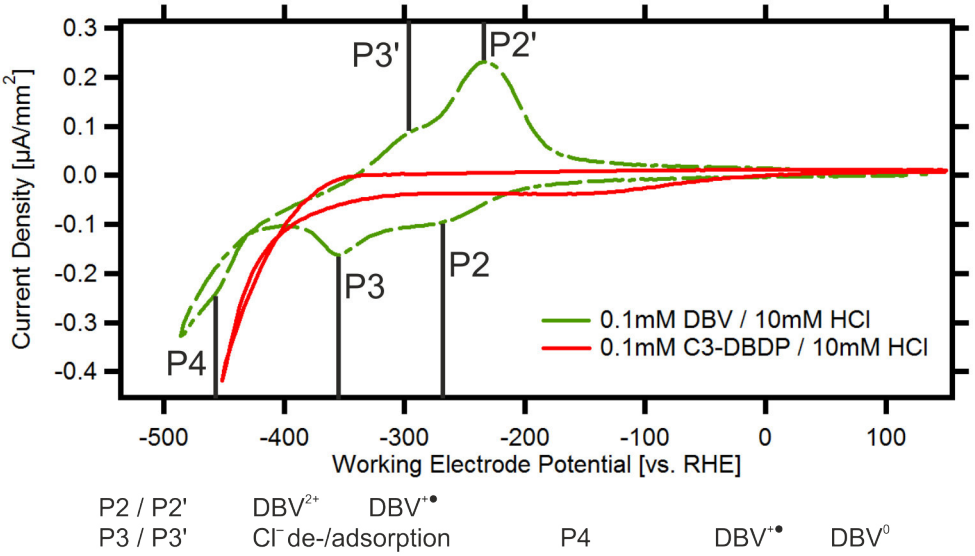

Figure 6.16: CVs of Cu(100) in {0.1 mM C3-DBDP + 10 mM HCl} (red, solid curve) and Cu(100) in {0.1 mM $DBVCl_2$ + 10 mM HCL} (green, dashed curve), both curves registered at a scan speed of 10 mV/sec. C3-DBDP shows no significant electrochemical processes. In contrast to this the previously discussed DBV molecule shows a number of processes (P2 - P4).

bipyridinium core can not occur when the pyridinium rings are separated by an saturated organic chain, such as by a propane-1,3-diyl chain in the C3-DBDP molecule. The missing possibility to delocalize the radical electron over both pyridinium π-systems is assumed to be energetically unfavored and therefore to lead to a lower redox activity of the dication C3-$DBDP^{2+}$, than of the comparable DBV^{2+}. This assumption agrees with the results of the electrochemical study of 4-benzoyl-N-(4-substituted benzyl)pyridinium cations [32], where the benzyl-pyridinium derivate is found to possess a reduction potential within the HER regime at potentials lower than -400 mV [vs. RHE].

Another difference between the CV of DBV^{2+} and C3-$DBDP^{2+}$ dications is the absence of the peak pair P3/P3' (related to the Cl anion desorption process) in the C3-DBDP CV. In order to clarify if the Cl anion desorption does take place scans at 200 mV/sec were made as presented in chapter 5.2 and illustrated in figure 5.2, which was reprinted here as figure 6.17. The high scan speed of 200 mV/sec reveals that the Cl anion desorption from the Cu(100) electrode surface takes place in both, pure 10 mM HCl and 0.1 mM C3-$DBDP^{2+}$ containing HCl solutions, at low electrode potentials.

The absence of the peak pair P3/P3' in the C3-DBDP CV registered at a speed of 10 mV/sec indicates a weaker interaction of C3-DBDP than of DBV to the Cl/Cu(100) substrate. Indeed, this is proven by figure 6.17, as the Cl anion desorption in presence and absence of C3-DBDP at the Cl/Cu(100) electrode occurs close to -290 mV [vs. RHE], whereas P3 occurs at -355 mV [vs. RHE] (fig. 6.16). However, although C3-DBDP does not hinder the desorption, it hinders the adsorption of Cl anions, which occurs when the

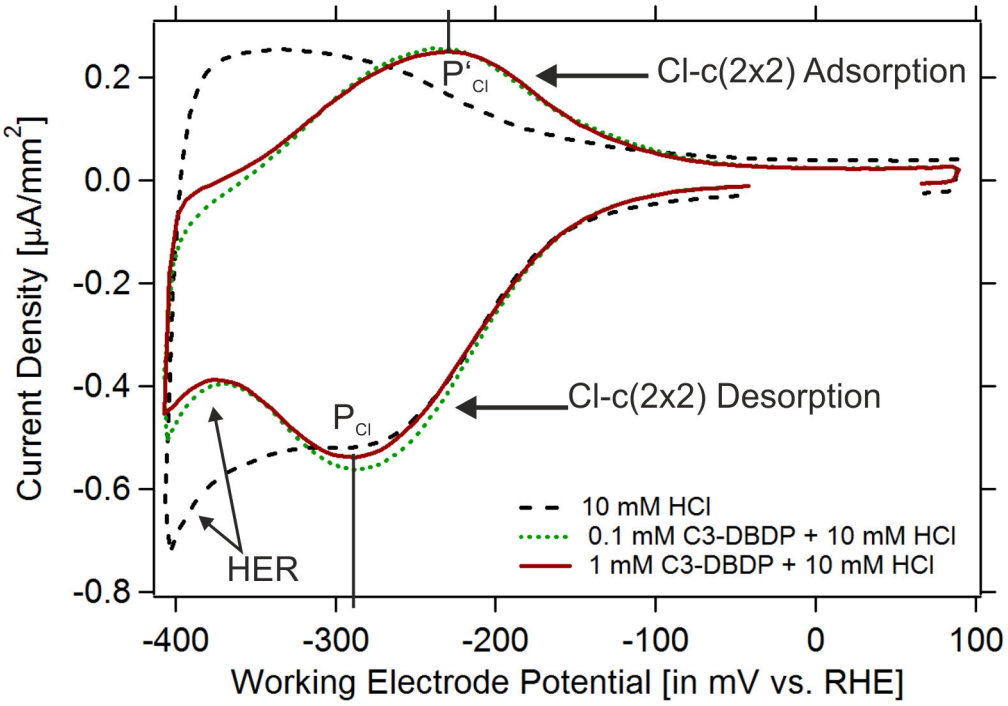

Figure 6.17: Reprint of figure 5.2. CV curves of the Cu(100) electrode surface in pure 10 mM HCl, 0.1 mM C3-DBDP + 10 mM HCl or 1 mM C3-DBDP + 10 mM HCl solution. Scan speed 200 mV/sec.

electrode potential is increased from the HER regime to potentials higher than -100 mV [vs. RHE]. This hindrance of the adsorption is expressed in a shift of the Cl anion adsorption to more positive potentials in the presence of C3-DBDP (fig. 6.17). In order to clarify further on the details of the Cl anion desorption process, specific STM series were registered, which will be presented in the STM section of the C3-DBDP molecule.

Besides the molecular and Cl anion related surface processes both molecules, DBV and C3-DBDP, also influence the Hydrogen Evolution Reaction (HER), by shifting the onset of the HER to more negative electrode potentials. This indicates the adsorption of C3-DBDP on the electrode surface and a blocking of at least a fraction of the HER reaction sites. As presented previously, DBV (mono- or di-) cations adsorbed on the electrode surface lead to a shift of the HER by -66 mV (at a current of -0.13 $\frac{\mu A}{mm^2}$) and a flattening of the exponential increase of the related reductive current. In agreement to this, the presence of C3-DBDP cations in the interfacial regime and on the surface (as will be proven later) cause a shift of the HER to more negative electrode potentials by -42 mV (at a current of -0.13 $\frac{\mu A}{mm^2}$, 10 mV/sec scan speed). However, it appears that in contrast to DBV, C3-DBDP does not affect the exponential increase of the reductive HER currents. This and the smaller shift of the HER indicates once again that C3-DBDP cations do interact less strongly with the underlying substrate. If this "less strong interaction" to the substrate occurs only to the Cl-c(2x2) monolayer adsorbed on the Cu(100) electrode surface or also on the bare Cu(100) electrode surface can not be decided with the given experimental data, because the Cl anion desorption process extends into the HER regime and influences the reaction dynamics significantly (as proven by Stuhlmann at al. [19] and discussed in chapter 5.2).

Redox State of C3-DBDP Adsorbed on the Electrode Surface

The via cyclic voltammetry revealed stability of C3-DBDP^{2+} *solution species* at the Cl/Cu(100) electrode surface does not exclude that C3-DBDP^{2+} may upon adsorption on the Cl/Cu(100) electrode surface be reduced to a lower molecular redox state. Indeed, this was proven to occur for DPV^{2+}, which upon adsorption is immediately reduced to the monocation radical state, even for potentials at which DPV^{2+} in solution stays unaffected, and subsequently forms the DPV$^{+\bullet}$ π-stacked stripe phase [9]. In order to probe the redox state and prove that C3-DBDP^{2+} conserves its initial dicationic state even upon adsorption on the Cl/Cu(100) electrode surface additional *ex situ* XPS experiments were performed.

The experimental strategy of the XPS experiments is to compare the redox state of electrochemically adsorbed C3-DBDP on the Cl/Cu(100) substrate (emersion potential 0 V [vs. RHE]) to reference XPS spectra, such as the spectrum of C3-DBDPCl_2 salt smeared on an inert polycrystalline gold foil. In order to determine the molecular redox state of these viologen related molecules their nitrogen 1s (N1s) signal was registered, as this has proven in previous studies to be an appropriate measure [9].

In order to maximize the significance of the XPS related conclusion the sample preparation was performed as similar as possible to the procedure for the STM experiments. This includes electrochemcial conditions, adsorption times and protection of the sample

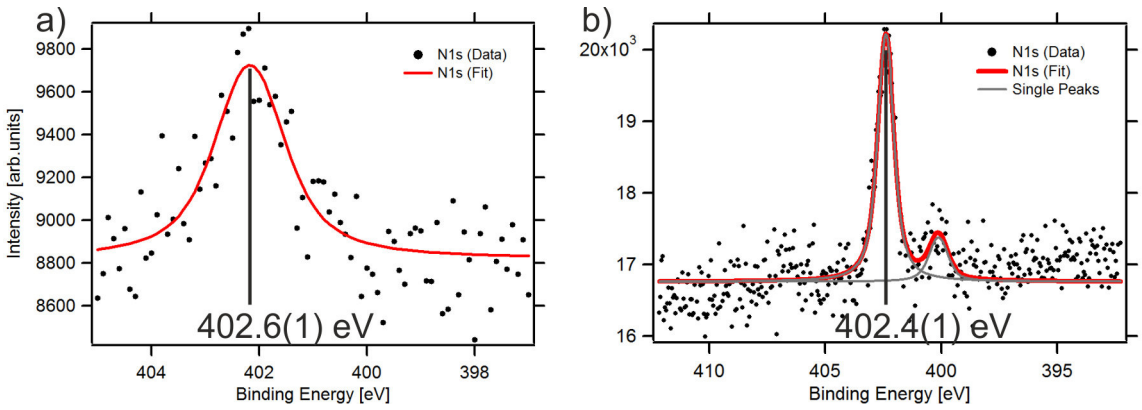

Figure 6.18: XPS (X-ray Photoelectron Spectroscopy) to confirm the redox state of C3-DBDP^{2+} adsorbed on the Cl/Cu(100) surface. Experimental error of the N1s electron binding energy E_B(N1s) is stated within the parenthesis and refers to the last digit of E_B(N1s). (a) N1s electron binding energy (E_B(N1s) = 402.6(1) eV) of C3-DBDP^{2+} salt species deposited on high purity polycrystalline gold plate. (b) Ex-situ measured N1s electron binding energy (E_B(N1s) = 402.4(1) eV) of electrochemically adsorbed C3-DBDP^{2+} on a Cl/Cu(100) surface. The small peak at 400.1(1) eV is attributed to beam damage [9].

surface from contamination. Therefore it can be stated that the registered XPS spectra represent only adsorbed C3-DBDP species. This was furthermore verified by registering survey spectra with low resolution over several hundred eV and subsequently identify all signals appearing within.

In contrast to the STM setup, in the XPS experiments the Cu(100) surface was brought into contact with the solution in the so-called hanging meniscus configuration [63]. After the sample preparation was completed, and the C3-DBDP electrochemically adsorbed, the Cu(100) surface was wetting-free emersed, which prevented a drying residue on the Cl/Cu(100) surface. Subsequently the protective argon atmosphere was removed by evacuating the preparation chamber and the sample was transferred without exposure to air into UHV, where the XPS spectra were measured.

Figure 6.18 shows both registered N1s signals, of C3-DBDPCl2 salt on gold and of electrochemically adsorbed C3-DBDP on the Cl/Cu(100) electrode surface. These spectra reveal C3-DBDP^{2+}, as genuine redox state of C3-DBDP dichlorid salt, to possess an N1s electron binding energy of E_B(N1s) = 402.6(1) eV. The N1s electron binding energy of the C3-DBDP species adsorbed on the Cl/Cu(100) surface is found to be E_B(N1s) = 402.4(1) eV, which differs only by 0.2 eV from the C3-DBDP^{2+} dications in a dichloride salt environment. The almost identical N1s electron binding energies prove that both C3-DBDP species are in the same redox state. The difference of 0.2 eV between the N1s electron binding energy is attributed to the differing chemical environment between the salt and electrochemically adsorbed species. Besides the main signal in figure 6.18b

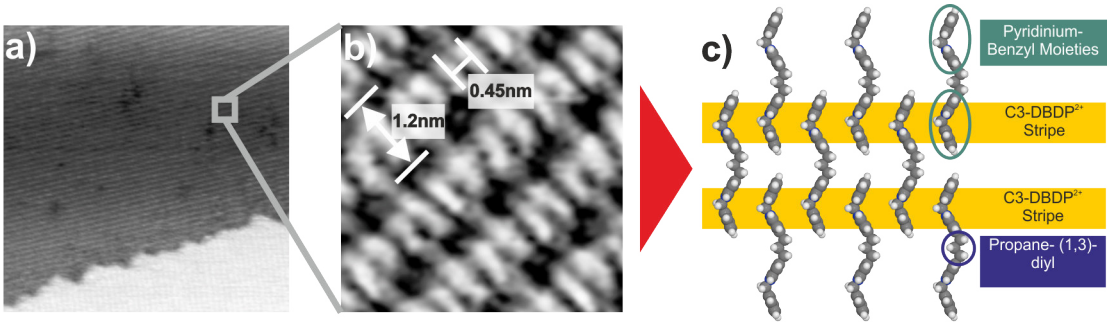

Figure 6.19: Ordered C3-DBDP^{2+} monolayer adsorbed on a Cl-c(2x2)/Cu(100) substrate. (a) Long-range ordered C3-DBDP^{2+} inter-linked stripe phase (61.7 nm x 61.7 nm, $E_{Work} = +0\,mV$, $U_{Bias} = +295\,mV$, $I_{Tunnel} = 0.1\,nA$) (b) Highly resolved STM image of the C3-DBDP^{2+} inter-linked stripe structure. (4.3 nm x 4.3 nm, $E_{Work} = +0\,mV$, $U_{Bias} = +156\,mV$, $I_{Tunnel} = 0.1\,nA$) (c) Model of the C3-DBDP^{2+} inter-linked stripe structure.

indications of a small second contribution at E_B(N1s) = 400.1(1) eV are found. This signal is attributed to a more reduced C3-DBDP species produced in the XPS experiment at the synchrotron radiation facility, due to an unavoidable x-ray beam induced "dry reduction process". This interpretation is inspired and in agreement with XPS studies of viologens, which made comparable observations [9].

The interpretation of the N1s electron binding energies is consistent to XPS studies of other dicationic and monocationic radical viologens adsorbed on a Cl/Cu(100) substrate [9] and literature data of viologens [81]. The N1s electron binding energy of DBV^{2+} as dichloride salt on a gold foil was published to be E_B(N1s) = 402.53(2) eV [9], which is between both N1s electron binding energy of the C3-DBDP species. Reducing viologens to their monocation radical state results in binding energies of 400.7 eV or lower [9, 81]. The decrease of the N1s electron binding energy by 1 eV upon reduction of the viologen dication to their monocation radical state is a reference point and therefore as well expected for C3-DBDP. This supports the interpretation of the measured C3-DBDP XPS signals (fig. 6.18) and essentially proves that C3-DBDP^{2+} retains its dication state even upon adsorption on the Cl/Cu(100) surface.

Ordered C3-DBDP^{2+} Layer on Cl-c(2x2)/Cu(100)

In situ STM results reveal a long-range ordered stripe phase formed by the C3-DBDP^{2+} dications on the Cl/Cu(100) substrate (fig. 6.19a), which in highly resolved images was found to be an "inter-linked" stripe structure (fig. 6.19b). Stripe phase formation were so far observed for viologen *monocation* radicals, but never in the structure formation of viologen *dications*.

As figure 6.19b shows the inter-linked stripe phase consists of stripes with a distance of 1.2(1) nm, which are alternatingly to the left and the right linked to the neighboring stripes via less brightly imaged "bridges". Such a "linking" to neighboring stripes

was not observed in the study of viologen π-stacked stripe phases [5, 9, 10]. The viologen π-stacked stripe phases are formed by the consecutive arrangement of one complete viologen monocation radical, e.g. $DPV^{+\bullet}$ and $DBV^{+\bullet}$. This was concluded as the experimentally obtained stripe distance of 1.88 nm for $DPV^{+\bullet}$[9] and 1.82 nm for $DBV^{+\bullet}$ [5] agree reasonably well with the *full* estimated molecular length of 1.77 nm for $DPV^{+\bullet}$[9] and 1.55 nm for $DBV^{+\bullet}$[9].

In comparison to the viologen π-stacked stripes, the C3-$DBDP^{2+}$ stripes are with a distance of 1.2(1) nm significantly closer, indeed they are too small to accommodate one complete C3-DBDP molecule with an estimated length of 2.3 nm. However, the C3-DBDP stripe distance agrees well with *half* of the estimated C3-DBDP length. Therefore it is proposed that each bright stripe element represents one pyridinium-benzyl moiety and consequently the less brightly imaged "stripe bridges" are attributed to the three carbon long propane-(1,3)-diyl chain. This assignment of visible STM features to molecular groups is consistent with the observations made in the STM study of DPV, DBV and DHV monolayers, where the bipyridinium core was found to be imaged significantly brighter than the viologen substituents (i.e. heptyl chains [10]). The structure parameters obtained from figure 6.19b, namely stripe distance of 1.2(1) nm and distance between consecutive stripe elements (= between pyridinium-benzyl moieties) of 0.45(2) nm permits to derive a model of the inter-linked stripe structure shown in figure 6.19c.

Although both, viologen monocation radicals $V^{+\bullet}$ and C3-$DBDP^{2+}$, adsorb in stripe structures on the Cl/Cu(100) substrate, the driving force behind their structure formation are fundamentally different. Between viologen monocation radical $V^{+\bullet}$ the inter-molecular attraction is a result of electron pairing between consecutive arrangement of monocationic bipyridinium *radicals*, which requires the overlap of consecutive bipyridinium π-systems and therefore leads to the adsorption of $V^{+\bullet}$ monocation radicals in one $V^{+\bullet}$ stripe. Arranging the C3-$DBDP^{2+}$ in a comparable manner maximizes the inter-molecular electrostatic *repulsion*, due to the direct facing of the cationic pyridinium rings as illustrated in figure 6.20 upper sketch. In contrast to viologen monocation radical $V^{+\bullet}$, the cationic pyridinium rings in C3-DBDP possess *no radical electron* and therefore no inter-molecular electron pairing takes place. The shift of consecutive C3-$DBDP^{2+}$dications by half the molecular length (orthogonal to the stripe orientation) leads to a separation of the cation charge and to a direct facing of the positively charged cationic pyridinium rings with the negatively charged aromatic π-system of the benzyl ring (fig. 6.20). The resulting inter-molecular interaction between the C3-$DBDP^{2+}$dications in this adsorption geometry is assumed to be a longer-ranged electrostatic attraction between the pyridinium cationic charge and benzyl π-system.

The revealed inter-molecular interaction between C3-$DBDP^{2+}$dications might as well play a role in the structure formation and ordering of other organic molecules, such as DBV^{2+}, whose cavitand structure is well described, but still lacks a detailed understanding of the cause of its formation. This assumption was introduced into the model of the DBV^{2+} cavitand phase presented earlier in this work (fig. 6.6). In contrast to the inter-linked stripe structure in which all pyridinium and benzyl groups interact with neighboring molecules, in the DBV^{2+} cavitand structure only half of the

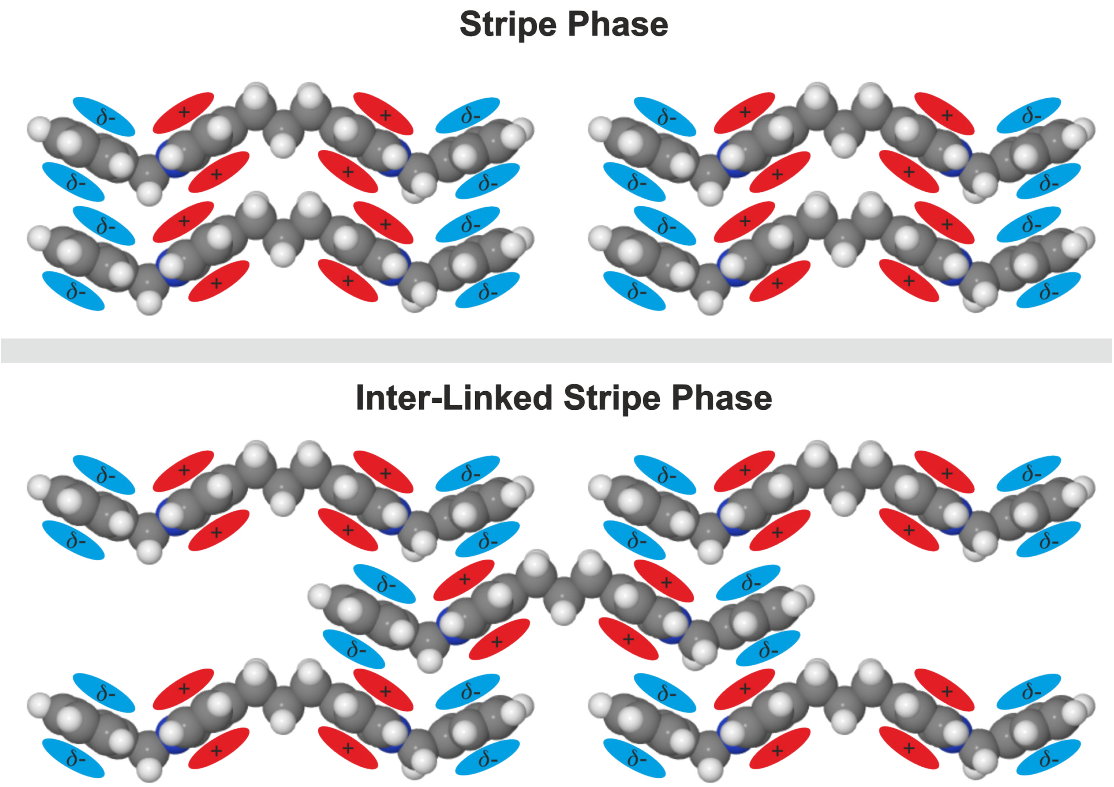

Figure 6.20: Model of the inter-molecular electrostatic interactions between C3-DBDP^{2+} dications in a stripe or inter-linked stripe phase.

present pyridinium rings and half of the present benzyl π-system interact attractively to neighboring molecules. Apparently the increase of intra-molecular flexibility permits the C3-DBDP^{2+} pyridinium-benzyl moieties to arrange in the more efficient and dense geometry, in which *all* pyridinium rings and benzyl π-system interact attractively with neighboring C3-DBDP^{2+} molecules.

The increased intra-molecular flexibility of C3-DBDP^{2+} not only affects the ordering of the C3-DBDP^{2+} within the monolayer, but also alters the adsorbate-substrate interaction. The DPV, DBV and DHV dication and monocation radical monolayers were found to order almost instantaneously and to form commensurable adlayers on the Cl/Cu(100) substrate [5, 9, 10]. The molecular axis, defined by the bipyridinium core, is in most of these viologen monolayers arranged along the close packed directions of the Cl-c(2x2) lattice, namely [100] and [010]. This molecular arrangement indicates a supporting role of the Cl-c(2x2) lattice in the viologen monolayers formation, e.g. due to geometric reasons. Indeed, the length of the bipyridinium core is found to be 0.71 nm [5, 9], which matches the double next neighbor distance (along the close packed directions) of the Cl anions with a value of 0.72 nm. Beside this geometric reason a chemical factor in the structure formation of viologen monolayers can not be excluded. This statement is based on the fact that DBV$^{+\bullet}$ is found to order instantaneously on the Cl anion lattice at any electrode potential, even for the most negative electrode potentials (= negative surface charge) close to the hydrogen evolution, but not on the bare Cu(100) surface.

In contrast to the viologen monolayer formation, the structure formation process of C3-DBDP^{2+} is found to be inhibited. The formation of C3-DBDP^{2+} domains extends over several tens of minutes. STM images registered within the first hour after the introduction of C3-DBDP^{2+} reveal a fragmented C3-DBDP^{2+} monolayer, consisting of small ordered as well as amorphous C3-DBDP^{2+} domains. The ordered domains subsequently grow in a post-adsorption ripening process, to finally form the presented long-range interlinked stripe structure seen in fig. 6.19. These observations are at first sight surprising, as the increased molecular flexibility of C3-DBDP, compared to DBV, is assumed to favor the C3-DBDP^{2+} monolayer formation and not to hinder it. The added propane-1,3-diyl chain increases the steric flexibility of C3-DBDP, due to intra-molecular rotations around all C-C single bonds between the saturated (tetrahedral) C-atoms. These extra degrees of rotational freedom permit C3-DBDP to arrange within a greater conformational space on the Cl/Cu(100) surface, i.e. to maximize the intermolecular adsorbate-adsorbate and adsorbate-substrate attraction as well as to minimize the electrostatic repulsion between the cationic pyridinium rings in the adlayer formation process.

Apparently the modification of DBV to C3-DBDP leads to an unfavorable molecular geometry, which hinders the structure formation of C3-DBDP^{2+} on the Cl-c(2x2) anion lattice. Two possible geometric factors behind the inhibited structure formation of C3-DBDP are the distance between the pyridinium rings or their orientation with respect to each other, originating from the tetrahedral bond condition between them. However, the given experimental data do not allow definite conclusions. A more likely explanation for the inhibited C3-DBDP^{2+} monolayer formation, despite the increased intra-molecular flexibility, is a misfit between the C3-DBDP^{2+}molecular structure and the substrate lattice resulting in a competition between adsorbate-substrate and inter-

adsorbate attractive forces, requiring differing arrangements (and periodicities) of the C3-DBDP^{2+} dications on the electrode surface. This assumption is supported by the fact that C3-DBDP^{2+} stripes are found to grow neither with one clear relation to the underlying Cl/Cu(100) substrate nor in arbitrary directions. Indeed, the C3-DBDP^{2+} stripe domains were found to grow within an angular range of 30° - 45° to the main crystallographic axis of the Cu fcc lattice, namely (100) and (010). The restriction of the stripe orientation to this narrow angular range indicates several arrangements on the Cl-c(2x2) lattice to be equally favored and/or to compete with the arrangement in the inter-linked stripe phase. The attempt to establish a commensurable relation between the C3-DBDP^{2+} stripe domains and the underlying Cl-c(2x2) monolayer failed. However, although the existence of a commensurable C3-DBDP^{2+} arrangement could not be proven, it can be neither fully excluded. Indeed, the conversion of these various inter-linked stripe domains into a final commensurable arrangement by a ripening or relaxation process can not be ruled out to occur after long time.

Chloride Anion Desorption Through the C3-DBDP^{2+} Dication Monolayer

The previously discussed missing commensurable relation between the C3-DBDP^{2+} inter-linked stripe structure and the underlying Cl anion lattice might be a result of strong inter-adsorbate attractive forces, which overrule the interaction of C3-DBDP^{2+} dications to specific adsorption sites of the Cl anion lattice. This assumption is supported by the observations made in the Cl anion desorption from the Cu(100) surface through the intact C3-DBDP^{2+} inter-linked stripe phase, visualized by a series of STM images in figure 6.21. Figure 6.21a, registered at an electrode potential of E_{work} = -120 mV [vs. RHE], visualizes the long-range ordered C3-DBDP^{2+} inter-linked stripe phase, as it exists for potentials up to the onset of the Cu dissolution at E_{work} = +170 mV [vs. RHE]. Despite the C3-DBDP^{2+} inter-linked stripe phase being adsorbed on the electrode surface significant Cu diffusion takes place, which results in the growth of the Cu terrace along the fcc directions (100) and (010), as imaged in figure 6.21b. The C3-DBDP^{2+}stripe structure occupies this new substrate areas, but remains besides this, unaffected. Reducing the electrode potential further to E_{work} = -250 mV [vs. RHE] results in the beginning of the Cl anion desorption, first at the energetically least favored kink sites, as proven by the STM (fig. 6.21c). The Cl anion desorption is concluded from the loss of the 90° angle of the Cu steps (fig. 6.21c). The loss of the 90° angle of the Cu steps results in a reorientation of the steps parallel to the C3-DBDP^{2+}stripe phase. From this it can be concluded that the C3-DBDP^{2+}stripe phase stabilize the underlying substrate along the growth direction of the inter-linked stripe phase.

Increasing the negative Cu surface charge further by reducing the electrode potential to E_{work} = -400 mV [vs. RHE] permits the desorption of the complete Cl anion monolayer, situated underneath the C3-DBDP^{2+}stripe structure. The Cl anions desorb through the intact C3-DBDP^{2+} inter-linked stripe phase, which does not lead to a breaking up of the inter-molecular electrostatic bonds between adsorbed C3-DBDP^{2+} dications, but results in the appearance of a Moiré pattern on the C3-DBDP^{2+}stripe structure, which most likely appears due to the change of the underlying substrate periodicity (fig. 6.21d).

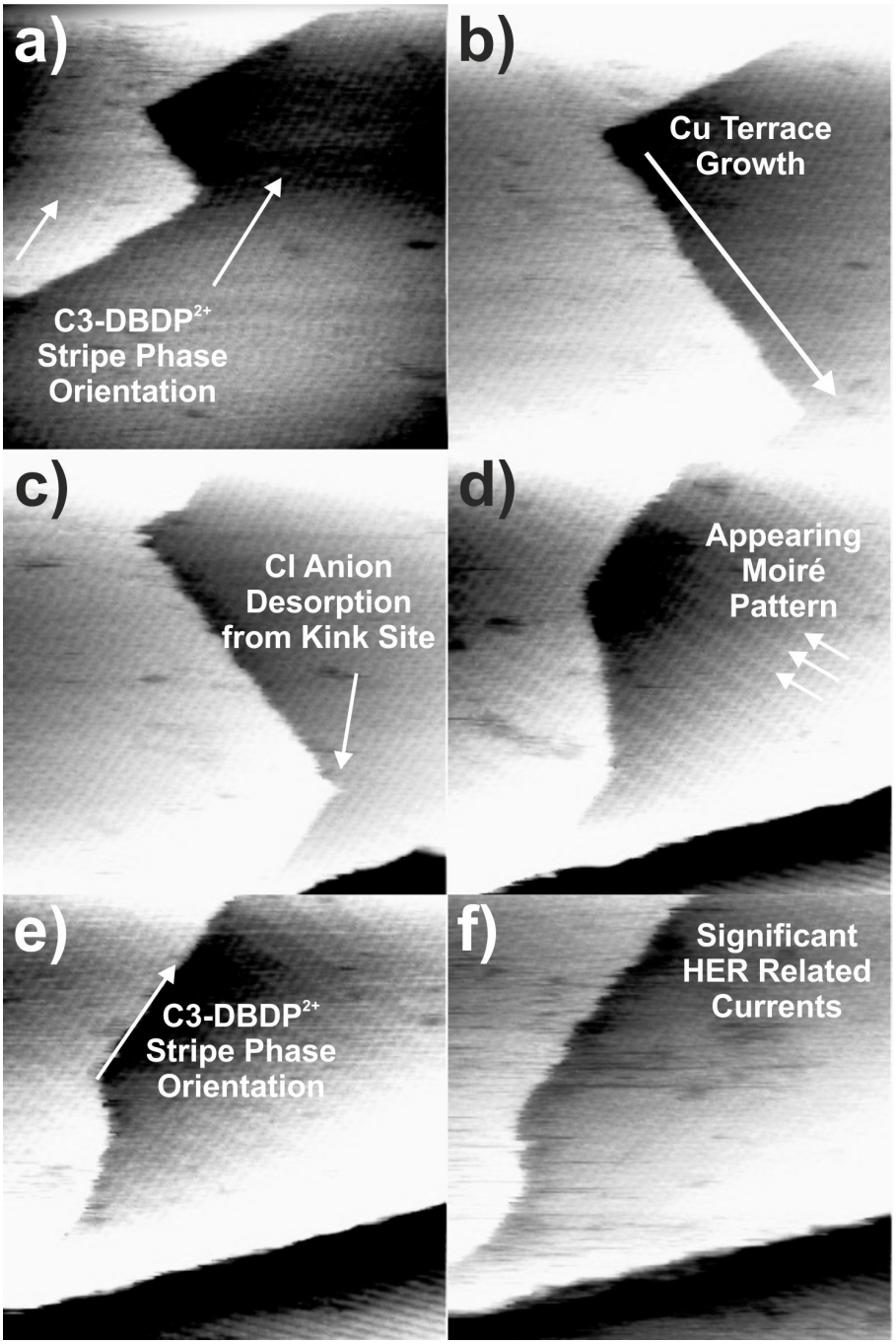

Figure 6.21: Series of STM pictures of the C3-DBDP^{2+} inter-linked stripe structure throughout the Cl anion desorption process. The extreme contrast of the STM images was achieved by cutting the intensity scale, which was necessary to guaranty the visibility of the stripe structure and the Moiré pattern on screen and in print. (43.2 nm x 43.2 nm, $U_{Bias} = +280\,mV$, $I_{Tunnel} = 0.1\,nA$) (a) $E_{Work} = -50\,mV$, (b) $E_{Work} = -90\,mV$, (c) $E_{Work} = -180\,mV$, (d) $E_{Work} = -330\,mV$, (e) $E_{Work} = -380\,mV$, (f) $E_{Work} = -430\,mV$.

This Moiré pattern, as well as the reorganization of the Cu steps from their [100] / [010] orientation to an orientation parallel to the C3-DBDP^{2+} inter-linked stripes, strongly indicates the desorption of the Cl anion monolayer. A further reduction of the working electrode surface to E_{work} = -500 mV [vs. RHE] (fig. 6.21f) leads to significant hydrogen evolution (HER) related currents of more than 0.1 $\frac{\mu A}{mm^2}$, which induces vibrations of the STM tip and therefore leads to a loss of image quality and resolution.

However, in order to unambiguously prove the Cl anion desorption to take place additional XPS experiments were performed, in which the presence of Cl anions on the sample surface is proved through the occurance of a unique signal originating from the Cl 2p electrons [9]. Indeed, electrochemically preparing the C3-DBDP^{2+} inter-linked stripe structure on the Cl-c(2x2)/Cu(100) electrode surface, and subsequently emersing the sample surface from the solution at an electrode potential of +0 mV [vs. RHE], results in a Cl2p signal, consisting of the spin-orbit split Cl $2p_{1/2}$ and Cl $2p_{3/2}$ peaks, appearing in the registered XPS spectra (fig. 6.22a). Reducing the electrode potentials to E_{work} = -360 mV [vs. RHE] prior to the emersion of the sample from the solution, leads to the desorption of Cl anion from the sample surface. Before the sample is finally emersed from solution, the electrolyte is exchanged from a 10 mM HCl to a 5 mM H_2SO_4 solution, which prevents the upon emersion occurring re-adsorption of Cl anions from the solution on the sample surface. The finally registered XPS spectra prove the Cl2p signal to be vanished (fig. 6.22a), which allows to conclude that the Cl anion desorption took place. However, an additional S2p signal appears, which is related to SO_4^{2-} anions adsorbed on the anion free Cu(100) electrode surface or related to co-adsorbed SO_4^{2-} anions within the C3-DBDP^{2+} monolayer. It might be argued that the Cl anion desorption may have not be induced by reducing the electrode potential to -360 mV [vs. RHE], but through substitution by SO_4^{2-} anions. This can be excluded, as such a anion substitution is unlikely to occur, due to the lower tendency of the SO_4^{2-} than Cl^- to specifically adsorb [3]. Indeed, such a substitution was, to the best knowledge of the author, never reported, whereas the substitution of adsorbed SO_4^{2-} by Cl^- was proven [3].

The now fully proven stability of the C3-DBDP^{2+} inter-linked stripe phase in the Cl anion desorption process is remarkable, particularly in comparison to the observations made in the study of viologen monolayers on the same Cl-c(2x2) anion substrate. In contrast to the unaffected C3-DBDP^{2+} inter-linked stripe phase, the π-stacked stripe phases of DBV$^{+\bullet}$ or DHV$^{+\bullet}$ monocation radicals undergo upon desorption of the Cl anion lattice a phase transition to an amorphous organic layer of DBV$^{+\bullet}$ [6] or a viologen-dimere structure of DHV$^{+\bullet}$ [10]. In both phase transitions the inter-molecular bonds between the DBV$^{+\bullet}$ or DHV$^{+\bullet}$ monocation radicals, known to rely on electron pairing between the radical bipyridinium cores, are broken up in the Cl anion desorption process. This indicates, despite the strong inter-molecular interaction between the viologen monocation radicals, a fundamental role of the Cl anion lattice in the structure formation of viologen π-stacked stripe phases, whereas the stability of the inter-molecular bonds between the C3-DBDP^{2+} dications in the Cl anion desorption process indicates a minor orientational influence of the substrate in the structure formation of the inter-linked stripe phase.

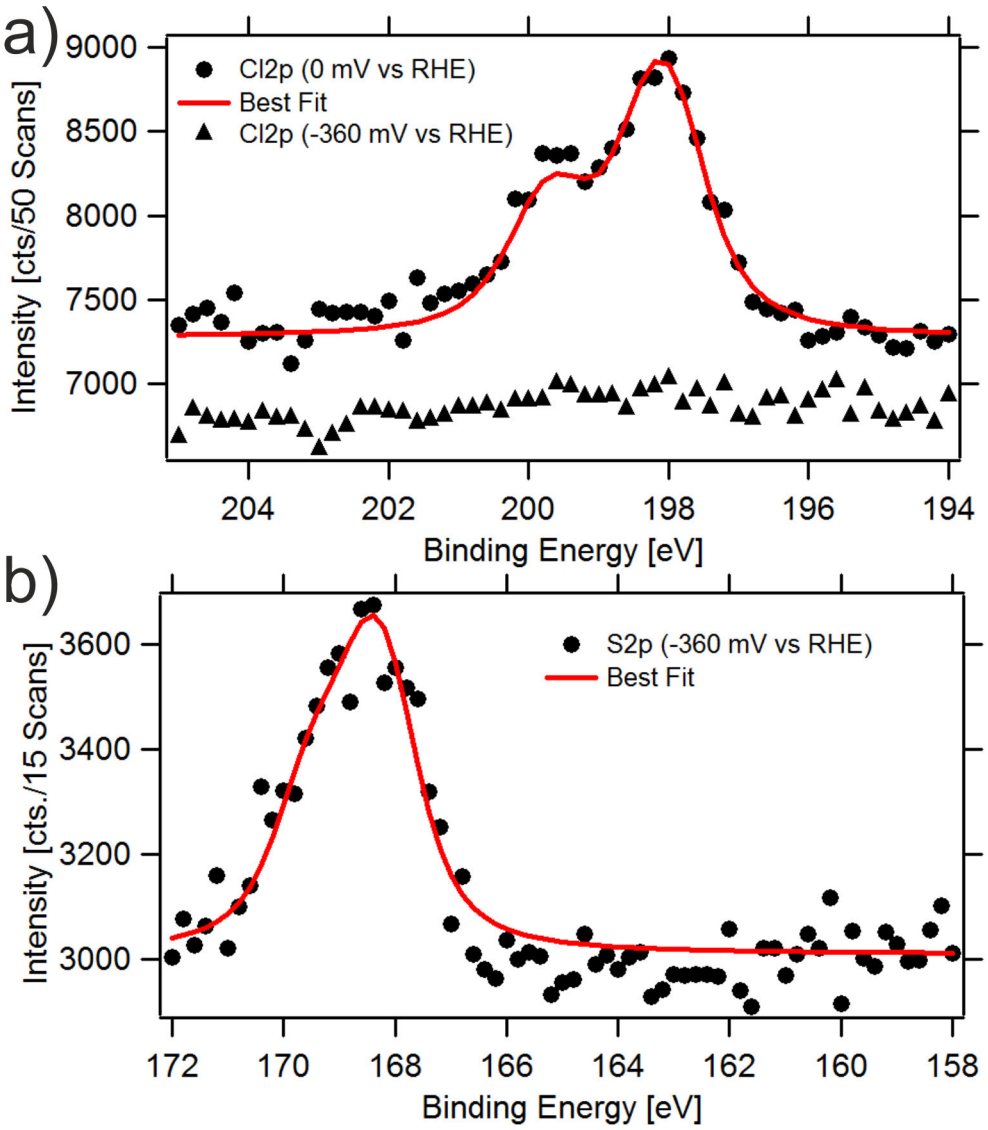

Figure 6.22: XPS spectra of the Cl anion desorption experiment. The sample preparation was verified by registering extended (survey) XPS spectra and high resolved spectra of the C2p and N1s signals (not shown here). (a) Cl2p signal obtained when emersing the sample at electrode potential +0 mV [vs. RHE], but vanished when emersing the sample at -360 mV [vs. RHE], i.e. at a potential below the Cl anion desorption regime. (b) S2p signal originating from SO_4^{2-}, which was introduced due to the performed electrolyte exchange from a 10 mM HCl to a 5 mM H_2SO_4 solution.

6.2.3 C7-DBDP as Building Block

The modification of DBV to C3-DBDP was made in order to increase the *intra*-molecular flexibility. This affected the monolayer structure formation, which for C3-DBDP^{2+} was found to be dominated by *inter*-molecular interactions. Indeed, the adsorbate-substrate interaction between C3-DBDP^{2+} and the Cl-c(2x2) anion lattice was assumed to hinder the structure formation of the C3-DBDP^{2+} inter-linked stripe phase, as it significantly extends the phase formation time. However, at least a fraction of adsorbed C3-DBDP^{2+} dications interacts to adsorption sites of the underlying anion lattice, as the orientation of the C3-DBDP^{2+} stripes is limited to an angular range between 30° and 45° to the main crystallographic Cu fcc directions, namely (100) and (010).

A further increase of the molecular flexibility allows the molecules to position their pyridinium-benzyl moieties even more freely from each other on the Cl anion lattice and therefore might weaken or even lift the competition between adsorbate-substrate and inter-adsorbate interactions observed in the structure formation process of the C3-DBDP^{2+} monolayer. Furthermore such a modification of the molecular structure permits to test and evaluate the robustness of the results obtained and conclusions drawn in the study of C3-DBDP monolayers on the Cl/Cu(100) substrate. The higher molecular flexibility is obtained by substituting the propane-(1,3)-diyl chain, which connects the two pyridinium-benzyl moieties in the C3-DBDP molecule, by a heptane-(1,7)-diyl chain. The resulting molecule is named C7-DBDP, as previously introduced and imaged in figure 6.12.

Electrochemical Characterization

The CVs of a Cu(100) electrode in a solution of 10 mM HCl without additive or with 0.1 mM C7-DBDP^{2+} dications are displayed in figure 6.23. Comparing these subsequently registered CV curves reveals that the presence of C7-DBDP molecules at the Cu(100) electrode surface affects the CV in three ways. At first the Cl anion desorption process is found to be inhibited, second an additional current wave appears at an electrode potential of -425 mV [vs. RHE], and third the HER is shifted to more negative electrode potentials. The shift of the HER to more negative electrode potentials occurs also when DBV or C3-DBDP is introduced into the solid/liquid interfacial regime, as presented in the previous sections. This shift is explained by the adsorption of the organic cations onto the electrode surface, where they block a fraction of the HER reaction sites and therefore at least inhibit the onset of the HER or even decrease the exponential rise of the HER related currents. In contrast to this expected effect, the inhibition of the Cl anion desorption, as well as the appearance of an additional current wave at -425 mV [vs. RHE] are, with respect to the results obtained in the study of C3-DBDP, surprising.

In order to better resolve the additional features in the CV of C7-DBDP, scans at higher speeds, such as e.g. 200 mV/s, were made and compared to equivalent scans obtained for 0.1 mM C3-DBDP^{2+} containing 10 mM HCl, or the pure 10 mM HCl electrolyte (fig. 6.24). The higher scan speed amplifies the electrochemical current

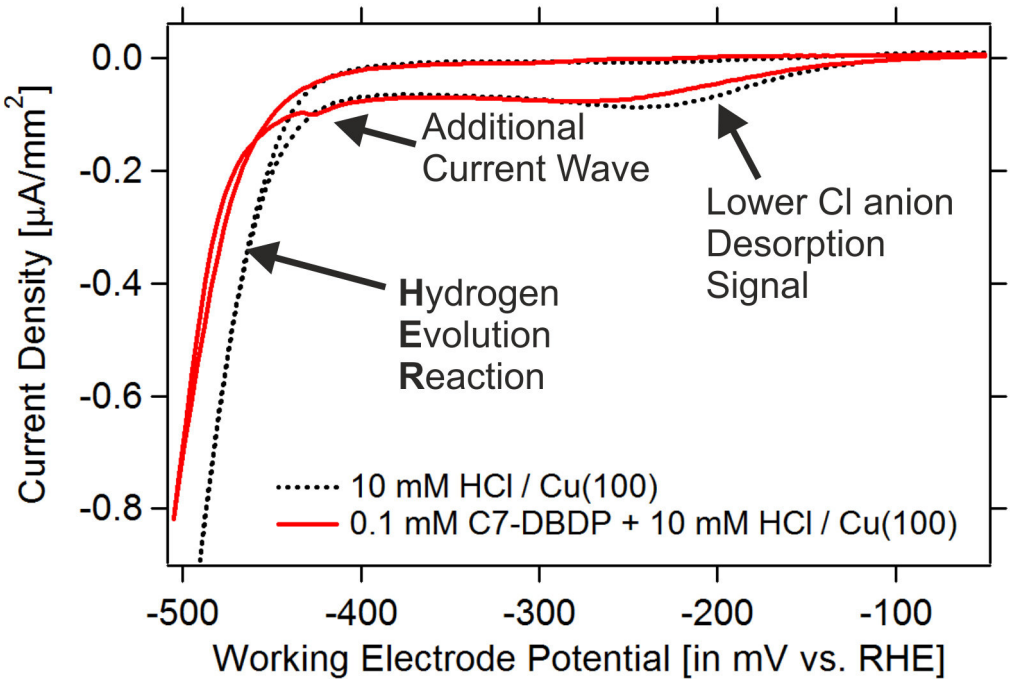

Figure 6.23: CVs of Cu(100) in {0.1 mM C7-DBDP + 10 mM HCl} (red, solid curve) and Cu(100) in {10 mM HCL} (black, dashed curve), both curves registered with a scan speed of 10 mV/sec.

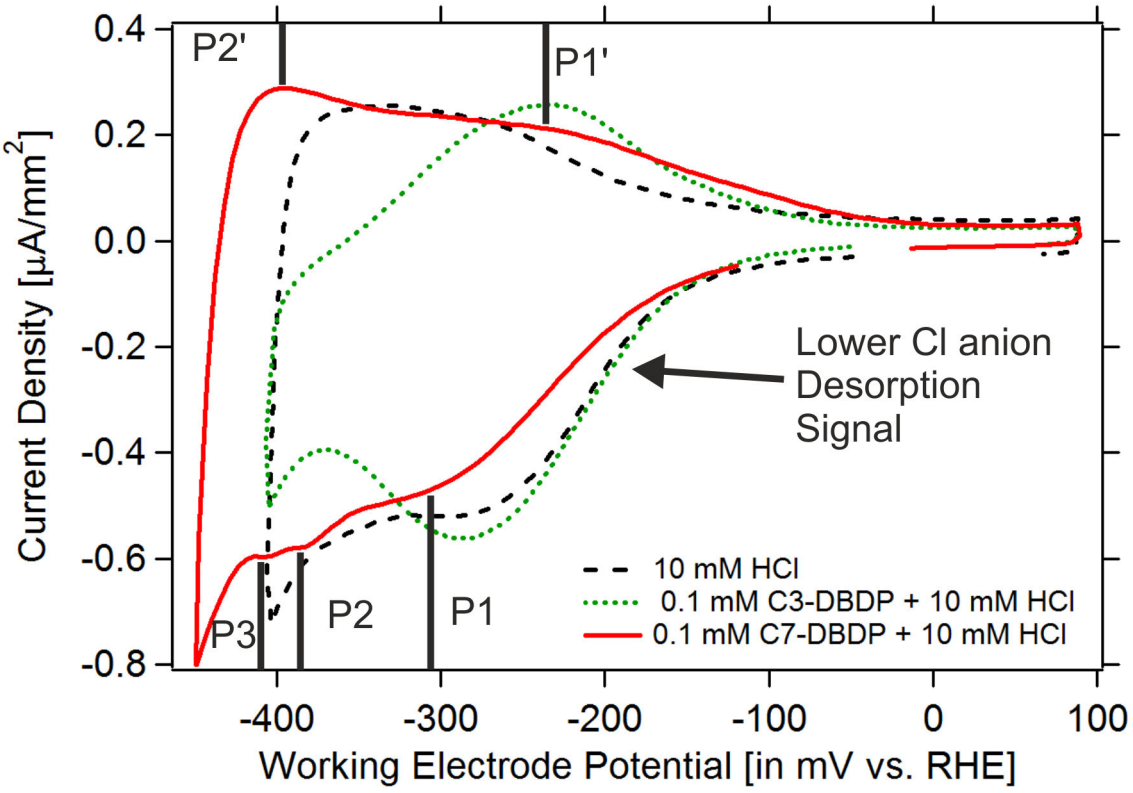

Figure 6.24: CVs registered at a scan speed of 200 mV/s of Cu(100) in {0.1 mM C7-DBDP + 10 mM HCl} (red, solid curve), Cu(100) in {10 mM HCl} (black, dashed curve) and Cu(100) in {0.1 mM C3-DBDP + 10 mM HCl} (green, dotted curve).

waves and makes weak signals more visible than in the initial CV curve registered at 10 mV/s (fig. 6.23).

Figure 6.24 reveals the Cl anion desorption (P1) and related Cl anion adsorption process (P1') in the C7-DBDP CV curve to differ from the equivalent processes in the presence of C3-DBDP^{2+} or in pure 10 mM HCl solution. Compared to the pure or C3-DBDP^{2+} containing 10 mM HCl solution the Cl anion desorption is shifted by -70 mV to a potential of -310 mV [vs. RHE] when C7-DBDP^{2+} is in solution. In addition, the peak width of P1 is slightly broadened and therefore the peak maximum lowered. The shift of the P1 peak maximum, as well as the broadening and therefore less pronounced electrochemical currents, indicate an inhibition of the Cl anion desorption by the presence of C7-DBDP, which is stronger than by a full monolayer of C3-DBDP^{2+} on the Cl anion lattice. This inhibition is, as STM results will confirm later, most likely a result of stronger adsorbate-substrate interactions between adsorbed C7-DBDP and its Cl/Cu(100) substrate, than between the reference molecule C3-DBDP^{2+} and the same Cl/Cu(100) substrate.

The reverse process to P1, named P1', is the Cl anion adsorption and appears in the reverse potential sweep. The CV curves reveal C3-DBDP^{2+} and C7-DBDP^{2+} to have comparable effects on the Cl anion adsorption process, as both organic cations lead to a shift of the current wave P1' to higher electrode potentials. This shift indicates an inhibition of the Cl anion adsorption. The inhibition of the Cl anion adsorption in the presence of C3-DBDP^{2+} was explained previously by the presence of the ordered interlinked stripe structure on the electrode surface (as described in sec. 6.2.2). Consistent with this, STM results of C7-DBDP will reveal that C7-DBDP^{2+} forms as well an ordered organic monolayer on the Cl anion free Cu(100) electrode surface, which is assumed to be the source of the observed inhibition of the Cl anion adsorption. However, in contrast to the C3-DBDP CV, the peak P1' in the C7-DBDP CV is broader and therefore its peak maximum lower. This lower amplitude of the peak P1' prevents a reliable determination of its position. However, via a simple CV analysis, in which the CV line shape was reproduced by a Gaussian shaped peak plus an exponential background, the peak maximum position was found to be at -242 mV [vs. RHE], which is *not shifted* in comparison to the Cl anion desorption found in the presence of C3-DBDP^{2+} at the electrode surface.

This analytical approach to the CV curve also permits to estimate the peak surfaces of the processes P1 and P1' in the presence of C3- or C7-DBDP. Although the peak width and height of both current waves differ between the C3- and C7-DBDP CV, their peak areas stay mostly unaffected. Indeed, the peak surfaces were found to differ by less than 10%, which is within the accuracy of the analysis. These almost identical peak areas indicate the current waves P1/P1' of both CV curves to originate from the same physical process. The relatively high uncertainty of the performed analysis is mainly a result of the role of the Cl anion lattice on the HER reaction, as revealed by Stuhlmann et al. [19]. In order to properly describe the relation between CV currents and surface process a more sophisticated and complex description was proposed [19]. However, the by Stuhlmann et al. used method reproduced the obtained experimental results

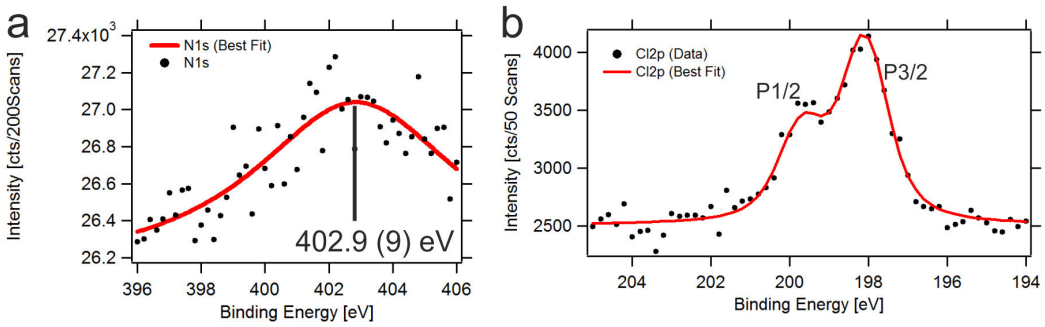

Figure 6.25: XPS spectra of electrochemically adsorbed C7-DBDP^{2+} on the Cl/Cu(100) substrate. Emersion potential 0 mV [vs. RHE]. Experimental error of the electron binding energy, namely E_B(N1s), is stated within parenthesis and refers to the last digit of E_B(N1s). (a) *Ex-situ* measured N1s electron binding energy (E_B(N1s)=402.9 (9) eV). (b) *Ex-situ* measured Cl2p electron binding energy.

only qualitatively and not quantitatively, therefore no significant benefit is expected by applying their method in this work.

In addition to the peak P1, current waves P2 at −385 mV [vs. RHE] and P3 at −406 mV [vs. RHE] appear in the cathodic sweep of the C7-DBDP CV, as shown in figure 6.24. The formation of two current waves may be a result of the proximity of P2 and P3 to the HER. Indeed, according to the study of Stuhlmann et al. [19] the mere proximity of a surface process to the HER may lead to complex and counter intuitive peak shapes. In comparison to the results of Stuhlmann et al. [19] the split of one current wave into two appears to be very plausible. In agreement to this assumption, only one surface process, namely an order-disorder transition of the C7-DBDP adlayer, could be identified during the STM experiments close to the current waves P2 and P3. A further indication for the assumption that one processes is the origin of both current waves P2 and P3 is the instability of the peaks P2/P3, as in subsequent CV scans they were found to unify to one current wave. Despite these strong indications a so far undiscovered/hidden process, which would result in a second current wave, can not be excluded with absolute certainty.

Redox State of C7-DBDP Adsorbed on the Electrode Surface

The molecular structure of C7-DBDP^{2+} and C3-DBDP^{2+} differ only by the length of their saturated organic chain, which connects the redox active pyridinium rings. Therefore the modification of C3- to C7-DBDP strongly affects the molecular flexibility, but not significantly – following common chemical intuition – their redox activity. In order to verify this statement and prove that C7-DBDP^{2+} conserves its dication charge upon adsorption on the Cl/Cu(100) electrode surface, as previously proven to occur for C3-DBDP^{2+}, additional XPS experiments were performed.

The experimental strategy of the XPS experiments aims (as previously in the study of C3-DBDP) at comparing the redox state of electrochemically prepared C7-DBDP adsorbed on the electrode surface (emersion potential 0 V [vs. RHE]) to reference XPS spectra of the previously investigated C3-DBDP and viologen molecules. As a measure to determine the redox state of the C7-DBDP pyridinium the N1s electron binding energy was chosen, which is consistent to previous XPS studies of C3-DBDP (sec. 6.2.2) and viologens [9].

The sample preparation procedure of electrochemical adsorbed C7-DBDP is identical to that used in the STM pre-studies, which will be presented later in this section. Furthermore the success of the XPS sample preparation was verified by survey spectra (not shown here) in order to reveal possible contamination of the sample surface.

In contrast to the STM setup, the so-called hanging meniscus configuration [63] was used in the sample preparation step of the XPS experiments. After the electrochemical preparation of the C7-DBDP monolayer on the Cl/Cu(100) substrate, the Cu(100) surface was wetting-free emersed, which prevented a drying residue on the electrode surface. Subsequently, the protective argon atmosphere was removed by evacuating the preparation chamber and the sample was transferred without exposure to air into UHV, where the XPS spectra were measured.

The subsequently measured highly resolved XPS spectrum of the N1s electrons is shown in figure 6.25, which reveals an N1s electron binding energy of E_B(N1s) = 402.9 (9) eV. The N1s signal is overlayed by significant noise, which is a result of the low amount of nitrogen atoms (about 3%) within a monolayer of C7-DBDP^{2+}. The previously presented XPS spectrum of the electrochemically prepared C3-DBDP^{2+} monolayer on the Cl/Cu(100) substrate was obtained at the synchrotron radiation facility BESSY in Berlin, at which the XPS experiments benefit from a higher photon flux and better energy resolution. Therefore the C3-DBDP XPS spectra are more intense and sharper defined along the binding energy axis. In contrast to the XPS spectrum of C3-DBDP, the C7-DBDP experiment was performed at the in-house XPS chamber. This results in a lower signal/noise ratio of 3.33.

An additional contribution close to a N1s electron binding energy of 400 eV, which would indicate an uncharged pyridinium ring, is excluded, as the XPS data analysis did not reveal any indications for such a contribution. Indeed, the XPS signal of C7-DBDP^{2+} is best described by one single Gaussian shaped peak. The Gaussian shape is a result of the high noise level, as XPS signals are usually best described by a Voigt-profile, which is the convolution of a Lorentz and a Gauss function.

The obtained N1s electron binding energy E_B(N1s) = 402.9 (9) eV proves adsorbed C7-DBDP^{2+} to conserve its dication state. This is concluded from the comparison of the E_B(N1s) of C7-DBDP^{2+} to the similar values of adsorbed C3-DBDP^{2+} on the same substrate (E_B(N1s) = 402.6(1) eV), C3-DBDP^{2+} as dichloride salt (E_B(N1s) = 402.6(1) eV) and adsorbed viologen dications V^{2+} [9, 81]. In contrast to these similar values, the N1s electron binding energy E_B(N1s) of reduced viologen, namely the monocation radicals $V^{+\bullet}$, are found to be lower than 400.7 eV [9, 81], which is 2 eV lower than for adsorbed C7-DBDP^{2+}. This interpretation of the XPS results, namely the conservation of the dication charge upon adsorption of C7-DBDP^{2+}, is in full agreement with the

electrochemical behavior of C7-DBDP^{2+} dications and the previously presented results obtained in the study of C3-DBDP^{2+} dications, in which no reduction of the dication was observed either.

C7-DBDP^{2+} Mesh Phase on Cl-c(2x2)/Cu(100)

In situ STM results (fig. 6.26) prove the adsorption of C7-DBDP^{2+} dications in an ordered "mesh like" phase on the Cl/Cu(100) electrode surface at 0 mV [vs. RHE]. Besides the C7-DBDP^{2+} mesh phase, a second – at 0 mV [vs. RHE] metastable – C7-DBDP^{2+} "stripe phase" is also observed on the Cl/Cu(100) electrode substrate. This stripe arrangement of C7-DBDP^{2+} will be discussed in detail in the following section (chap. 6.2.3), while in this section the focus will lie exclusively on the structure analysis of the C7-DBDP^{2+} mesh phase.

The features visible in the C7-DBDP^{2+} mesh phase are found to be oriented along the close packed directions of the Cl anion lattice, as imaged in figure 6.26b. This indicates adsorbate-substrate interactions to play a supporting role in the structure formation of this organic cation monolayer. The average distances between the in STM images visible features are shown in figure 6.26c, however, for a detailed understanding of the mesh phase higher resolved images, such as shown in figure 6.27, are necessary.

The C7-DBDP^{2+} mesh phase consists of bright circular features, which are connected by less bright and more diffuse features, as imaged in figure 6.27. Consistent with the results of viologens, namely DPV and DBV (chap. 6.1), and C3-DBDP (chap. 6.2.2), the bright circular features are attributed to the in STM images usually bright pyridinium rings, which are marked by red dots in the STM image (fig. 6.27). In contrast to the pyridinium rings, the attribution of the remaining features to either the heptane-(1,7)-diyl chains or benzyl groups remains ambivalent.

In order to determine a model of the C7-DBDP^{2+} mesh phase the position of the C7-DBDP^{2+} dications within the mesh phase has to be determined. However, a direct determination fails, due to the above mentioned ambiguity of the diffuse features of the STM image. Therefore the structure parameters, such as distances and symmetries, are analyzed, as this delivers information on the assignment of pyridinium rings to C7-DBDP^{2+} molecules.

For instance, the whole C7-DBDP^{2+} mesh phase is found to be symmetric to a 90° rotation plus mirror operation. The repetition of this operation (rotation plus mirror operation) results in a simple 180° rotation, as the mirror operations cancel out. This indicates vertical and horizontal features to represent the same molecular groups. Further, the distances of the pyridinium rings within one "row of four pyridinium rings" is not constant. Figure 6.27 shows, that the two central pyridinium rings are only 0.72 nm apart from each other, whereas the two external ones are situated 1.1 nm from the central pyridinium rings. A distance of 0.72 nm between two pyridinium rings (or pyridinium-benzyl moieties) is assumed to be insufficient to accommodate one entire heptane-(1,7)-diyl chain between them. Therefore these two pyridinium-benzyl moieties are attributed to two different, but neighboring, C7-DBDP^{2+} dications. In contrast to 0.72 nm, 1.1 nm is a sufficiently wide distance between two neighboring pyridinium rings

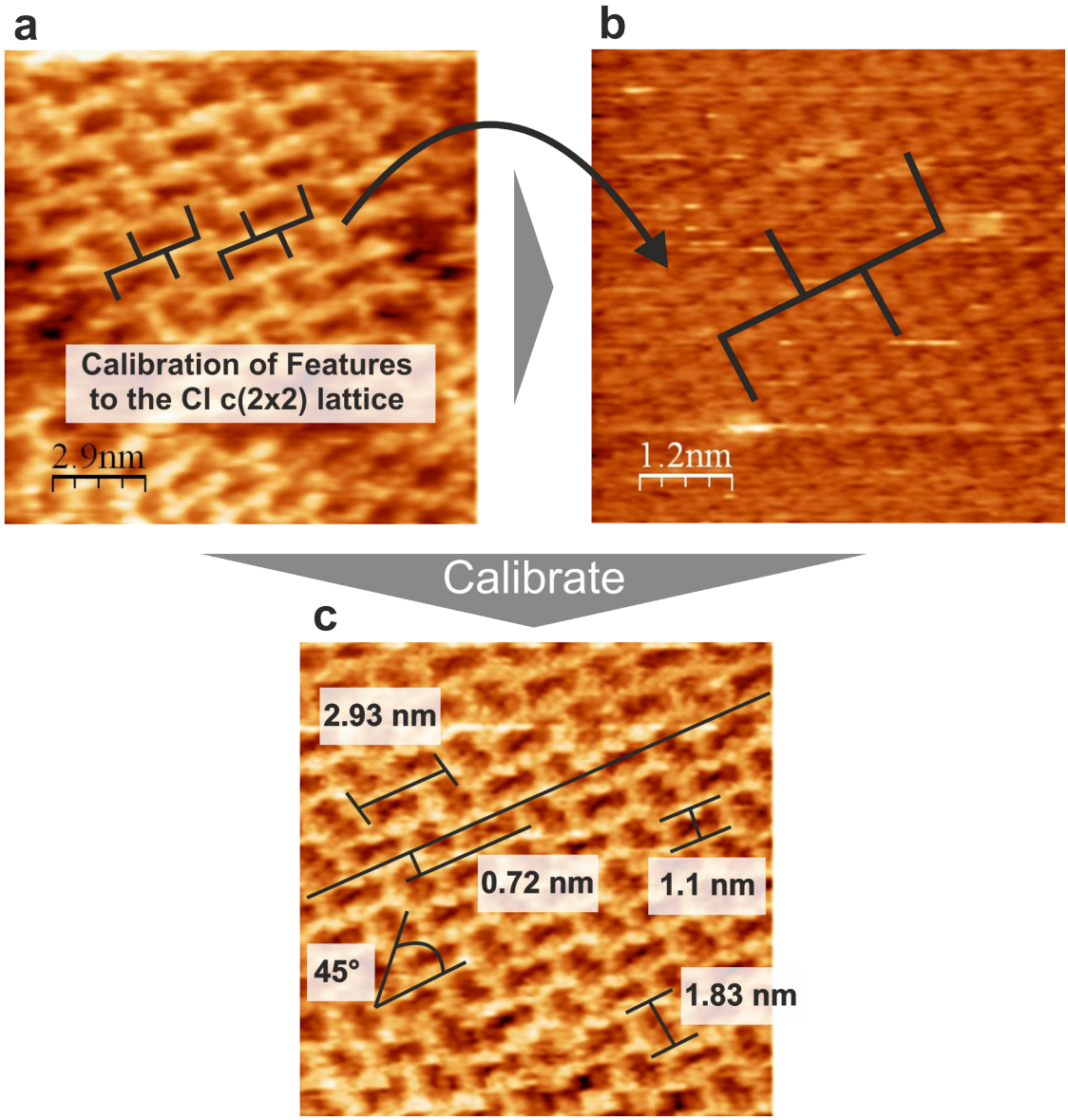

Figure 6.26: Calibration of STM images of the "mesh-like" C7-DBDP^{2+} monolayer to the underlying and well defined Cl-c(2x2) lattice. (a) 14.7 nm x 14.7 nm, $U_{Bias} = +275\,mV$, $I_{Tunnel} = 0.1\,nA$, $E_{Work} = +0\,mV$ [vs. RHE]. (b) 5.78 nm x 5.78 nm, $U_{Bias} = +50\,mV$, $I_{Tunnel} = 9\,nA$, $E_{Work} = +0\,mV$ [vs. RHE]. (c) 17.0 nm x 17.0 nm, $U_{Bias} = +310\,mV$, $I_{Tunnel} = 0.1\,nA$, $E_{Work} = +0\,mV$ [vs. RHE].

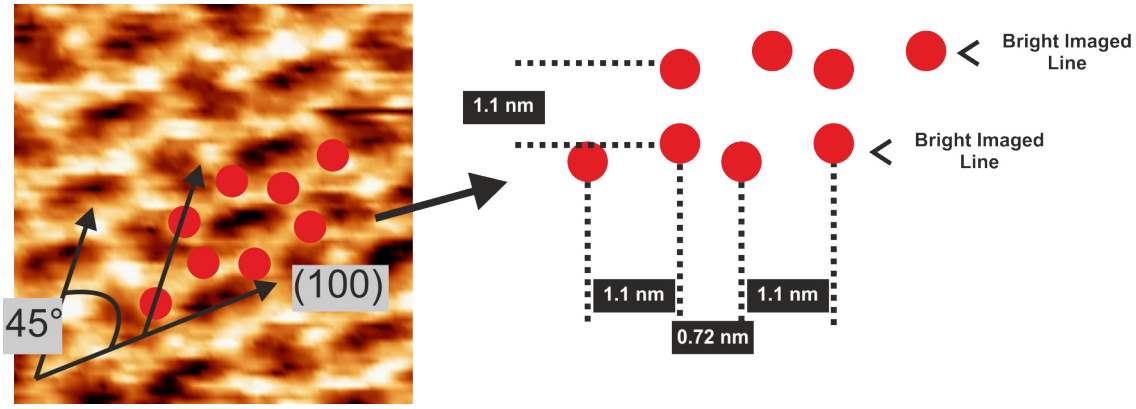

Figure 6.27: Distances of pyridinium rings within the C7-DBDP^{2+} mesh phase exemplary shown in the horizontal direction, but valid as well for the vertical direction. 7.92 nm x 7.92 nm, $U_{Bias} = +255\,mV$, $I_{Tunnel} = 0.1\,nA$, $E_{Work} = +0\,mV$ [vs. RHE].

to accommodate one whole heptane-(1,7)-diyl chain. Consequently all pyridinium rings at a distance of 1.1 nm from each other may be part of the same C7-DBDP^{2+} dication. Unfortunately all pyridinium rings possess two neighboring pyridinium rings at a distance of 1.1 nm, which again results in an ambiguity in the analysis procedure, because only two of them can be attributed to one C7-DBDP^{2+} dication. However, as each pyridinium ring possess only one neighboring pyridinium ring at 0.72 nm the number of plausible molecular arrangements is limited.

Therefore as a starting point for the development of an structure model the pairwise interacting pyridinium-benzyl moieties, marked by arrows in figure 6.28b, were chosen. The STM image (fig. 6.28b) highlights the periodicity of the inter-molecular interaction throughout the whole C7-DBDP^{2+} mesh arrangement. As stated before, each pyridinium ring has exactly one neighboring pyridinium ring at a distance of 0.72 nm but two at a distance of 1.1 nm, as visible in figure 6.28b. Consequently in figure 6.28c and d, the two only possible combinations of the orientation of two interacting C7-DBDP^{2+} dications are sketched, namely the so-called linear and angular motif. In both STM images pyridinium rings are marked by circles and the heptane-(1,7)-diyl chain connecting two pyridinium rings is marked by a line between the circles.

From the mathematical point of view four possible motifs exist, as two either vertically (V) or horizontally (H) oriented C7-DBDP^{2+} dications can be combined in four different ways, namely VV, VH, HV, HH. However, the rotational symmetry of the C7-DBDP^{2+} mesh phases reduces these four to two distinguishable basic motifs, namely VV = HH (linear) and VH = HV (angular). In addition to the remaining two, a mixed motif, involving a more complex arrangement of both basic motives, can not be fully excluded.

At this point it must be stated, that non of the basic motifs, namely linear or angular, explains the obtained experimental significantly better than the other. However, with respect to the results obtained in the study of the C3-DBDP^{2+} inter-linked stripe

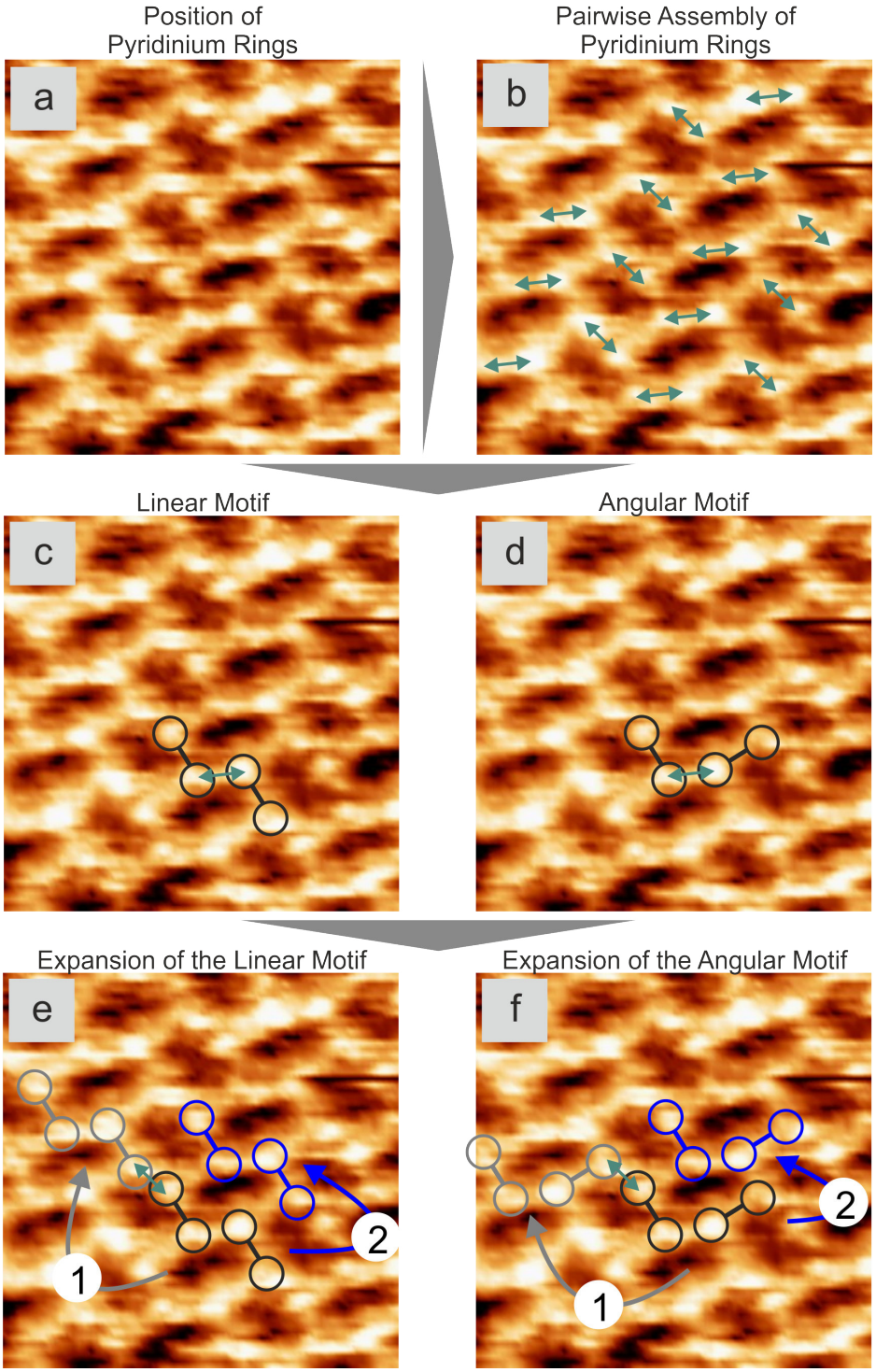

Figure 6.28: Highly resolved STM image of the "mesh-like" C7-DBDP^{2+} monolayer adsorbed on Cl/Cu(100) substrate and sequence of its analysis (a - e). Pyridinium rings are marked by circles and the possible position of the heptane-(1,7)-diyl chain between two pyridinium rings by the line connecting them. Description and details see text. 7.92 nm x 7.92 nm, $U_{Bias} = +255\,mV$, $I_{Tunnel} = 0.1\,nA$, $E_{Work} = +0\,mV$ [vs. RHE].

phase one questions may be asked: " Why does the linear arrangement (fig. 6.28c) not lead to the formation of long extended inter-linked stripes, as they appear in the C3-DBDP^{2+} inter-linked stripe phase?" This question would rather point to the DBV-cavitand like "angular arrangement" of C7-DBDP^{2+} dications. However, reasons, such as stress within the C7-DBDP^{2+} mesh structure originating from the competition between the inter-molecular and adsorbate-substrate, may be possible explanation for the breaks in the linear "C3-DBDP^{2+}-like" motif. Consequently both motives remain possible explanations, as non can be excluded with absolute certainty.

The two basic motifs, linear (fig. 6.28c) and angular (fig. 6.28d), must be periodically repeated in order to obtain the C7-DBDP^{2+} mesh phase. This repetition is sketched in figure 6.28e for the linear motif and in figure 6.28f for the angular motif. As mentioned before, each pyridinium ring has only one neighboring pyridinium ring at a distance of 0.72 nm. Therefore the logic step in the construction of the mesh phase is to add C7-DBDP^{2+} dications at the points of "pairwise inter-molecular interaction". This step is marked with the arrow number 1 in figure 6.28e and f. The repetition of this operation results in either straight (fig. 6.28e) or zigzag shaped (fig. 6.28f) rows of C7-DBDP^{2+} dications. This single operation is insufficient to reproduce the whole C7-DBDP^{2+} mesh phase. Therefore a second operation must be performed, which is the periodic repetition of the by operation 1 constructed C7-DBDP^{2+} rows in a direction 45° off the close packed Cl anion rows, (100) or (010). This second operation is marked in figure 6.28e and f by the arrow number 2. The formation of the rows of C7-DBDP^{2+} dications can be understood as a result of the inter-molecular interaction, i.e. between neighboring pyridinium-benzyl moieties, as found for C3-DBDP^{2+} (sec. 6.2.2) or assumed for DBV^{2+} (sec. 6.1). In contrast to this, the interaction between neighboring rows of C7-DBDP^{2+} dications (operation number 2 in fig. 6.28e and f) remains unclear. Indeed, the STM images reveal a diffuse intensity between the 1.1 nm distant pyridinium rings of neighboring rows, which can no longer be explained by the heptane-(1,7)-diyl chain. Therefore these intensities are attributed to benzyl groups or Cl anion build inbetween the C7-DBDP^{2+} rows. However, further study is needed to conclude on or exclude these first assumptions.

Based on the in figure 6.28e and f sketched "linear" and "angular" mesh phases and the extracted structure parameters (fig. 6.26), two different models of the C7-DBDP^{2+} mesh phase can be derived, which are shown in figure 6.29a and b, respectively. Both models must be understood as a first conclusion of the up to here discussed structure of the C7-DBDP^{2+} mesh phase. Beside the well known periodicity of the pyridinium rings within the organic monolayer adsorbed on the substrate, most structure parameters remain unproven or unknown. For instance, in the linear mesh phase model, figure 6.29a, an inter-molecular interaction is assumed, which is based on those proposed for the C3-DBDP^{2+} inter-linked stripe phase (sec. 6.2.2). This choice might be questioned due to the almost substrate independent properties of the C3-DBDP^{2+} phase, whereas the C7-DBDP^{2+} mesh phase is found to be strongly related to the underlying Cl-c(2x2) lattice. Therefore in 6.29b an arrangement of the pyridinium-benzyl moieties is suggested, in which the pyridinium rings align with their ring plane along the close packed directions of the Cl anion lattice, (100) and (010), similar to what is known to be the case in DPV

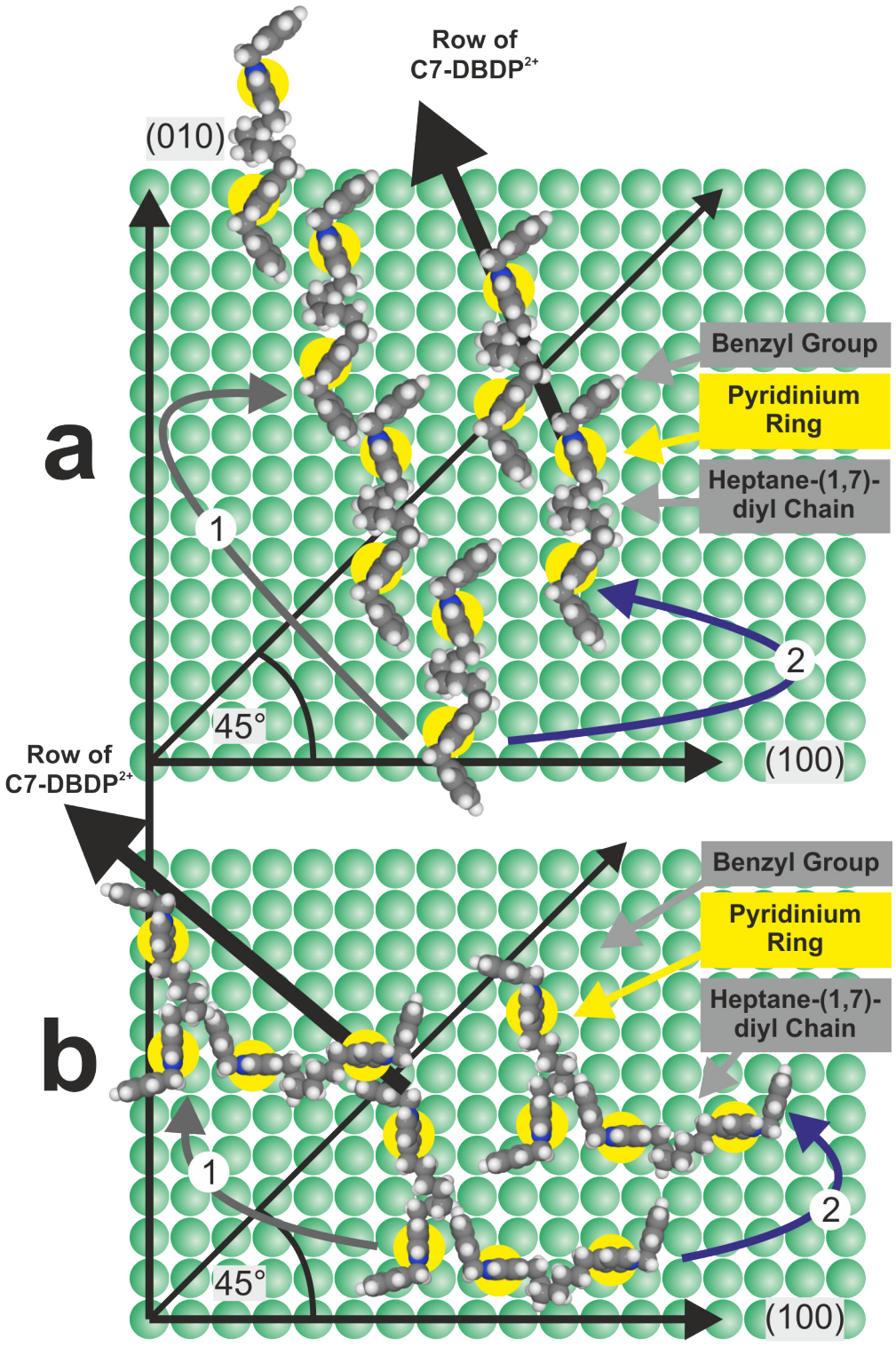

Figure 6.29: Model of the C7-DBDP^{2+} mesh phase on the Cl/Cu(100) electrode surface.

and DBV phases (sec. 6.1). However, these choices are not intrinsice to the linear or angular motif and should therefore only be understood as a first suggestion.

However, a particular difference between the two arrangements of pyridinium-benzyl moieties (fig. 6.29a and b) must be pointed out. Namely, the inter-molecular interaction inspired by the C3-DBDP^{2+} inter-linked stripe phase (fig. 6.29a) involves both benzyl groups and pyridinium rings of the neighboring pyridinium-benzyl moieties. In contrast to this, the by the DBV^{2+} cavitand phase inspired inter-molecular interaction (fig. 6.29b) involves only one benzyl group and one pyridinium ring, which can be assumed to represent lower inter-molecular attractive forces. This reduced inter-molecular attraction can be assumed to be compensated by stronger adsorbate-substrate interactions, which is, indeed, one of the core properties of the C7-DBDP^{2+} mesh phase.

In both models of the C7-DBDP^{2+} mesh phase (fig. 6.29a and b) the C7-DBDP^{2+} dications are found to form rows, along which all molecules are found to be connected via attractive forces between their pyridinium-benzyl moieties. Despite the clear attraction between C7-DBDP^{2+} dications within one row, the inter-molecular interaction between C7-DBDP^{2+} dications situated in different rows remains unclear within both suggested models of the mesh phase. This is a direct consequence of the ambivalent experimental results, as was discussed previously.

C7-DBDP^{2+} Stripe Phase on Cl-c(2x2)/Cu(100)

Beside the C7-DBDP^{2+} mesh phase, the adsorbed C7-DBDP also form domains of stripes at 0 mV [vs. RHE] on the Cl/Cu(100) electrode surface (fig. 6.30). These domains of stripes are energetically less favored than the C7-DBDP^{2+} mesh phase structure and therefore eventually vanish from the Cl/Cu(100) substrate in favor of the C7-DBDP^{2+} mesh structure. The phase transition from the stripe to the mesh phase occurs within several hours, which indicates an inhibition of this process. This inhibition may result from an activation energy for the phase transition process or from a very small driving force for the process, resulting from almost identical adsorption energies of both phases on the Cl/Cu(100) substrate.

In order to draw conclusions, at first the charge state of C7-DBDP within the stripe phase has to be studied. For this the previously presented XPS spectra were carefully examined. The XPS spectrum (fig. 6.25a) represents a freshly electrochemically prepared sample surface, as the adsorption and structure formation of C7-DBDP molecules occurred in only 10 minutes. After these to this 10 minutes, the sample was wetting-free emersed from the electrolyte solution at 0 mV [vs. RHE], which is known to conserve the sample state [9]. The sample preparation time is of particular importance in the investigation of C7-DBDP adlayers, as freshly prepared C7-DBDP samples ensure a maximum of the metastable – over several hour decaying – stripe phase domains to be present on the Cl/Cu(100) substrate.

Subsequently to the electrochemical adsorption of C7-DBDP, the XPS spectrum of the N1s electrons, shown in figure 6.25a, was registered. This spectrum can only be described by one Gaussian shaped peak, indeed no stable fit with two peaks could be obtained in the analysis of this spectrum. This indicates that all C7-DBDP adsorbed

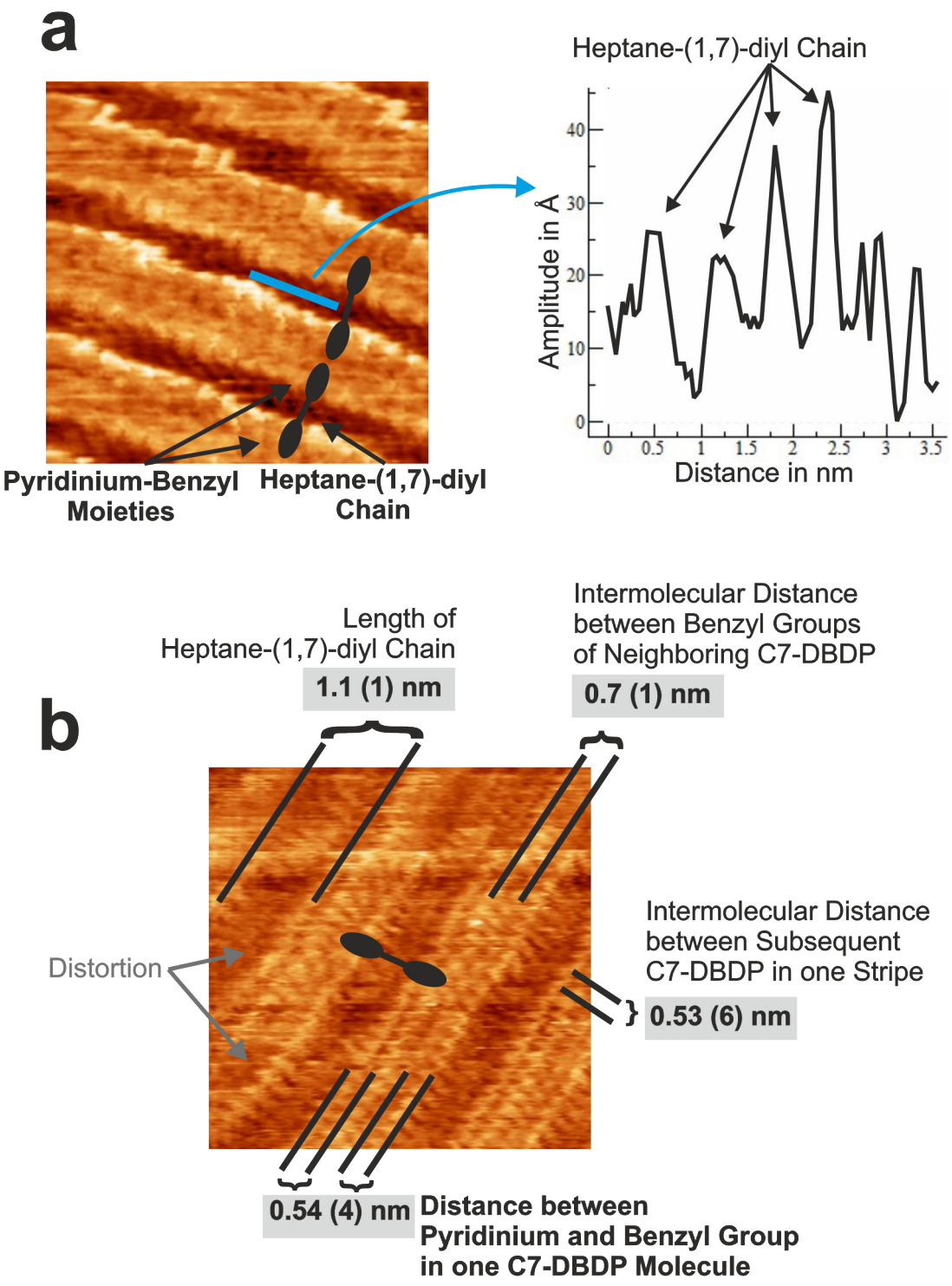

Figure 6.30: STM images of the C7-DBDP^{2+} "stripe structure" adsorbed on the Cl/Cu(100) substrate. Description and details see text. (a) 9.6 nm x 9.6 nm, $U_{Bias} = +150\,mV$, $I_{Tunnel} = 0.1\,nA$, $E_{Work} = +0\,mV$ [vs. RHE]. (b) 9.6 nm x 9.6 nm, $U_{Bias} = +47\,mV$, $I_{Tunnel} = 0.1\,nA$, $E_{Work} = +0\,mV$ [vs. RHE].

on the Cl/Cu(100) surface at 0 mV [vs. RHE] possess the same, namely the dication state C7-DBDP^{2+}. Consequently it can be concluded that the C7-DBDP stripe phase consists of C7-DBDP^{2+} dications. This result is not surprising, indeed the reduction of only a fraction of C7-DBDP^{2+} dications, namely those forming the C7-DBDP^{2+} stripe phase, would have actually been a surprising result.

In addition to this direct prove of the redox state of C7-DBDP within its stripe phase, an indirect prove exists. Assuming that the stripe phase consists of reduced C7-DBDP, then increasing the electrode potential from 0 mV to +175 mV [vs. RHE] would be expected to increase the decay rate of the stripe phase. This can be stated, as the phase transition from the C7-DBDP stripe phase to the C7-DBDP^{2+} mesh phase would then involve the oxidation of the reduced C7-DBDP, which must be favored at more positive electrode potentials. As STM results prove, the decay rate of the C7-DBDP stripe phase is not significantly increased at higher electrode potentials, i.e. +175 mV [vs. RHE]. Consequently no oxidation is assumed to play a role in the phase transition from the stripe to the mesh phase, which therefore both can be taken to consist of C7-DBDP^{2+} dications.

Within the C7-DBDP^{2+} stripe phase the cationic pyridinium rings directly face each other, despite the electrostatic repulsion between them. This appears at first sight surprising, however, such a close proximity of cation charges was also observed in viologen monocation radical π-stacked stripe phases, in which the monocationic bipyridinium cores directly face each other and are situated only 0.36 nm from each other. In contrast to this viologen phase, in the C7-DBDP^{2+} stripe phase the cation NND is 47% wider (0.53 nm), which weakens the intermolecular electrostatic repulsion by 53% (following the Coulomb law). This permits to reject the initial doubts, as already a small expansion of the NND between the cation charges strongly reduces the electrostatic repulsion between them, which is assumed to permit the attractive forces to stabilize the C7-DBDP^{2+} stripe structure.

The conclusion that C7-DBDP^{2+} dications are, indeed, the building blocks of the C7-DBDP stripe phase raises the question, which attractive interactions are involved in the stabilization of the stripe arrangement of C7-DBDP^{2+} dications. This can be best addressed by analyzing the C7-DBDP^{2+} stripe phase structure in all its details. Figure 6.30 shows the structure parameters obtained in the *in situ* STM study of the C7-DBDP^{2+} stripe phase. After calibrating the STM images versus the underlying Cl anion lattice, line scans were made and all relevant structure parameters extracted. The line scan along the dark imaged trench (fig. 6.30a), revealed a periodic structure, which is hardly visible with bare eyes. Based on the study of heptylviologen [10] and the in this work resolved C3- and C7-DBDP^{2+} phases, the trenches are attributed to the, in general dark imaged, alkane chains, namely the heptane-(1,7)-diyl chains, which connect the two pyridinium-benzyl moieties of one C7-DBDP^{2+} dication. In better resolved STM images, such as figure 6.30b, the bright C7-DBDP^{2+} stripes were found to consist of bright circular features alignd in rows of four. The circular features are attributed to the pyridinium rings and benzyl groups. This assignment is based on the arrangement of the circular features in rows of four and the ratio between circular features and heptane-(1,7)-diyl chains, namely four circular features per one heptane-(1,7)-diyl chain. The

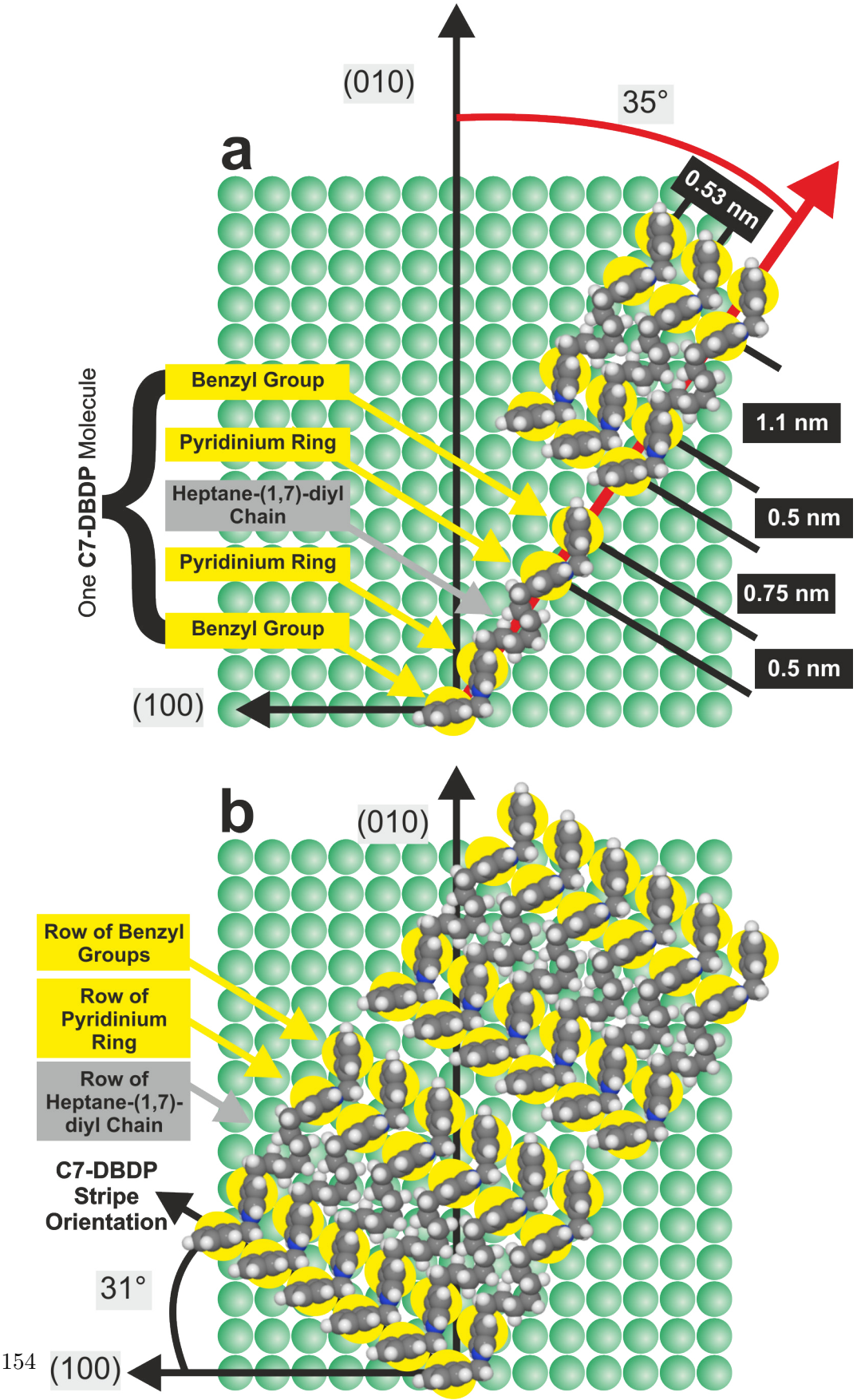

Figure 6.31: Model of the C7-DBDP^{2+} stripe phase on the Cl/Cu(100) electrode surface.

extracted structure parameters, such as distances and orientations, permit finally to construct a model of the C7-DBDP^{2+} stripe phase, shown in figure 6.31.

The distances stated in the model of the C7-DBDP^{2+} stripe phase (fig. 6.31) are theoretical values for an epitaxial organic cation monolayer. These theoretical distances match, within the experimental accuracy, the average values obtained in the analysis of the STM images (fig. 6.30b). Not included in the proposed model is the "wave-like distortion" of the C7-DBDP^{2+} stripe boarders (fig. 6.30). These wave-like distortions, marked by gray arrows in fig. 6.30b, are assumed to originate from the adaption of the cationic pyridinium rings to the adsorption sites of the Cl-c(2x2) anion lattice along 31° off the close packed direction of the substrate.

The arrangement of C7-DBDP^{2+} dications in stripes results in significant intermolecular electrostatic repulsion between consecutive C7-DBDP^{2+} molecules in one stripe. This repulsive force must be compensated by attractive forces, such as adsorbate-substrate, inter-molecular and counterion-adsorbate attractions. The adsorbate-substrate attraction is based on the electrostatic attraction between the C7-DBDP^{2+} dication and Cl anion monolayer underneath, which is assumed to be maximized at specific adsorption sites of the substrate. The inter-molecular attractions are assumed to be based on a Van der Waals like attraction between neighboring benzyl groups and between consecutive heptane-(1,7)-diyl chains (fig. 6.31). In addition to these two interactions, indications for counterion-adsorbate interactions were found (sec. 6.2.3). Counterions, namely Cl anions, may adsorb into or onto the C7-DBDP^{2+} stripe phase, most likely close to the cationic pyridinium rings. The mere presence of a Cl anion between two pyridinium rings would transform the net electrostatic repulsion into a net electrostatic attraction, as can be easily understood by Coulombs law. The presence of Cl anions close to the organic cation monolayer is in full agreement with the SXRD results presented in sec. 5.4, which proved that solvated couterions not only accumulate at the electrode surface, but moreover form an in-plane ordered layer. This indicates significant interactions between solvated counterions and the electrode surface, making the presence of Cl anion within or above the cationic pyridinium rings a more likely process.

Electrode Potential Induced C7-DBDP^{2+} Phase Transitions

Processes at surfaces are usually controlled by the parameters pressure/concentration and temperature. At the interface of conductive fluids, such as electrolytes, and conductive solids, such as metals, processes can be additionally controlled through the variation of the electrochemical potential of the solid electrode. The electrochemical potential can trigger redox reactions or other charge related surface processes (including phase transitions [5] or adlayer ad-/desorptions [6]) at/from electrode surfaces. Therefore the impact of the electrochemical potential on C7-DBDP^{2+} dications at the surface is of particular interest and consequently studied in this sub-section.

Figure 6.32 images the C7-DBDP^{2+} stripe and mesh phase co-adsorbed on the Cl-c(2x2) covered Cu(100) substrate at various electrode potentials. The experimental results prove that both C7-DBDP^{2+} phases, stripe and mesh phase, are stable till the onset of the Cu corrosion process at +175 mV [vs. RHE] (fig. 6.32a), in which the Cu

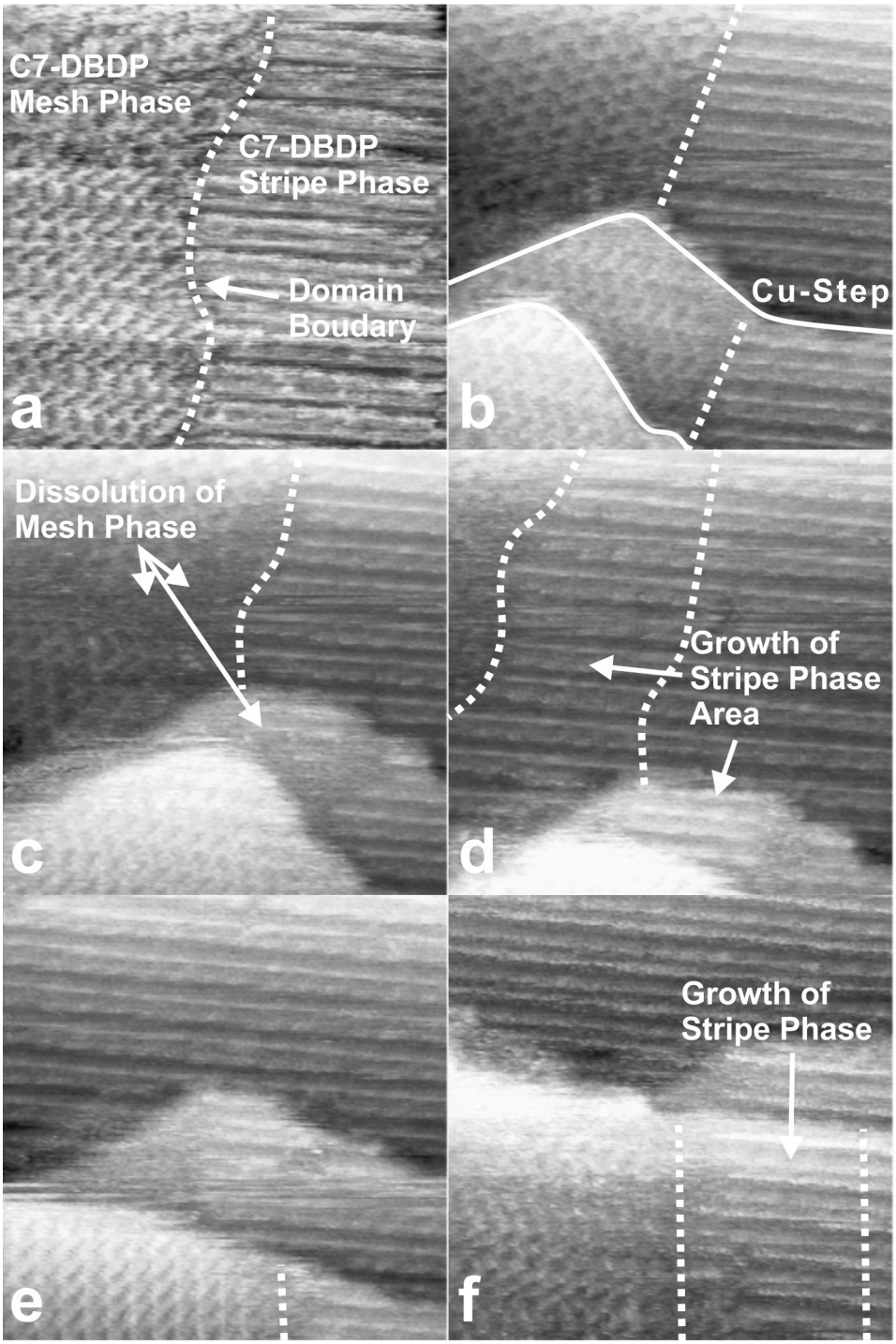

Figure 6.32: Series of STM images. Probing the potential dependence of the C7-DBDP^{2+} stripe and mesh phase adsorbed on the Cl/Cu(100) substrate. Description and details in text. 29.4 nm x 29.4 nm, $U_{Bias} = +312 mV$, $I_{Tunnel} = 0.1 nA$, (a) $E_{Work} = +175\, mV$ [vs. RHE]. (b) $E_{Work} = -250\, mV$ [vs. RHE]. (c) $E_{Work} = -290\, mV$ [vs. RHE]. (d) $E_{Work} = -300\, mV$ [vs. RHE]. (e) $E_{Work} = -400\, mV$ [vs. RHE]. (f) $E_{Work} = -150\, mV$ [vs. RHE].

substrate is oxidized and Cu ions are released into the electrolyte solution. Lowering the working electrode potential into the onset of the Cl anion desorption at -250 mV [vs. RHE] (fig. 6.32b) and subsequently deep into the Cl anion desorption regime to -290 mV [vs. RHE] (fig. 6.32c) results in the desorption of Cl anions from the electrode surface, which is visible through the reconstruction of Cu steps. The Cu steps are found to rearrange in order to follow the C7-DBDP^{2+} stripe direction, instead of following the by Cl anion stabilized (100) and (010) directions.

In addition to the Cl anion desorption, the C7-DBDP^{2+} mesh phase undergoes an order-disorder transition, beginning at its domain boarders. In contrast to the mesh phase, the C7-DBDP^{2+} stripe phase shows no indication for a decay process upon desorption of the Cl anion monolayer. Indeed, the contrary can be observed, as the existing C7-DBDP^{2+} stripe domains expand into the – formerly by the mesh phase occupied – amorphous C7-DBDP^{2+} domains on the bare, i.e. Cl anion free, Cu(100) electrode surface (fig. 6.32d).

The order-disorder transition upon desorption of the Cl anion lattice also occurs at a DBV$^{+\bullet}$ π-stacked stripe covered Cl/Cu(100) surface [6], however, distinct differences between both order-disorder transition can be observed. The phase transition of DBV$^{+\bullet}$ π-stacked stripes to an amorphous DBV$^{+\bullet}$ layer takes place not only at the domain boarders, but also within the DBV$^{+\bullet}$ π-stacked stripe domains. Further the phase transition rate is found to be dependent of the electrode potential. Indeed, the sudden reduction of the electrode potential induces the instantaneous desorption of Cl anions and therefore the instantaneous breakdown of the order DBV$^{+\bullet}$ structure. In contrast to these observations, the order-disorder transition of the C7-DBDP^{2+} mesh phase is limited to the domain boarders, as no decay centers within intact mesh domains were observed. Further the phase transition rate is found to be slow, as it extends over several minutes, and to be independent of the electrode potential, as lowering the electrode potential to -400 mV [vs. RHE] does not induce an immediate break down of the C7-DBDP^{2+} mesh phase (fig. 6.32e). Both stated differences between the order-disorder transition of the DBV$^{+\bullet}$ and C7-DBDP^{2+} phases point to a higher stability of the C7-DBDP^{2+} mesh phase. It can be assumed that the higher intra-molecular flexibility of C7-DBDP^{2+} dications permits them to adapt more easily to changes of the substrate surface. In agreement with this conclusions is the stability of the other C7-DBDP^{2+} structure, namely the stripe phase, throughout the desorption of the Cl anions substrate, which also points to a fundamental role of the intra-molecular flexibility in the stability of organic monolayers.

In the at first presented potential depended study (fig. 6.32) the electrode potential was lowered till the onset of the HER at -400 mV [vs. RHE]. This did not reveal any processes, which might be related to the, in the CVs observed, current waves situated close to -400 mV [vs. RHE] (fig. 6.23 and 6.24). Therefore a second experiment was performed, in which the electrode potential was lowered deeper into the HER regime (which usually is avoided to prevent an increase of the surface roughness induces by the HER).

Figure 6.33 illustrates the obtained STM images of this experiment. Lowering the electrode potential from -100 mV [vs. RHE] (6.33a) to -370 mV [vs. RHE] (6.33b)

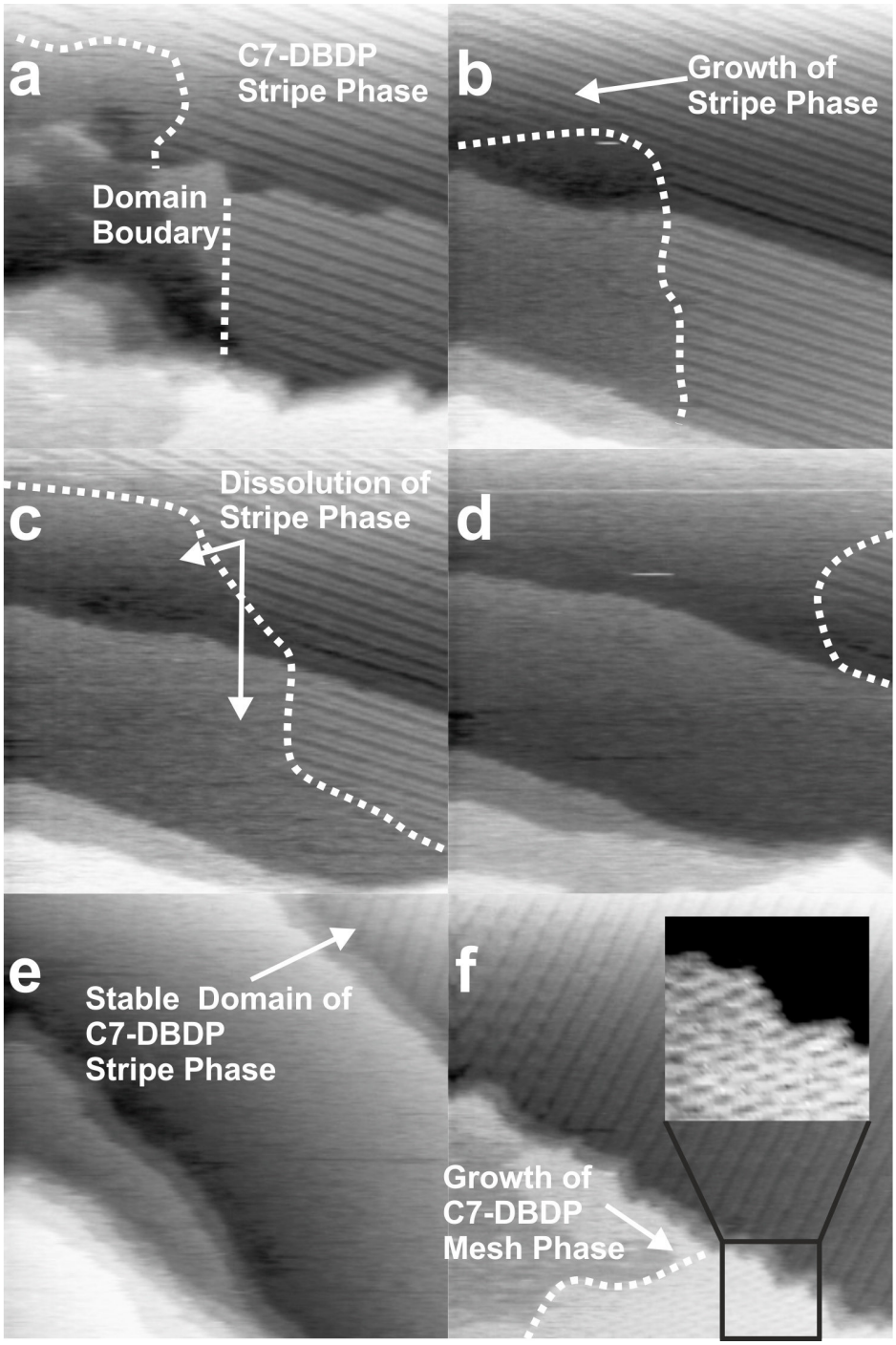

Figure 6.33: Series of STM images. Probing the potential dependence of the C7-DBDP^{2+} stripe phase adsorbed on the Cl/Cu(100) substrate. Between the STM images (d) and (e) the working electrode potential was lowered for about 2.5 min lower than -460 mV [vs. RHE]. Further descriptions and details in text. 58.4 nm x 58.4 nm, $U_{Bias} = +290\,mV$, $I_{Tunnel} = 0.1\,nA$, (a) $E_{Work} = -100\,mV$ [vs. RHE]. (b) $E_{Work} = -370\,mV$ [vs. RHE]. (c) $E_{Work} = -400\,mV$ [vs. RHE]. (d) $E_{Work} = -430\,mV$ [vs. RHE]. (e) $E_{Work} = -430\,mV$ [vs. RHE]. (f) $E_{Work} = -130\,mV$ [vs. RHE].

leads, as in the previous experiment, to the Cl anion desorption, which triggers the order-disorder transition of the C7-DBDP^{2+} mesh phase and the subsequent growth of the C7-DBDP^{2+} stripe phase in the amorphous C7-DBDP^{2+} domains. Lowering the electrode potential further to potentials beyond the current waves observed close to -400 mV [vs. RHE] (fig. 6.23) induces a second order-disorder transition, namely of the C7-DBDP^{2+} stripe phase to an amorphous monolayer of C7-DBDP^{2+} dications on the electrode surface, as proven by figure 6.33c. This order-disorder transition is, as in the case of the C7-DBDP^{2+} mesh phase, limited to the domain boarders and does not affect the stripe domain centers (fig. 6.33d). Between 6.33d and 6.33e the working electrode potential was lowered for several minutes to potentials of -460 mV [vs. RHE], in order to study the possible dependence of this phase transition rate on the electrode potential. However, this reduction of the electrode potential did not lead to a sudden and complete breakdown of the C7-DBDP^{2+} stripe phase, as proven by figure 6.33e. These observations prove a particular stability of the C7-DBDP^{2+} stripe phases, as previously found to be the case for the C7-DBDP^{2+} mesh phase. The most likely explanation is the higher intra-molecular flexibility, which permits the C7-DBDP^{2+} dications to reach new equilibrium states more easily and without significantly weaken the inter-molecular interactions. However, strong intra-molecular attraction can not be ruled out to play as well a fundamental role in these observations. Finally increasing the electrode potential again to -130 mV [vs. RHE] leads to the Cl anion re-adsorption, which subsequently forces remaining amorphous C7-DBDP^{2+} monolayers to undergo an disoder-order transition, e.g. to the C7-DBDP^{2+} mesh phase as imaged in figure 6.33f or on long term forces the C7-DBDP^{2+} stripe domains to decay to the more favored C7-DBDP^{2+} mesh arrangement.

It remains unproven what induces the observed order-disorder transition of the C7-DBDP^{2+} stripe phase. It is unlikely that the phase transition is induced by the onset of the HER, as at -400 mV the HER reaction rate is still rather low. This is consistent with the observations made in the study of the C3-DBDP^{2+} inter-linked stripe phase, which was found to be stable even for potentials deep within the HER regime. It appears also unlikely that the Cl-c(2x2) anion monolayer is involved, as the specifically adsorbed Cl anions are at -400 mV [vs. RHE] supposed to be fully desorbed from the Cu(100) electrode surface. Indeed, the C7-DBDP^{2+} stripe phase domains are found to grow even into the amorphous C7-DBDP^{2+} domains, in which no Cl anion layer is anymore present on the Cu(100) surface. Therefore the order-disorder transition of the C7-DBDP^{2+} stripe phase is either a result of the weakening of the adsorbate-substrate interactions or related to the vanishing of a so far unknown for the structure formation of the C7-DBDP^{2+} stripe phase essential element.

A weakening of the adsorbate-substrate interactions between C7-DBDP^{2+} dications and negatively charged Cu(100) electrode surfaces appears unlikely. Indeed such a weakening is impossible, if the adsorbate-substrate interactions are mainly based on electrostatic forces, as the lowering of the electrode potential would increase the electron density in the metal electrode and therefore more strongly attract the C7-DBDP^{2+} dications. However, if the adsorbate-substrate interaction would be based on a covalent bond, then the increase of the electron density in the metal might affect such an covalent bond

negatively. To the best knowledge of the author such a bond type is unobserved so far and in contradiction to common chemical intuition. Therefore it appears more likely that a so far unknown element exists, which stabilizes the C7-DBDP^{2+} stripe phase on the electrode surface.

The recently via SXRD studied ions situated in solution and their interaction with the solid surface (chap. 5.4) revealed that even strongly solvated ions (such as K cations) can interact strongly to specific adsorption sites of the electrode surface, which results in an in-plane ordered layer of counterions despite the presence of their solvation shell. This result of the SXRD study points, with regard to the here discussed C7-DBDP^{2+} stripe phase, to Cl anions in solution to interact with the C7-DBDP^{2+} stripe phase. These Cl anion are most likely in between or close to the cationic pyridinium rings. The presence of the Cl anions could reduce the intermolecular electrostatic repulsion between the cation charges and therefore be an additional stabilizing element in favor of the C7-DBDP^{2+} stripes. Such Cl anions would be invisible in STM experiments, as they might be not strongly co-adsorbed into the C7-DBDP^{2+} stripes but only weakly attached to the cationic pyridinium rings and therefore easily removable by the STM tip. Following this idea, lowering the electrode potential into the regime of the Cl c-(2x2) monolayer desorption would affect at first the, on the Cu electrode specifically adsorbed, Cl-c-(2x2) anion monolayer, whereas Cl anions above/within the C7-DBDP^{2+} monolayer would be less affected, as they are further from the negatively charged Cu(100) surface and as they are – at least partial – screened from the Cu electrode by the cationic C7-DBDP^{2+} monolayer. Lowering the electrode potential further to the onset of the HER increases the negative charge density in the metal and therefore increases the repulsive forces acting on the Cl anions above/within the C7-DBDP^{2+} stripes. Therefore at a critical (low) electrode potential the desorption of this second Cl anion species from their adsorption sites above/within the C7-DBDP^{2+} stripe phase may occur. The consequence of the desorption of these additional Cl anions is the increase of the intermolecular repulsion between the pyridinium cations, which then is assumed to induce the decay of the C7-DBDP^{2+} stripe phase, as observed in the potential dependent STM studies presented previously.

6.3 Modification of the Cu Dissolution and (Re-)Deposition by Organic Cation Monolayers

The adsorption of organic cations on the Cl/Cu(100) surface affects the boundary conditions of all surface processes. Consequently, all surface processes, including the hydrogen evolution reaction (HER) and Cu dissolution/deposition, can be influenced and (up to a certain degree) controlled by tailoring appropriate organic monolayers. The proves for this statement were presented in this work, e.g. by the effect of organic cation monolayers on the onset of the HER and its exponential increase. In addition to this and more eminent is the effect of the various studied organic cation monolayers on the Cu dissolution/deposition process, as will be discussed in this chapter.

The CVs in figure 6.34 prove that both, the Cu dissolution and Cu deposition process,

can be inhibited by the presence of organic cations at the solid/liquid interface, compared to the same surface processes in additive free 10 mM HCl solution. This inhibition of both processes is an expected property of the formation of an organic monolayer, as such a monolayer is assumed to act – in general – as a physical and chemical barrier for surface processes. In addition to this expected property, the Cu deposition was found to be almost fully suppressed by adding C3-DBDP^{2+} or C7-DBDP^{2+} dications into the electrolyte solution. This is proven by the CVs 6.34d and e, in which a damping of the Cu deposition peak appears, with -81% $\frac{\mu A}{mm^2}$ (C3-DBDP^{2+}) and -91%$\frac{\mu A}{mm^2}$ (C7-DBDP^{2+}), respectively.[3] This property makes C3-DBDP^{2+} and C7-DBDP^{2+} dications possible candidates for the control of copper plating in industrial manufacturing processes.

The signals of surface processes in CVs may be shifted, due to the unsteadiness of the electrochemical reference potential. This unsteadiness usually results in an experimental uncertainty of ±10 - 15 mV [vs. RHE] between different experiments. Indeed, this value was verified by calibrating various reference CV curves registered in additive free 10 mM HCl solution.

The best strategy to exclude shifts of the reference potential, which may occur between CVs registered prior and subsequently to an electrolyte exchange or the formation of an organic monolayer, is to use a CV specific internal reference for the definition of the electrode potential. Such an internal reference permits to define the potential of surface processes, i.e. of the Cu deposition peak, versus a reference process, i.e. the onset of the Cu dissolution, as sketched in figure 6.35a. The benefit of this definition of the electrochemical potential ΔE_{Work} is the canceling out of constant potential offsets, as they affect all signals in one CV equally.

Choosing the Cu dissolution as internal potential reference leaves one degree of freedom, namely the Cu dissolution current density. For instance, the Cu deposition peak can be defined vs. the electrode potential at which the Cu dissolution reaches a current of +0.05 $\frac{\mu A}{mm^2}$, as well as at which the Cu dissolution reaches a current of +0.7 $\frac{\mu A}{mm^2}$. The first reference point (+0.05 $\frac{\mu A}{mm^2}$) is expected to be a more suitable internal reference, as it is less affected by the adsorption of one full monolayer of organic cations than the latter reference point (+0.7 $\frac{\mu A}{mm^2}$). This can be concluded from the CVs imaged in figure 6.34.

Therefore all CVs, which are discussed in this section, are calibrated with their onset of the Cu dissolution (+0.05 $\frac{\mu A}{mm^2}$) to +200 mV. The position of the Cu deposition/adsorption peak is then defined by ΔE_{Work}(ad). In contrast to the Cu deposition, the Cu dissolution does not form a peak up to a current density of +0.7 $\frac{\mu A}{mm^2}$. Significantly higher current densities should be avoided in CV scans, as this would result in a massive oxidation and roughening of the Cu(100) electrode surface. Therefore the potential distance between the onset of the Cu dissolution (+0.05 $\frac{\mu A}{mm^2}$) and the dissolution current density reaching +0.7 $\frac{\mu A}{mm^2}$ is defined as ΔE_{Work}(dis). Comparing ΔE_{Work}(dis)

[3] The higher current densities of the Cu deposition peak in presence of DBV or DB-3,3'-BP are not surprising, as the inhibition of the Cu dissolution by organic monolayers required to extend the CV scan range to more positive electrode potentials. This extension increases also the amount of dissolved Cu (compared to the reference CV) and consequently the Cu deposition peak must increase as well.

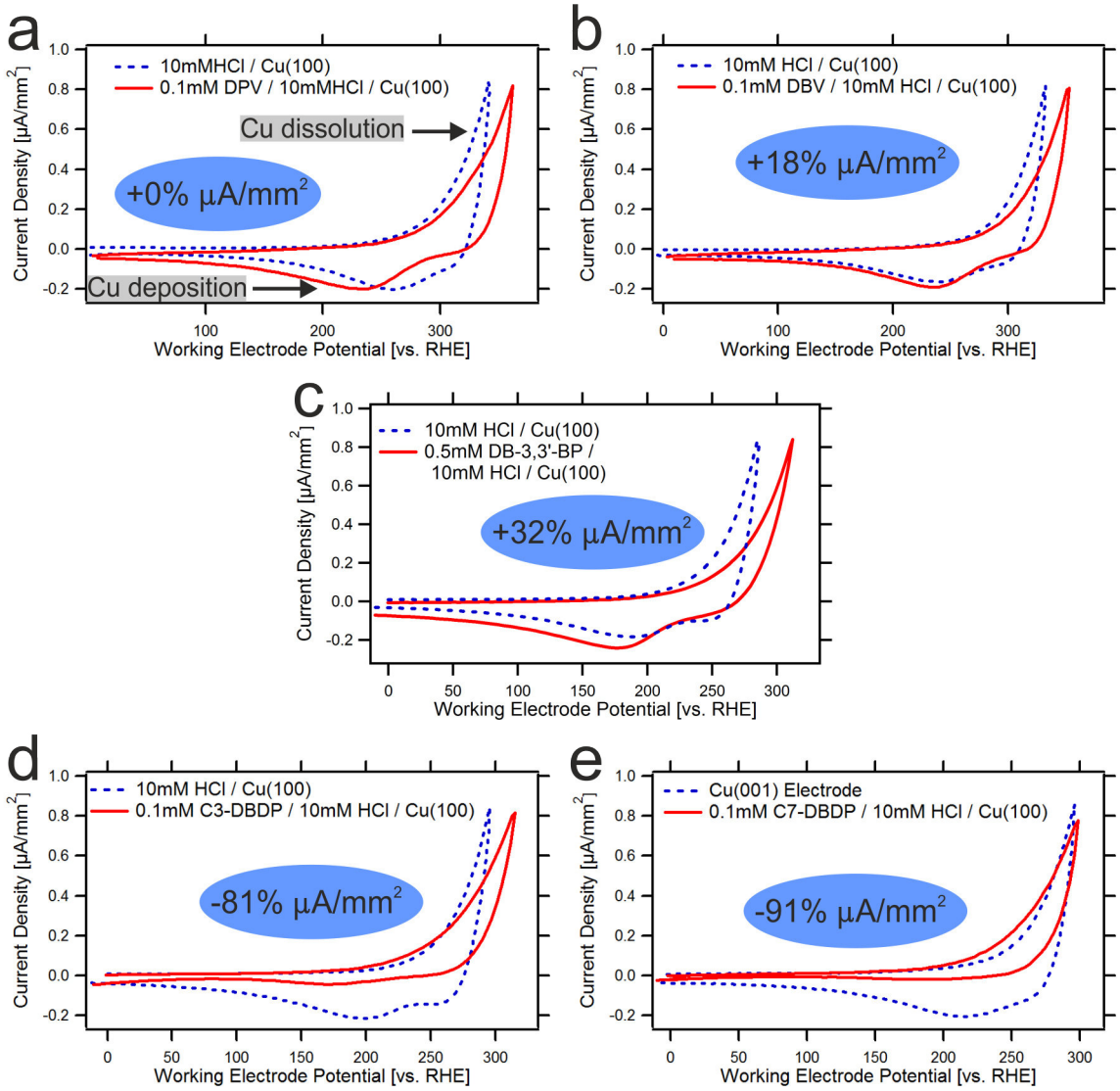

Figure 6.34: CV of the Cu dissolution and subsequent Cu deposition process of the Cu(100) electrode, in additive free 10 mM HCl solution (blue dottet lines) or in presence of one additive,(a) DPV, (b) DBV, (c) DB-3,3'-BP, (d) C3-DBDP or (e) C7-DBDP (red solid lines). The highlighted current density is the difference between the Cu deposition peaks, proving the almost complete blocking of the Cu deposition, due to the presence of C3-DBDP^{2+} or C3-DBDP^{2+} within the interfacial regime.

for Cl/Cu(100) surfaces covered with different organic monolayers delivers the information on how these different organic monolayers affect the growth of the Cu dissolution current, which essentially expresses their capability to inhibit the Cu dissolution process.

All experimental values extracted from the CV curves imaged in figure 6.35a are summarized in the table imaged in figure 6.35b. The first column contains the potential distance $\Delta E_{Work}(ad)$, which expresses the potential separation between the Cu deposition and onset of the Cu dissolution ($+0.05\ \frac{\mu A}{mm^2}$). In the additive free 10 mM HCl solution an average value of 20 mV was found, whereas adding most organic cations – except C7-DBDP^{2+} – results in a stronger separation of Cu deposition and Cu dissolution processes. C7-DBDP^{2+} dications appear to have an inverted effect, as adding those organic cations results in a shrinking of $\Delta E_{Work}(ad)$ to 16 mV. With respect to figure 6.34e, it could be concluded that C7-DBDP^{2+} dications enhance the Cu dissolution. However, in order to conclude on this with certainty and develop an understanding of the underlying processes further studies are needed.

Adding the dications DPV^{2+}, DBV^{2+} or C3-DBDP^{2+}, which all three form differently ordered full monolayers on the Cl/Cu(100) surface, results in each case in a separations of the Cu dissolution and deposition by about 30 mV, which is 50% larger than in the additive free 10 mM electrolyte. The by these organic cations formed ordered monolayers act as a physical and chemical barrier for the reduction and subsequent deposition/adsorption of Cu cations from solution on the Cu(100) surface.

In contrast to these organic cations, DB-3,3'-BP^{2+} forms an amorphous organic cation layer (sec. 6.2.1) on the Cl/Cu(100) surface. However, this amorphous layer is found to separate the Cu deposition and dissolution even stronger than the ordered monolayers, namely by a separation of the Cu deposition and onset of the dissolution by $\Delta E_{Work}(ad)$ = 43 mV, which is about twice the value obtained in the additive free electrolyte solution. This result is astonishing, as it can be assumed that the amorphous DB-3,3'-BP^{2+} layer interacts weaker with the Cl/Cu(100) surface than ordered monolayers consisting of DPV$^{+\bullet}$, DBV^{2+} or C3-DBDP^{2+}. Consequently a weaker shielding of the Cu surface by the amorphous DB-3,3'-BP^{2+} layer was expected.

The most likely explanation, also with respect to the results presented within the SXRD section of this work (sec. 5.4), is that ordered organic monolayers, such as formed by DPV$^{+\bullet}$, DBV^{2+} and C3-DBDP^{2+} interact strongly with the halide anion lattice and therefore with the halide anion charge. This attraction of the halide anion charge by the organic cations diminishes the partial transfer of the anion charge into the Cu(100) surface, which is responsible for an increased Cu bond strength between the topmost Cu layers (see sec. 5.4 for details). Following this idea, the adsorption of DPV$^{+\bullet}$, DBV^{2+} or C3-DBDP^{2+} reduces the strengthening effect of the Cl anion lattice, whereas the weakly adsorbed DB-3,3'-BP^{2+} dications leave the charge transfer mainly unaffected. Consequently the Cu dissolution would be – compared to DB-3,3'-BP^{2+} – enhanced by DPV$^{+\bullet}$, DBV^{2+} or C3-DBDP^{2+} monolayers. Appart this peculiarity, the net effect of all organic cation monolayers is – as expected – the inhibition of the Cu adsorption/deposition.

More important than the presented *inhibition* of the Cu deposition, concluded from the small shift of the Cu deposition peak along the potential axis, is the *blocking* of

a

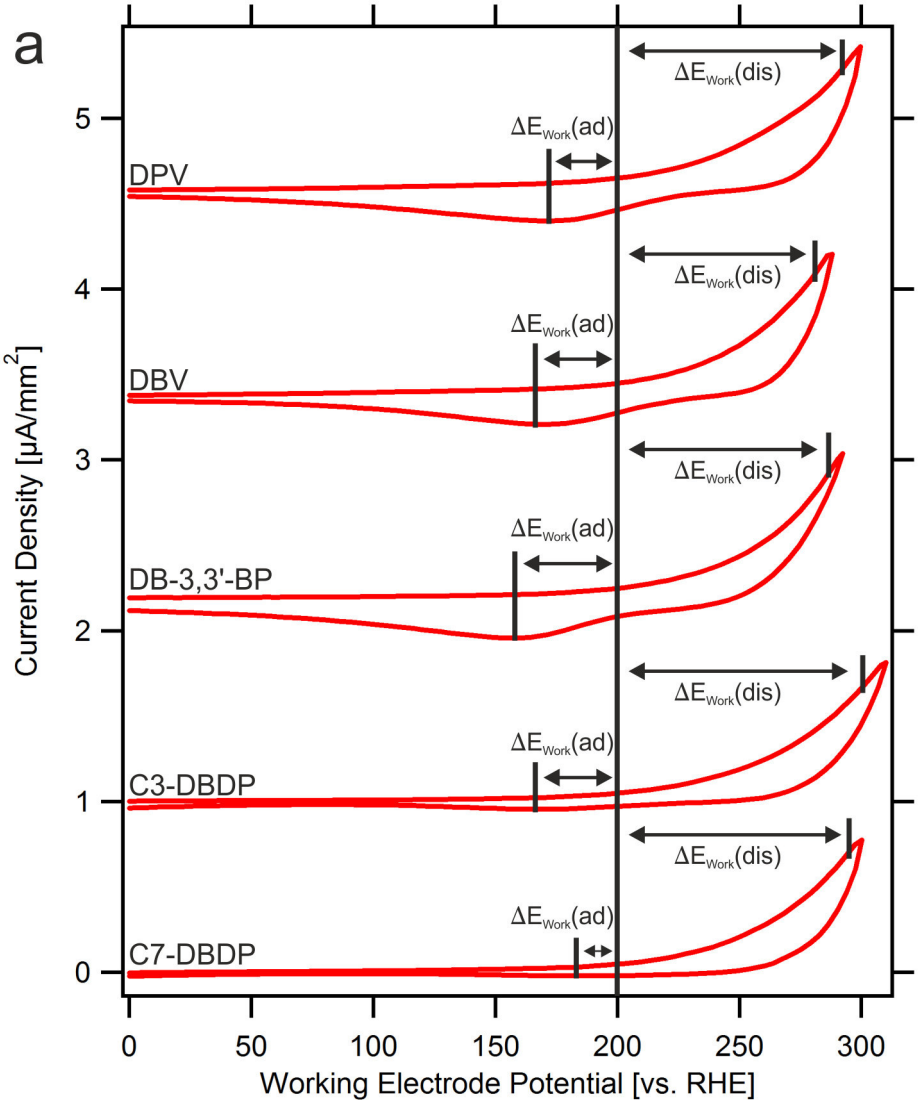

b

	ΔE_{Work}(ad)	ΔE_{Work}(dis)
Additive Free	20 mV	60 mV
DPV	27 mV	93 mV
DBV	33 mV	81 mV
DB-3,3'-BP	43 mV	86 mV
C3-DBDP	33 mV	102 mV
C7-DBDP	16 mV	95 mV

Figure 6.35: (a) Calibration of CV curves to (+0.05 $\frac{\mu A}{mm^2}$ at +200 mV). The Cu dissolution with current density of +0.05 $\frac{\mu A}{mm^2}$ was chosen as internal references of the potential axis to express the position of the Cu deposition/adsorption ΔE_{Work}(ad) and Cu dissolution ΔE_{Work}(dis), both sketched. (b) From the CVs extracted potential values of the Cu dissolution and Cu deposition/adsorption. Detailed description see text.

the reduction and subsequent adsorption of Cu cations, which results in the suppression of the Cu deposition peak by -81% $\frac{\mu A}{mm^2}$ (C3-DBDP^{2+}) and -91% $\frac{\mu A}{mm^2}$ (C7-DBDP^{2+}), respectively (fig. 6.34d and e). This blocking of the Cu deposition is only observed in the presence of C3-DBDP^{2+} and C7-DBDP^{2+} dications at the electrode surface, non of the other studied organic cations shows even signs of a comparable effect. The blocking of the metal cation reduction and deposition on electrode surfaces is no new phenomena per se, as it was also observed in a number of other studies [82, 83, 3]. The blocking of such metal deposition processes can be provoked by all Cu cation binding processes, via a complex formation between metal cation and organic molecules (e.g. between Cu cations and porphyrins [82]) or the formation of metal salts/metal oxides. The latter process may in addition passivate the electrode surface. The blocking of the Cu deposition occurring in the presence of C3-DBDP^{2+} and C7-DBDP^{2+} dications is assumed to be neither related to a complex formation, nor to Cu salt/Cu-oxide formation. The exclusion of these process types is based on literature results, which – to the best of the knowledge of the author – never reported a complex formation for organic cations similar to C3-DBDP^{2+} or C7-DBDP^{2+} with metal cations and never reported the passivation of the electrode surface by a Cu-chloride salt formation at low Cu cation and Cl anion concentrations as used in this work. Furthermore the formation of a passivating Cu-oxide film can be excluded, due to the measures taken in this work to prevent any oxygen contamination.

Additional CV experiments revealed that the blocking of the Cu deposition vanishes after several cycles reaching deep into the Cu dissolution regime. This indicates that either a specific surface topography and/or (more likely) the defect free C3-DBDP^{2+} and C7-DBDP^{2+} monolayers are responsible for the observed blocking of the Cu deposition process, as repetitive cycling into the Cu dissolution destroys the Cu substrate and therefore must also affect the integrity of the organic monolayers. This is in agreement with the obtained STM results, which prove the C3-DBDP^{2+} and C7-DBDP^{2+} monolayers are stable up to the onset of the Cu dissolution process. Consequently it can be assumed that low Cu dissolution rates over short times not significantly destroy these two organic cation monolayers. This is, however, not the case for repetitive cycling deep into the Cu dissolution regime.

Despite these information and their comparison to literature results, it remains unclear which properties of the C3-DBDP^{2+} and C7-DBDP^{2+} dications/monolayers lead to the blocking of the Cu deposition process. One thinkable answer would be a shielding of the usually accessible Cu step and kink sites, by an organic monolayer extending defect-free over the Cu steps. This would explain why the more flexible C3-DBDP^{2+} and C7-DBDP^{2+} dications possess this property, whereas the in this work studied, more stiff viologens do not. However, no clear evidence was obtained in STM experiments in order to state this with absolute certainty. Therefore in order to conclude on this surprising property of C3-DBDP^{2+} and C7-DBDP^{2+} a new series of experiments, which are out of focus of the present work, are necessary and highly suggested for future studies.

Besides the Cu deposition, organic cation monolayers also affect the Cu dissolution. This is described in this work by the potential distance between the onset of the Cu dissolution at a current density of +0.05 $\frac{\mu A}{mm^2}$ and the heavily oxidized Cu surface at

a current density of $+0.7\ \frac{\mu A}{mm^2}$. The difference between these two stages of the Cu dissolution lies in the dynamics of the Cu dissolution process. At a current density of $+0.05\ \frac{\mu A}{mm^2}$ mainly weakly bound Cu atoms at Cu step and kink sites can be assumed to be oxidized. In contrast to this, at $+0.7\ \frac{\mu A}{mm^2}$ in addition to the Cu step and kink sites also Cu atoms embedded within intact terraces are oxidized and consequently new defects are created.

The here studied organic monolayers act with different strength on the Cu dissolution process, as becomes clear by a comparison of the values of ΔE_{Work}(dis) listed in figure 6.35b. In the additive free 10 mM HCl electrolyte solution the onset of the Cu dissolution and the current density of $+0.7\ \frac{\mu A}{mm^2}$ are only 60 mV apart. This distance is extended by about 40% to 81 mV / 86 mV in presence of the DBV^{2+} cavitand phase or the amorphous layer of DB-3,3'-BP^{2+}, respectively. A stronger inhibition of the Cu dissolution can be achieved in presence of the $DPV^{+\bullet}$ π-stacked stripe phase or the C7-$DBDP^{2+}$ mesh phase on the Cl/Cu(100) surface, as this leads to an about 57% larger value of ΔE_{Work}(dis). Finally C3-$DBDP^{2+}$ outperforms all other studied organic cations, as the inter-linked stripe phase is found to extend the initial additive free ΔE_{Work}(dis) by 70% to 102 mV. This strong inhibition of the Cu dissolution might result from the strong inter-molecular interactions between adsorbed C3-$DBDP^{2+}$ dications and their higher intra-molecular flexibility, as this was assumed to cause the lower substrate dependents of the C3-$DBDP^{2+}$ inter-linked stripe phase (see sec. 6.2.2 for details). Consequently it can be assumed that despite the ongoing oxidation of the underlying Cu substrate, which may include the desorption of Cl anions, the C3-$DBDP^{2+}$ inter-linked stripe phase is less affected than other organic monolayers.

However, the most remarkable result of this limited CV study is that C3-$DBDP^{2+}$ and C7-$DBDP^{2+}$ show in both Cu processes, the Cu dissolution and Cu deposition, remarkably strong effects, compared to the other studied organic cations. Indeed, only the dense $DPV^{+\bullet}$ π-stacked stripe phase is found to have a comparable stabilizing effect on the underlying Cl/Cu(100) substrate, therefore preventing its oxidative decomposition, whereas non of the studied organic monolayers shows any signs for the in presence of C3-$DBDP^{2+}$ and C7-$DBDP^{2+}$ dications occurring almost full suppression of the Cu deposition process. These results make – as stated initially – C3-$DBDP^{2+}$ and C7-$DBDP^{2+}$ dications interesting candidates for the control of metal dissolution and more importantly metal deposition processes.

7 Summary

Cl or Br Covered Cu(100) Surfaces

Despite the well characterized 2D-structure of the Cl/Cu(100) substrate, its 3D-structure and dependence on the applied electrode potential are still under discussion in literature. Therefore in addition to recently published works on Cl-c(2x2) and Br-c(2x2) covered Cu(100) substrates, *in situ* Surface X-Ray Diffraction (SXRD) data of the model system $\{10$ mM KBr + 0.5 mM $H_2SO_4\}_{liq}$ / Br-c(2x2)/Cu(100) were analyzed and a 3D-structure model of the whole interfacial regime derived, which includes the liquid electrolyte and solid halide covered Cu(100) surface.

The SXRD data analysis proves the symmetry transfer from the Cu(100) substrate into the highly mobile liquid phase, as solvated cations are found to form an in-plane ordered Layer of Solvated CounterIons (LSCI), consisting of solvated potassium or oxonium cations, situated above the specifically adsorbed full Br-c(2x2) monolayer on the Br/Cu(100) electrode. The solvated K (or oxonium) cations adsorb into the fourfold hollow sites of the Br-c(2x2) lattice and therefore form themselves a c(2x2) cation layer. The coverage of the c(2x2) cation LSCI is about 20% of a full c(2x2) ML and was found to be independent of the electrode potential. In agreement to this, the distance between the Br-c(2x2) anion layer and the LSCI was found to be – within the experimental accuracy – also independent of the electrode potential. This is assumed to indicate that Br anions are the dominant binding partner of the LSCI, which is consistent with an IRRAS study of viologen cation monolayers on the halide covered Cu(100) substrates.

In contrast to the cation-anion distance, the solvation layer between them was found to react to the charge state of the electrode surface. At +50 mV [vs. RHE] the solvation layer is at a distance of 0.07 nm from the K cations, but 0.18 nm from the Br anion. Therefore the solvation layer is fully attributed to the K cation solvation shell. This situation is inverted at an electrode potential of -150 mV [vs. RHE], at which the solvation layer is 0.17 nm from the K cations but 0.09 nm from the fully charged Br anions. Consistent to the first interpretation, at low electrode potentials the solvation layer is attributed fully to the Br anions.

The up to here discussed liquid side in the model of the solid/liquid interface is the new element, whereas the solid side, namely the Br/Cu(100) electrode, was already discussed in previous publications. Therefore the 3D-structure results of the solid electrode surface are only briefly sketched.

The results of the SXRD analysis confirm a partial transfer of the Br anion charge into the electrode surface, i.e. at high electrode potentials. The Br anion charge is assumed to be at -150 mV [vs. RHE] mostly situated within the Br anion monolayer. Increasing the electrode potential to -50 mV [vs. RHE] leads to a contraction of the Br-

Cu layer distance by 2.2%, whereas the topmost Cu-Cu layer distance remains almost unaffected. This indicates a partial transfer of the Br anion charge into the first Cu layer and consequently to a strengthening of the Br-Cu bond. In the second potential step, from -50 mV [vs. RHE] to +50 mV [vs. RHE], the Br-Cu layer distance stays unaffected, whereas the topmost Cu-Cu layer is found to contract by 1.4%. Consistent with the interpretation of the first potential step, the Br anion charge is assumed to be transferred partially even deeper into the Cu(100) electrode, screening the positive Cu cores of the first and second Cu layer from each other and therefore reducing the repulsive forces between them, despite the overall reduced electrondensity within the Cu surface.

The assumed partial transfer of the Br anion charge into the Cu(100) surface is confirmed by the potential dependence of the subsurface buckling. The subsurface buckling of the 2nd Cu layer results from the symmetry transfer from the Br-c(2x2) anion lattice into the Cu(100) electrode surface. The Br anions occupy only half of all fourfold hollow sites of the Cu(100) surface. Consequently two types of Cu atoms in the 2nd Cu layer are distinguishable, those underneath Br anions and those underneath unoccupied fourfold hollow sites of the Cu(100) surface. This Br anion induced subsurface buckling is most different at low electrode potentials, i.e. -150 mV [vs. RHE], which results in a buckling amplitude of 0.029 Å, whereas at higher electrode potentials, i.e. +50 mV [vs. RHE], a significant smaller amplitude of 0.0063 Å is found. The reduction of the buckling amplitude is assumed to result from the partial transfer of the Br anion charge into the Cu surface at high electrode potentials.

Competition Between DPV and DBV at the Cl/Cu(100) Electrode Surface

Subsequently to the characterization of the substrate, the structure formation of pyridinium containing organic cations is studied at the Cl-c(2x2) precovered Cu(100) electrode surface. At first the individually well known Diphenyl- (DPV) and Dibenzylviologen (DBV) are studied in competition for adsorption and reaction sites at the Cl/Cu(100) substrate.

DPV^{2+} is upon adsorption reduced even at most anodic potentials to the monocationic radical $DPV^{+\bullet}$ and forms on the Cl/Cu(100) substrate a full monolayer of a π-stacked stripe phase. This $DPV^{+\bullet}$ π-stacked stripe phase prevents the adsorption of the DBV^{2+} dications and therefore the formation of the – in pure DBV^{2+} solution observed – DBV^{2+} cavitand phase on the Cl/Cu(100) electrode surface at $E_{work} = 0\,mV$ [vs. RHE]. This proves the DBV^{2+} cavitand phase to be energetically less favored than the more dense $DPV^{+\bullet}$ π-stacked stripes.

Lowering the electrode potential into the reduction regime of the DBV^{2+} dications, i.e. to $E_{work} = -270\,mV$ [vs. RHE], leads to displacement of the adsorbed monocation radicals $DPV^{+\bullet}$ by $DBV^{+\bullet}$ monocation radicals on the Cl/Cu(100) substrate. Consequently the $DPV^{+\bullet}$ π-stacked stripe phase is substitued by growing $DBV^{+\bullet}$ π-stacked stripe domains. This indicates the $DBV^{+\bullet}$ π-stacked stripes to be energetically favored, which is assumed to result from their higher molecular flexibility. A higher intra-molecular flexibility permits $DBV^{+\bullet}$ to maximize the inter-molecular attractive forces, i.e. be-

tween neighboring benzyl groups. In contrast to $DBV^{+\bullet}$, the rigid $DPV^{+\bullet}$ forces its phenyl rings into one specific arrangement, which – in general – does not have to be the energetically most favored one.

A further reduction of the electrode potential increases the electrostatic repulsion between the Cu(100) surface and the Cl-c(2x2) monolayer, which at $E_{work} = -360\,mV$ [vs. RHE] leads to the desorption of all Cl anions through the full monolayer of the $DBV^{+\bullet}$ π-stacked stripe phase. This desorption eliminates the attraction between the Cl anion monolayer and the adsorbed $DBV^{+\bullet}$ π-stacked stripe phase. Consequently the $DBV^{+\bullet}$ π-stacked stripe phase undergoes an order-disorder transition to an amorphous viologen layer.

This order-disorder transition can be quasi-reversed by re-increasing the electrode potential to $E_{work} = -230\,mV$. At this potential state Cl anions are re-adsorbed through the amorphous viologen layer onto the Cu(100) surface and form again their Cl-c(2x2) monolayer. Cosequently the $DBV^{+\bullet}$ π-stacked stripe phase reappears, but with a different domain distribution than prior to the Cl anion desorption.

Increasing the electrode potential further leads at first to the oxidation of the monocation radicals $DBV^{+\bullet}$ in solution (at -230 mV [vs. RHE]) and later to the oxidation of the *adsorbed* monocation radicals $DBV^{+\bullet}$ (at -100 mV [vs. RHE]). The at -100 mV [vs. RHE] formed DBV^{2+} dications are displaced from the electrode surface by the monocation radicals $DPV^{+\bullet}$, which then again form their (initial) $DPV^{+\bullet}$ π-stacked stripe phase on the electrode surface.

DB-3,3'-BP at the Cl/Cu(100) Electrode Surface

The redox active dicationic 4,4'-bipyridinium core of DBV^{2+} looses its redox activity by the modification to DB-3,3'-BP^{2+} (1,1´-Dibenzyl-3,3´-bipyridinium), as proved by the absence of any current wave in the CV of Cu(100) in DB-3,3'-BP^{2+} containing 10 mM HCl solution. Additionally the modification from DBV^{2+} to DB-3,3'-BP^{2+} is found to disturb the self-assembly process of the dications, as no ordered DB-3,3'-BP^{2+} monolayer is formed on the Cl/Cu(100) electrode surface. DB-3,3'-BP^{2+} dications adsorb into a highly mobile and amorphous organic layer on the Cl/Cu(100) surface.

In order to exclude that this amorphous phase appears only at special experimental conditions two parameters, namely the electrode potential and the DB-3,3'-BP^{2+} concentration in solution, were varied. However, neither reducing the applied electrode potential, nor a stepwise increase of the DB-3,3'-BP^{2+} concentration in solution from 0.1 mM to 25 mM did trigger the formation of an ordered DB-3,3'-BP^{2+} monolayer. The most likely explanation for the absence of an ordered organic cation monolayer are sterically and geometrically hindered adsorbate-substrate interactions, although a lowered inter-molecular attraction can not be ruled out to play a role.

C3-DBDP at the Cl/Cu(100) Electrode Surface

Introducing a propane-1,3-diyl chain between the 4,4'-connected bipyridinum core of DBV results in the C3-DBDP (1,1'-Dibenzyl-4,4'-(propane-1,3-diyl)-dipyridinium) mole-

cule. The introduced organic chain fragments the bipyridinium π-system into two isolated pyridinium π-systems, as the delocalization of the π-system electrons over both pyridinium rings is prevented by the saturated chain of sp^3-hybridized carbon atoms between them.

As observed in the modification of DBV^{2+} to DB-3,3'-BP^{2+}, also the modification of DBV^{2+} to C3-$DBDP^{2+}$ lowers the redox activity of the dications, proven again by the absence of any current wave within the potential window of the Cu(100) electrode in C3-$DBDP^{2+}$ containing solution. In order to determine also the redox state of the adsorbed C3-DBDP species XPS spectra were registered, which doubtlessly proved the persistance of the C3-$DBDP^{2+}$ dication state upon adsorption on the Cl/Cu(100) electrode surface.

In contrast to DB-3,3'-BP^{2+}, C3-$DBDP^{2+}$ possesses a significantly higher intra-molecular flexibility than the initial DBV^{2+}, due to the additional rotations around all C-C single bonds between the saturated (tetrahedral) C-atoms of the propane-1,3-diyl chain. The more flexible C3-$DBDP^{2+}$ forms an inter-linked stripe phase on the Cl/Cu(100) electrode surface, in which the pyridinium-benzyl moieties of C3-$DBDP^{2+}$ arrange consecutively with a distance of 0.45 nm between them. This results in long unbroken rows of consecutive pyridinium-benzyl moieties, with a row-to-row (or stripe-to-stripe) distance of 1.2 nm. These rows/stripes of pyridinium-benzyl moieties are alternatingly to the left and the right connected – via the propane-1,3-diyl chain – to the neighboring rows, which results in the "inter-linking" of the C3-$DBDP^{2+}$ stripes. Therefore consecutive C3-$DBDP^{2+}$ dications within the inter-linked stripe structure are shifted by half a molecular length perpendicular to the pyridinium-benzyl stripe orientation.

The arrangement of consecutive pyridinium-benzyl moieties along one C3-$DBDP^{2+}$ stripe suggests that the inter-molecular attraction is based on the electrostatic attraction between the directly facing negative benzyl π-systems and cationic pyridinium rings. The adsorbate-substrate interaction is of minor importance, which can be concluded from three facts. First, no epitaxial relation between the C3-$DBDP^{2+}$ monolayer and the underlying Cl-c(2x2) substrate was found. Second, the inter-linked stripe phase is stable throughout the desorption of the whole Cl-c(2x2) anion layer (at $E_{work} < -250\,mV$ [vs. RHE]) situated underneath the organic cation monolayer. Third, no reconstruction of the Cu steps is induced by the formation of the C3-$DBDP^{2+}$ monolayer, which was the case in the formation of viologen monolayers, known to strongly interacting to the underlying Cl anion substrate, i.e. the $DBV^{+\bullet}$ π-stacked stripe phase.

Although no epitaxial relation between the C3-$DBDP^{2+}$ monolayer and the Cl anion covered substrate was found, the C3-$DBDP^{2+}$ stripes do not grow fully arbitrary, as they are oriented within an angular space of 30° to 45° off the main crystallographic directions (100) and (010). These various C3-$DBDP^{2+}$ stripe orientations indicate several arrangements in that angular space to be equally favored.

Adsorbate-substrate interactions are assumed to be of minor importance for the final C3-$DBDP^{2+}$ inter-linked stripe structure, but they certainly do affect its structure formation process. Indeed the structure formation of the C3-$DBDP^{2+}$ inter-linked stripe phase was found to extend over several tens of minutes, which is very long compared to the almost instant formation of viologen phases. This long monolayer formation time is

most likely the result of a competition between inter-adsorbate and adsorbate-substrate interactions, which require different molecular arrangements and/or periodicities.

Besides the formation of an ordered organic cation monolayer, C3-DBDP^{2+} dications were found to inhibit both Cu processes, namely the Cu dissolution and deposition process, occurring at $E_{work} > +200mV$ [vs. RHE]. In addition to this expected property of an full organic cation monolayer, the presence of C3-DBDP^{2+} dications within the solid liquid interface blocks the Cu deposition, resulting in the damping of the related current wave by 81% $\frac{\mu A}{mm^2}$. Indications were found that this observation results from the intact C3-DBDP^{2+} inter-linked stripe on the Cl/Cu(100) substrate, however, the identification of the monolayer properties provoking the blocking of the Cu deposition processes demands further study.

C7-DBDP at the Cl/Cu(100) Electrode Surface

Introducing a heptane-1,7-diyl chain between the 4,4'-connected bipyridinum core of DBV results in the C7-DBDP molecule (1,1'-Dibenzyl-4,4'-(heptane-1,7-diyl)-dipyridinium). In agreement to the results of C3-DBDP^{2+}, the two isolated cationic pyridinium π-systems of C7-DBDP^{2+} were found to possess a lower redox activity than the dicationic bipyridinium core of DBV^{2+}. Consequently within the potential window of the Cu(100)/electrolyte interface no reduction of C7-DBDP^{2+} dications is observed.

What distinguishes C7-DBDP^{2+} from C3-DBDP^{2+} is the even higher intra-molecular flexibility, due to the longer saturated chain, which makes a wider conformational space accessible. This higher flexibility permits C7-DBDP^{2+} to form at $E_{work} = 0$ mV [vs. RHE] a commensurable monolayer, namely the C7-DBDP^{2+} mesh phase, in contrast to the incommensurable C3-DBDP^{2+} inter-linked stripe phase. The conservation of the dication charge of C7-DBDP^{2+} throughout the adsorption was proven – as previously for C3-DBDP^{2+} – via XPS.

The C7-DBDP^{2+} mesh phase consists of pairwise – along (100) or (010) – arranged pyridinium-benzyl moieties with a distance of 0.72 nm between the moieties. The distance between consecutive pairs is 1.08 nm. Both structure parameters, 0.72 nm and 1.08 nm, are multiples of the Cl anion next neighbor distance in the (100) and (010) directions, namely 0.36 nm. This highlights the strong influence of the Cl-c(2x2) anion lattice in the mesh phase formation.

The interaction between the two pyridinium-benzyl moieties forming one pair is assumed to be based on the electrostatic attraction between directly facing negative benzyl π-systems and cationic pyridinium rings, as already observed in the study of C3-DBDP^{2+}. However, in contrast to the formation of the C3-DBDP^{2+} inter-linked stripe phase, there is no competition between inter-molecular and adsorbate-substrate interactions in the formation of the C7-DBDP^{2+} mesh phase. This is concluded from the fact, that – as typical for viologen monolayers – the C7-DBDP^{2+} mesh phase monolayer is formed almost instantaneously.

Within the dominant C7-DBDP^{2+} mesh phase also domains of a metastable C7-DBDP^{2+} stripe phase were found at 0 mV [vs. RHE]. These C7-DBDP^{2+} stripe domains vanish over several hours in a post-adsorption ripening process in favor of the energeti-

cally more favored C7-DBDP^{2+} mesh phase. This long phase transition time indicates either a significant activation barrier and/or a small difference between the adsorption energies of both C7-DBDP^{2+} phases.

The C7-DBDP^{2+} dications are within the stripe domains consecutively arranged, with a constant intermolecular distance of 0.53 nm, and form long unbroken stripes. The length of these stripes is limited by the diameter of the C7-DBDP^{2+} stripe domains, which was found to reach up to several tens of nm. The orientation of these C7-DBDP^{2+} stripes is 31° to the main crystallographic directions of the substrate, namely (100) and (010). An epitaxial relationship of C7-DBDP^{2+} dications could not be doubtlessly proven. However, significant adsorbate-substrate interactions are assumed, as the pyridinium-benzyl moieties appear in highly resolved STM images of the C7-DBDP^{2+} stripe phase to be not arranged along the stripe boarder but in a wave-like fashion. These wave-like stripe boarders point to pyridinium-benzyl moieties adapting to the underlying Cl anion substrate in order to maximize the adsorbate-susbtrate attraction. The theoretical intermolecular distance for the epitaxial growth of C7-DBDP^{2+} dications in a 31° angle on the Cl-c(2x2) anion layer is 0.51 nm, which lies within the experimental error of the average intermolecular distance extracted from the STM images.

Within the C7-DBDP^{2+} stripe phase all molecular groups (benzyl groups, pyridinium rings and heptane-1,7-diyl chains) directly face the same molecular groups of a neighboring C7-DBDP^{2+} dication. Therefore the resulting electrostatic repulsion between directly facing cationic pyridinium rings must be compensated by the inter-molecular and adsorbate-substrate attractions.

Lowering the electrode potential into the Cl anion desorption regime, i.e. to $E_{work} < -290$ mV [vs. RHE], induces an order-disorder transition of the C7-DBDP^{2+} mesh phase, but not of the C7-DBDP^{2+} stripe domains. The C7-DBDP^{2+} mesh phase decays from its domain boarders and forms an amorphous phase of C7-DBDP^{2+} dications. This phase transition of the C7-DBDP^{2+} mesh phase proves the fundamental role of the Cl-c(2x2) anion substrate in the formation and stability of the mesh structure. C7-DBDP^{2+} stripe domains neighboring the amorphous C7-DBDP^{2+} areas expand into the – previously by C7-DBDP^{2+} mesh phase occupied – amorphous C7-DBDP^{2+} domains on the bare, i.e. Cl anion free, Cu(100) surface.

A further reduction of the electrode potential to the onset of the HER (Hydrogen Evolution Reaction) at -400 mV [vs. RHE] leads to a second order-disorder transition, namely of the C7-DBDP^{2+} stripe phase to an amorphous C7-DBDP^{2+} phase. This phase transition is assumed to be induced by the desorption of a second Cl anion species, which is co-adsorbed above or between the cationic pyridinium rings of the C7-DBDP^{2+} stripe phase. This assumption is in agreement with SXRD results, which proved that the symmetry of the solid electrode surface is transferred even into the liquid and highly mobile electrolyte phase, which provokes the formation of an in-planed ordered Layer of Solvated CounterIons (LSCI). The postulated "outer" Cl anion species would then desorb at a lower (more negative) electrode potential than the Cl-c(2x2) monolayer, due to its greater distance from the negatively charged Cu(100) surface.

Consistent to C3-DBDP^{2+}, C7-DBDP^{2+} dications also inhibit the Cu dissolution and

deposition process, occurring at $E_{work} > +200\,mV$ [vs. RHE]. Also C7-DBDP^{2+} dications are found to block the Cu deposition processes, leading to a damping of the current wave by 91% $\frac{\mu A}{mm^2}$. This confirms the observations made in the study of C3-DBDP^{2+}, and points to a fundamental property of C3-DBDP^{2+} and C7-DBDP^{2+} monolayers responsible for the blocking of the Cu deposition and makes a detailed understanding of the underlying processes even more desirable.

Bibliography

[1] D. Josell, D. Wheeler, W. H. Huber, and T. P. Moffat. Superconformal Electrodeposition in Submicron Features. *PRL*, 87:016102.

[2] T.P. Moffat, D. Wheeler, and D. Josell. Electrodeposition of Copper in the SPS-PEG-Cl Additive System. *J. Electrochem. Soc.*, 151, 2004.

[3] O.M. Magnussen. Ordered Anion Adlayers on Metal Electrode Surfaces. *Chem. Rev.*, 102:679, 2002.

[4] C. Safarowsky, K. Wandelt, and P. Broekmann. Formation of Supramolecular Cavitands on Copper Eletrode Surfaces. *Langmuir*, 20:8261, 2004.

[5] D.-T. Pham, K. Gentz, C. Zoerlein, N.T.M. Hai, S.-L. Tsay, B. Kirchner, S. Kossmann, K. Wandelt, and P. Broekmann. Surface redox chemistry of adsorbed viologens on Cu(100). *New J. Chem.*, 30:1439, 2006.

[6] D.-T. Pham, S.-L. Tsay, K. Gentz, C. Zoerlein, S. Kossmann, J.-S. Tsay, B. Kirchner, K. Wandelt, and P. Broekmann. Quasi-Reversible Chloride Adsorption/Desorption through a Polycationic Organic Film on Cu(100). *J. Phys. Chem. C*, 111:16428, 2007.

[7] D.T. Pham. *Self-assembly of viologen molecules at metal/electrolyte interfaces under non-reactive and reactive conditions.* Ph.D Thesis, University of Bonn, Germany, 2011.

[8] C.L. Bird and A.T. Kuhn. Electrochemistry of Viologens. *Chem. Soc. Rev.*, 10:49, 1981.

[9] S. Breuer, D.T. Pham, S. Huemann, K. Gentz, C. Zoerlein, R. Hunger, K. Wandelt, and P. Broekmann. Organic layers at metal/electrolyte interfaces: molecular structure and reactivity of viologen monolayers. *New J. of Phys.*, 10:125033, 2008.

[10] M. Jiang, E. Sak, K. Gentz, A. Krupski, and K. Wandelt. Redox Activity and Structural Transition of Heptyl Viologen Adlayers on Cu(100). *Chem. Phys. Chem.*, 11:1542, 2010.

[11] C.H. Hamann and W. Vielstich. *Elektrochemie I.* VCH Verlagsgesellschaft, 1985.

[12] Southampton Electrochemistry Group. *Instrumental Methods in Electrochemistry.* Horwood Publishing Ltd., 2006.

[13] M.S. Röefzaad. *Ordnungsphänomene redox-aktiver Moleküle auf Elektrodenoberflächen unter reaktiven Bedingungen.* Ph.D Thesis, University of Bonn, Germany, 2011.

[14] K. Gentz. *Einfluss der Substituenten auf die Struktur selbstorganisierter Bipyridinschichten.* Ph.D Thesis, University of Bonn, Germany, 2011.

[15] H.L.v. Helmholtz. *Wied. Ann.*, 7:337, 1879.

[16] G. Gouy. *J. Phys.*, 9:457, 1910.

[17] D.L. Chapman. *Phil. Mag.*, 25:475, 1913.

[18] D.C. Grahame. *Chem. Rev.*, 41:441, 1947.

[19] C. Stuhlmann, B. Wohlmann, Z. Park, M. Kruft, P. Broekmann, and K. Wandelt. Chloride Adsorption on Cu(111) Electrodes: Electrochemical Behavior and UHV Transfer Experiments. *K. Wandelt, S. Thurgate (Eds.): Solid-Liqid Interfaces, Topics Appl. Phys.*, 85:199, 2003.

[20] M.R. Vogt and F.A. Möller and C.M. Schilz and O.M. Magnussen and R.J. Behm. Adsorbate-induced step faceting of Cu(100) electrodes in HCl. *Surf. Sci.*, 367, 1996.

[21] M.R. Vogt, A. Lachenwitzer, O.M. Magnussen, and R.J. Behm. In-situ STM study of the initial stages of corrosion of Cu(100) electrodes in sulfuric and hydrochloric acid solution. *Surf. Sci.*, 399:49, 1998.

[22] D.C. Grahame and R. Parson. *J. Am. Chem. Soc.*, 83:1291, 1961.

[23] W. Schmickler. Electronic effects in the electric double layer. *Electrochim. Acta*, 41:2329, 1996.

[24] S. Huemann, T.M.H. Nguyen, P. Broekmann, K. Wandelt, H. Zajonz, H. Dosch, and F. Renner. X-ray Diffraction and STM Study of Reactive Surfaces under Electrochemical Control: Cl and I on Cu(100). *J. Phys. Chem. B*, 110:24955, 2006.

[25] Y. Gründer, D. Kaminski, F. Golks, K. Krug, J. Stettner, and O.M. Magnussen. Reversal of chloride-induced Cu(001) subsurface buckling in the electrochemical environment: An in situ surface x-ray diffraction and density functional theory study. *PRB*, 81:174114, 2010.

[26] M. Saracino, P. Broekmann, K. Gentz, M. Becker, H. Keller, F. Janetzko, T. Bredow, and K. Wandelt H. Dosch. Surface relaxation phenomena at electrified interfaces: Revealing adsorbate, potential, and solvent effects by combined x-ray diffraction, STM and DFT studies. *PRB*, 79:115448, 2009.

[27] M. Röefzaad, M. Jiang, V. Zamlynny, and K. Wandelt. Potential dependent structure transitions of heptyl Viologen layers on Cu(100) studied by in situ STM and IRRAS. *J. of Electroanal. Chem.*, 662:219, 2011.

[28] R. Smoluchowski. Anisotropy of the electronic work function of metals. *Phys. Rev.*, 60:661, 1941.

[29] M.E. Straumanis and L.S. Yu. Lattice parameters, densities, expansion coefficients and perfection of structure of Cu and of Cu-In α phase. *Acta Crystallogr.*, 25.

[30] L. Michaelis and E.S. Hill. *J. Gen. Physiol*, 16:859, 1933.

[31] S. Hünig and W. Schenk. Einfluss von N-Substituenten in 4,4'-Bipyridylen auf das Redoxverhalten, die Radikalstabilität und die Elektronenspektren. *Liebigs Ann. Chem.*, page 1523, 1979.

[32] N. Leventis, G. Zhang, A.-M. M. Rawashdeh, and C. Sotiriou-Leventis. Electrochemical reduction of 4-benzoyl-n-(4-substituted benzyl)pyridinium cations: substitution effects and linear free energy relationships. *Electrochim. Acta*, 48:2799, 2003.

[33] A. Messiah. *Quantenmechanik Band 1*, volume 1. Aufl., Nachdruck. Walter de Gruyter, 1981.

[34] J. Tersoff and D.R. Hamann. Theory of the scanning tunneling microscope. *PRB*, 31:2, 1985.

[35] F.C. Simeone, D.M. Kolb, S. Venkatachalam, and T. Jacob. Current - distance - voltage characteristics of electron tunneling through an electrochemical STM junction. *Surf. Sci.*, 601:1401, 2008.

[36] D.-H. Woo, E.-M. Choi, Y.-H. Yoon, K.-J. Kim, I.C. Jeon, and H. Kang. Current - distance - voltage characteristics of electron tunneling through an electrochemical stm junction. *Surf. Sci.*, 601:1554, 2007.

[37] P.W. Atkins. *Physikalische Chemie*, volume 2. Aufl. VCH Verlagsgesellschaft mbH, 1996.

[38] A. Einstein. Über die von der molekularkinetischen Theorie der wärme geforderte Bewegung von in ruhenden Flüssigkeiten suspendierten Teilchen. *Ann. d. Physik*, 17:549, 1905.

[39] M. Smoluchowski. Zur kinetischen Theorie der Brownschen Molekularbewegung und der Suspension. *Ann. d. Physik*, 21:756, 1906.

[40] Jens Als-Nielsen and Des McMorrow. *Elements of Modern X-Ray Physics*. John Wiley & Sons, 2001.

[41] E. Vlieg. X-Ray Diffraction from Surfaces and Interfaces. In *Surface and Interface Science: Concept and Methods*, volume 1, page 375. Wiley-VCH Weinheim, 2012. Ed. K. Wandelt.

[42] M.V. Linkoaho. The X-ray Debye Temperatures of V, Ni, Cu, Nb and Ag from the measured integrated intensities at 300 K and 4 K. *Philosphical Magazine*, 23:191, 1970.

[43] I.K. Robinson. Crystal truncation rods and surface roughness. *PRB*, 33:3830, 1986.

[44] H. Keller, M. Saracino, H.M.T. Nguyen, and P. Broekmann. Templating the near-surface liquid electrolyte: In situ surface x-ray diffraction study on anion/cation interactions at electrified interfaces. *PRB*, 82:245425, 2010.

[45] C. Jogl. *Quasi-in-situ Photoelektronen-Spektroskopie an elektrochemisch hergestellten Filmen.* Ph.D. Thesis, Technische Universität Wien, Austria, 2005.

[46] R. Hesse. *Verbesserung der qualitativen und quantitativen Analyse von Photoelektronenspektren und deren Verifizierung mittels mathematisch-numerischer Verfahren - Entwicklung und Test einer Bearbeitungs- und Analyse-Software.* Ph.D. Thesis, University of Leipzig, Germany, 2006.

[47] *http://www.mateck.de/.* Mateck.

[48] *http://www.merck-chemicals.de/.* Merck.

[49] M. Saracino, S. Breuer, G. Barati, E. Sak, K. Hingerl, U. Müller, M. Müller, S. Höger, and K. Wandelt. The impact of intramolecular π-coupling and steric flexibility on the ordering of organic films at solid/liquid-interfaces. *Surf. Sci.*, 607:74, 2013.

[50] *http://www.airliquide.de/.* AirLiquid.

[51] G.M. Brisard, E. Zenati, H.A. Gasteiger, N. Markovic, and P.N. Ross. Underpotential Deposition of Lead on Copper(111): A Study Using a Single-Crystal Rotating Ring Disk Electrode and ex Situ Low-Energy Electron Diffraction and Auger Electron Spectroscopy. *Langmuir*, 11:2221, 1995.

[52] P. Broekmannm, M. Wilms, M. Kruft, C. Stuhlmann, and K. Wandelt. In-situ STM investigation of specific anion adsorption on Cu(111). *J. of Electrochem. Chem.*, 467:307, 1999.

[53] D.M. Kolb. *Ber. Bunsen-Ges.*, 98:1421, 1994.

[54] M. Wilms. *Potentiodynamische Rastertunnelmikroskopie an Fest/Flüssig-Grenzflächen: Apparative Entwicklung und Untersuchungen zur Sulfat-Adsorption auf Cu(111).* Ph.D. Thesis, University of Bonn, Germany, 1999.

[55] M. Wilms, M. Kruft, G. Bermes, and K. Wandelt. A new and sophisticated electrochemical scanning tunneling microscope design for the investigation of potentiodynamic processes. *Rev. Sci. Instrum.*, 70:3641, 1999.

[56] G. Binnig, H. Rohrer, Ch. Gerber, and E. Weibe. Surface Studies by Scanning Tunneling Microscopy. *Phys. Rev. Lett.*, 49:57, 1982.

[57] R. Sonnenfeld and P.K. Hansma. Atomic-Resolution Microscopy in Water. *Science*, 232(4747):211, 1986.

[58] K. Besocke. An Easily Operable Scanning Tunneling Microscope. *Surf. Sci.*, 181:145, 1987.

[59] M. Wilms, M.Schmidt, G. Bermes, and K. Wandelt. New and versatile ultrahigh vacuum scanning tunneling microscope for film growth experiments. *Rev. Sci. Instr.*, 69(7):1149001, 1998.

[60] T. Michely. Ph.D. Thesis, University of Bonn, Germany, 2004.

[61] *http://whs-sondermetalle.de/*. WHS Sondermetalle.

[62] I. Horcas, R. Fernandez, M.J. Gomez-Rodriguez, J. Colchero, J. Gomez-Herrero, and A.M. Baro. Wsxm: A software for scanning probe microscopy and a tool for nanotechnology. *Rev. Sci. Instrum.*, 78:013705, 2007.

[63] D. Dickertmann, F. Koppitz, and J.W. Schultze. Method for Eliminating Side Effects in Electrochemical Measurements on Single Crystals – Tests With the Aid of the Adsorption Systems Ag/Pb Two Plus and Au/Cu Two Plus. *Electrochimica Acta.*, 21:967, 1976.

[64] Elias Vlieg. Integrated Intensities Using a Six-Circle Surface X-ray Diffractometer. *JAC*, 30:532, 1997.

[65] *http://henke.lbl.gov/optical_constants/getdb2.html*, 2011.

[66] F. Richarz, B. Wohlmann, U. Vogel, H. Hoffschulz, and K. Wandelt. Surface and electrochemical characterization of electrodeposited PtRu alloys. *Surf. Sci.*, 335:361, 1995.

[67] T. Mayer, M. Lebedev, R. Huger, and W. Jägermann. Elementary processes at semiconductor/electrolyte interfaces: perspectives and limits of electron spectroscopy. *Surf. Sci.*, 335:361, 1995.

[68] C.Y. Nakakura, G. Zheng, and E.I. Altman. Atomic-scale mechanisms of the halogenation of Cu(100). *Surf. Sci.*, 401:173, 1998.

[69] H.C.N. Tolentino, M. De Santis, Y. Gauthier, and V. Langlais. Chlorine chemisorption on Cu(001) by surface X-ray diffraction: Geometry and substrate relaxation. *Surf. Sci.*, 601:2962, 2007.

[70] C.Y. Nakakura and E.I. Altman. Scanning tunneling microscopy study of the reaction of Br, with Cu(100). *Surf. Sci.*, 398:281, 1998.

[71] E. Riedel and C. Janiak. *Anorganische Chemie*. de Gruyter, 2004.

[72] A. Hommes, A. Spaenig, P. Broekmann, and K. Wandelt. Low coverage p(2x2) iodide phase on Cu(100). *Surf. Sci.*, 547:239, 2003.

[73] J.G. Dillard, L.T. Taylor, R.D. Seals, and R. Alexander. *Inorg. Chem.*, 12:2485, 1973.

[74] C.D. Wagner, J.F. Moulder, L.E. Davis, and W.M. Riggs. Perking-Elmer Corporation, Physical Electronics Division.

[75] W. Ostwald. Über die vermeintliche Isomerie des roten und gelben Quecksilberoxyds und die Oberflächenspannung fester Körper. *Z. phys. Chem.*, 34:495, 1900.

[76] L.-Q. Wang, A.E. Schach von Wittenau, Z.G. Ji, L.S. Wang, Z.Q. Huang, and D.A. Shirley. c(2x2)Cl/Cu(001) adsorbate geometry and substrate-surface relaxation using low-temperature angle-resolved photoemission extended fine structure. *PRB*, 44:1292, 1991.

[77] M. Röefzaad and K. Wandelt. In Preparation. .

[78] S. Raugeia and M.L. Klein. An ab initio study of water molecules in the bromide ion solvation shell. *J. of Chem. Phys*, 116:196, 2001.

[79] M. Carrillo-Tripp, H. Saint-Martin, and I. Ortega-Blake. A comparative study of the hydration of Na^+ and K^+ with refined polarizable model potentials. *J. of Chem. Phys*, 118:7062, 2003.

[80] G.-J. Su, H.-M. Zhang, L.-J. Wan, C.-L. Bai, and T. Wandlowski. Potential-induced phase transition of trimesic acid adlayer on au(111). *J. Phys. Chem. B*, 108:1931, 2004.

[81] X. Liu, K.G. Neoh, and E.T. Kang. Viologen-Functionalized Conductive Surface: Physicochemical and Electrochemical Characteristics, and Stability. *Langmuir*, 18:9041, 2002.

[82] T.M.H. Nguyen. *Preparation and characterization of copperiodide thin films and organic supramolecular layers at copper/electrolyte interfaces*. Ph.D Thesis, University of Bonn, Germany, 2007.

[83] P. M. Vereecken, R.A. Binstead, H. Deligianni, and P.C. Andricacos. The chemistry of additives in damascene copper plating. *IBM J. of Res. and Dev.*, 49:3, 2005.

Acknowledgment

I would like to thank all those, who made this work possible, who supported it or accompanied me in this period of my life. Among those some particular individuals have to be distinguished:

Professor Dr. Klaus Wandelt for giving me the opportunity to perform this research in his group, at the Institute of Physical and Theoretical Chemistry of the University of Bonn. His enthusiastic guidance, suggestions and extensive support in scientific questions and beyond were invaluable.

Professor Dr. Rudolf Merkel, Professor Dr. Sigurd Höger and Professor Dr. Wilhelm Barthlott for dedicating a part of their limited time to the evaluation of my thesis and the related exam, which makes this publication possible at all.

Professor Dr. Sigurd Höger, Ute Müller und Manfred Müller for the synthesis of the organic molecules.

Martin Böhmer and all members of the electronic workshop, Heinz-Peter Königshoven and all members of the precision mechanical workshop, Knut Hintzen from the IT office and Beatrix Jurofsky form the purchase office for their help.

Professor Ueli Heiz, PD Dr. Friedrich Esch and M.Sc. Sarah Wieghold from the Technische Universität München for their support in the final stage of my thesis.

My particular gratitude goes to Anne Kirschfink and Hamed Alaei, for their extraordinary commitment in solving any kind of problem throughout my PhD study. Stephan Breuer for the support, supervision and discussions related but not limited to the XPS experiments, as well as his companionship during our time at the University of Bonn. Dr. Duc-Thanh Pham and Dr. Nguyen Thi Minh Hai for their introduction to the EC-STM setup and especially tip etching procedure. Dr. Patrick Meisner, Tobias Pertram, Michael Schneider, Dr. Knud Gentz, Dr. Melanie Röefzaad, Dr. Christian Schlaup, Dr. Jan Haubrich and Dr. Enrico Barletta for their help in solving numerous problems, for their advices and their support in various scientific questions.

Finally M.Sc. Emilia Sak-Saracino for her extensive scientific and moral support during my whole research at the University of Bonn and the analysis/writing at home, as well as the other members of my family for their continuous unconditional support.